UNDERSTANDING THE PHYSICAL PHENOMENA LIMITING THE INKJET PRINTED PEM WATER ELECTROLYZER PERFORMANCE

by

Manas Kumar Mandal

A thesis submitted in partial fulfillment of the requirements for the degree of

Doctor of Philosophy

Department of Mechanical Engineering
University of Alberta

©Manas Kumar Mandal, 2022

Abstract

Polymer electrolyte membrane water electrolysis (PEMWE) are a promising technology to generate hydrogen using electricity from renewable sources of energy and water. The hydrogen can be used to reduce the emission of greenhouse gases in a number of industrial processes, such as power grid, fertilizer industry, and transportation sector. PEMWE cells however suffer from high cost and low performance and durability. The focus of this thesis is to find the physical phenomena limiting the PEMWE cell performance and propose novel electrode designs that could reduce these limitations. To achieve above goal, a catalyst layer (CL) fabrication method capable of manufacturing well controlled CL, is required, as the PEMWE cell performance is highly dependent on the CL manufacturing method, composition, and microstructure.

In the first part of the thesis, a novel fabrication method, inkjet printing, was used to fabricate the CLs. Its drop-by-drop deposition allows for precision deposition of catalyst ink. An unsupported IrO_2 catalyst ink suitable for jetting was developed. After depositing IrO_2 CLs on the membrane, various ex-situ methods were used to characterize the surface and thickness of the CL and in-situ methods were used to obtain a measure of electrochemical surface area (ECSA), kinetic parameters, and cell performance. Scanning electron microscopy (SEM) images showed the CL was uniform and well adhered to the membrane. Energy dispersive X-ray spectroscopy imaging showed even distribution of catalyst and ionomer in the CL. A kinetic study revealed Tafel slopes similar to those in literature, however the exchange current

density was lower, showing that the catalyst might not be very active. Still, the electrochemical performance outperformed most of the previously reported results in literature. The catalyst coated membranes (CCMs) also showed stable performance when tested for 24 hours. These results suggested that the inkjet printing can be used to fabricate electrolyzer electrodes with great control and good performance.

A novel setup utilizing a hydrogen pump technique was developed to measure the protonic conductivity of the IrO_x CL for the first time in PEMWE literature. The through-plane electronic conductivity of the anode CL was also measured using a two-probe method. The conductivities were obtained with varying ionomer loading. The measured conductivities showed that the limiting charge transport parameter in the studied IrO_x catalyst can be either protonic or electronic depending on the ionomer loading in the CL. A second catalyst made of Ir black was also studied. In this case, protonic conductivity was found to be always limiting. The implication of the obtained results is that the oxygen evolution reaction would be more active at CL–membrane interface for the Ir CL and at CL–porous transport layer (PTL) interface for the IrO_x CL with an ionomer loading above 15 wt.%. These results suggested that there might be an optimal catalyst and ionomer loading for each catalyst material to achieve a high catalyst utilization that depends on protonic and electronic CL properties, as well as catalyst activity.

The porosity of the PEMWE cell anode CL is low due to the use of an unsupported catalyst (typically Ir/IrO_x), possibly resulting in mass transport losses and low CL surface area. By increasing the porosity of the anode CL, it is hypothesized that mass transport losses will be alleviated, and more catalyst surface area will be exposed to the reactant. Addition of carbon to the Ir or IrO_x catalyst ink was investigated for the first time in literature to increase the porosity of the anode CL. The Ir and IrO_x CL porosity increased from 58% to 71% and from 23% to 41%, respectively, even without removing carbon. Then added carbon was oxidized in-situ to create further pore spaces. SEM images revealed that by adding carbon decreased the CL cracks. With an increase in the CL porosity, the ECSA of CCMs with Ir increased and CCMs with IrO_x, first, increased and then decreased. The decrease might be due to the detachment of the catalyst from the IrO_x CL as seen from SEM images. The CCMs with Ir showed an improved performance at low current density due to the increased ECSA and at high current density due to the decreased high frequency resistance (HFR). At 1.8 V, the current density increased from 3.16 to 3.70 A/cm^2 with increasing carbon content for Ir CCMs. The reason for the decreased HFR is hypothesized to be due to better contact between the PTL and the Ir CL, as identified by SEM imaging showing PTL fibers indenting into the CL. On the other hand, the CCM with IrO_x catalyst showed improved cell performance at lower current density due to the increased ECSA but did not at higher current density due to increased HFR. The increased HFR might be due to the increased CL thickness with carbon content, which increased the proton transport resistance of the IrO_x CL. A short-term degradation test of CCM with Ir showed improved degradation from 626 to 529 $\mu V/h$ with carbon addition. Volcano-shaped cracks, observed in post operation Ir CL without carbon, disappeared with the addition of carbon. These cracks are hypothesized to be caused by high gas pressures within the CL, which are reduced due to improved mass transport. These results demonstrated that, for Ir catalyst, the addition of carbon can improve both cell performance and CL integrity. On the other hand, CCMs with IrO_x catalyst had a beneficial impact at low current density only.

Overall in this thesis, different aspects of CL development were studied in order to improve the PEMWE cell performance. Firstly, a novel fabrication technique capable of fabricating well controlled CLs was developed. Secondly, a novel setup was developed to measure the proton transport resistance of the anode CL. And

finally, the CL porosity was increased using carbon, thereby enhancing the PEMWE cell performance.

Keywords: Inkjet printing, catalyst layer conductivity measurement, pore former

Preface

Parts of chapter 2 of this thesis have been published as M. Mandal, A. Valls, N. Gangnus, and M. Secanell, “Analysis of Inkjet Printed Catalyst Coated Membranes for Polymer Electrolyte Electrolyzers”, *Journal of The ELectrochemical Society*, 2018, Volume **165**, Issue 7, pp. F543–F552. I was responsible for electrode fabrication method review, catalyst coated membrane fabrication, testing, data analysis, and manuscript writing. A. Valls was responsible for developing the initial catalyst ink, software used to record the polarization curve and preliminary electrolyzer testing. N. Gangnus was responsible for the development of the experimental setup. M. Secanell was the supervisory author and contributed with the concept formation, intellectual guidance, and helped shape the manuscript objective, manuscript composition and editing.

Parts of chapter 3 of this thesis have been published as M. Mandal, M. Moore, and M. Secanell. “Measurement of the Protonic and Electronic Conductivities of PEM Water Electrolyzer Electrodes”, *ACS Applied Materials and Interfaces*, 2020, Volume **12**, Issue 44, pp. 49549–49562. I was responsible for the literature review, catalyst coated membrane fabrication, testing, data analysis, and manuscript writing and revision. M. Moore helped with the numerical model development and implementation, and helped in reviewing the manuscript. M. Secanell was the supervisory author and helped with the manuscript concept, writing, and review.

Parts of chapter 4 of this thesis was submitted for publication as M. Mandal and M. Secanell. “Improved Polymer Electrolyte Membrane Electrolyzer Performance by using Carbon Black as a Pore Former in the Anode Catalyst Layer” *Journal of Power Sources*, XX, XXX. I was responsible for the catalyst coated membrane fabrication, testing, data analysis and manuscript writing. M. Secanell was the supervisory author and helped with the manuscript objective, writing, and review.

To my mother

Acknowledgements

Throughout the writing of this thesis, I received a great deal of support and assistance. First and foremost, I would like to thank my supervisor, Professor Marc Secanell, for providing me the opportunity to be part of his research group and to pursue cutting edge electrolyzer research under his guidance. Over the years, he has been a constant source of inspiration and motivation for me and I have gained valuable lessons about conducting research. His ability to bring out the best in everyone has helped me to gain a scientific mindset and raise the bar on the quality of my work. His profound belief in my abilities, constructive criticism, insightful advise, and boundless patience saw me through the highs and lows of my time here as a graduate student. Had it not been for his guidance and support, I doubt that this thesis would have ever been written.

I would like to thank Michael Moore at Energy Systems Design Laboratory (ESDL), University of Alberta, for developing and implementing the modelling work required to verify the results obtained in the third chapter of the thesis and for many many insightful technical discussion regarding the conductivities of the catalyst layers helped shape the third chapter.

I acknowledge the financial support from Future Energy Systems (FES). As a part of the University of Alberta Future Energy Systems research initiative, this research was made possible; thanks to funding from the Canada First Research Excellence Fund (https://futureenergysystems.ca; Grant No. T06-P04).

I would like to thank my colleagues and friends at the ESDL for helping me out on a number of occasions and ease out the stress during the graduate studies by organizing many outdoor activities such as camping, canoeing, and indoor activities such as beer sessions and cooking sessions. The time we spent together were fun and will be cherished.

Saving the best for the last, I would like to acknowledge my family for the emotional support and unconditional love that really made all the difference. Firstly, my parents, who are the reason why I was able to received a great education. They have been a source of love and encouragement for me and without their emotional support, it would have been impossible to stay away from home all this time. Secondly, my beloved wife, Shobha, who believed in me all this time and was there for me during the long working hours cooking the delicious foods, that kept me going.

This thesis would not have been made possible without the support and guidance of these people. Thank you everyone :).

Contents

List of Tables

List of Figures

Chapter 1

Introduction

1.1 Motivation

Over the past 100 years, the greenhouse gas (GHG) emission rate has increased from 5 Gt/yr to 30 Gt/yr due to deforestation, the use of fossil fuels, and other human-related activities [1–3]. There is now great concern about the impact of climate change, such as increasing number of forest fires, heavy rains, and cyclones, [4, 5] which is due to the increase in GHG in the atmosphere [6].

The amount of energy consumed each year from different fuel sources has steadily increased, with currently more than 80% of the world's energy coming from fossil fuels [7, 8]. The transportation sector alone consumed nearly 30% of the primary energy in the US and Canada, mostly in the form of fossil fuels [9, 10]. Emissions from fossil fuels continue to increase as we burn more each year for energy.

In order to limit GHG emission from fossil fuels, its consumption must be reduced by increasing the use of renewable energy. As of 2019, only around 17.3% of the total primary energy consumption in Canada came from renewable sources of energy [11]. Canadian government pledged to reduce its GHG emissions by 30% of the 2005 value by 2030 and by 80% by 2050 [12] and Alberta is committed to producing 30% of its electricity with renewable energy by 2030 [13].

Renewable energy sources, such as wind and solar, are intermittent, making it difficult to match supply and demand. In order to match seasonal supply and demand, large scale energy storage is required. Among the various energy storage technologies, such as hydrogen, pumped hydro, batteries, super capacitor, and flywheels, hydrogen is one of the few options that can store large quantities of energy, i.e., GWh scale, and over a broad power range [14]. Hydrogen energy storage would allow GWh of excess energy from renewable sources of energy to be used to reduce the use of fossil fuels for electricity, heating, and transportation.

Hydrogen is a versatile fuel that can be produced from many sources such as fossil fuels, biomass, and electricity and water [15]. Most hydrogen produced today comes from steam methane reforming, which results in CO_2 emissions and low purity hydrogen [15, 16]. A safe and environmentally friendly way of producing hydrogen is water electrolysis, using renewable electricity during periods of low electricity demand [17, 18]. The hydrogen produced can then be used to generate heat in a furnace/boiler or electricity and heat in a fuel cell. Hydrogen is now dominantly used directly in industrial processes, such as crude oil refining, upgrading of Fischer-Tropsch Gas-to-Liquid products, and ammonia and urea production [15]. It is easily transported, stored and blended with current fuels [15]. The production of hydrogen using electrolysis and its consumption in heating, fuel cell and industrial processes do not produce GHG, therefore the use of hydrogen could potentially decarbonize a number of energy sectors.

Currently, hydrogen costs about \$5 per kilogram when generated from renewable energy. The U.S. Department of Energy's Energy Earthshots initiative launched the "Hydrogen Shot" program on June 7, 2021 to reduce the cost of clean hydrogen by 80% to \$1 per 1 kilogram in 1 decade. Achieving this goal requires innovations in hydrogen technology.

Several electrolysis technologies have been investigated in the past. The five most prominent are: i) alkaline electrolysis (AE), ii) proton exchange membrane water electrolysis (PEMWE), iii) solid oxide electrolysis (SOE), iv) alkaline exchange membrane water electrolysis (AEMWE), and v) microbial electrolysis (ME) [19]. Of these technologies, AE technology is the most mature while the least developed are SOE, AEMWE and ME, which remain at an early research stage [19, 20]. PEMWE has reached the commercial market, but only for small-scale niche applications. PEMWE technology has been investigated since the 1960s, when General Electric introduced it for its inherent advantages over AE. PEMWE cells are safer compared to AE cells because of the use of a solid electrolyte membrane, which minimizes the gas cross-over and eliminates the use of highly caustic liquid electrolyte in AE cells [21]. PEMWE cell also provide higher purity hydrogen (99.99%) due to better gas separation [22], and they can be made more compact as high current densities (between 2–4 A/cm^2) are possible [23]. Finally, it is also possible to produce pressurized gases directly (70 bar [24], 130 bar [25] and 138 bar [26] have been reported) and even differential pressurization between the anode and cathode (systems with approximately 20 bar and 70 bar pressure difference have been reported [27–31]).

Despite the inherent advantages outlined above, PEMWE cell has not seen widespread utilization/deployment due to its high cost, low availability of the precious catalyst used in the electrodes, and low durability [32–34]. Hence, research and development is necessary to decrease the cost and to improve the performance and durability of PEMWE cells. Numerous studies have been carried out to better understand and optimize the catalyst and electrode [35–44], membrane [45–52], porous transport layer (PTL) [22, 53, 54], bipolar plate [55–58], and auxiliary power unit analysis and design [59]. One way to reduce the cost is by operating the cell at a higher current density [33]. Current densities as high as 5 A/cm^2 have been recorded in recent years [60–62]. However, to increase the current density without increasing the cell voltage, and in turn increasing the overall efficiency, the electrode must be redesigned to increase catalyst utilization and reduce transport losses.

This thesis aims at developing experimental techniques to understand the key limiting factors affecting the cell performance in order to optimize the use of existing materials.

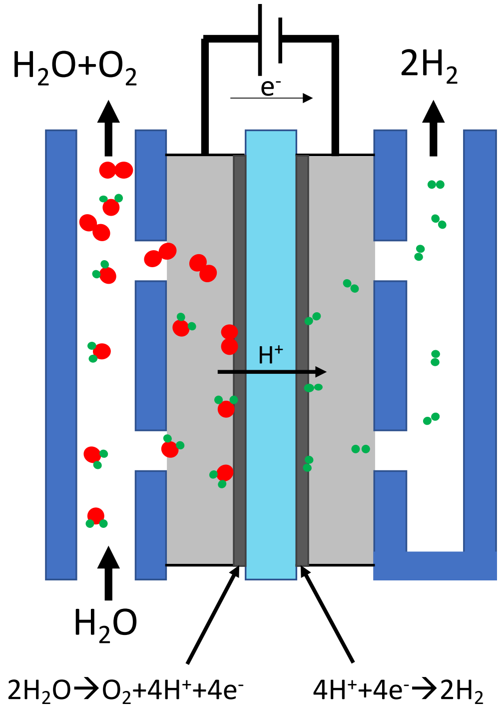

Figure 1.1 – Schematic of the working of the PEMWE cell.

1.2 Literature review

1.2.1 Background

1.2.1.1 Working of the PEMWE cell

An electrolyzer is a system that uses electricity to oxidize the water supplied to the anode into oxygen and produce hydrogen in the cathode. A schematic of the working of the PEMWE cell is shown in Figure 1.1. In the anode water oxidation produces protons and electrons via the oxygen evolution reaction (OER),

$$2H_2O_{(l)} \rightarrow O_{2\,(g)} + 4H^+_{(aq)} + 4e^-_{(s)} \tag{1.1}$$

Protons migrate through the proton exchange membrane (PEM) and electrons through the external electrical circuit to the cathode, where they recombine to produce hydrogen via the hydrogen evolution reaction (HER),

$$4H^+_{(aq)} + 4e^-_{(s)} \rightarrow 2H_{2\,(g)} \tag{1.2}$$

1.2.1.2 Construction of the PEMWE cell

The PEMWE cell hardware consists of a PEM, CL, PTLs, bipolar plates, current collector plates, and end plates. A schematic of the PEMWE cell hardware is shown in Figure 1.2. The hearts of the PEMWE cell are the CLs, where the electrochemical reactions (OER and HER) take place. The anode and cathode CLs are separated by a PEM (typically Nafion), which prevents product gases from mixing.

PTLs are kept in contact with the CL to aid transport of reactant, products, charge, and heat. A titanium PTL is used on the anode side of the cell, as the highly electro-oxidative environment in the anode prevents the use of carbon materials. A carbon based PTL is used on the cathode side of the cell to minimize the cost and enhance the electronic conductivity.

Produced gases are transported through the CLs and PTLs to the channels in the bipolar plates. As the anode is flooded with water, the oxygen produced will be transported as bubbles. These bubbles are thought to hinder the transportation of water to the catalyst active sites when operating at high current density [63, 64]. The bipolar plates are used to distribute the water evenly on the anode side and to remove gases produced in anode and cathode. A titanium bipolar plate is usually used on the anode side, whereas a graphite bipolar plate is used on the cathode side. End plates are used to provide a uniform pressure distribution between the various components of the electrolyzer cell and consequently reduce the contact resistance between them. In order to achieve a high cell performance, the transport of reactants, products, charge, and heat must be optimized, and a catalyst must be used in the electrodes to activate the electrochemical reactions.

1.2.1.3 Catalyst layer fabrication

In order to study the impact of the parameters that control the CL microstructure and transport properties, first it is important to understand how a CL is manufactured. A schematic of a conventional CL is shown in Figure 1.3. PEMWE cell CLs are thin (i.e., 5-10 μm) and porous. They are composed of catalyst nanoparticles,

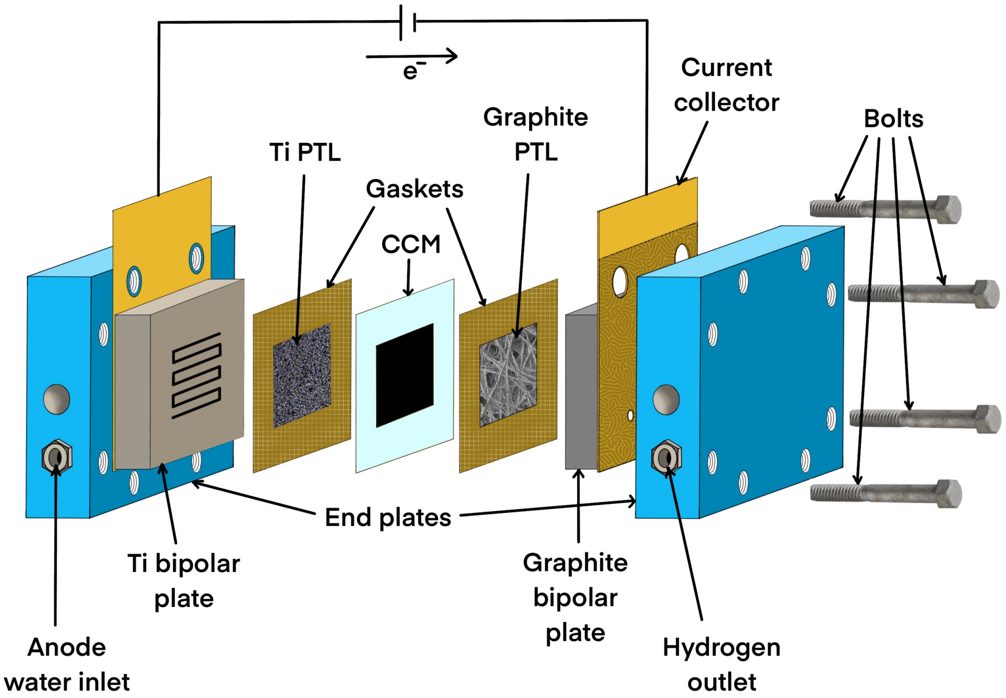

Figure 1.2 – PEMWE cell exploded view.

which can be either supported or unsupported and an ionomer, usually a perfluorosulfonic acid (PFSA) polymer. The catalyst is used to activate the electrochemical reactions and also to provide a path for electron transport. A proton conducting polymer transport protons through the CL. Pores provide a path for reactant and product gas transport. An optimal CL structure should contain an optimal amount of each material, a well-connected network of pores with an optimized pore size distribution to aid reactant (liquid) and product (gas) transport, numerous well-dispersed catalyst active sites to enhance the reaction rate, and a well-connected catalyst and ionomer phase to minimize electron and proton-transport resistances.

Metal or metal oxides (e.g., Ir, IrO_x, and RuO_2) are used as the anode catalyst because they have been shown to have the highest activity towards the OER [33, 65, 66]. IrO_2 is usually used as the standard catalyst because it achieves a good balance between the performance and the stability as the oxidation of RuO_2 to RuO_4 occurs at a potential above 1.39 V. This will dissolute RuO_4 as the PEMWE cell operates at a higher potential [67]. In some cases, a catalyst support is also used to increase the

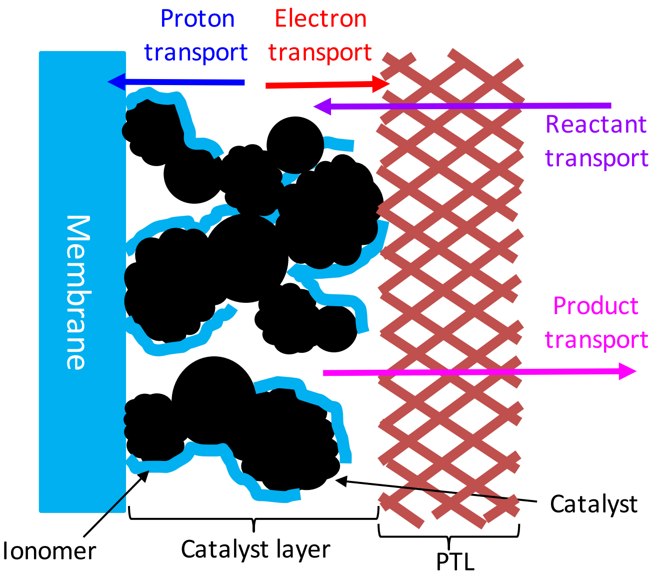

Figure 1.3 – Schematic of the catalyst layer microstructure.

catalyst utilization.

Platinum nanoparticles are used as the cathode catalyst as it is the most active material for the HER [65, 66]. To increase the Pt utilization, Pt supported on a porous carbon, such as Vulcan or Ketjen black, is used. Pt/C is not likely to be replaced as the HER catalyst of choice for PEMWE application in the near future, as non-platinum group metal catalysts are yet to achieve the level of activity and durability of the Pt [66].

1.2.1.4 Factors affecting PEMWE cell performance

PEMWE cell performance depends on various parameters such as operating conditions (e.g., temperature [45, 68], pressure [26, 68], and water flow rate [68]), membrane type and thickness [45, 46, 69], assembly pressure [70], PTL type and thickness [22, 71], catalyst loading [72] and type [73], ionomer loading and type [72], CL thickness [74], CL structure (including porosity, pore size distribution), and pH of the water [66, 75].

The performance of a PEMWE cell is usually assessed by means of a polarization

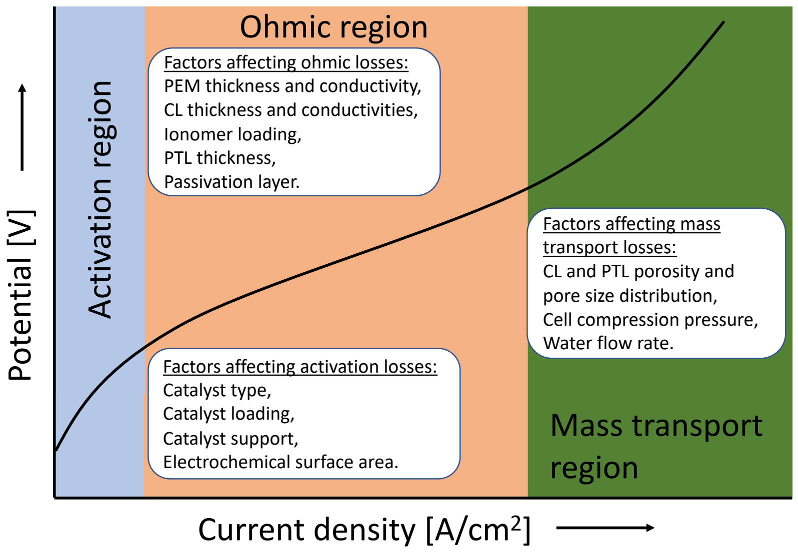

Figure 1.4 – Conceptual representation of performance factors of polarization curve.

curve, which is a plot of the current density against the cell voltage. While an ideal electrolyzer would exhibit a straight horizontal line at a voltage determined by its Nernst potential, various irreversible energy losses result in the voltage increase as the operating current density increases. Figure 1.4 shows a typical polarization curve of a PEMWE cell where three distinct regions can be observed [76]: i) activation region at low current density, ii) ohmic region in the intermediate current density where ohmic resistance becomes predominant, and iii) mass transport region at higher current density.

1.2.1.4.1 Activation region

In this region, an increase in the cell voltage is caused by the overpotential required to overcome the activation energy of the electrochemical reactions on the catalytic surface [63]. This type of loss dominates at low current density until the ohmic resistance starts to become significant. The HER overpotential is usually small because of the fast kinetics of the reaction [77, 78]. The OER overpotential is usually much higher due to the sluggish four-electron reaction [66, 77] and it is therefore the most significant source of voltage loss. Due to the sluggish nature of the OER, highly active catalysts and large active surface area are required to facilitate the reaction, with CL design focusing on maximizing the number of active sites for the reaction. Some key properties of the CL, such as catalyst loading, type of catalyst, and catalyst dispersion play a role in determining the number of active sites and activity and in turn determine the potential losses occurring in this region [33, 76, 79, 80].

For any electrochemical reaction, the simplest model that can be used to predict the current produced in the anode at moderate overpotentials is the Tafel equation [81], which is shown here to illustrate key parameters that can be controlled to reduce the activation losses, i.e.,

$$j = m_{cat}\ A_0\ j_0^{eq}\ \left[\prod_{i=1}^{N}\left(\frac{c_i}{c_i^{eq}}\right)^{\nu_i}\right]\ exp\left(\frac{\alpha F}{RT}\ \eta_{act}\right) \tag{1.3}$$

where j is current density (A/cm^2 CL), m_{cat} is the catalyst loading (g/cm^2 CL), A_0 is the specific electrochemical surface area (ECSA) (cm$^2_{cat}$/g), j_0^{eq} is the exchange current density (A/cm$^2_{cat}$), c_i is the concentration of the reactant at the catalyst surface, c_i^{eq} is the reference concentration used to calculate E^{eq}, α is the charge transfer coefficient, F is Faraday constant, R is the universal gas constant, T is the temperature and η_{act} is the activation overpotential ($\eta_{act} = \phi_s - \phi_{electrolyte} - E^{eq}$), where ϕ_s is the solid phase potential, $\phi_{electrolyte}$ is the electrolyte phase potential, and E^{eq} is the Nernst potential for the half-cell reaction at the given reference concentrations.

There have been numerous attempts in literature to reduce activation losses, which are categorized as follows:

1. Developing novel catalysts with increased intrinsic activity towards the OER [82, 83]. In Equation (1.3), j_0 and α are intrinsic to a given catalyst material and surface state, therefore they require the use of new materials and synthesis methods. Synthesis of the catalyst is, however, not considered in this thesis.
2. Increasing the catalyst utilization by finding the optimal catalyst loading that provides large total surface area in the CL, while keeping transport losses to a minimum [40, 69, 72, 74, 84, 85]. An optimal value will exist for each catalyst, and therefore catalyst loading optimization is better address by numerical

simulation once a well-validated numerical model has been developed. In this work, CL characterization tools will be developed to better understand the relationships between catalyst type and loading, ECSA and transport properties, thereby aiding in the development of numerical models for CL optimization.

3. The third way of decreasing activation losses is by increasing the specific ECSA, i.e., $\frac{cm^2 catalyst}{cm^3 CL}$, for the same catalyst loading. This can be achieved by:

   (a) The optimal dispersion of the catalyst. Rather than using bulk catalyst in the CL, nano particles can be dispersed on a support, as is done in the hydrogen CL, where platinum is supported on carbon black [86–92]. Some supports characterized in literature are indium tin oxide (ITO) [93], TiO_2 [94, 95], antimony doped tin oxide (ATO) [91], SiC–S [90], and metal carbides [89]. There are numerous articles on the topic of catalyst support characterization for PEMWE [86–92], hence, this path was not taken to study the activation losses.

   (b) Increasing particle surface roughness for a given particle size. For example, Tan et al. [96] synthesized a pompon-like Ir superstructure with a high surface roughness. Various methods can be used to increase particle surface roughness, such as modifying the particle morphology. Since the aim of the thesis is the development of electrodes with existing catalyst, this route was not explored.

   (c) Enhancing the catalyst-electrolyte surface area. It might be achieved by changing the CL microstructure. For example, it is hypothesized that, by increasing porosity of the CL, more catalyst surface area might be exposed to the electrolyte. An increased porosity can be achieved by decreasing catalyst particle size [97] or by using pore formers [98]. ***One of the aims of this thesis is to study the effect of the anode CL porosity on the ECSA and PEMWE cell performance.***

   The catalyst-electrolyte surface area can also be enhanced by improving the dispersion of the catalyst and ionomer in the CL to achieve a good cell performance with low catalyst loading [99]. Uneven dispersion of ionomer will lead to a lower catalyst utilization. An appropriate fabrication method which helps in uniform distribution of CL materials onto the substrate is required. ***One of the aims of this thesis is to develop the CL fabrication method to control the parameters affecting the CL microstructure.***

1.2.1.4.2 Ohmic region

The potential drop in the ohmic region arises from the resistance to electron flow through the electrodes and cell components, as well as the resistance to the flow of protons through the CL and the membrane [100]. The ohmic losses become significant at mid to high current densities [101]. Some key properties that play a role in determining the ohmic losses are catalyst loading, ionomer content in the CL, membrane and CL protonic conductivity, membrane and CL thickness, contact resistance between the layers, and electronic conductivity of the PTLs [76]. The protonic resistance of the membrane and CL, and the electronic resistance of CL and all other cell components result, usually, in a linear voltage loss with current density. A thin membrane capable of maintaining low gas cross-over and an appropriate cell design are required to keep these resistances as low as possible.

Previous studies in the literature aimed at reducing ohmic losses. The proton transport resistance was reduced by:

1. Increasing the conductivity of the membrane. This would require developing new membrane materials or a new membrane fabrication technique [102, 103].

2. Using thinner membranes. However, hydrogen cross-over would increase with a thinner membrane. If cross-over can be mitigated, while using the thinner membrane, for example by using recombination to reacting hydrogen that crosses over, then the efficiency of the PEMWE cell can be improved [104].

3. Increasing the ionomer content in the CL. However, since there exists an optimum ionomer loading for a given CL, increasing ionomer content may decrease CL porosity, leading to a reduced reactant/product transport, and increase the

electronic resistance as the ionomer prevents good contact between catalyst particles [52, 105].

Methods of decreasing the electronic resistance are:

1. Reducing the ionomer content in the CL. A trade-off exists between the protonic and electronic resistance. The ionomer might wrap around the catalyst particles [106] reducing the particle connectivity and removing electron conducting pathways, however the ionomer is needed for proton conductivity.
2. Decreasing PTL thickness. Mo et al. [71] decreased electronic resistance by decreasing the PTL thickness. However, a trade-off exist between electrical resistance and mass transport, since a thin PTL might not be able to effectively transport reactant/product to the channel from under the land areas.
3. Minimizing the formation of a passivation layer, which leads to an increase in the contact resistance over time. Platinum coated Ti PTL and bipolar plate are used to avoid passivation [107, 108].

Given the trade-offs between electron and proton transport losses, it is important to understand the type of ohmic losses limiting the cell performance, so that an optimal ionomer and catalyst loading can be achieved. To the author's knowledge, no studies in the literature have reported the protonic and electronic resistances of the CL explicitly. Without this information, it is difficult to determine the optimal ionomer loading. ***One of the objectives of this thesis is to develop a technique to measure the protonic and electronic resistance of the CL.***

1.2.1.4.3 Mass transport region

At higher current densities, voltage losses might be induced when oxygen gas bubbles partially block the liquid network in the CL and PTL, thus limiting the mass transport of water to active sites [63, 64]. Properties such as the layer porosity, pore size distribution, and the cell compression pressure will determine how well water is transported through each layer [76]. Mass transport losses have been neglected by many authors because transport limitations in thin electrodes have been shown to be insignificant until 3 A/cm^2 as compared to the other losses [85, 101, 109–111], and

PEMWE cells usually operate at lower current densities. Indeed, no mass transport losses were observed till 20 A/cm^2 for one cell construction [61].

The performance of a PEMWE cell can change during cell operation due to the accumulation of product gases within an electrode resulting in unreliable performance (stability), and during its lifetime due to the chemical and mechanical degradation of cell components [112]. The transient performance of the cell can be studied by current holds and accelerated tests [112]. In this thesis, however, research was restricted to the beginning of life performance of the cell. Degradation studies were not conducted due to the limited number of experimental test stations, making long term testing prohibitive.

The performance of PEMWE cells are highly dependent on the anode CL microstructure and hence, the focus of the thesis is to understand the parameters that effect the ECSA and transport properties of the anode CL. Before any study on the anode CL could be performed however, a fabrication technique that could be used to manufacture well-controlled anode CLs with a variety of catalyst, different ionomer loading, and with pore formers was needed.

1.2.2 Electrode fabrication

Membrane electrode assembly fabrication can influence the performance of the PEMWE cell as well its operational lifetime [113]. The catalyst ink formulation, catalyst deposition method and substrate, ionomer and catalyst loading, porosity of the CL, and gas diffusion layer (GDL)/PTL, all influence the PEMWE cell performance.

Over the past three decades, a variety of CL fabrication methods and CL substrates have been explored in the literature. Irrespective of the CL fabrication method, the CL can either be deposited on GDLs/PTLs or membranes. If CLs are coated directly on the GDL or the PTL, the new layer is known as catalyst coated gas diffusion electrode (GDE) or catalyst coated porous transport electrode (PTE). To make the membrane electrode assembly (MEA), a PEM is sandwiched between two GDEs or

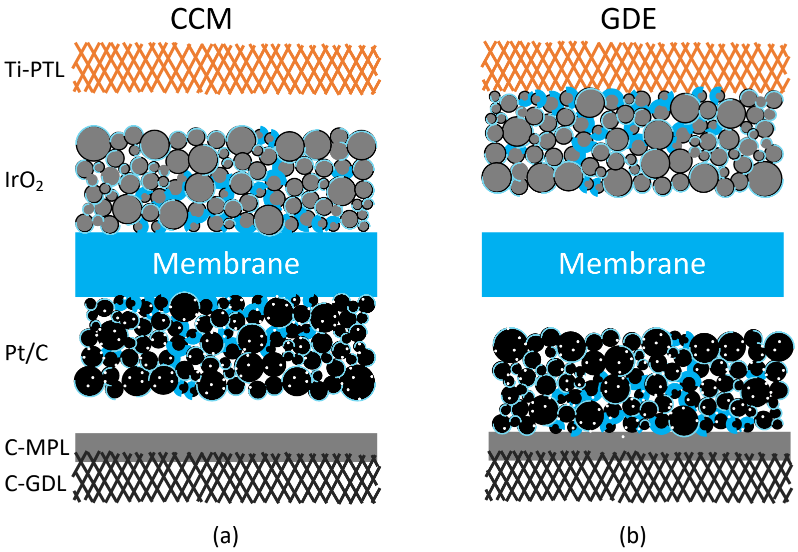

Figure 1.5 – State-of-the art membrane electrode assembly fabrication methods: (a) schematic of the catalyst coated membrane (CCM) fabrication method, and (b) schematic of the gas diffusion electrode (GDE) or the porous transport electrode (PTE) fabrication method.

PTEs. If CLs are deposited directly on a membrane, then it is called a catalyst coated membrane (CCM). An MEA is then manufactured by sandwiching the CCM between two PTLs. A schematic of the two MEA fabrication processes is shown in Figure 1.5.

GDEs/PTEs have three technical problems: i) structural deformation due to the hot pressing step, ii) catalyst loss through the porous PTL, and iii) poor protonic conduction between the CL and PEM [113–115]. CCMs are known to offer higher cell performance than GDEs/PTEs due to a better PEM-CL interface [113, 116–119]. CCM fabrication by direct catalyst coating to the PEM is simpler and more efficient than by indirect coating, since the transfer of the CL to the membrane after coating on a sacrificial substrate is not required [116]. Hence, in this thesis, CLs were deposited on the PEM.

To understand the parameters that affect the PEMWE cell performance, a suitable CL manufacturing method capable of achieving accurate control of CL parameters, such as porosity, catalyst and ionomer loading, is required. CLs are usually fabricated by either dry or wet deposition methods. The main difference between the two is that in wet methods first a catalyst ink or slurry is fabricated and then deposited instead of the dry, direct deposition of the materials. Examples of dry deposition methods are dry catalyst spraying [120], chemical vapour deposition (CVD) [76, 117], and physical vapour deposition (PVD) [40, 76, 117]. Examples of wet deposition methods include hand-brushing [121], screen-printing [122], doctor blade [116], roll-coating [123], spraying [124], electrodeposition [125], and electro-spraying [126].

All CL fabrication methods have their own advantages and disadvantages. The dry spraying method was developed at German aerospace center (DLR), where a dry mixture of catalyst powder and dry ionomer was deposited on a GDL or membrane [120]. The method is very fast and avoids the use of any solvents and drying steps during the CL fabrication. It might allow continuous production for industrial purpose. The main disadvantage of the dry catalyst spraying method is large ionomer particle size and heterogeneous distribution, which limit high cell performance [120]. Chemical and physical vapour deposition methods are good for low catalyst loading CLs, but are expensive due to costs associated with clean rooms, catalyst targets, and ultra-high vacuum equipments. Moreover, the electrolyte cannot be deposited simultaneously with the catalyst [127]. Therefore, there was a visible drop in performance at very high current densities [117].

In wet deposition methods, a catalyst ink composed of catalyst and ionomer dispersed in an organic solvent is deposited on a substrate [40, 44, 74, 84]. This method is known to cast a continuous network of ionomer that enhances the proton transport [117]. Fabrication methods such as brush painting, screen printing, and doctor blade are cheaper in terms of equipment and operating cost, but the CL thickness uniformity [74], CL surface smoothness [121, 122], and catalyst loading [121] are difficult to control, which limits their ability to create functionally graded CLs. For screen printing, another drawback is that larger particles tend to clog the screen and produce irregular patterns on the substrate surface [121]. Roll-coating facilities are difficult to set up and optimize for a given job and are better suited to large-scale, high-speed production [128]. Spraying method could produce more uniform distribution of catalyst material, however a considerable amount of catalyst wastage occurs in the feed line due to periodic clogging which could increase the cost of production. The electrodeposition method is capable of producing low platinum loading of 0.05 mg/cm^2, however a dendritic structure is likely to form leading to an inhomogeneous surface. The performance of the polymer electrolyte membrane fuel cell (PEMFC) varied due to the CL fabrication method, even with the similar CL composition [129–132]. Table 1.1 shows a comprehensive list of the fabrication methods used for the PEMWE CL fabrication.

A promising approach for CCM fabrication is inkjet printing (IJP) because the method, based on drop-by-drop deposition, allows for precise deposition control enabling the fabrication of low catalyst loading electrodes with high catalyst utilization [129], conventional loading electrodes [130] and patterned electrodes [142]. Patterned electrodes help in reducing the mass-transport losses at the macro-scale by having pathways for the reactant gas and water transport across the electrodes. Further, the method results in a very low catalyst waste. The method was introduced by Towne et al. [128] and Taylor et al. [127], and has been successfully used in PEMFCs for several years [129, 143–145]. However, the IJP method has not been used to fabricate PEMWE cell CLs.

Inkjet printing method appears as a suitable fabrication method for PEMWE cells and therefore, it was studied in this thesis. It is well suited for scientific studies due to its high degree of control and the use of very small amount of catalyst. Given that the anode of a PEMWE cell is commonly based on unsupported iridium or its oxide, however, a substantially different ink for PEMWE cell is needed.

1.2.3 Controlling the catalyst layer porosity

The catalyst in a PEMWE cell is typically unsupported IrO_2, and as a result, the porosity of the CL is low, resulting in high activation and transport losses [74, 146]. As discussed earlier, the activation losses can be decreased by increasing the number of active surface areas. It is hypothesized that increasing the CL porosity might

Table 1.1 – Summary of PEMWE cell CL fabrication methods described in the literature. The numbers in parentheses indicate the loading in mg/cm^2.

Ref.	Fabrication Method	Anode	Cathode	Membrane	Temp [°C]	E [V] @ 1 A/cm^2
[133]	Decal	IrO_2 (3)	Pt black (3)	PFSA	80	1.59
[134]	Decal	IrO_2 (3)	Pt black (0.5)	PFSA	80	1.53
[135]	S-Decal	IrO_2 (4)	Pt black (3)	PFSA	80	1.56
[136]	S-Decal	IrO_2 (0.5)	Pt black (0.5)	N115	80	1.78
[137]	Spraying	IrO_2 (2)	40%Pt/CXC72 (2)	N115	-	1.68
[23]	S-Membrane	IrO_2 (2)	10%Pt/C JM (0.4)	N115	80	1.65
[88]	S-Membrane	IrO_2 (2)	20%Pt/C Etek (0.4)	N115	80	1.65
[138]	S-Membrane	IrO_2 (2)	Pt black (2.5)	N115	80	1.6
[40]	Sputtering	IrO_2 (0.2)	Pt/C (-)	N117	80	1.85
[139]	S-Membrane	IrO_2 (3)	30%Pt/C TKK (0.5)	N112	80	1.66
[38]	S-Membrane	IrO_2 (1.5)	30%Pt/C TKK (0.5)	N1035	80	1.67
[42]	Spraying	IrO_2 (3)	30%Pt/Vul XC72 (0.6)	N115	80	1.72
[84]	Spraying	IrO_2 (0.5)	Pt/C (0.5)	N212	80	1.57
[140]	S-Membrane	IrO_2 (2.5)	30%Pt/C Etek (0.5)	N115	80	1.7
[86]	Decal	IrO_2 (1)	40%Pt/C JM (0.2)	N212	80	1.64
[125]	Electrodeposition	IrO_2 (0.1)	46%Pt/C TKK (0.4)	N112	90	1.6
[74]	Decal	IrO_2 (0.5)	46%Pt/C TKK (0.25)	N115	80	1.72
[69]	Brushing	Ir (1.5)	Pt (1)	N112	80	1.69
[141]	S-Mem	IrO_2-Spectrum (5)	30%Pt/C_{Etek} (0.8)	N115	80	1.9

Abbreviations: *TKK* = Tanaka Corp; *JM* = Johnson Matthey; *Etek* = BASF; S = sprayed catalyst; Mem = membrane; E = Electrodeposition.

increase the active surface area because more catalyst surface might be exposed to the electrolyte. This hypothesis is supported by literature in direct methanol fuel cell (DMFC) that showed an increase in ECSA with increased porosity [147]. The increased porosity might also aid in the removal of gas bubbles from the electrode, thereby leading to a lower overpotential at high current densities.

The porosity of the CL can be increased using pore formers. A pore former is a sacrificial material that is added to the ink during preparation and removed after the CL has been fabricated, leaving behind empty pores. A brief summary of literature on pore formers used in PEMFC is presented in Table 1.2. Pore formers used in PEMFC can be broadly categorized in two groups based on how they were removed after CL fabrication. The first group of pore formers, such as ammonium carbonate [148, 149], ammonium bicarbonate [149], and ammonium oxalate [150], are removed by thermal decomposition. For example, ammonium carbonate and ammonium oxalate completely decomposed to ammonia, water, and carbon dioxide above 130 and 180 °C respectively [148]. The second group is removed by immersing the CL in a solvent. For example, carbonate and bicarbonate of alkali- or alkaline-earth metals can be dissolved in an acid [150, 151] and polystyrene latex microspheres are dissolved in toluene and ethyl acetate [98, 152].

Researchers have utilized pore formers in order to increase electrode specific surface area, porosity, and performance in PEMFC. Huang et al. [147] showed that, in DMFCs, the electrode specific surface area in $\mathrm{cm}^2_{cat}/\mathrm{g}$ increased substantially with an increase in the porosity facilitated by the addition of an MgO nanoparticles in the CL, which were removed by immersing the MEA into a 0.5 M H_2SO_4 aqueous solution overnight. Hartmut et al. [151] reported an improvement in the electrochemical performance of PEMFC by using ammonium carbonate, ammonium oxalate, and carbonate and bicarbonate of alkali- or alkaline-earth metals, which increased the porosity between 0.4–0.75. Using a proprietary pore former, Gamburzev and Appleby [153] were also able to improve the porosity of a PEMFC electrode. Zlotorowicz et al. [98] used monodispersed polystyrene particles with diameters of 0.5 and 1 μm as pore formers in PEMFC. These studies [98, 147–153] have demonstrated that the addition

Table 1.2 – Pore former summary.

Ref.	Pore former used	Electrode type	Fabrication method	Characterization method used	Cell type
[148]	Ammonium carbonate	CCM	Spray	MIP, IV curve, CV, TGA	PEMFC
[149]	Ammonium carbonate and hydrocarbonate	CCM	Spray	SEM, BET, MIP, IV curve, EIS, TGA	DMFC
[147]	Magnesium oxide	GDE	blade-coated	SEM, EIS, IV curve, CV	DMFC
[98]	Polystyrene beads	CCM	Manual spray	SEM, IV curve	PEMFC
[150]	Various	CCM	Spray	SEM, IV curve, EIS	PEMFC
[152]	Polystyrene beads	CCM	Spray	SEM, MIP, CV IV curve, EIS	DMFC

MIP: Mercury intrusion porosimetry, CV: cyclic voltammetry, TGA: Thermogravimetric analysis, SEM: scanning electron microscopy, EIS: electrochemical impedance spectroscopy, BET: Brunauer–Emmett–Teller.

of pore formers can be used to increase the porosity, ECSA, and the performance of PEMFCs. Hence, it may be able to improve the porosity, ECSA, and the performance of a PEMWE. To the author's knowledge, no studies have been performed on the use of pore formers in PEMWEs.

The geometry of pore formers and the associated removal step can adversely affect the electrode pore size distribution, and the membrane and catalyst, respectively. For example, using ammonium carbonate and bicarbonate will generate ammonia during thermal decomposition [148–150]. Song et al. [148] noted that the PEMFC cell performance could decrease due to the presence of these small traces of ammonia [154]. Thermal decomposition requires heating of electrodes to a higher temperature where membrane could get damaged. Inorganic pore formers, on the other hand, might have very large size, e.g., the polystyrene particles used in ref. [98, 152] were 0.5 to 1 µm in size, and /or might have irregular shape and sizes, leading to an excessively large pore size distribution [152].

The choice of material used as pore former and the method to remove it after the CL fabrication have to be carefully chosen to limit the CCM damage. In the case of PEMWE, carbon particles could potentially be used as pore former. Carbon is known to undergo corrosion according to $C + 2H_2O \rightarrow CO_2 + 4H^+ + 4e^-$ at a potential of 0.2 V vs. reversible hydrogen electrode (RHE), with meaningful corrosion occurring between 0.8 and 1 V [33, 155, 156]. A PEMWE cell anode operates under even stronger oxidative conditions, therefore any carbon incorporated in the anode CL will be quickly oxidized to CO_2 during cell operation, thereby eliminating the potentially harmful intermediate steps that are used to remove other pore formers, such as heating or immersing the CCM. This makes carbon an ideal pore former for the anode CL of a PEMWE cell. This thesis will investigate the use of carbon as a pore former to increase the porosity of the anode CL and the resulting impact on ECSA and the PEMWE cell performance.

1.2.4 Electrode Characterization

One of the disadvantages of PEMWEs is their high cost. Cost reductions could be achieved by operating the electrolyzer at high current densities, however this would require reducing ohmic and mass transport overpotentials. The membrane protonic conductivity, PTL electronic conductivity, and CL protonic and electronic conductivities play a critical role in determining the ohmic overpotential [76]. While the membrane protonic conductivity and PTL electronic conductivity have been thoroughly investigated [54, 157–160], the measurement of the CL effective protonic and electronic conductivities are seldom reported in the literature. In order to reduce the cost of PEMWE cell by operating at high current densities, understanding the protonic and electronic conductivity of the CL is necessary.

The electron and proton transport properties are highly dependent on the bulk properties of the constituting materials, as well as the volume fraction and connectivity of the solid and ionomer percolating networks. Therefore, the electronic and protonic resistances of the CLs are likely to change significantly depending on the catalyst used, e.g., iridium vs. iridium oxide, the amount of ionomer in the electrodes, and the fabrication method. As discussed previously, if the amount of ionomer is low, the protonic resistance is likely to be high because a percolating network of ionomer might not form. Increasing the amount of ionomer will reduce the protonic resistance, but it may increase the electronic resistance by reducing the number of contact points between catalyst particles. Further, the ionomer might reduce the CL porosity, leading to a reduction in reactant and product transport [52, 105]. Similarly, the use of either pure metals or metal oxides could severely affect the CL electronic resistance; therefore, developing a methodology to measure protonic and electronic resistances is of paramount importance.

Measuring the protonic and electronic resistances of the PEMWE cell CLs is a challenging endeavour because they are very thin, need to be supported by a substrate, and can easily be damaged by contact. An ex-situ method to measure the protonic resistance of the PEMWE cell anode CLs has not yet been developed, and thus far the CL protonic resistance has only been estimated using either semi-empirical models, e.g., ref [62], or using electrochemical impedance spectroscopy (EIS) with H_2 and N_2, where H_2 is used as the reference/counter electrode and N_2 as the working electrode [161, 162]. Bernt and Gasteiger [62] have reported protonic conductivities of CLs in liquid water in the range of 3.1×10^{-2} to 0.63 S/cm with varying ionomer loading and Babic et al. [161, 162] have reported in the range of 9.4×10^{-4} to 3.2×10^{-2} S/cm for fully humidified CLs, depending on their thickness and the type of PTL used. These methods however have several drawbacks. For example, the method used in ref. 62 assumed an ionomer conductivity equal to that of a membrane despite reports showing a substrate-dependent conductivity that is much lower than in membranes [163], and used a tortuosity value estimated for PEMFC CL. Similarly, the H_2/N_2 EIS method is only easy to interpret when the electronic resistance of the CL is negligible and the potential distribution in the CL is uniform. Both works [62, 161] assumed that the proton transport was limiting, as the electronic resistance of the anode CL was neglected. As will be shown in this thesis, the electronic resistance of CLs made of unsupported IrO_x nanoparticles is not negligible, and the EIS spectra is therefore difficult to interpret using standard equivalent circuits [164].

In the PEMFC literature, several methods to measure the CL protonic resistance have been proposed, which could serve as an excellent starting point for the development of a method appropriate for the PEMWE cell CL protonic resistance measurement. These methods are not directly applicable to PEMWE because they rely on the assumption of a highly conductive catalyst support, usually carbon, and the electronic conductivity of PEMWE cell CLs might be low. For example, the H_2/N_2 EIS method discussed above (see also Ref. 165–167) is commonly used in PEMFC; however, it might not give accurate results for the PEMWE cell CL due to the underlying assumption during the model development that the electronic resistance is negligible. An alternate to the EIS method, Boyer et al. [168] estimated the protonic resistance of a PEMFC CL by adding an intermediate layer (IL) between either two membranes or electrode and membrane, and measuring the increase in cell resistance. The ohmic cell resistance, R, was measured for each MEA by fitting the low current density region of the polarization curve, i.e., 5 to 800 mA/cm^2, to the standard electrode equation,

$$E_{cell} \;=\; E_0 \;-\; b\,log(j) \;-\; j\,R \tag{1.4}$$

where E_{cell} is the cell potential, E_0 is the Nernst potential, b is the Tafel slope, and j is the current density. They stated that the accurate measurement of the effective protonic conductivity is difficult using this method, as keeping the same cell conditions for all MEAs is challenging. Iden et al. [169] measured the protonic resistance of the PEMFC CLs by using a hydrogen pump technique where an IL, made only of carbon support and ionomer, is sandwiched between two membranes and the protonic resistance is obtained by one of two methods: 1) the difference between the overall cell resistance during a H_2 pump test for a CCM with and without the IL; or 2) the difference between the overall cell resistance from the H_2 pump test and the high frequency resistance (HFR) of the same CCM with the IL. They found that, for an IL made of carbon and ionomer, similar results could be obtained using both techniques.

The hydrogen pump method proposed by Iden et al. [169, 170] has been shown to be suitable for evaluating the protonic resistance of an IL, however it is interesting to note that Iden et al. [169] did not include platinum in their IL. No discussion was provided regarding the omission of the platinum. It is hypothesized, therefore, that the presence of a catalyst in the IL that is active to both the hydrogen oxidation and evolution reactions, such as platinum, could render the IL 'invisible' to the protons crossing from the anode to the cathode. While Iden et al. [169, 170] could remove the catalyst from their IL and still obtain protonic conductivity that would be representative of a PEMFC CL, this is not possible for the unsupported catalysts that are used in PEMWE cell. Therefore, the possibility of using this method to measure the proton conductivity of a PEMWE cell anode CL and the possible appearance of the reactive pathway must be investigated.

In order to fully understand the ohmic losses in the CL, the electronic conductivity of the CL also needs to be determined. The through-plane (TP) electronic conductivity of compressed IrO_2 powder was reported in the range of 3.9–64.2 S/cm [91, 94, 171, 172]. The electronic conductivity of iridium powder has been shown to increase with oxidation state, i.e., from +3 to +4 [173, 174]. The conductivity values of catalyst powder provide on approximation of the CL electronic conductivity; however, these cannot be directly compared to a CL conductivity as the catalyst might not be closely packed. Its compression level is unknown in the cell, and the addition of the polymer electrolyte to the CL will likely decrease the number of electronic pathways [171]. The in-plane (IP) electronic conductivity has been measured by several authors in literature [71, 79, 160]. Schuler et al. [160] used a four-probe method to measure the electronic conductivity of several IrO_2/TiO_2 CLs with different ionomer loadings under varying relative humidity (RH). They reported values in the range of 3–7 S/cm. The electronic conductivity, however, decreased by nearly three orders of magnitude when the CL was immersed in liquid water. Mo et al. [71] used a four-probe method to determine the electronic conductivity of a dry $IrRuO_x$ based CL. They reported a value of 0.83 S/cm, significantly lower than the conductivity of a PTL. Mo et al. [71] and Yang et al. [175] have shown that the in-plane electronic conductivity affects the reaction site, i.e., the reaction occurs closer to the CL-PTL interface as electron transport is limiting. Therefore, the catalyst utilization is low [71, 79, 175, 176]. Given the wide range of measured electronic conductivity, and the extremely low value measured in liquid water, accurate measurements of the electronic conductivity of anode CLs is clearly needed to fully understand ohmic losses in CLs.

In PEMFC literature, the reported values of the CL in-plane and through-plane electronic conductivity vary by up to three orders of magnitude. For example, IP electronic conductivity values of 0.1–3.9 S/cm [177–181] and TP electronic conductivity values of 7×10^{-4}–2.5×10^{-3} S/cm have been reported [181]. Ahadi et al. [181] hypothesized that the lower values of the TP electronic conductivity are due to inhomogeneities in the CLs. As PEMFC and PEMWE cell CLs are fabricated using similar methods, it is hypothesized that the TP electronic conductivity of IrO_x layers might be as low as the protonic conductivity, however to date, the TP electronic conductivity of the PEMWE cell CL has not been studied. In order to provide further insight into the ohmic losses in the PEMWE cell CLs, in-plane and through-plane electronic conductivity of the PEMWE cell CLs need to be measured.

From the literature review, both proton and electron transport have been assumed to be limiting; however, no study has performed a direct comparison between the conductivity of the two phases in order to determine which is limiting, in large part, because an experimental technique to determine the CL protonic conductivity had not been proposed. This thesis aims to estimate the protonic and electronic resistances of the unsupported anode PEMWE CLs at varying ionomer loading and RH. These results provide the first ex-situ measurements of the through plane protonic and electronic resistances of PEMWE cell CLs, and show that the electronic resistance can be a significant source of ohmic overpotential for these electrodes.

1.3 Objectives

The overall objective of this thesis is to develop experimental fabrication and characterization techniques to achieve the optimal design of anode PEMWE cell CLs. To achieve this goal, three sub-projects were identified:

1. Development of inkjet printing as a technique for PEMWE electrode fabrication.

2. Development of a hydrogen pump setup to measure protonic conductivity of PEMWE cell electrodes.
3. Introduction of carbon nanoparticles as a pore former to control anode CL porosity of PEMWE cell.

Inkjet printing is selected as the electrode fabrication method as it offers superior control, uniformity, and repeatability for manufacturing a variety of CLs with different compositions and in turn microstructure.

To minimize the ohmic losses in the CL, protonic and electronic conductivity need to be measured. Therefore, the second objective of this thesis is to build a unique setup to measure the protonic conductivity and to study the effect of ionomer loading on protonic and electronic CL conductivities.

It is hypothesized that carbon can be used as a pore former in PEMWE cell anode CLs to increase the porosity. Therefore, the third objective of this thesis is to study the effect of a pore former on the CL porosity, ECSA, and PEMWE cell performance.

1.4 Structure of the report

This thesis is organized into five chapters. This chapter has provided the motivation and objective of the work. A detail literature review was performed to identify the gaps in knowledge. In Chapter 2 the experimental methods used for the fabrication, ex-situ and in-situ characterization of the CCM, and obtained results, analysis, and discussion are described to demonstrate inkjet printing is a novel and suitable CCM fabrication method for the PEMWE cell CLs. In Chapter 3, a novel experimental method used for the measurement of the protonic and electronic conductivity of anode PEMWE cell CLs are described, and the obtained results, analysis, discussion are presented. In Chapter 4, the experimental methods used for the fabrication of anode PEMWE CLs with a pore former are described and results from ex-situ and in-situ characterization are presented. Finally, Chapter 5 summarizes the findings of this work and provides an outlook on the future directions.

Chapter 2

Inkjet printed PEMWE catalyst coated membranes[1]

In order to find the physical phenomena limiting the PEMWE cell performance, a CL fabrication method capable of manufacturing well-controlled anode CLs with different catalysts and varying ink composition was required. In this chapter, a novel fabrication method, inkjet printing, was investigated to fabricate PEMWE cell CLs for the first time. Compared to traditional fabrication methods, such as ultrasonic spray and doctor blade, inkjet's drop-by-drop deposition allows for accurate deposition control, enabling the fabrication of variety of CLs, such as low catalyst loading, conventional loading, patterned electrodes, while reducing catalyst waste. In this work, catalyst ink suitable for inkjet printing using IrO_2 from Alfa Aesar was developed. Using the knowledge gained on ink development and printing conditions, ink recipes were also developed for Ir and IrO_x catalysts in next two chapters. Various ex-situ and in-situ characterization methods were used to characterize the inkjet printed PEMWE cell CLs.

---

[1] This chapter is partly based on M. Mandal, Antoni Valls, Niklas Gangnus, and Marc Secanell, "Analysis of Inkjet printed catalyst coated membranes for polymer electrolyte electrolyzers", Journal of The Electrochemical Society, vol. 165 (7), p. F543-F552, 2018.

2.1 Methods and materials

In order to demonstrate the suitability of inkjet printing for PEMWE cell CL fabrication, an ink formulation suitable for jetting that enabled rapid evaporation of the deposited ink needed to be developed, as well as, the development of suitable hardware for PEMWE cell construction and testing.

2.1.1 Ink fabrication

The ink preparation and CL fabrication process can have a substantial impact on the cell performance [114, 117]. In the case of inkjet printing, only inks with appropriate viscosity, and surface tension can be successfully jetted. A dimensionless Ohnesorge number, which relates the viscous forces to the inertial and surface tension forces, can be used to characterize the formation of liquid drops for inkjet printing [182]. The Ohnesorge number (Oh) is given by:

$$\mathrm{Oh} = \frac{\mu}{\sqrt{\rho \sigma L}} \tag{2.1}$$

where μ, ρ, and σ are the dynamic viscosity, density, and surface tension of the fluid, respectively, and L is the characteristic length scale (typically drop diameter).

Derby [182] proposed that the Ohnsorge number should be between 0.1 and 1 for stable drop formation. At higher values of Oh, viscous dissipation prevents drop ejection, whereas, at low values, the primary drop is accompanied by numerous satellite droplets. These satellite drops can create unwanted splashes on the target substrate and a reduction in printing quality. Furthermore, to overcome fluid/air surface tension at the nozzle for ejection, a drop must have sufficient energy. Duineveld et al. suggested a minimum velocity, v_{min} for drop ejection of [182]:

$$v_{min} = \left(\frac{4\sigma}{\rho d_n}\right)^{1/2} \tag{2.2}$$

where d_n is the nozzle diameter.

Fluid formulation guidelines from Dimatix Fujifilm [183], the inkjet printer used in this thesis, suggests that the ink formulation should have a viscosity between 10-

12 cPs (1.0×10^{-2}–1.2×10^{-2} Pa·s) at the operating temperature, a surface tension between 28 and 33 dynes/cm (0.028–0.033 N/m), and have well-dispersed particles, which must not settle rapidly or agglomerate. The latter would lead to the clogging of 21 μm nozzles that were used to jet the ink. Previous literature has shown that the use of isopropyl alcohol (IPA) and propylene glycol (PG), IPA and ethylene glycol (EG), and even IPA and glycerol provide an ink with suitable viscosity and surface tension. Shukla et al. [106] found IPA to be the best dispersing agent for carbon among other solvents. IPA evaporates fast, which is ideal to create a porous structure, but, at the same time, it would not achieve proper jet due to the low viscosity (Oh = 0.09, assuming jetted from a square nozzle of side 21 μm). Hence, PG was added to increase its viscosity (Oh = 1.33) in ref. [130].

In order to disperse catalyst particles in fuel cells, the ionomer used in the electrode has been shown to be suitable [106]. Based on the above, it was proposed in this work to use an IPA-PG mixture with the desired ionomer content to achieve the appropriate CL ionomer loading. The calculated Ohnesorge number of 50-50 wt.% of IPA-PG mixture is 0.46, i.e., within the 0.1 and 1 range for a stable drop. To obtain this number, the viscosity of the mixture is calculated using Grunberg-Nissan mixing rule for liquid:

$$ln\ \eta_{lmix} = \sum_{i=1}^{N} x_i\ ln\ \eta_{li} \tag{2.3}$$

where η_{lmix} is the viscosity of the liquid mixture, η_{li} is the viscosity of the fluid component i, and x_i is the mole fraction of the component i. The calculated viscosity is 5.3 mPa.s compared to the measured viscosity of 5.68 mPa.s from experiments. The total density of the mixture is given by:

$$\rho_{lmix} = \sum_{i=1}^{N} m_i / \sum_{i=1}^{N} V_i \tag{2.4}$$

where ρ_{lmix} is the density of the liquid mixture, m_i and V_i are the mass and volume of the components i, respectively. Due to the lack of experimental equipment to measure the surface tension of IPA and PG, the surface tension is taken to be the average of individual values of IPA and PG.

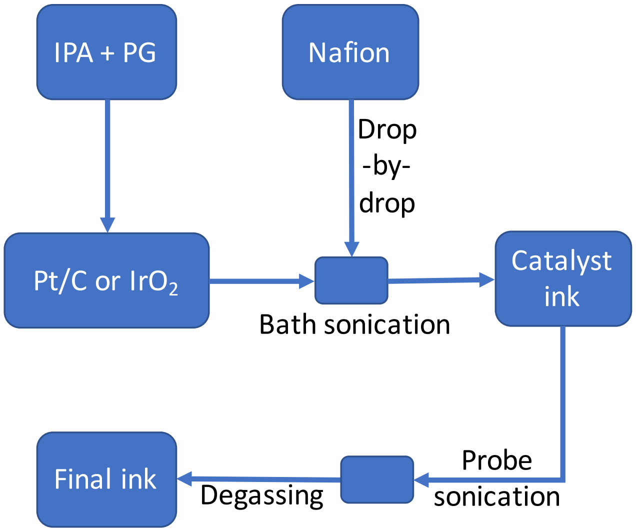

Figure 2.1 – Flowchart of the catalyst ink preparation.

Once an appropriate solvent was obtained, catalyst inks for the anode CL were prepared by mixing 44.7 mg of IrO_2 (99%, A17849, Alfa Aesar) with a total of 500 mg of 50:50 wt.% mixture of IPA and PG. The mixture was ultra-sonicated at room temperature for 60 minutes in a water bath (Branson 1800) having an output frequency of 40 kHz since such a technique has been shown to improve the cell performance [184]. Then 47 mg of Nafion solution (Liquion solution LQ-1105 1100EW 5 wt.%, Ion Power) were added during continued sonication, drop-by-drop, to achieve a 5 wt.% Nafion content in the anode CL. The mixture was then probe sonicated (QSonica S4000) for 15 minutes (Amplitude 20, 2 minutes on, 1 minute off) and degassed for another 60 minutes. A flow chart of the catalyst ink preparation is shown in Figure 2.1. The amount of ionomer added was calculated using the following relation

$$Y_{el} = \frac{m_N}{m_N + m_{Pt/C}} \tag{2.5}$$

where Y_{el} is the Nafion loading in the CL, m_N is the amount of solid Nafion to be added and $m_{Pt/C}$ is the amount of catalyst added.

The cathode ink was fabricated by mixing 37.5 mg of Pt/C (46.7 wt.%, Tanaka Kikinzoku International (TKK)) in a 48:52 wt.% ratio mixture of IPA and PG following the process as described above. A 321 mg of Nafion solution was added to achieve a 30 wt.% Nafion content in the cathode CL.

2.1.2 CCM fabrication

A commercial inkjet material printer (Dimatix DPM-2800 series, Fujifilm) was used to print the CL on Nafion membrane as shown in Figure 2.2a. Dimatix DPM-2800 is a bench-top materials deposition system designed for micro-precision jetting of a variety of functional fluids onto virtually any surface, including plastic, glass, ceramics, and silicon, as well as flexible substrates from membranes, gels, and thin films to paper products. The printer uses a piezo-electric material to control the drop formation by inducing a pressure pulse inside the ink cavity by a mechanical actuator as shown in Figure 2.3. A rapid change in volume inside the cavity forces the ink to jet through the nozzle and draw more ink from the reservoir [182]. The The cartridge used (DMC-11610), shown in Figure 2.2b, has 16 nozzles (21×21 μm nozzle) that are spaced 254 μm apart from each other and achieve a drop volume of 10 pL. In order to print, first the ink was degassed and then the cartridge was filled with it. The "Dimatix Drop manager software" was used to control the printing process. The droplet shape and size can be controlled by varying the applied voltage waveform and voltage. In this case, the piezo-electric waveform in Figure 2.2c and three different piezo-voltages (20 V, 26 V, and 32 V) were used (only for anode CL). Our hypothesis was that this could be used to control CL structural properties, such as porosity, to some degree because smaller drops would result in decreasing drying time and increasing number of printed layers. Small droplets with minimal tails and satellite droplets were achieved at lower piezo-voltage as shown in Figure 2.2d. For printing, a drop spacing of 20 μm was used.

The catalyst was printed on a 5 cm^2 area on the surface of either Nafion NRE211 or N117 membrane as shown in Figure 2.4. The catalyst loading was controlled by the number of layers printed on top of the membrane. The vacuum platen in the printer was maintained at 60 °C while printing on the membrane. After finishing the printing, the membrane was dried at 80 ^{o}C for 2-3 hours before printing on the other side of the membrane. The membrane was reversed and replaced on the same backing sheet before printing the other side of the membrane.

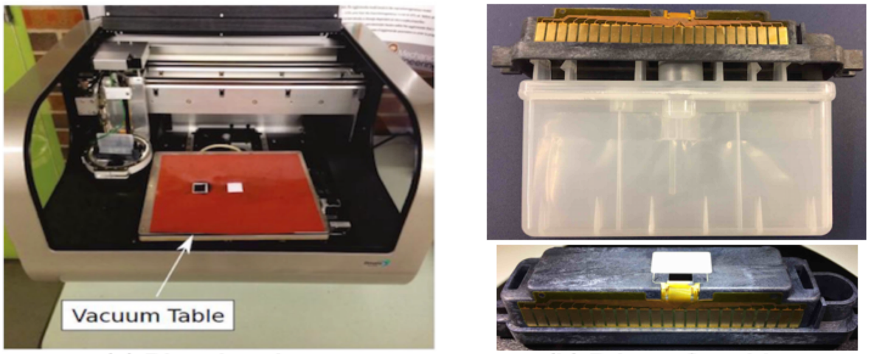

(a) Dimatix printer (b) Printer Cartridge

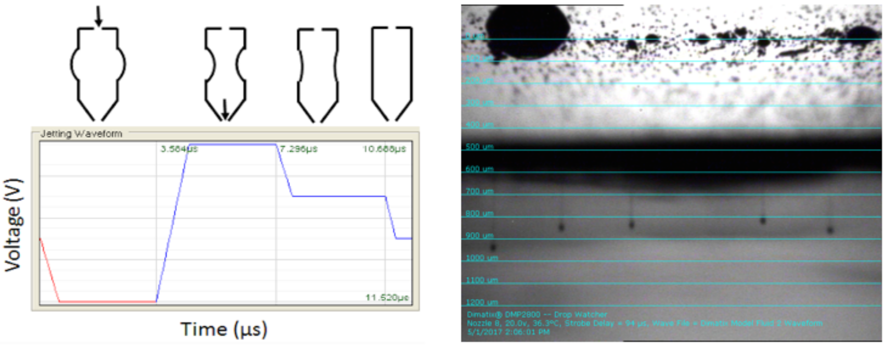

(c) Actuation of the piezo-driven nozzle (d) Piezo-voltage: 20V

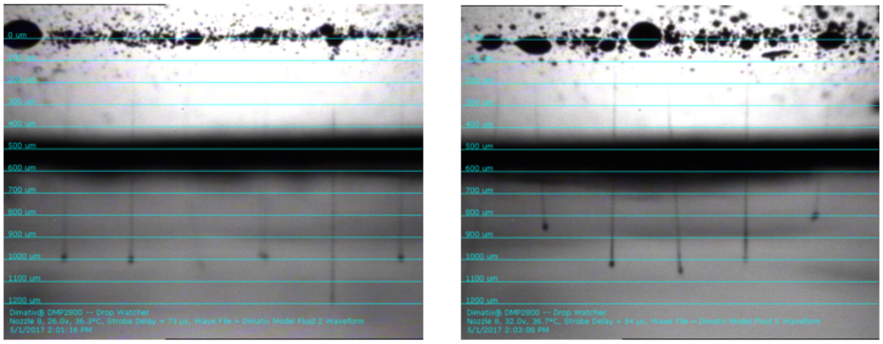

(e) Piezo-voltage: 26V (f) Piezo-voltage: 32V

Figure 2.2 – Inkjet printer (a), cartridge (b), and waveform (c) used to fabricate the electrodes. Droplet shape and size at piezoelectric voltage of 20 V (d), 26 V (e), and 32 V (f).

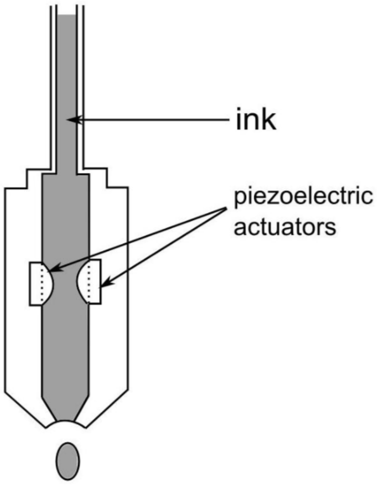

Figure 2.3 – Piezo-electric drop-on-demand nozzle schematics showing jetting of the ink drop by actuating the piezoelectric material.

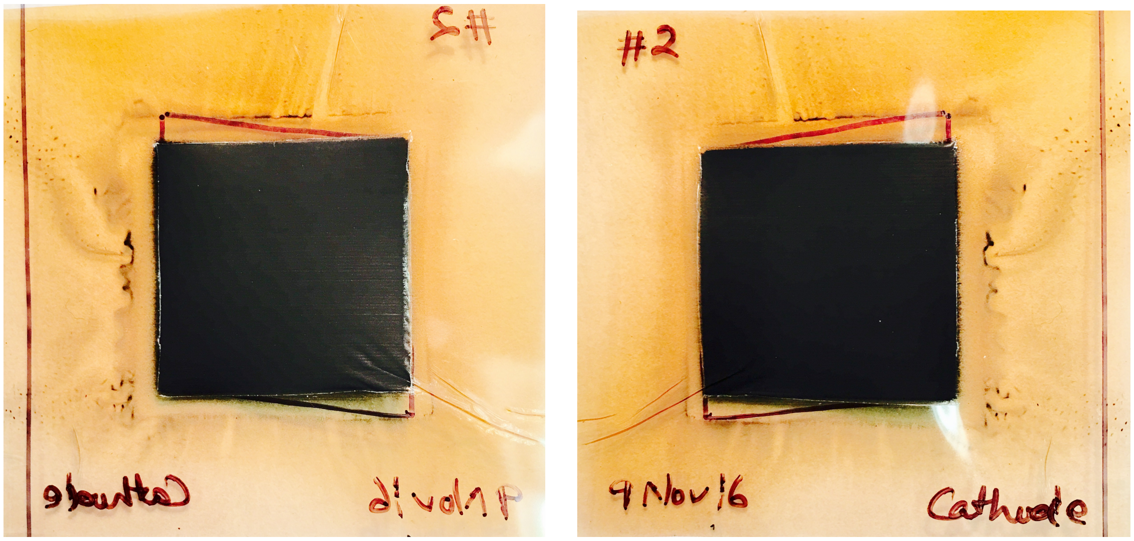

(a) Anode electrode

(b) Cathode electrode

Figure 2.4 – Printed CCM. (a) anode (IrO_2), (b) cathode (Pt/C).

2.1.3 Cell assembly and experimental setup

A single cell with a custom-made titanium plate with a single-serpentine channel in the anode and a graphite plate also with a single-serpentine channel in the cathode were used for testing. A sintered titanium PTL was used on the IrO_2 (anode) side, and a GDL (SGL 24BC, Sigracet) was used on the Pt/C (cathode) side. All the components of the cell were arranged and tightened with 8 nuts and bolts using a star-cross pattern to ensure uniform compression. A torque of 50 inch/lbs was applied on the cell. The cell and water temperatures were maintained at 80 °C by a thermal regulator/control (CN414-R1-R2, OMEGA). A variable power supply (1688B, BK Precision) was used to power the electrolyzer in the range of current from 0.02 to 2 A/cm^2 while a potentiostat (VersaSTAT 4, Princeston Applied Research (PAR)) was used for current in the range of 0.2 to 100 mA/cm^2. Cell voltage recording in the range of 0 to 2 A/cm^2 is performed by means of an Arduino card and a custom-built software. Water supply at a rate of 9.1 ml/min (20 rpm) was provided by a peristaltic pump (Minipulse 3, Gilson). Energy System Design laboratory have developed its own experimental set-up, both hardware and software to carry out the research on the electrolyzer. A schematic and an actual experimental set-up are shown in the Figures 2.5 and 2.6, respectively.

2.1.4 Microscopic imaging

To understand the properties of the CL, characterization is necessary. As discussed in the literature review, morphological features of the CL, such as porosity, pore size distribution, CL thickness, and ionomer and catalyst dispersion, all contribute to the cell performance. To study the surface defects such as cracks, CL thickness and adherence of the CL to the membrane, various imaging techniques, such as scanning electron microscopy (SEM), helium ion microscopy (HIM), focused ion beam SEM (FIB-SEM), can be used. As observed in the literature, these structural features of the CL is expected to be in the microscale range. For this range, SEM imaging could provide the information needed on these defects. Studying the CL surface defects is important because reactants can come in contact with the membrane through the cracks; this might cause local membrane degradation and lead to the lifetime decrease

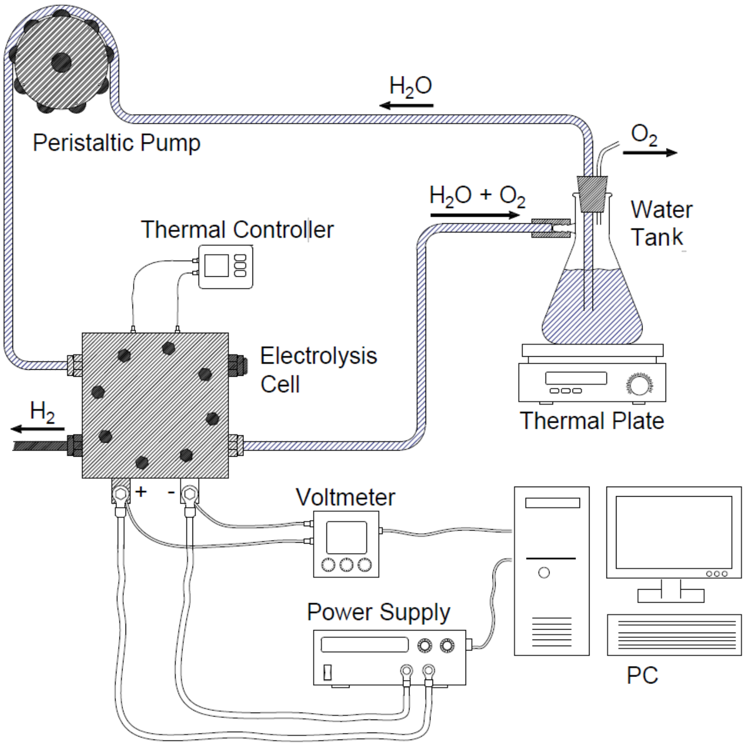

Figure 2.5 – Schematic of the experimental setup.

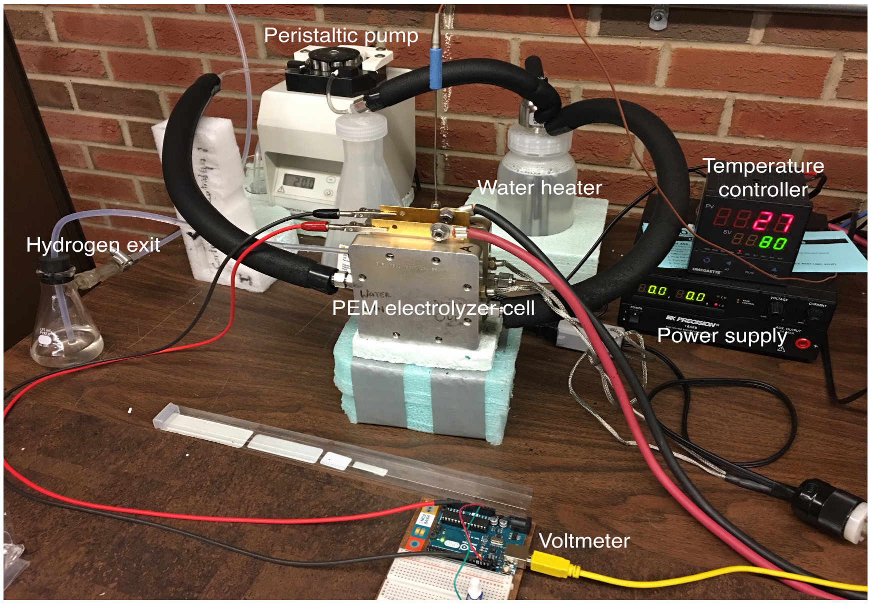

Figure 2.6 – The experimental setup.

[185]. Before SEM imaging, the CLs were analyzed for surface defects using transmitting optical (Micromaster, BS200, Fisher Scientific (FS)) and stereoscopic (S8 APO, Leica) microscopes before electrochemical experiments were performed.

SEM (Zeiss Sigma 300 VP-FESEM) was used to study the CL thickness and microstructure. To take into account the inhomogeneities in the CL thickness, the thickness was measured at several locations of a SEM image and several images were taken into account. Using the CL thickness and ink composition, the CL porosity was calculated to understand the effect of piezo-voltage on the porosity of CL. An increase in the porosity with a decrease in piezo-voltage is expected.

The porosity of the CL was calculated based on the IrO_2 layer thickness (t_{CL}) and composition using

$$porosity = \frac{V_{tot} - V_s}{V_{tot}} \tag{2.6}$$

where V_{tot} is the total IrO_2 layer volume ($= 5\ cm^2 \times t_{CL}$) and V_s is the solid (IrO_2+ionomer) volume of the IrO_2 layer, which is obtained from

$$V_s = \frac{m_s\,(1 - W_N)}{\rho_{IrO_2}} + \frac{m_s\,W_N}{\rho_N} \tag{2.7}$$

where m_s is the mass of the CL, i.e., iridium oxide and Nafion, W_N is the ionomer loading, and the densities used for IrO_2 (ρ_{IrO_2}) and Nafion (ρ_N) are 11.66 and 2 g/cm^3, respectively.

One of the advantages of the inkjet printing is to disperse the catalyst and ionomer evenly. To study the catalyst and ionomer distribution in the in-plane and through-plane directions of the CL, various techniques can be employed such as energy dispersive X-ray spectroscopy (EDX) and scanning transmission X-ray microscopy (STXM). Elemental analysis is required on a wider area of the sample to observe dispersion of the catalyst and ionomer. STXM has high resolution mapping on the 20 nm scale. A low resolution technique (EDX) would be sufficient to observe dispersion in the CL. Moreover, most of the SEM equipment are equipped with EDX imaging capability. Therefore, EDX imaging was chosen in association with the SEM imaging in this thesis. EDX (Bruker Xflash Detector 6||60) was used to observe the catalyst and ionomer distribution in the in-plane and through-plane direction of the CL.

Sample preparation is an important step for ex-situ characterization. A proper sample will enable to take quality images. SEM samples can be prepared by two methods i) cryo-fracturing the CCMs using liquid nitrogen, and ii) embedding CCMs in epoxy and then polishing it. The cryo-fracturing method is less time-consuming than epoxy embedding, and samples prepared by epoxy embedding are prone to charging of the sample during imaging. Charging of the sample could be avoided by HIM or carbon coating the SEM sample. With the latter, CL microstructure features would be lost. Therefore, the cryo-fracturing using liquid nitrogen was chosen to prepare the samples for imaging due to its simplicity and quality of the images. The main drawback of this method is that a perfect perpendicular cross-section would not be achieved. This drawback can be minimized by taking into account many images.

2.1.5 Cyclic voltammetry

In addition to the CL morphology, the literature review has shown that a good CL has a high CL surface area and a good balance between proton, electron, and reactant transport parameters. The number of active sites at the cathode and anode is a key factor which determines the kinetic/activation loss in the cell. In PEMFC, it is common to estimate the ECSA of a porous CL through the application of cyclic voltammetry (CV) in the hydrogen underpotential deposition (HUPD) region in H_2/N_2 or H_2/water saturated electrolyte [186–188]. However, hydrogen underpotential is ineffective for oxide catalysts used for water oxidation [189]. Therefore, a relative measure of ECSA can be estimated from the voltammetric charge obtained by integrating the voltammogram in the potential range of 0.05 V to 1.2 V [190].

Cyclic voltammograms were obtained at 30 °C by flowing 0.2 slpm fully humidified H_2 in the Pt/C (reference) electrode and either 0.05 slpm fully humidified N_2 or stagnant water in the IrO_2 (working) electrode. Potential scans were performed at 40 mV/s from 0.05 to 1.2 V. The double layer capacitance (C_{dl}) was calculated using [81]:

$$C_{dl} = \frac{(\triangle l/2)}{\nu} \tag{2.8}$$

where $\triangle l$ is the thickness of the cyclic voltammogram in the double layer region (see Figure 2.13) and ν is the scan rate.

2.1.6 Hydrogen crossover

Hydrogen cross-over measurement is important for the safe and efficient operation of electrolyzers. A higher H_2 cross-over can result in the formation of an explosive environment in the anode channel. It also represents a loss of product hydrogen, thereby decreasing the electrolyzer efficiency [191]. Hydrogen cross-over can be determined using the cross-over current from a voltammogram [192]. In addition to a CV, chronoamperometry tests was carried out at different voltages in order to estimate hydrogen cross-over. The same cross-over from both the techniques is expected. If cross-over is higher for the given membrane type then it will be known that the membrane is damaged during the fabrication process.

Chronoamperametry tests were used to measure H_2 cross-over. Experiments were conducted at varying potential from 0.1 V to 0.5 V with a step increment of 0.1 V for 200 seconds at each step. All other operating conditions were maintained as for the cyclic voltametry test. The hydrogen cross-over flux (J_{H_2}) was calculated using [193]:

$$J_{H_2} = \frac{i}{n\ F} \tag{2.9}$$

where i is the cross-over current density produced at a specific voltage, n is the number of electrons transferred for hydrogen production, and F is the Faraday constant (96485 C/mol).

2.1.7 Polarization curve

To perform the experiments, the cell was conditioned first by applying current densities of 0.02, 0.1, 0.2 and 1 A/cm^2 for 15 minutes each and 5 minutes at 2 A/cm^2.

Then, polarization curves were obtained using the power supply by applying current densities from 0.02 to 0.2 A/cm^2 in 0.02 A/cm^2 increments and from 0.2 to 2 A/cm^2 in 0.2 A/cm^2 increments. The cell was ran for 2 minutes at each current density and the data was averaged over the last 10 seconds. Three forward sweep experiments were performed to complete a full “Run”. Finally, the cell was cooled to room temperature and the feed water was exchanged with fresh deionised water. The experiment was then repeated to complete another full “Run”. This way, 3-4 Runs were carried out. All the iV data (9–12 polarization curves) were averaged and then reported. To compare the obtained cell potential with literature data, all the potentials were iR corrected using:

$$E_{iR} = E - \rho\, i\, t_{mem} \tag{2.10}$$

where E_{iR} is the corrected potential, E is the actual potential, ρ is the resistivity, taken as 6.67 Ω·cm for iR correction, i is the current density, and t_{mem} is the membrane thickness. The value of resistivity (6.67 Ω·cm) is based on a fully humidified membrane conductivity of 0.15 S/cm at 80 °C which is in agreement with data from ref. [194, 195].

Electrochemical impedance spectrometry (EIS) was used to measure the HFR of the assembled cells. The HFR of 0.2 and 0.08 Ω·cm^2 were obtained for CCMs with N117 and NRE211 membranes, respectively. A linear fit of the HFR with membrane thickness was used to estimate a membrane resistivity of 7.88 Ω·cm, which is in line with the value of 6.67 Ω·cm used to correct for membrane thickness as discussed above.

2.1.8 Kinetic parameters

To understand the activity of the catalyst, kinetic studies were carried out. Tafel curves were obtained using a potentiostat (VersaSTAT 4, PAR) for current densities in the range of 0.2 to 100 mA/cm^2. To obtain kinetic parameters, the curves were fitted to a line using MATLAB. The overpotential is calculated as the difference between the cell potential and the theoretical potential (1.18 V) at operating conditions.

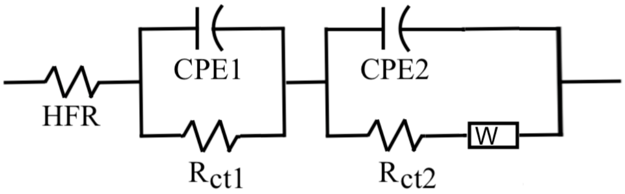

Figure 2.7 – Equivalent circuit for analysis of the impedance spectra.

2.1.9 Electrochemical impedance spectroscopy

As the PEMWE cell is an electrochemical device, different voltage loss mechanisms occurring in the cell at different current densities need to be studied. The impedance spectra can determine both the resistive and capacitive properties of the cell. It can also reveal if there are any mass transport losses. The impedance spectra are generally fit to the equivalent circuit as shown in Figure 2.7. The high-frequency impedance spectra intercept with the real axis is the HFR which includes protonic resistance of the membrane and the CL, electronic resistance of the CL, bipolar plates, PTLs, and all interfacial contact resistances. The cathode charge transfer resistance accompanied by double layer effects in the electrode is given by R_{ct1} and CPE1, respectively. The charge transfer and the mass transport resistance in the anode are represented by R_{ct2} and Warburg element (W), respectively. The constant phase element (CPE2) in parallel to R_{ct2} and W represents the double-layer capacitance of the anode. Therefore, the EIS test was carried out and inkjet printing will be considered successful if the obtained resistances of the cell are lower or comparable to the literature.

Galvanostatic EIS measurements were performed at constant current densities of 0.02, 0.05, 0.1, 0.15, 0.2, 0.5, 1, 1.5, and 2 A/cm^2 using a sinusoidal current of amplitude less than 10% of the total current except at 0.02 A/cm^2 (20%) and a frequency range between 30 kHz–50 mHz (50 points per decade). The Pt/C electrode was used as the reference electrode and the IrO_2 electrode (anode) was used as the working electrode. The cells were maintained at 80 °C and the water flowrate was set to 9.1 ml/min. The impedance spectra were fitted to different equivalent circuit depending on the obtained spectra using “zfit” MATLAB code [196] in order to estimate the HFR (R_Ω), charge transfer resistance (R_{ct}) and double layer capacitance (C_{dl}).

2.1.10 Stability test

The degradation of the PEMWE cell can be categorized into three categories: i) degradation of the membrane [197], ii) degradation of the catalyst [107], and iii) passivation of the titanium components [107]. As mentioned earlier, cracks in the CL may lead to membrane degradation [185]. Improper distribution of ionomer may lead to catalyst dissolution and aggregation [198]. The fabrication method influences crack formation [185, 199] and ionomer dispersion [113]. Hence, knowing the stability of the CCMs is important, which determines the suitability of the fabrication method. The cell was run for 24 h to determine the degradation rate of the CCMs and compared to the literature. If the degradation is lower or comparable to the literature, then fabricating CLs by inkjet printing method will be considered successful. In order to study the inkjet printed CL stability, the cell was run at 0.3 and 1 A/cm^2 for 24 h at 80 °C with water flow rate of 9.1 mL/min.

2.2 Results and discussion

A summary of all the fabricated CCMs and their loadings are presented in Table 2.1. The loading was calculated using the gravimetric method [200]. CCMs that were printed at the same time have the same loading.

2.2.1 Ex-situ characterization

2.2.1.1 Microscopic imaging

The microscopic images of half CCMs were captured using the optical transmission microscope as shown in Figure 2.8. It can be seen from Figures 2.8a and 2.8b and Table 2.1 that the IrO_2 CLs prepared at high piezoelectric voltage require fewer layers but have many microscale cracks. The cracks, however, disappeared when the printing piezo-voltage was decreased (Figures 2.8e and 2.8f). These cracks appear to play a

Table 2.1 – Summary of fabricated CCMs

Name	Piezo-voltage (V)	Membrane	No. of layers of anode side	Loading (mg/cm^2)	
				IrO_2	Pt
CCM-1-32V-N117	32	N117	8	1.17	0.10
CCM-2-32V-N117	32	N117	8	1.17	0.10
CCM-1-26V-N117	26	N117	25	1.11	0.11
CCM-1-20V-N117	20	N117	43	1.11	0.11
CCM-1-32V-N211	32	NRE211	8	1.17	0.10
CCM-1-20V-N211	20	NRE211	43	1.11	0.11

minor role in the electrochemical performance.

2.2.1.2 SEM and EDX imaging

Figure 2.9 shows SEM cross-sectional and surface images of the IrO_2 CL printed on N117 with a piezo-voltage of 32 V. Figures 2.9a and 2.9b show very good attachment between the electrode and the membrane. Figure 2.9d shows the catalyst particle size is non-uniform. The measured anode CL thickness is shown in the Table 2.2 along with the literature data. Based on the ink composition, loading and the CL thickness, the porosity of the IrO_2 electrode was calculated to be as shown in Table 2.2. The porosity of the inkjet printed CLs is much lower than the 50-60 %, usually observed on Pt/C CLs in fuel cells and other values reported in literature for electrolyzer electrodes. It is close to the densest regular packing (rhombohedral packing) of uniform spheres, i.e., 25.95% [201]. As the particles are non-uniform, the expected porosity can be lower than that of a rhombohedral packing as in the case of CL printed at 20 V piezoelectric voltage. The higher porosity of the CLs printed at 32 V and 26 V is likely due to the cracks in the CLs.

Figure 2.10 shows the EDX imaging of the CL cross-section. From the image, it can be seen that the catalyst and the ionomer are distributed evenly in the cross-section of the CL. The estimated mass percentage of fluorine, iridium and oxygen is 4, 79.7 and 16.3 respectively, in the cross-section of the CL by forcing all other elements to be zero. These are in agreement with the expected amounts of F, Ir and

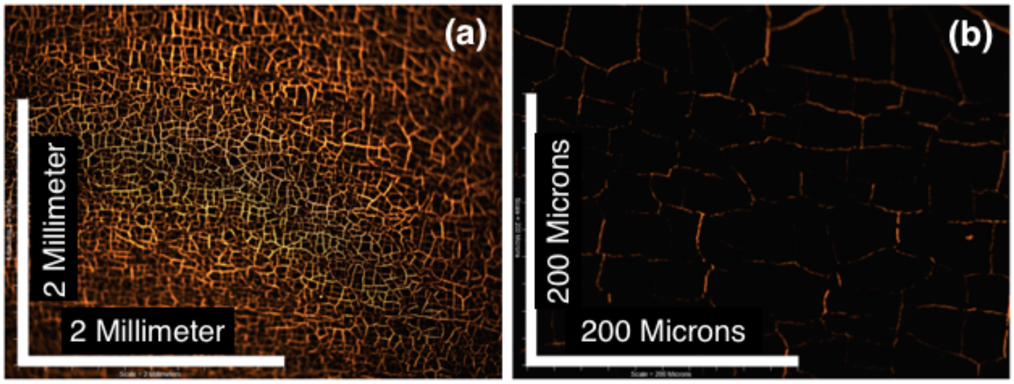

CCM-1-32V-N117

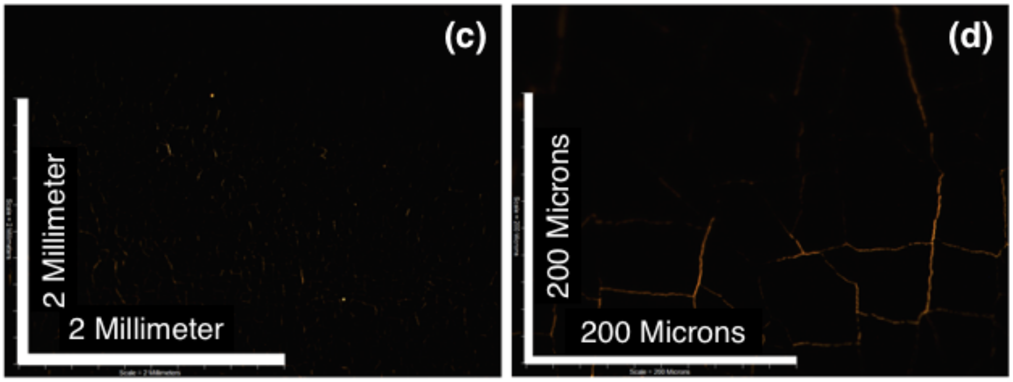

CCM-1-26V-N117

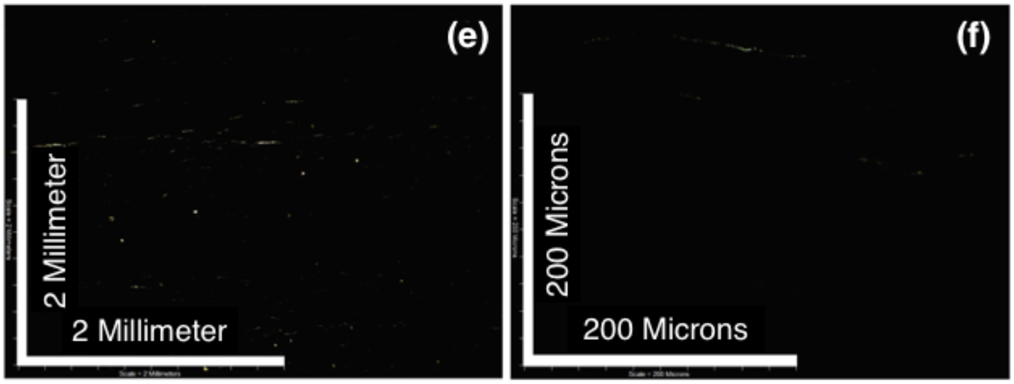

CCM-1-20V-N117

Figure 2.8 – Optical transmission microscope images at magnification of 4 X (a), (c), (e) and 10 X (b), (d), (f).

Table 2.2 – Comparison of CL thickness for different fabrication methods

Ref	Fabrication method	Anode catalyst loading (mg/cm^2)	CL thickness (μm)	CL thickness ($\mu m/(mg/cm^2)$)	Porosity (%)
[74]	Decal	0.4 (IrO_2)	1.1	2.75	49
[52]	Spray Decal	1.5 ($Ru_{0.7}Ir_{0.3}O_2$)	20-30	13.3-20	78-86
[202]	Electrodeposition	0.1 (IrO_2)	0.5	5	72
CCM-1-32V-N117	Inkjet	1.17 (IrO_2)	1.87 ± 0.15	1.6	29
CCM-1-26V-N117	Inkjet	1.11 (IrO_2)	1.69 ± 0.14	1.52	26
CCM-1-20V-N117	Inkjet	1.11 (IrO_2)	1.38 ± 0.15	1.32	10

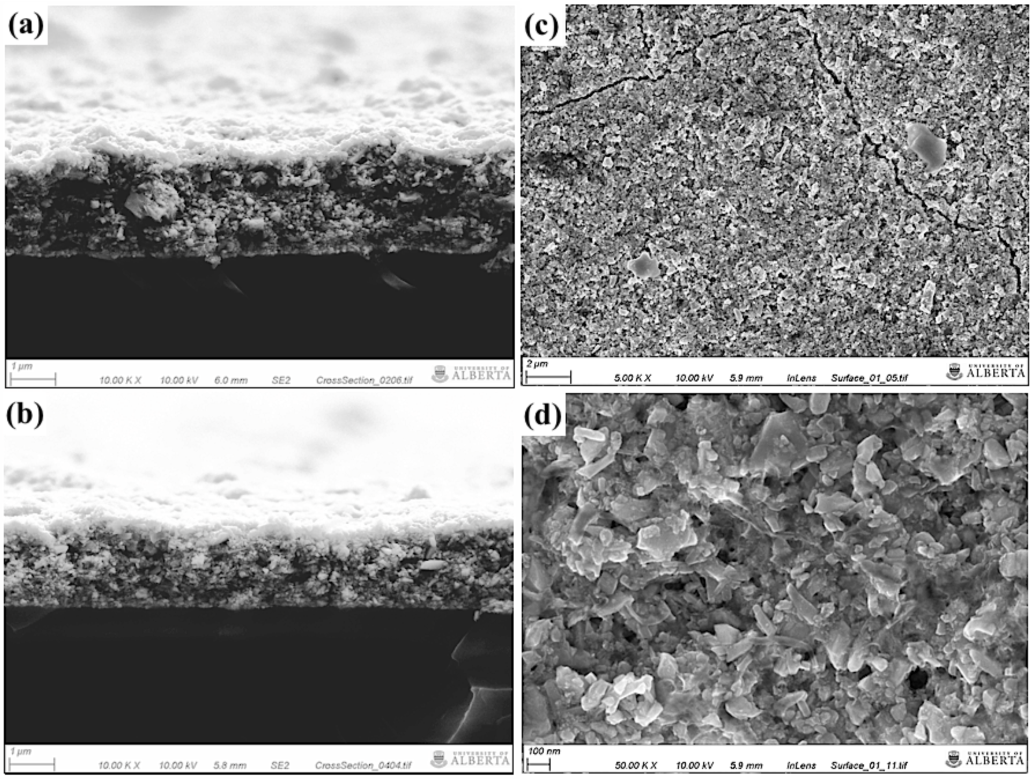

Figure 2.9 – SEM images of the anode of CCM-1-32V-N117 CL. Cross-section (10k X) (a) and (b), and top surface at 5k X (c) and 50k X (d).

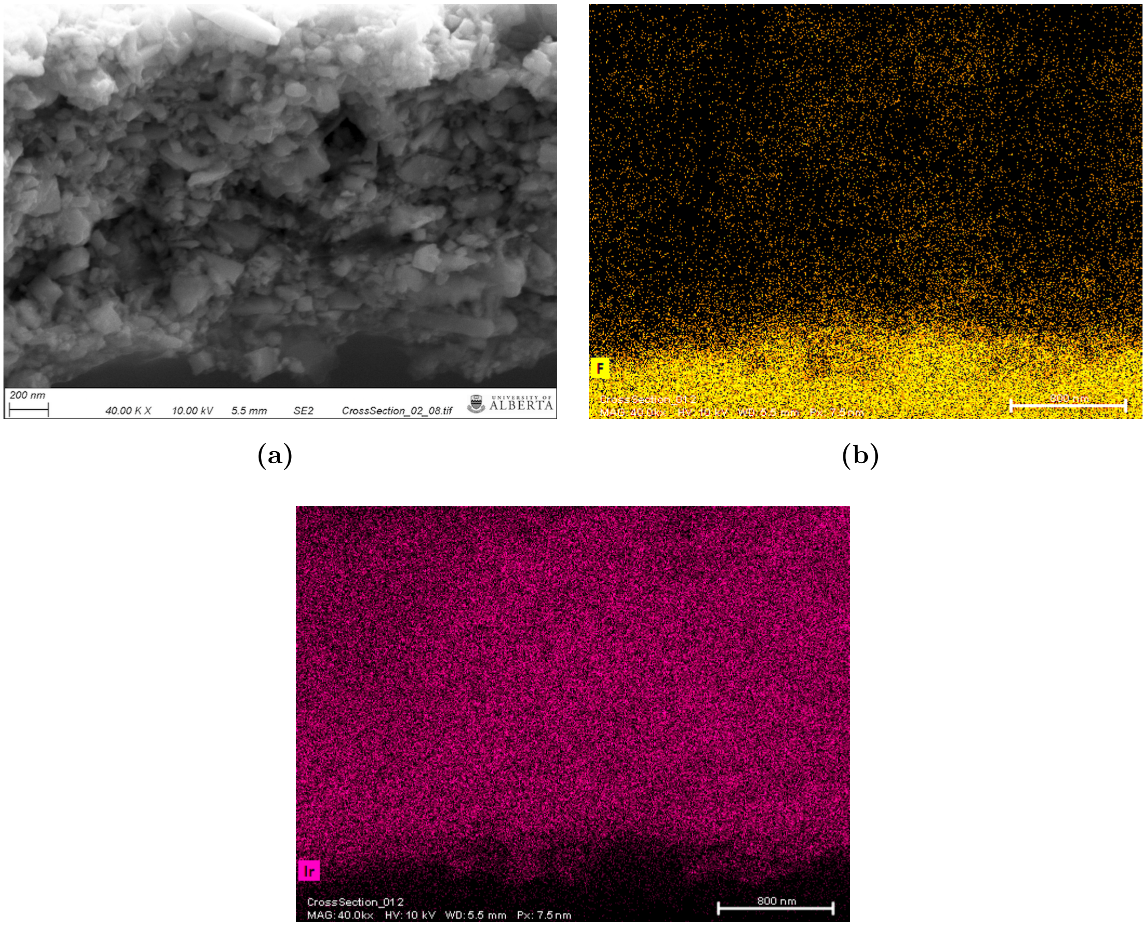

(a) **(b)**

(c)

Figure 2.10 – SEM (a), and EDX fluorine (b), and iridium (c) maps of the catalyst layer cross-section after the electrochemical tests.

O assuming IrO_2 catalyst was used and 5 wt.% Nafion, i.e., 3, 80.3 and 14.2 taking carbon and sulphur into account. These demonstrate the ink mixing and drop-by-drop deposition do not alter the catalyst morphology and can print Nafion well. The homogeneous Nafion distribution is in agreement with STXM results in literature for fuel cell CLs fabricated by IJP [131]. A Nafion rich layer near the membrane can also be observed from the F-map (Figure 2.10b).

2.2.2 Polarization curves

Electrolyzer performance was measured on the fabricated CCMs. To estimate the reproducibility of the experiment, two cells printed at 32 V piezo-voltage with N117 membrane were tested. Figures 2.11a and 2.11b show that only small difference exist between the two printed cells, thereby proving the repeatability of the method.

The effect of printing piezo-voltage on polarization curve is shown in Figures 2.11c and 2.11d. From the figures, it can be observed that the performance increased slightly with decreasing piezo-voltage. The increased performance might be associated with the change in morphology and crack density observed in Section 2.2.1.1. The increased performance, however, might not be enough to justify the increase in the printing time associated with the increase in number of layers. Figure 2.11e shows the effect of membrane thickness on the cell polarization curve. The thinner membrane offers less transport resistance and hence better performance.

Figure 2.12 shows the comparison of the obtained iR-corrected potential of inkjet printed CCMs at 1 A/cm^2 with the published iR-corrected potentials at the same current density. It can be observed that the inkjet printed CCMs outperformed most data in the literature. Ref. [84] and ref. [86] have similar performance to inkjet printed CCMs at similar operating condition and for similar catalyst loading per square centimeter. Only ref. [125] has a better performance with a lower catalyst loading than inkjet printed CCMs due to a higher cell operating temperature (90 °C).

2.2.3 Cyclic Voltammetry

Estimation of the ECSA of iridium oxide CLs used in electrolysis is challenging because hydrogen underpotential deposition and carbon monoxide oxidation are ineffective [189], therefore C$_{dl}$ is used in this section as a relative measure of the ECSA by assuming that the ECSA will scale proportionally to the total surface area as also proposed in previous literature [139]. The voltammetric charge, q^*, obtained by integration of the voltammogram over the whole potential scan range i.e. from 0.05 V to 1.2 V (both positive and negative sweep), which has also been assumed to

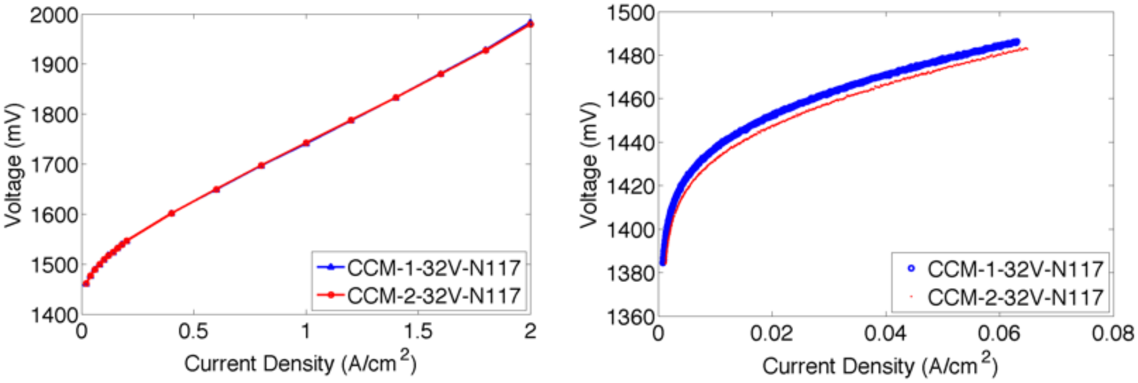

(a) Repeatability **(b) Repeatability low J**

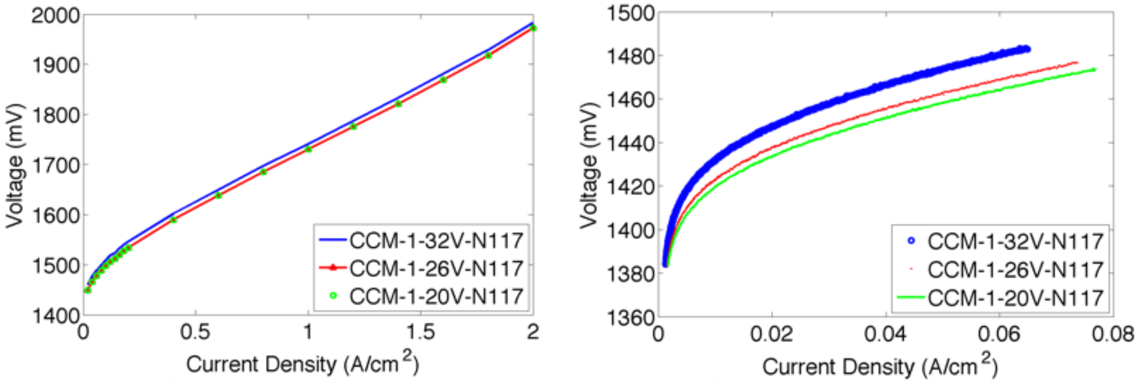

(c) Effect of piezo-voltage **(d) Effect of piezo-voltage low J**

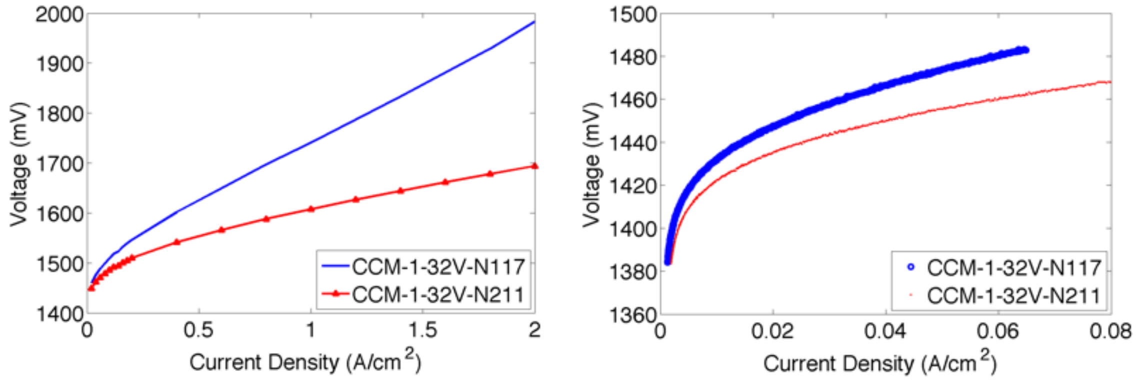

(e) Effect of membrane **(f) Effect of membrane low J**

Figure 2.11 – Polarization curves for two similar samples (a) and (b), samples fabricated at different piezo-voltage (c) and (d), and samples with different membrane thickness (e) and (f).

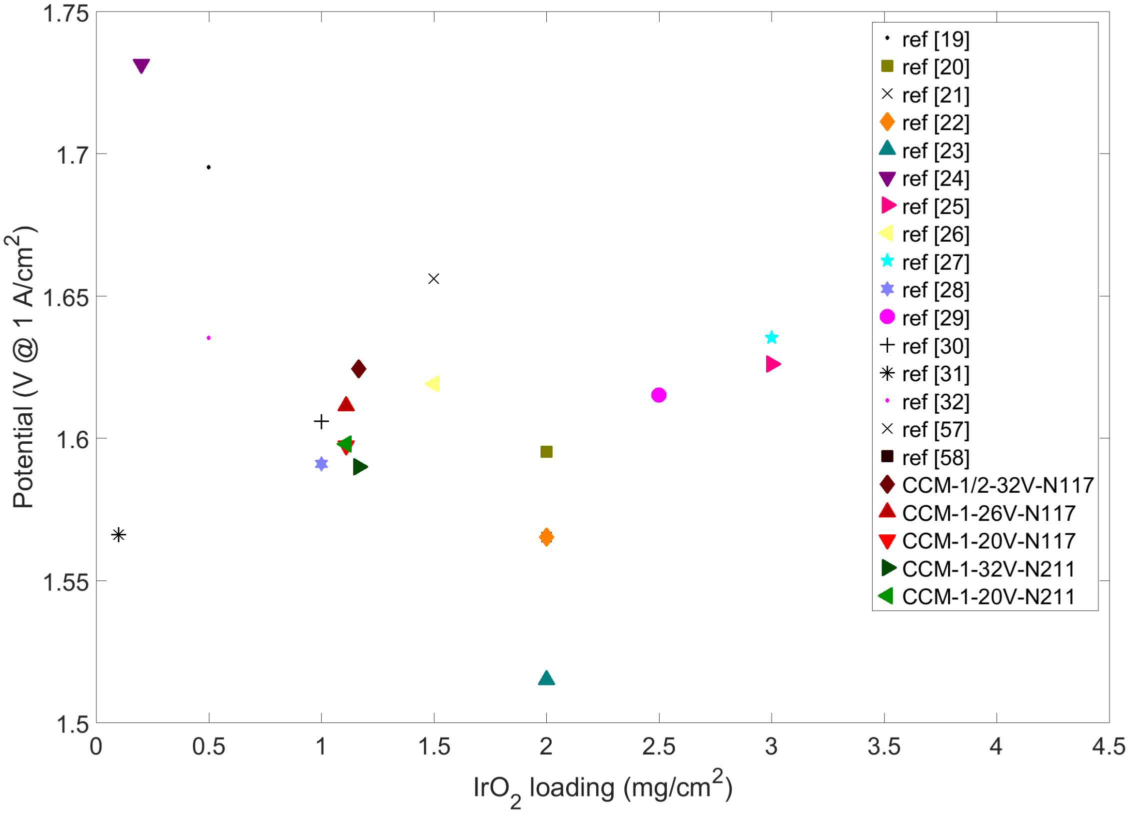

Figure 2.12 – Potential at 1 A/cm^2 as a function of anode loading.

be proportional to the ECSA in previous literature [190, 203]. The computed charge density is shown in Table 2.3 and found out that it is, in fact, proportional to the C_{dl}. Hence, it would not be wrong to say that C_{dl} can also provide relative measure of the ECSA. Figure 2.13 shows the voltammograms obtained by CV test of different CCMs. The CV tests were carried out with both water and nitrogen on the anode side of the electrolyzer cell to achieve an inert environment [187]. Overall features of the voltammograms are similar to those observed in the literature [23, 139, 204]. It can be observed that a double layer region extends from 0.35 to ca. 0.5 V.

Table 2.3 shows the estimated double layer capacitance (C_{dl}) obtained from the voltammograms for the different cells tested. The calculated C_{dl} from ref. [23] is in the range of 18–65 mF/cm^2 using the Equation 2.8. The C_{dl} obtained in this work is in the range 18–27 mF/cm^2, similar to that reported in ref. [23]. The reason for the higher C_{dl} in ref. [23] is due to the higher catalyst loading (2 mg_{IrO_2}/cm^2) and smaller particle size (5-100 nm).

Table 2.3 also shows the estimated voltammetric charge (q^*) obtained from integration of the voltammogram current for the different cells tested. The q^* value reported in ref. [190] is between 6–300 mC/cm^2 for $Ir_{0.3}Ti_{0.7}O_2$ catalyst. Pathiraja et al. [205] reported 67.93 and 102.8 mC/cm^2 for Ti/IrO_2-SnO_2 catalyst prepared from two different Ir metal concentration precursors. Papaderakis et al. [164] reported 103.95 mC/cm^2 for IrO_2 catalyst with 1 mg/cm^2 catalyst loading. Alvesa et al. [206] reported in the range of 50–250 mC/cm^2 for Ti/$Ir_{0.3}Ti_{(0.7-x)}Ce_xO_2$ catalyst. The obtained q^* in this article is in good agreement with the literature data.

2.2.4 Hydrogen crossover

In order to study the membrane damage during the fabrication process, hydrogen crossover tests were carried out. Table 2.3 also shows hydrogen cross-over flux for all the cells. The obtained hydrogen crossover is inversely proportional to the PEM thickness. Membrane permeability was estimated to be between 1.13×10^{-14} to 1.92×10^{-14} mol(m·Pa·s)$^{-1}$, in agreement with literature values which are in the range

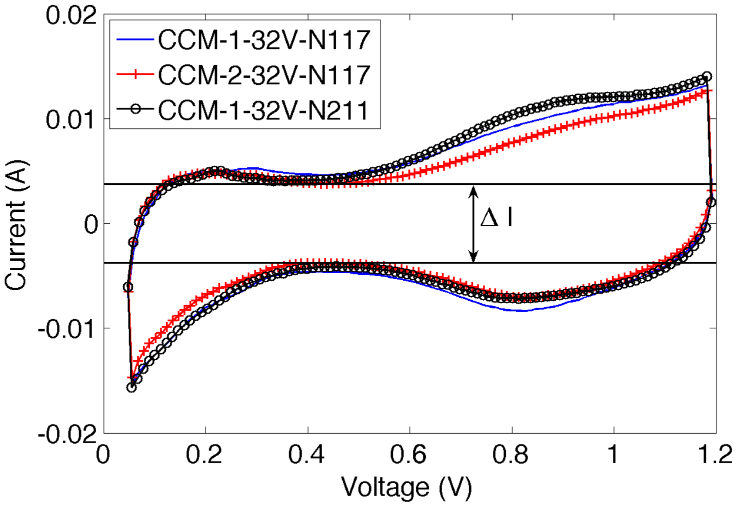

Figure 2.13 – Cyclic voltammograms of N117 and NRE211 CCMs.

Table 2.3 – Double layer capacitance, Charge and H_2 cross-over of all CCMs.

Name	with water			with N_2		
	C_{dl} [F/cm^2]	Charge (q^*) [mC/cm^2]	$J_{H_2} \times 10^{-10}$ $[mol/(cm^2 s)]$	C_{dl} [F/cm^2]	Charge (q^*) [mC/cm^2]	$J_{H_2} \times 10^{-10}$ $[mol/(cm^2 s)]$
CCM-1-32V-N117	0.0229	77.17	8.638	0.0216	75.39	6.653
CCM-2-32V-N117	0.0187	66.81	7.902	0.0151	59.61	7.851
CCM-1-26V-N117	0.0254	86.72	9.61	0.0231	82.16	7.34
CCM-1-20V-N117	0.0271	92.28	10.93	0.0250	88.52	7.05
CCM-1-32V-N211	0.0178	62.41	44.97	0.0177	62.98	47.54
CCM-1-20V-N211	0.0205	77.69	58.71	0.0198	76.67	58.67

of 0.987×10^{-14} to 1.97×10^{-14} $\mathrm{mol(m{\cdot}Pa{\cdot}s)^{-1}}$ [191, 207–210].

The hydrogen cross-over flux was observed to be higher when experiments were carried out with liquid water than fully humidified nitrogen in the case of Nafion N117 membrane CCMs, and similar in the case of Nafion NRE211 membrane CCMs. The hydrogen cross-over flux of Nafion membranes is expected to increase with membrane water content [211–214]. The amount of water per sulfonic acid group is ∼20 when Nafion 117 is immersed in water and is ∼13 for fully humidified gas at 30 °C [214]. Whereas, the water content of Nafion NRE211 membrane is similar for both fully humidified gas and liquid water (∼13) [195]. Hydrogen permeability values for vapour and water equilibrated N117 membranes were not found in the literature, however, Schalenbach et al. [211] reported that the H_2 permeability of Nafion N212 at 80 °C as a function of relative humidity and found, as expected based on the small change in the water content observed by Peron et al. [195] in NRE211 membrane, only small differences in H_2 permeability, i.e., ∼3.5%, when measured using a fully humidified gas carrying liquid water and a fully humidified gas.

2.2.5 Kinetic parameter

To understand the activity of the catalyst, kinetic studies were carried out. Figure 2.14 shows the Tafel plot for CCM-1/2-32V-N117 and CCM-1-32V-N211 cells. Table 2.4 shows the comparison between obtained kinetic parameter for all the inkjet printed CCMs with kinetic parameters calculated from literature data. The obtained Tafel slopes are similar to those in literature [23, 84, 138]. The exchange current density, once normalized to be per gram of IrO_2, appears to be in line with literature data. It is higher than the values obtained in ref. [23] and [88] but 2-4 times lower than Ref. [138], [40] and [84]. The low exchange current density observed highlights that the commercial catalyst used might not be very active, which makes the good performance of the IJP electrodes more remarkable.

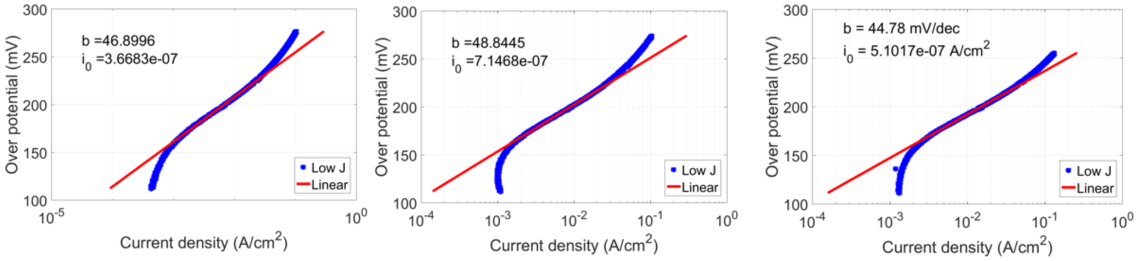

(a) CCM-1-32V-N117 **(b)** CCM-2-32V-N117 **(c)** CCM-1-32V-N211

Figure 2.14 – Tafel plot for CCM-1-32V-N117 (a), CCM-2-32V-N117 (b), and CCM-1-32V-N211 (c) CCMs.

Table 2.4 – Comparison of obtained kinetic parameters from Tafel plot with literature data.

Name	i_0 (A/cm^2)	b (mV/dec)	i_0 (A/mg$_{IrO_2}$)
From data in ref. [23]^a	2.304×10^{-8}	49	1.15×10^{-8}
From data in ref. [88]^a	4.778×10^{-7}	38	2.39×10^{-7}
From data in ref. [138]^a	4.033×10^{-6}	51	2.02×10^{-6}
From data in ref. [40]^a	6.743×10^{-6}	55	1.69×10^{-5}
From data in ref. [84]^a	5.521×10^{-6}	48	1.84×10^{-6}
CCM-1-32V-N117	3.67×10^{-7}	46.89	3.14×10^{-7}
CCM-2-32V-N117	7.15×10^{-7}	48.88	6.11×10^{-7}
CCM-1-26V-N117	6.45×10^{-7}	46.24	5.86×10^{-7}
CCM-1-20V-N117	6.98×10^{-7}	45.77	6.35×10^{-7}
CCM-1-32V-N211	5.10×10^{-7}	44.79	4.36×10^{-7}
CCM-1-20V-N211	3.55×10^{-7}	44.11	3.23×10^{-7}

^{a} Calculated by fitting a Tafel curve to the extracted data from polarization curve below 100 mA/cm^2 current density provided in the articles.

2.2.6 Electrochemical impedance spectroscopy

Galvanostatic EIS tests were performed to study different voltage loss mechanism. Figure 2.15 shows EIS results at different operating currents and the fitted spectra based on the equivalent circuit in Figure 2.16a which is used to obtain the HFR (R_Ω), charge transfer resistance (R_{ct}), and double layer capacitance (C_{dl}). The figure shows the model to be appropriate for reproducing the experimental data. The absence of a 45° line at high frequency for all the cells indicates that the CL proton transport losses are small in comparison to the charge transfer losses [129].

Using the model and plotting the different parameters versus current density in Figure 2.16 shows the charge transfer resistance, R_{ct}, decreased with an increase in the current as expected. It is observed that the R_{ct} remained constant irrespective of the membrane thickness at a given current, i.e., 0.13 $\Omega\cdot\text{cm}^2$ at 1 A for all IJP CCMs. The obtained R_{ct} value is in line with the data reported by Siracusano *et al.* (0.14 $\Omega\cdot\text{cm}^2$ at 1.5 V) [42].

The value of the double layer capacitance, C_{dl}, obtained by CV and EIS are similar at low current, i.e., 0.0229 and 0.0209 F/cm^2 for CCM-1-32V-N117, respectively. At higher current, the value of the C_{dl} decreases. This decrease might be an indication of liquid water being displaced by oxygen bubbles in the CL. Tests at lower temperature, however, where O_2 solubility is higher, did not change the observed trend. Therefore, the reason for the decrease in double layer capacitance needs further study.

The obtained HFR value is proportional to the membrane thickness which is similar to the value reported by Siracusano *et al.* (0.18 $\Omega\cdot\text{cm}^2$, N115) [42] and Su *et al.* (0.167 $\Omega\cdot\text{cm}^2$, N212) but lower than those reported in ref. [215] (1.53 $\Omega\cdot\text{cm}^2$, N117) and [216] (1 $\Omega\cdot\text{cm}^2$, N117).

Comparing the values for the different fabricated CCMs shows that R_Ω and R_{ct} remain constant with decreasing piezo-voltage. The C_{dl} for cell printed at 32 V piezo-voltage is slightly lower as compared to the cells printed at 26 and 20 V, in agreement

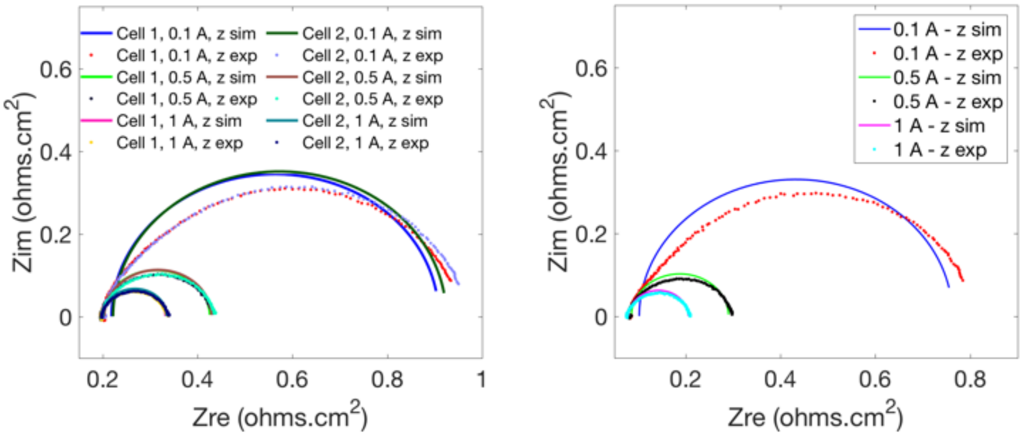

(a) CCM-1/2-32V-N117 **(b) CCM-1-32V-N211**

Figure 2.15 – Electrochemical impedance spectroscopy and numerical fits used to estimate parameters for N117 CCMs (a), and N211 CCM (b).

with CV data.

2.2.7 Stability test

Figure 2.17 shows the cell potential over 24 hours for CCM-1-32V-N211 at 0.3 and 1 A/cm^2 along with the data from [139] and [84]. The degradation rate obtained for CCM-1-32V-N211 cell at 0.3 A/cm^2 is 1.413 $\times 10^{-4}$ mV/sec, half that in ref. [139] (2.833 $\times 10^{-4}$ mV/sec). At 1 A/cm^2 the degradation rate is 3.66 $\times 10^{-4}$ mV/sec compared to 2.174 $\times 10^{-4}$ mV/sec in ref. [84]. The cell potential is more stable than the data from ref. [139] where an N112 membrane and 3 mg$_{IrO_2}$/cm^2 catalyst loading on the anode side were used.

2.2.8 Comparison with literature data

In order to evaluate the performance of inkjet printed CLs, Figure 2.18 compares the obtained polarization curves with published polarization curves from 2010 to 2012 for all catalysts such as Ir, IrO_2, RuO_2, Pt/Ir, IrO_2/SnO_2, and $Ru_xIr_yO_2$ [33] and a commercial CCM (Ion Power) tested in our laboratory. It can be observed that the obtained polarization curve lies within the published data. However, due to the low

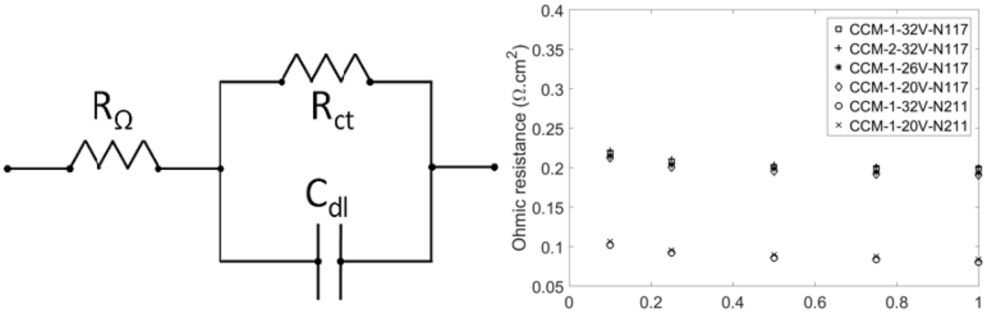

(a) Equivalent circuit for impedance data fit

(b) Ohmic resistance

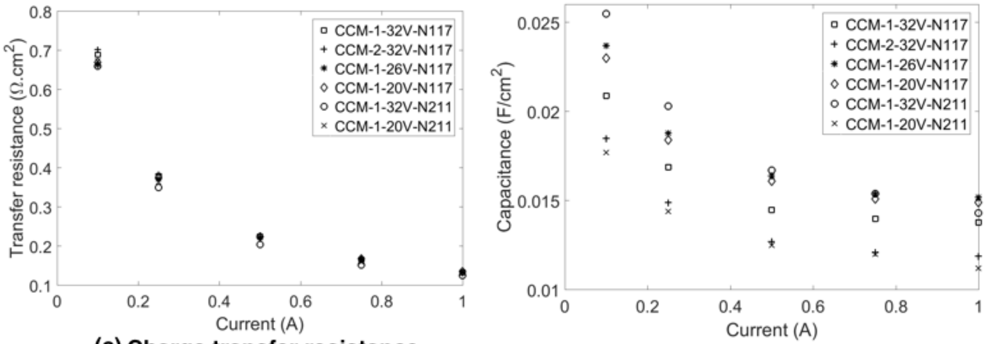

(c) Charge transfer resistance

(d) Double layer capacitance

Figure 2.16 – Parameters evaluated from EIS data fitting to the equivalent circuit shown in (a).

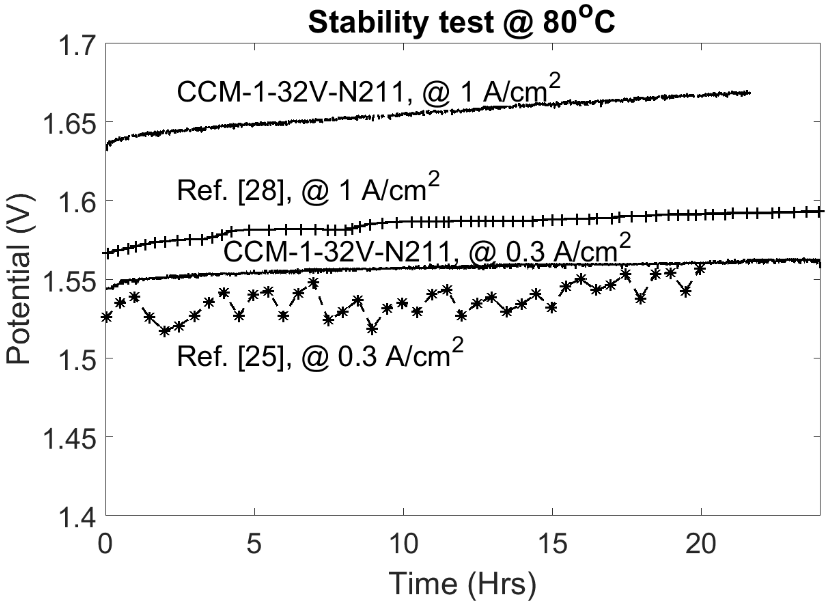

Figure 2.17 – Comparison of stability test at 1 A/cm^2, Ref. [139] and [84] have loading of 3 mg$_{IrO_2}$/cm^2.

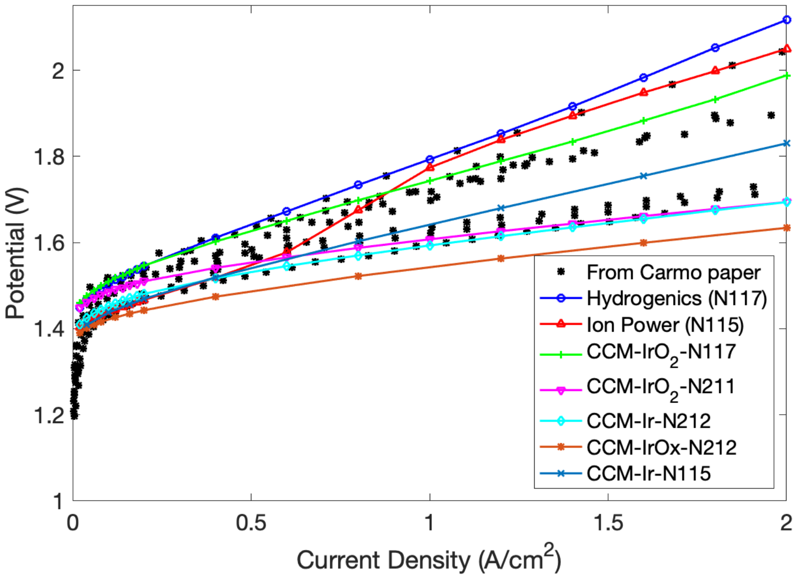

Figure 2.18 – Comparison of polarization curves with published data

kinetic activity of the commercial catalyst and the low IrO_2 loading of the inkjet printed CCMs, the kinetic losses are higher than most of the data in the literature. The activity of the commercial CCM is much better than the IJP CCMs. However, it seems to suffer from mass transfer losses at higher current density.

In order to provide a more meaningful comparison and remove ohmic resistance effect, the potential obtained at a current density of 1 A/cm^2 and 80 °C is tabulated in Table 2.5 with data from the literature for electrolyzers with similar IrO_2 loading. The iR corrected potentials are obtained using the PEM resistivity value discussed in the previous section (6.67 Ω·cm) for all cases. It can be observed that the IJP CCMs performance is similar or better than most of the CCM in the literature with similar loading and catalyst, even though the catalyst activity was shown to be poor (low exchange current density). Only one CCM has a higher performance, however the catalyst loading is double. These results show that the IJP can produce CCMs that are competitive with current fabrication techniques.

Table 2.5 – Summary of PEM water electrolysis described in the literature. The numbers in parentheses indicate the loading in mg/cm^2. All data is at 80 °C cell temperature.

Ref	Fabrication method	Anode	Cathode	Membrane	E [V]	E_{iR} [V]
					@ 1 A/cm^2	
[136]	S-Decal	IrO_2 (0.5)	Pt black (0.5)	N115	1.78	1.695
[137]	S	IrO_2 (2)	40%Pt/CXC72(2)	N115	1.68	1.595
[23]	S-Mem	IrO_2 (2)	10%Pt/C_{JM} (0.4)	N115	1.65	1.565
[88]	S-Mem	IrO_2 (2)	20%Pt/C_{Etek} (0.4)	N115	1.65	1.565
[138]	S-Mem	IrO_2 (2)	Pt black (2.5)	N115	1.6	1.515
[40]	Sputtering	IrO_2 (0.2)	Pt/C	N117	1.85	1.731
[139]	S-Mem	IrO_2 (3)	30%Pt/C_{TKK} (0.5)	N112	1.66	1.626
[38]	S-Mem	IrO_2 (1.5)	30%Pt/C_{TKK} (0.5)	N1035	1.67	1.619
[42]	Spraying	IrO_2 (3)	30%Pt/CXC-72 (0.6)	N115	1.72	1.635
[84]	Spraying	IrO_2 (1)	Pt/C (0.5)	N212	1.625	1.591
[140]	S-Mem	IrO_2 (2.5)	30%Pt/C_{Etek} (0.5)	N115	1.7	1.615
[86]	Decal	IrO_2 (1)	40%Pt/C_{JM} (0.2)	N212	1.64	1.606
[125]	E	IrO_2 (0.1)	46%Pt/C_{TKK} (0.4)	N112	1.6	1.566
[74]	Decal	IrO_2 (0.5)	46%Pt/C_{TKK} (0.25)	N115	1.72	1.635
[69]	Brushing	Ir (1.5)	Pt (1)	N112	1.69	1.656
CCM-1/2-32V-N117	Inkjet	IrO_2 (1.17)	46%Pt/C_{TKK} (0.1)	N117	1.743	1.624
CCM-1-26V-N117	Inkjet	IrO_2 (1.11)	46%Pt/C_{TKK} (0.1)	N117	1.73	1.611
CCM-1-20V-N117	Inkjet	IrO_2 (1.11)	46%Pt/C_{TKK} (0.1)	N117	1.716	1.597
CCM-1-32V-N211	Inkjet	IrO_2 (1.17)	46%Pt/C_{TKK} (0.1)	N211	1.608	1.591
CCM-1-20V-N211	Inkjet	IrO_2 (1.11)	46%Pt/C_{TKK} (0.1)	N211	1.615	1.598

Abbreviations: TKK = Tanaka Corp; JM = Johnson & Matthey; $Etek$ = BASF; S = sprayed catalyst; Mem = membrane; E = Electrodeposition.

2.3 Summary and discussion

The inkjet printing method was studied as a novel fabrication method for PEMWE CCMs. The anode catalyst ink recipe was developed using IrO_2 catalyst from Alfa Aesar. IrO_2 and Pt/C inks were deposited with varying piezoelectric voltage over the membrane to fabricate anode and cathode CLs, respectively. The printing time increased by more than five times when printed at piezoelectric voltage of 20 V as compared to at 32 V. The fabricated CCMs were assembled to test the cell. An electrolyzer test station was built to test the assembled cells.

Optical microscopy, SEM, and EDX were used for ex-situ characterization of the anode CL morphology for surface and thickness characterization. SEM images showed the CL was uniform and well adhered to the membrane. The CL printed at a high piezoelectric voltage of 32 V had many cracks in it and the crack density decreased with a decrease in the piezoelectric voltage. The CL porosity decreased with a decrease in the piezoelectric voltage, which can be ascribed to the decreased crack density, a decrease in CL thickness due to higher number of printed layers which compacted the layer, and non-uniform catalyst particle size. However, it might be possible that the majority of the CL porosity when printed at higher piezoelectric voltage is due to the CL cracks. If the porosity due to cracks is subtracted, then it might be possible that the actual CL porosity is lower than the CL porosity when printed at lower piezoelectric voltage. The EDX images showed even distribution of the catalyst and ionomer in the CL.

Hydrogen cross-over, CV, and EIS tests were performed to estimate hydrogen cross-over, double layer capacitance, and HFR. Cross-over results showed that the membrane was not damaged during the printing process. A kinetic study revealed Tafel slopes similar to those in literature. The CV test showed an increase in the active area with a decrease in the piezo-voltage, which might be due to a well dispersed catalyst and ionomer. This mean that the active area increased with a decrease in porosity. However, the actual CL porosity at high piezoelectric voltage might be lower than the CL porosity at lower piezoelectric voltage as discussed above. Inkjet printed electrolyzer CCMs showed repeatable electrochemical performance. The electrolyzer performance improved slightly when the printing piezo-voltage decreased, which might be due to a thinner CL. The degradation rate from the stability test of the cell was inline with literature data.

The fabricated CCMs outperformed most of the previously reported electrolyzer data in the literature using commercial IrO_2 catalyst. The ex-situ and in-situ characterization of the inkjet printed CCM showed that the inkjet printing method is suitable to fabricate PEMWE electrodes with small amount of catalyst ink and minimal wastage. This will enable the fabrication of CCMs with variety of catalysts, better control of parameters that affects the CL microstructure such as catalyst and ionomer loading, which is required for the next two objectives of the thesis. Due to longer printing time at lower piezoelectric voltage with only a slight improvement in performance, a piezoelectric voltage of 32 V was used for CCM printing in subsequent chapters to minimize the printing time and to avoid the compaction of CLs.

Chapter 3

Novel technique to estimate effective protonic conductivity of PEMWE anodes[1]

The cost of the PEMWE could be reduced by operating the PEMWE at high current density. One of the ways this could be achieved by decreasing the ohmic losses. The PEMWE anode CL protonic resistance has only been estimated using either semi-empirical models [62] or using EIS with H_2 and N_2 [161, 162]. These methods are associated with several drawbacks, such as assuming an ionomer conductivity equal to that of a membrane, neglecting electronic resistance of the CL, and uniform potential distribution on the CL. An ex-situ method to measure the protonic resistance of the PEMWE anode CLs has not yet been developed. In this chapter, the protonic conductivity of the anode CL is measured by using a novel setup utilizing a hydrogen pump technique. In order to fully understand the ohmic losses in the CL, the electronic conductivity of the CL was also measured using a two-probe method. Two

---

[1] This chapter is partly based on M. Mandal, Michael Moore, and Marc Secanell, "Measurement of the Protonic and Electronic Conductivities of PEM Water Electrolyzer Electrodes", ACS Applied Material & Interfaces, vol.12 (44) p. 49549-49562, 2020.

catalysts, Ir and IrO_x, were used to understand the effect of protonic and electronic conductivities on the OER distribution in the anode CL.

3.1 Experimental and modelling section

3.1.1 Fabrication

Catalyst inks for the intermediate layer (IL) were prepared by mixing 44.7 mg of IrO_x (ELC-0110, Tanaka Kikinzoku Kogyo (TKK)) or Ir (3000020267, Umicore) with a mixture of PG, IPA, and Nafion solution (Liquion solution LQ-1105 1100EW 5 wt.%, Ion Power), following the process discussed in Section 2.1.1. The Nafion solution content was varied to achieve 5 to 60 wt.% Nafion in the IrO_x layer and 5 to 30 wt.% in the Ir layer. A higher ionomer loading range was chosen for the IrO_x layer, as the best electrochemical performance was observed at an ionomer loading of 25 wt.% for this particular catalyst as shown in Figure 3.4. Ionomer loadings above and below this value were tested to investigate the impact of ionomer loading on the protonic and electronic conductivities. The ink for anode/cathode CLs was prepared by mixing 37.5 mg of Pt/C (46.7 wt.% Pt/C, TEC10EA50E, TKK) in a 48:52 wt.% ratio mixture of IPA and PG following the process described in Section 2.1.1.

The same inkjet material printer (Dimatix DPM-2800 series, Fujifilm) was used to print the CLs on the NRE211 membrane following the procedure described in previous section. The NRE211 membrane was used as-is. For printing, a piezo-voltage of 32 V and a drop spacing of 20 μm were used.

3.1.2 Microscopic imaging

Scanning electron microscopy (SEM) (Zeiss Sigma 300 VP-FESEM) was used to study the Ir/IrO_x layer thickness. SEM samples were prepared by freeze fracturing the CCMs using liquid nitrogen.

3.1.3 Polarization curve of an electrolyzer cell

In order to show the IrO_x CL compositions are relevant for the technology, polarization curves of the several ILs with IrO_x were studied. The experimental setup used to obtain the polarization curve of the electrolyzer cell can be found in the previous electrode fabrication section (Section 2.1.3). A titanium mesh (Fuel Cell Store, Product code: 592780) was used on the IrO_x side whereas a Sigracet SGL 28BC gas diffusion layer (GDL) was used on the Pt/C side.

To perform the experiments, the cell was conditioned first by applying current densities of 0.02, 0.1, 0.2 and 1 A/cm^2 for 15 minutes each and 5 minutes at 2 A/cm^2. Then, polarization curves were obtained using Biologic potentiostat (SP-300) by scanning the voltage from 1.3 V to 1.8 V at a scan rate of 1 mV/s.

3.1.4 Protonic resistance measurement

3.1.4.1 MEA assembly

For the measurement of the protonic resistance of the IL, the anode and cathode (Pt/C) CLs were printed on an area of 5 cm^2 on two separate membranes. The IL was printed on the other side of one of the two membranes. An insulating sheet (polyester plastic, McMaster-Carr, Product # 8567K102) of thickness 12.5 μm with a 5 cm^2 cut-out area was bonded to the surrounding areas of the IL to ensure proton conduction through the IL only. The 5 cm^2 cut-out piece from the insulation sheet was used while hot pressing the whole assembly to ensure that good adherence of the IL to both membranes is achieved, as the IL thickness is lower than the insulation sheet thickness. This cut-out piece was later removed and was not part of the final assembly. The CCMs and the insulation sheet were arranged as shown in Figure 3.1b and hot pressed together at 130 °C and 130 kPa for 10 minutes to obtain the MEA shown in Figure 3.1c, using Carver press (MODEL C #3851). An MEA without the IL was also fabricated by hot pressing two half CCMs together. This MEA was used to determine the protonic resistance of the CCM without the IL and served as a reference case.

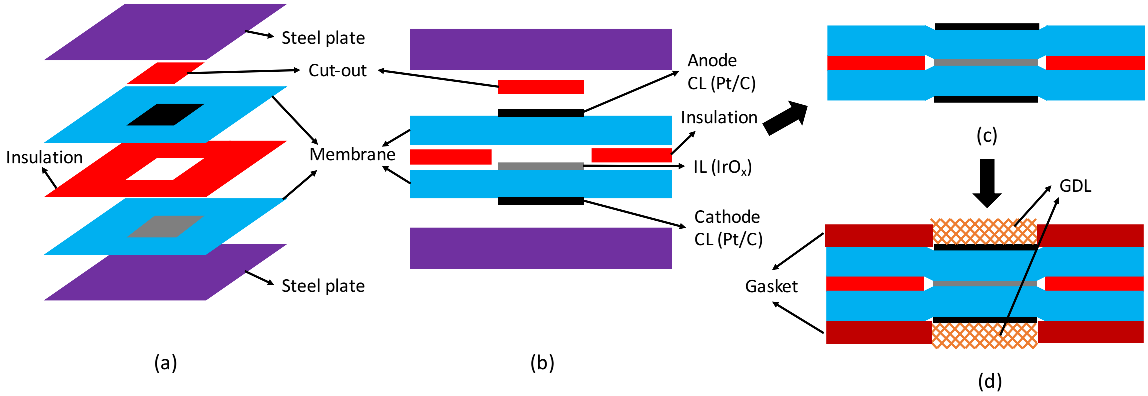

Figure 3.1 – Fabrication of MEA using hot press. (a) isometric view of the assembly for hot press, (b) front view of (a), (c) hot pressed MEA, and (d) MEA assembly with gaskets and GDLs.

Table 3.1 – Test conditions for the protonic and electronic resistance measurement of the intermediate layer.

	Hydrogen pump	TP electronic resistance measurement
Anode/cathode gas	Hydrogen/Hydrogen	Nitrogen/Nitrogen
Anode/cathode back pressure	Ambient/Ambient	
Cell temperature	80 °C	
Anode/cathode RH	30/30, 40/40, 50/50, 60/60, 70/70, 80/80, 90/90, and 100/100	
Anode/cathode flow rate	0.5 slpm/0.5 slpm	

3.1.4.2 H_2 pump experimental setup

A 5 cm^2 single cell with a single serpentine channel bipolar plate (BPP) made of graphite was used to assemble the cell (Scribner Association Inc.). GDLs with microporous layers (28BC, Sigracet SGL) were placed on both sides of the MEA, along with the gaskets (rigid fibreglass coated with PTFE) before assembling the cell. Two fuel cell test stations (Scribner Association Inc.) were used to maintain a gas flow rate of 0.5 slpm and the desired RH of the flowing gas on each side of the cell, and one of the test stations was used to maintain the cell temperature at 80 °C. Table 3.1 shows the experimental conditions for the H_2 pump test with and without the IL.

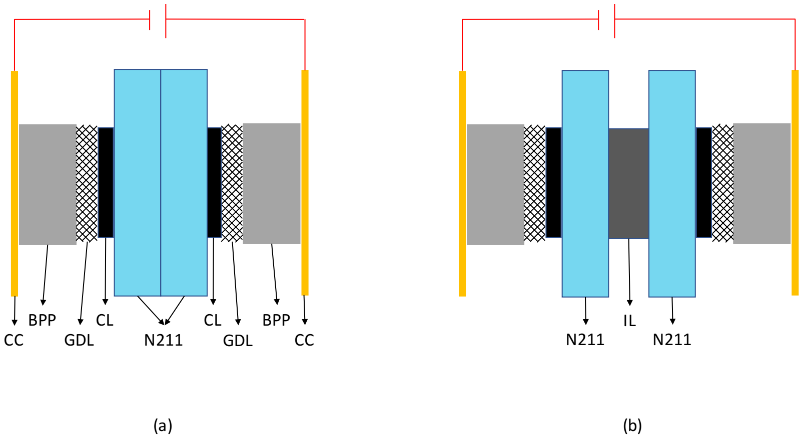

Figure 3.2 – Schematics of the two cases for hydrogen pump test without (a) and with (b) an intermediate layer.

3.1.4.3 Polarization curve measurement of H_2 pump cell

In order to measure a polarization curve, first the cell was maintained at a fixed RH for at least 30 minutes to properly humidify the cell. Then, a potentiostat (SP-300, Biologic) was used to perform a chronopotentiometry test in the current density range of 0–0.6 A/cm^2 with current steps ranging from 0.02 A/cm^2 at lower RH, to 0.1 A/cm^2 at higher RH, and with a current hold of 3 minutes per step. The slope of the resulting polarization curve was used to estimate the direct current (DC) cell resistance.

The polarization curve measurements were carried out in two cases as shown in Figure 3.2. In the first case, two NRE211 membranes were sandwiched between the anode and cathode Pt/C CLs, and the cell was assembled with two GDLs and two BPPs (Figure 3.2a). In the second case, two NRE211 membranes and an IL were assembled with GDLs and BPPs (Figure 3.2b). The protonic resistance of the IL was calculated by measuring the difference in the DC resistance between the cell without and with an IL [169]. Only this technique was used because the other method proposed by Iden et al. [169], which involves the difference between the DC cell resistance and the HFR of the cell with an IL, requires the electronic resistance of the IL to be negligible. As will be shown later, this is not the case for the IL studied here.

3.1.4.4 Analysis of data

According to Iden et al. [169], the protonic resistance of the intermediate layer (IL), $R^{IL}_{H^+}$, can be obtained as

$$R^{IL}_{H^+} = R^{w/IL}_{DC} - R^{w/oIL}_{DC} - 2R^{IL-PEM}_{C,\,DC} + R^{PEM-PEM}_{C,\,DC} \tag{3.1}$$

where $R^{w/oIL}_{DC}$ and $R^{w/IL}_{DC}$ are the DC resistances of the cell without and with an IL, respectively. $R^{IL-PEM}_{C,\,DC}$ is the contact resistance between the IL and the membrane, and $R^{PEM-PEM}_{C,\,DC}$ is the contact resistance between the two membranes. To accurately calculate the IL protonic resistance, $R^{IL-PEM}_{C,\,DC}$ needs to be subtracted and $R^{PEM-PEM}_{C,\,DC}$ needs to be added to the right-hand side of Equation (3.1). The contact resistance between the two membranes for the hydrogen pump case was estimated by subtracting the resistance of the cell with one N212 membrane (50.8 μm thickness) from the resistance of the cell with two NRE211 membrane (25.4 μm thickness) without an IL. The measured contact resistance was 13.8 mΩ·cm^2 which is approximately 15% of the resistance of the ILs on average, which was neglected. In order to determine this resistance of the IL, the protonic resistance of ILs of different thicknesses could be measured and used to separate contact resistances from IL resistances. Unfortunately, these measurements were not done for the protonic resistance measurement due to the time-consuming nature of the experiment. As the contact resistance between the IL and the membrane is not easy to isolate, both contact resistances between the IL and the membrane, and between the two membranes were neglected in the calculation of $R^{IL}_{H^+}$. In addition, the contact resistance between the IL and the membrane was minimized by printing the CL directly onto the membrane and the subsequent hot pressing of the MEA. Now, the protonic resistance of the IL, $R^{IL}_{H^+}$, can be obtained as

$$R^{IL}_{H^+} = R^{w/IL}_{DC} - R^{w/oIL}_{DC} \tag{3.2}$$

The protonic conductivity of the IL, $\sigma^{IL}_{H^+}$, is then calculated using the measured $R^{IL}_{H^+}$ and the IL thickness, t_{IL}, using

$$\sigma^{IL}_{H^+} = \frac{t_{IL}}{R^{H^+}_{IL}} \tag{3.3}$$

3.1.5 Electronic resistance measurement

3.1.5.1 Through-plane electronic resistance

For the through-plane (TP) electronic resistance measurement of the Ir/IrO$_x$ layer, a gold coated metal plate was first cleaned with IPA and dried. Then, the catalyst ink was inkjet printed on a 5 cm^2 area on the surface of the plate and dried at room temperature. A GDL with microporous layers (28BC, Sigracet SGL) was placed on top of the CL, along with the gaskets (rigid fibreglass coated with PTFE) and a BPP before assembling the cell. Table 3.1 shows the experimental conditions for the TP electronic resistance measurement with and without the CL.

3.1.5.1.1 Polarization curve measurement The assembled cell was maintained at a fixed RH for at least 30 minutes to properly humidify the CL. Then the polarization curve was obtained using linear sweep voltammetry (LSV) with a potentiostat from 0 to 20 mV at a scan rate of 1 mV/s. The slope of the polarization curve provides the electron-transport DC cell resistance.

To measure the TP electronic resistance of the CL, the polarization curves were carried out in two cases as shown in Figure 3.3. The first case includes two current collectors (CCs), a BPP, and a GDL (Figure 3.3a). In the second case, a CL is introduced into the setup of the first case (Figure 3.3b).

3.1.5.1.2 Analysis of data In the first method, the TP electronic resistance of the CL, $R_{e^-}^{IL}$, was calculated as

$$R_{e^-}^{IL} = R_{e^-}^{case2} - R_{e^-}^{case1} - R_C^{CC-IL} - R_C^{IL-GDL} + R_C^{CC-GDL} \tag{3.4}$$

where $R_{e^-}^{case1}$ and $R_{e^-}^{case2}$ are the DC resistances of the cell without and with a CL, respectively. R_C^{CC-IL}, R_C^{IL-GDL}, and R_C^{CC-GDL} are the contact resistances between the current collector and the IL, between the IL and the GDL, and between the current collector and the GDL, respectively. All the contact resistances were neglected from Equation (3.4) to calculate the TP electronic resistance of the IL as shown in Equation (3.5).

$$R_{e^-}^{IL} = R_{e^-}^{case2} - R_{e^-}^{case1} \tag{3.5}$$

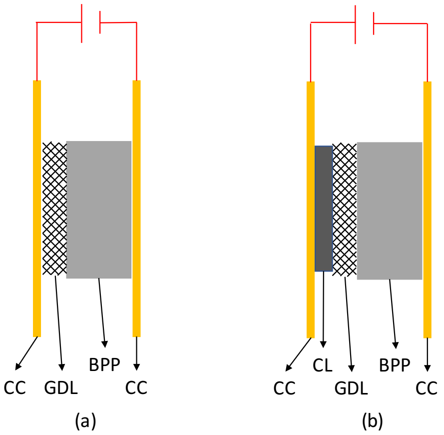

Figure 3.3 – Schematics of the two cases for the electrical resistance measurement without (a) and with (b) an IrO_x layer.

Then, using the TP electronic resistance of the CL and its thickness, the electronic conductivity was calculated. The impact of the contact resistances are removed from calculation of electronic conductivity when the two-thickness method was used. The two methods (Equation (3.5) and the two thickness method) resulted in a similar electronic conductivity, showing that the contact resistances are negligible compared to the CL electronic resistances.

In order to validate the results, the TP electronic conductivity of the CL is also calculated by measuring the resistance of two CLs with different thickness (i.e., different catalyst loading). Then the TP electronic conductivity, $\sigma_{e^-}^{IL}$, was calculated as: [217]

$$\sigma_{e^-}^{IL} = \frac{(t_{S2} - t_{S1})}{(R_{case2}^{S2} - R_{case2}^{S1})A} \tag{3.6}$$

where R_{case2}^{S1} and R_{case2}^{S2} are the electronic resistances of the two cells, each with a different CL thickness, t_{S1} and t_{S2} are the thicknesses of the two IrO_x layers which were 2 and 4 μm, respectively, and A is the printed geometric area of the IrO_x layer.

3.1.5.2 In-plane electronic resistance

In order to understand the anisotropy in the IL, the IP electronic resistance of the CL was also measured. To fabricate the CLs for the IP electronic resistance measurement, the catalyst ink was printed on a 5 cm^2 area on the surface of a Nafion membrane. The IP electronic resistance of the various samples were measured using the four-point collinear probe (4PP) method, using a Lucas Labs Pro4 4000 (the same instrument was used by Mo et al. [71]) with a Keithley 2601A sourcemeter, which have a probe spacing of 0.04 inch. The resistance was measured in 0° and 90° orientations of the sample before averaging it. The IP electronic conductivity was then calculated from the measured IP electronic resistance of the samples. The CL was dry while measuring the IP electronic resistance and the resistance at 100% RH is likely to be higher due to the expansion of the ionomer, which will decrease the number of contact points between the catalyst particles[160]. For the validation of the 4PP method, the IP electronic resistance of several GDLs, and carbon and ionomer layers were also measured. Samples with an area of 5 cm^2 were used for the measurement. Note that the four-point collinear probes penetrated the CL, which is not ideal; however, since Ref. 71 used the same equipment, the method was still attempted to measure the in-plane electronic conductivity in order to compare to those results.

3.1.6 Optical profilometer

The microstructure of the CL printed on the gold plate and on the membrane might be different due to the varying substrate. Therefore, the CL thickness of two CLs with a 5 and 10 wt.% ionomer loading printed on a gold plate were measured and compared to the CL printed on a membrane. The CL thickness on the gold plate was measured using a Zygo optical profilometer at six different locations.

3.1.7 Modelling of the hydrogen pump

In order to study the effect on the protonic resistance measurements of possible H_2 reduction and oxidation reactions occurring in the IrO_x IL, the hydrogen pump experiment was simulated using a 2-D macro-homogeneous model by Michael Moore. His modelling work is included in this thesis to strengthen the results obtained for this objective. The model, implemented in OpenFCST [218], was adapted from a previous work in PEMFCs [219]. The model is single-phase and isothermal. Species transport was neglected, as the concentration of hydrogen and water vapour is not expected to vary significantly, due to the low current densities and the presence of humidified hydrogen in both electrodes. The potentials of the solid and ionomer phases were solved for using Ohm's Law. The membrane water content in the CLs and membrane was solved for using a Springer model [219]. The governing equations and the domain used are shown in the appendix A, along with the key parameters for the model. The parameters that had the strongest impact on the results were the effective protonic and electronic conductivities of the membranes and CLs; the effective conductivities measured in this work were used directly. The simulation of the hydrogen reaction in the anode and cathode Pt/C CLs is based on the kinetic model from Elbert et al. [220] using the activation free energies reported for a platinum catalyst. The kinetics of the IrO_x IL were modelled using the Butler-Volmer equation, using kinetic parameters determined from a hydrogen pump experiment with a Pt electrode as the reference/counter electrode and IrO_x electrode as the working electrode. The use of the Butler-Volmer model allows for the oxidation or evolution reaction to proceed according to the local potentials of the two phases, no assumptions need to be made regarding which reaction occurs where in the IL, or if they occur at any meaningful rate.

3.2 Results and discussion

A summary of all the fabricated CCMs and their loadings is presented in Table 3.2 for the protonic conductivity measurement. The loading was calculated using a gravimetric method [200]. The CCM-w/o-IL in Table 3.2 is without an IL, and the rest CCMs are with an IL, where the IL consists of Ir or IrO_x. The platinum and Nafion loading in the anode and cathode CLs were maintained at 0.1 mg_{Pt}/cm^2 and 30 wt.% respectively. Note that the IrO_x loading of IL with 55 wt.% is lower compared to the other ILs because fabricating a CL with such a high ionomer loading is impacted by nozzle clogging and lengthy printing time. Since the CL thickness has been shown to increase linearly with catalyst loading between 0 and 2.5 mg_{IrO_x}/cm^2 [40, 74], the microstructures of ILs with different IrO_x loadings (in terms of mg_{IrO_x}/cm^2), but the same ionomer loading (in terms of wt.%), are assumed to be similar. The conductivity measurement for the lower IrO_x loading IL is therefore assumed to be comparable to an IL with the same volume fractions but a IrO_x loading of 1 mg/cm^2. This as-

Table 3.2 – Summary of the fabricated CCMs for the protonic resistance measurement.

	Cells tested	Cat. loading [mg/cm^2]	Naf. loading IL [%wt.]	Thickness [μm]	Naf. vol. frac.	Porosity	Ir or IrO$_x$ vol. frac.
CCM-w/o-IL	3	-	-	-	-	-	-
CCM-IrO$_x$-N05-IL	1	0.969	05	6.4±0.53	0.04	0.83	0.13
CCM-IrO$_x$-N10-IL	1	1.044	10	5.5±0.99	0.11	0.73	0.16
CCM-IrO$_x$-N15-IL	1	1.003	15	4.7±0.51	0.19	0.63	0.18
CCM-IrO$_x$-N25-IL	1	1.035	25	3.3±0.65	0.51	0.22	0.27
CCM-IrO$_x$-N35-IL	3	0.975	35	4.1±0.53	0.64	0.15	0.21
CCM-IrO$_x$-N55-IL	1	0.801	55	6.3±0.73	0.78	0.11	0.11
CCM-Ir-N05-IL	1	1.08	5	4.47±1.01	0.06	0.83	0.11
CCM-Ir-N10-IL	1	1.03	10	3.38±0.48	0.17	0.69	0.13
CCM-Ir-N15-IL	1	1.02	15	3.13±0.37	0.28	0.57	0.14
CCM-Ir-N25-IL	1	1.01	25	3.80±0.78	0.44	0.44	0.12

sumption is further validated by comparing the through-plane electronic conductivity (later in the thesis) of two ILs with 35 wt.% ionomer loading and varying IrO$_x$ loading using the two-thickness method. In that case, the obtained conductivities are similar.

3.2.1 Polarization curve of electrolyzer cell

Figure 3.4 shows the obtained polarization curves together with several polarization curves from Ref. 33. As shown in Figure 3.4, the IrO$_x$ electrodes in this study achieved performances that are on-par with state-of-the-art electrodes. The best performance was obtained for an anode CL with 25 wt.% ionomer loading.

3.2.2 SEM imaging

In order to study the variation in the IL thickness with varying ionomer loading, SEM cross-sectional images of the Ir and IrO$_x$ IL were captured as shown in Figures 3.5 and 3.6 respectively. In order to verify the thickness measurement was not affected by imaging artifacts such as tilting, the thickness of the PEM was also measured and compared to the manufacturer's specification. An error of less than 3% was observed. The IL thickness was measured at ten different locations of an image,

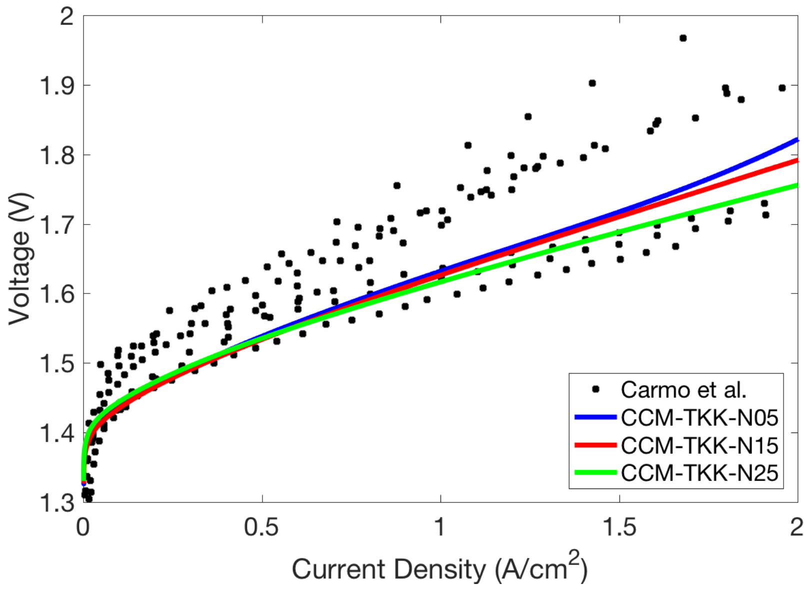

Figure 3.4 – Electrochemical performance of the investigated ILs with IrO$_x$ catalyst.

and several images were used to take into account the possible inhomogeneities in the IL thickness. The measured IL thickness is shown in Table 3.2. Using the volume fractions in Table 3.2, an effective thickness of each component is obtained and shown in Figure 3.7 for varying ionomer loading. With an increase in the ionomer loading, the IL thickness first decreased and then increased for both Ir and IrO$_x$ layers. In general, the thickness of the IrO$_x$ CLs is higher than the Ir CLs. This might be due to the catalyst particle morphology which is not particulate in the case of Umicore Ir, but flake like structure, whereas the TKK IrO$_x$ particles are particulate and the surface are corrugated and rich in pore as shown in Figure 3.10, and also described the same in Ref. [96].

The decrease in the IrO$_x$ IL thickness is likely due to the reduction of cracks and layer porosity. Surface SEM images of the IrO$_x$ CLs are shown in Figure 3.8, which shows a decrease in the surface cracking of the IL from 15 %wt. to 25 %wt. ionomer loading. Ahadi et al. [181] also reported a decrease in crack density with increasing ionomer loading in the case of PEMFC CLs. There are no cracks to be observed in Ir CLs shown in Figure 3.9. The reason for having surface cracks in the case of IrO$_x$ CLs and not in the case of Ir CLs might be due to the difference in the catalyst surface area. The BET surface area of IrO_x and Ir is 106 and 26 m^2/g, respectively. It is hypothesized that due to a higher BET surface area of IrO_x particles, a higher amount of ionomer loading is required to bind the particles together than for the Ir particles. Because of the above hypothesis, it might be possible that for the same amount of ionomer loading, cracks can be seen in IrO_x CL and not in the Ir CL. The decrease in the Ir CL thickness with an increase in the ionomer loading from 5 to 15 wt.% might be due to a better binding of Ir particles with an increase in the ionomer loading. The increase in the Ir or the IrO_x CL thickness at higher ionomer loading is likely simply due to an increase in the amount of solid required to reach the same catalyst loading as more ionomer is introduced, given that the void and Ir/IrO_x thickness remain the same, as shown in Figure 3.7. Gode et al. [177] reported similar behaviour in the case of PEMFC CLs, while Soboleva et al. [221] observed the opposite trend in PEMFC CLs such that the thickness increased and then decreased with an increase in the ionomer loading.

The volume fractions of each phase in the IL are shown in Table 3.2. The volume fraction calculations are presented in the Appendix A. The ionomer volume fraction increases with an increase in the ionomer loading as expected, while the porosity decreases with an increase in the ionomer loading. The catalyst volume fraction varies between 11–27% for IrO_x and between 11-14% for Ir; these fractions are generally lower than those measured in Ref. 62. This difference is likely caused by the use of a different catalyst and fabrication method. Ref. 62 used an IrO_2 catalyst on TiO_2, which was fabricated using a Mayer Bar with decal transfer. For the same fabrication method and composition, different catalysts can produce CLs with very different thicknesses and porosity (for the IrO_x catalyst in this chapter thicknesses of 6.4 μm and porosity of 83% were obtained, whereas thicknesses of around 1.4–1.9 μm and porosity between 10-29% were obtained for the Alfa Aesar IrO_2 catalyst in the previous chapter 2). Other works that used unsupported catalysts with low ionomer loadings, have shown porosities of a similar range to that measured in this work for the 5 wt.% ionomer loading CL [52, 74, 202].

The IrO_x volume fraction increased from 0.13 to 0.27 with an increase in the

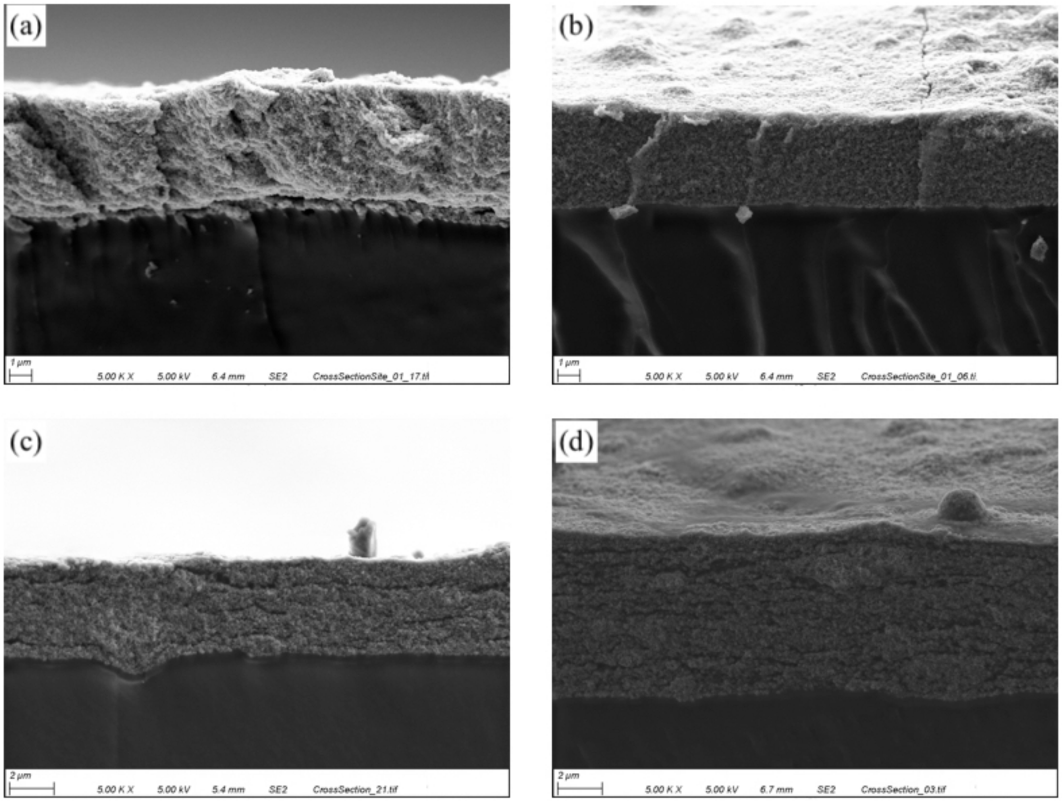

Figure 3.5 – SEM images of the IrO_x layer cross-section. (a) CCM-IrO_x-N15-IL, (b) CCM-IrO_x-N25-IL, (c) CCM-IrO_x-N35-IL, and (d) CCM-IrO_x-N55-IL.

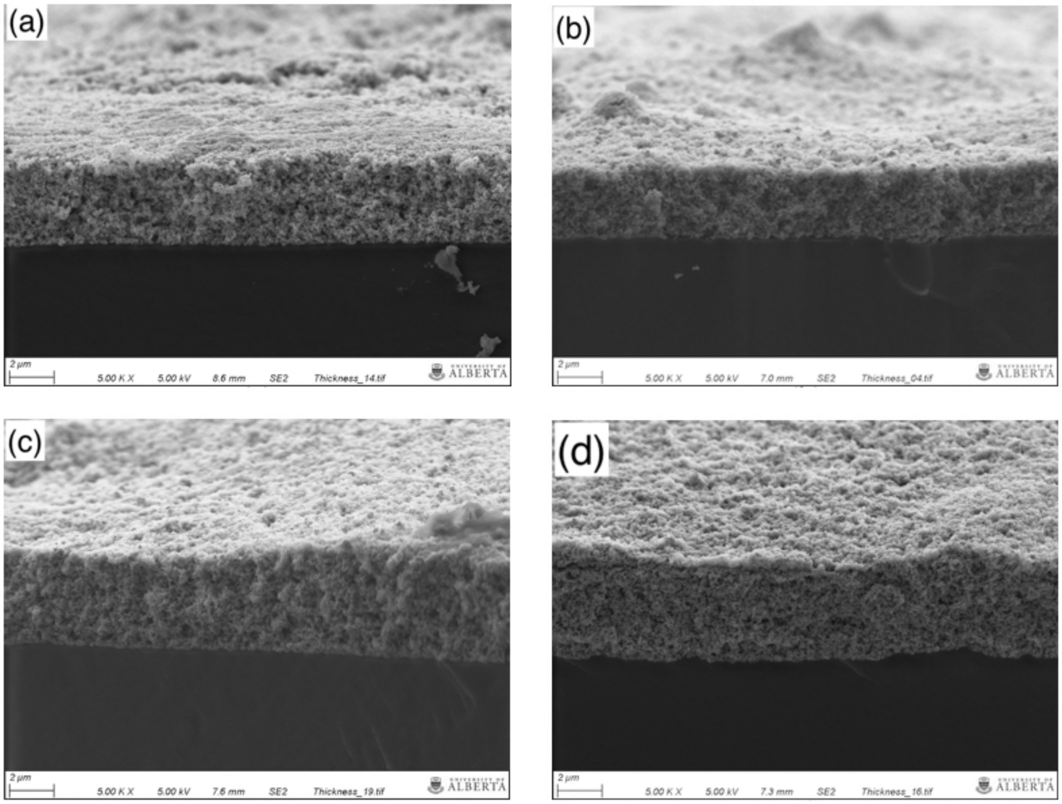

Figure 3.6 – SEM images of the Ir layer cross-section. (a) CCM-Ir-N5-IL, (b) CCM-IrO-N10-IL, (c) CCM-IrO-N15-IL, and (d) CCM-Ir-N25-IL.

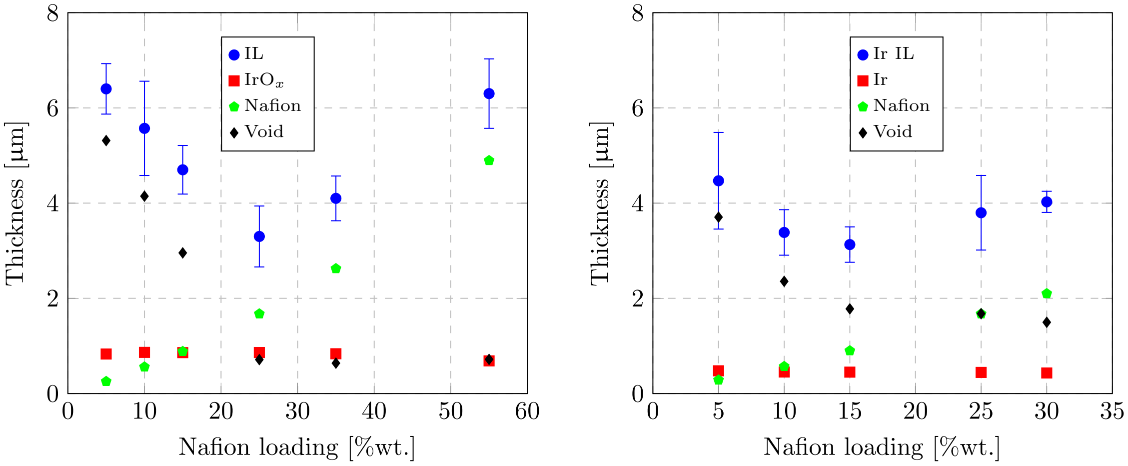

(a) Intermediate layer with IrO_x

(b) Intermediate layer with Ir

Figure 3.7 – Effective thickness of the different components of the IrO_x layer, i.e., the IrO_x, ionomer, and void space along with the total thickness which is denoted as IL.

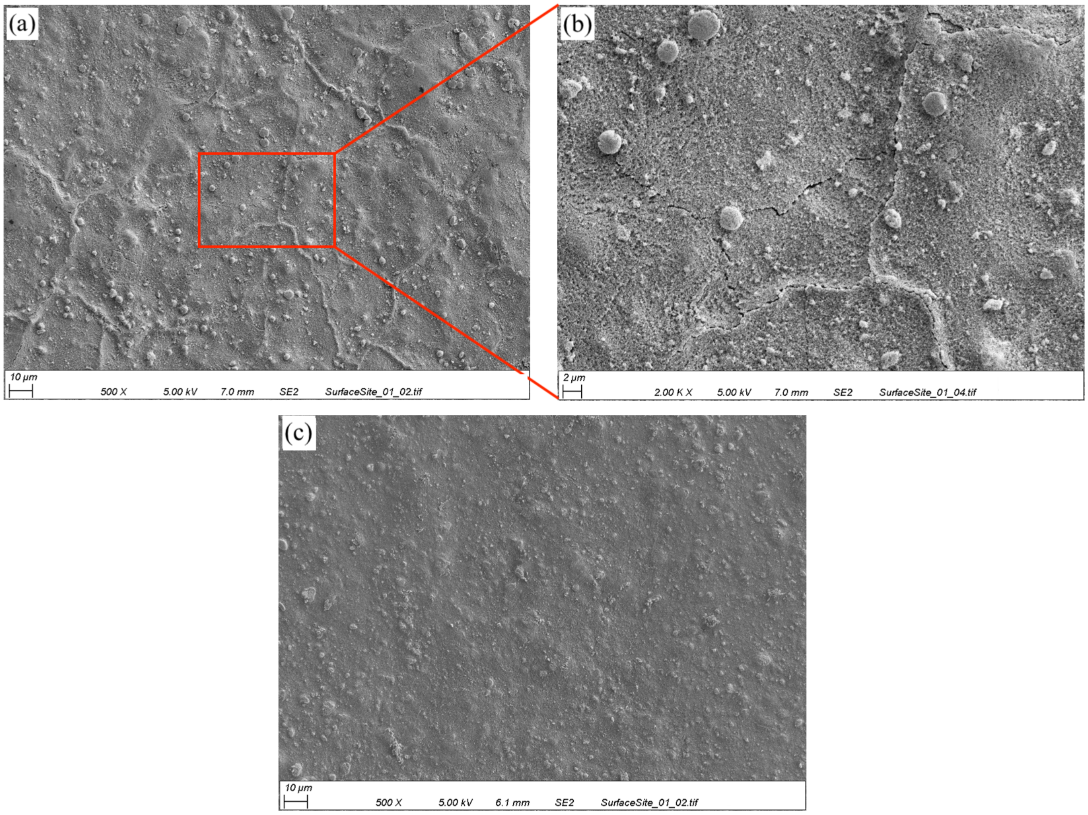

Figure 3.8 – (a) SEM images of the IrO_x layer surface with 15 wt.% ionomer loading, (b) magnified image of image (a), and (c) 25 wt.% ionomer loading.

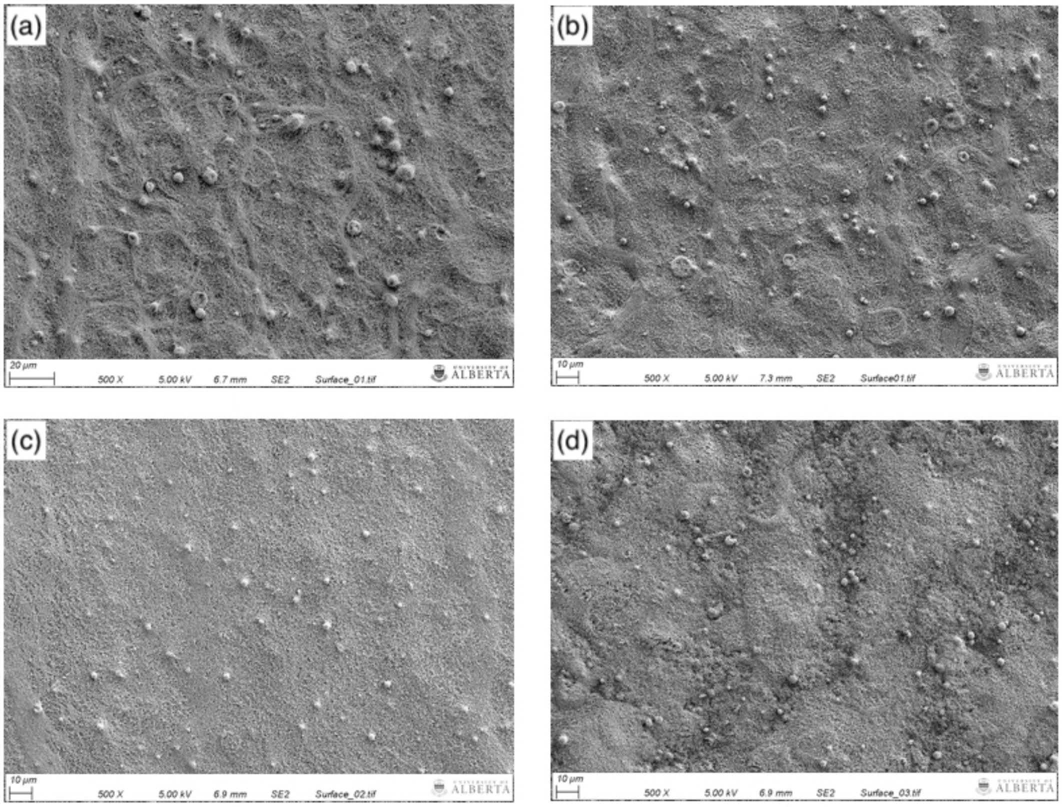

Figure 3.9 – Surface SEM images of the Ir layer with an ionomer loading of 5 wt.% (a), 10 wt.% (b), 15 wt.% (c), and 25 wt.% (d).

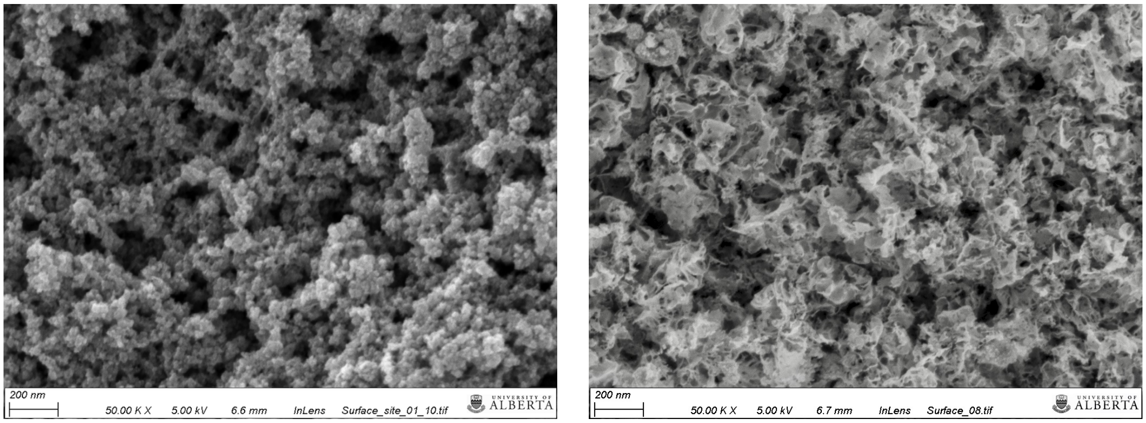

(a) IrO_x CL with 5 wt.% ionomer loading

(b) Ir CL with 5 wt.% ionomer loading

Figure 3.10 – Comparison of the catalyst particle of TKK IrO_x and Umicore Ir.

ionomer loading from 5 to 25 wt.% and decreased from 0.27 to 0.11 with further increase in the ionomer loading from 25 to 55 wt.%. This trend may be caused by the presence of cracks in the layers at ionomer loadings below 25 wt.%. It is speculated that at low ionomer loadings, there is insufficient ionomer to bind the CL, resulting in a higher than expected porosity and therefore a lower IrO_x volume fraction. Increasing the ionomer loading then rapidly reduces the porosity, as the ionomer fills the pores and reduces the cracks, leading to a reduced layer thickness. At 25 wt.% ionomer loading a minimum thickness is reached and further increase in the ionomer loading causes the IL thickness to increase. In this case, the IrO_x volume fraction decreased with increasing ionomer loading, as expected. The variation in the IrO_x volume fraction is relatively constant, however, compared to the variation in the ionomer and void volume fractions. A relatively constant solid volume fraction with ionomer loading was also observed in PEMFC catalyst layers by Gode et al. [177]. The variation in the Ir volume fraction is relatively constant as expected due to the absence of the CL crack.

3.2.3 Optical profilometer

To measure the electronic conductivities of the CLs, the thickness of the CL printed on the gold plate is required. In order to compare the protonic and electronic conductivities of a CL, the microstructure of the CL printed on the gold plate and on the membrane need to be comparable to each other. In order to compare the microstructure of the CLs fabricated on two different substrate, i.e., PEM membrane and gold plate, the thicknesses of the CLs printed on gold plate were measured using a Zygo optical profilometer (). Images at several locations were taken into account to measure the variation in the CL thickness.

Figure 3.11 shows the data obtained from the profilometer for an IrO_x CL with 5 wt.% ionomer loading at one location. The averaged thicknesses of IrO_x layers with a 5 and 10 wt.% ionomer loading obtained from the profilometer and from the SEM, where the substrate is a membrane, are summarized in Table 3.3. Note the thickness error from the profilometer of the IL with a 10 wt.% ionomer loading is higher due

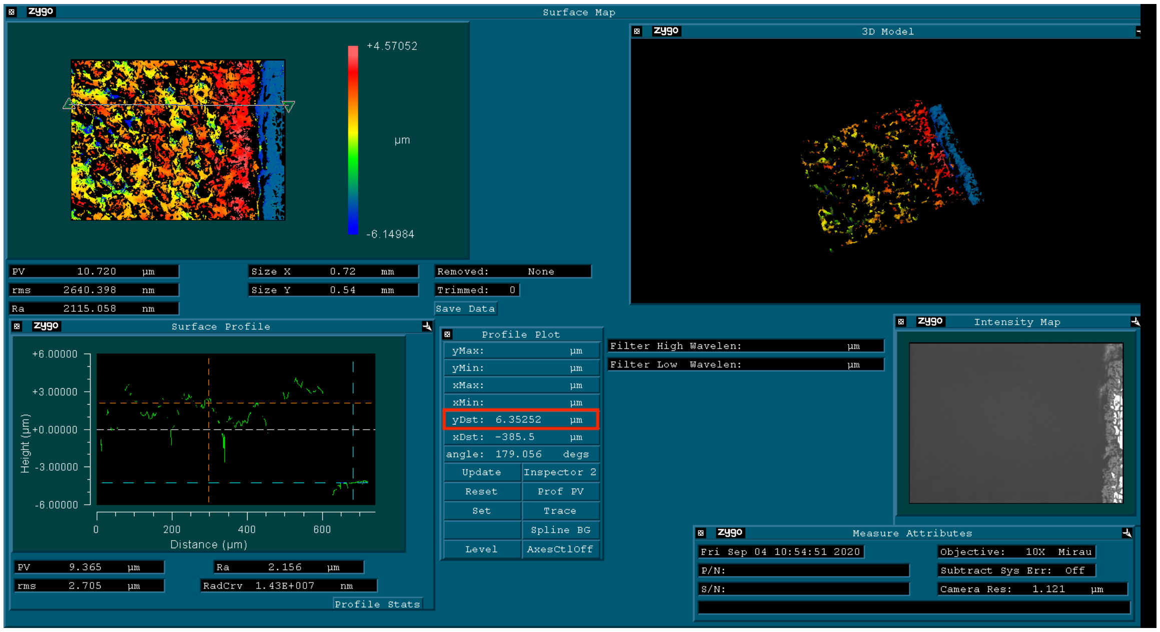

PV 10.720 µm
rms 2640.398 nm
Ra 2115.058 nm
Size X 0.72 mm
Size Y 0.54 mm
Removed: None
Trimmed: 0

PV 9.365 µm
rms 2.705 µm
Ra 2.156 µm
RadCrv 1.43E+007 nm

yMax: µm
yMin: µm
xMax: µm
xMin: µm
yDst: 6.35252 µm
xDst: -385.5 µm
angle: 179.056 degs

Filter High Wavelen: µm
Filter Low Wavelen: µm

Fri Sep 04 10:54:51 2020
P/N:
S/N:
Objective: 10X Mirau
Subtract Sys Err: Off
Camera Res: 1.121 µm

Figure 3.11 – Thickness of the IrO_x layer with 5 wt.% ionomer loading using Zygo optical profilometer.

Table 3.3 – Comparison of the IrO_x layer thickness obtained from the SEM images and using profilometer.

	SEM imaging [µm]	Profilometer [µm]
IrO_x-N05-IL	6.4±0.53	6.32±0.45
IrO_x-N10-IL	5.57±0.99	5.67±1.8

to the uneven surface of the gold plate and poor reflectivity of the CL. The error decreased significantly after polishing the gold plate surface before printing the CL with 5 wt.% ionomer loading, resulting in a lower thickness error. The thicknesses of two CLs with varying ionomer loading printed on a gold plate (measured via optical profilometry) and on a membrane were similar, therefore the volume fractions should also be comparable and, as a result, it was assumed the resulting microstructures would also be similar.

The thickness of Ir CLs with varying Ir loading printed on the gold plate was also measured. Figure 3.12 shows the measured thickness of the CLs using profilometer. The Ir CL thickness increased with an increase in the catalyst loading almost linearly.

Table 3.4 – Summary of the fabricated Ir CLs on the gold plate.

	Ir loading [mg/cm^2]	Naf. loading [wt.%]	CL thickness [µm]	Porosity	Ir Vol. fraction	Naf. Vol. fraction
Ir-N30-Pt1	1.022	30	4.03±0.22	0.34	0.11	0.55
Ir-N30-Pt2	2.016	30	7.54±0.44	0.31	0.12	0.57
Ir-N30-Pt3	2.996	30	9.93±0.93	0.22	0.13	0.65

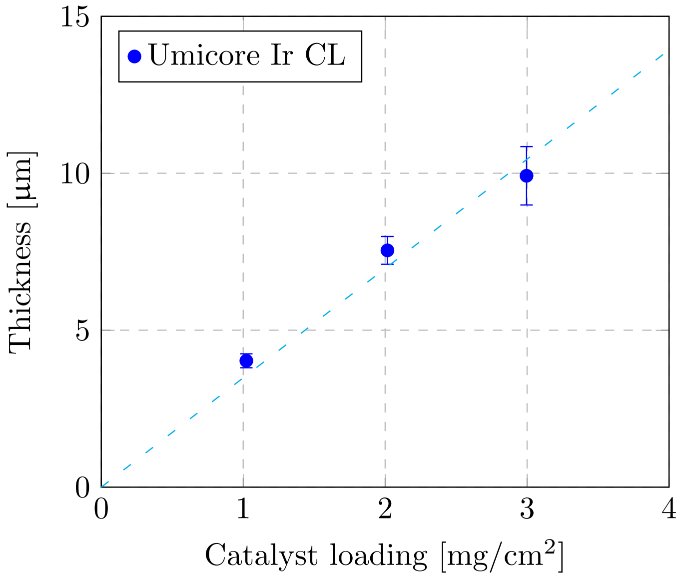

Figure 3.12 – The Ir CL thickness measured using profilometer.

The porosity of the CL decreased and the ionomer volume fraction increased with an increase in the catalyst loading. This might be due to the compaction of the CL due to the increase in the number of printed layers to achieve a higher catalyst loading. This effect was also observed in ref. [130] for PEMFC CLs of varying catalyst loading.

The measured thickness of the Ir CL with 30 wt.% ionomer loading using profilometer is included in Figure 3.7b along with the other CL thickness measured from SEM images. The measured CL thickness using profilometer is in accordance with the thickness measured from SEM images. This shows that the microstructure of the CL printed on a PEM and on a gold plate would be similar in nature.

3.2.4 Protonic conductivity of IrO_x layer

First, the repeatability of the experimental setup is examined, and then experimental results are compared to literature for validation. Then, the protonic conductivity values are provided and discussed.

3.2.4.1 H_2 pump polarization curve

Figure 3.13 shows the relationship between the voltage drop and the current density under various RH conditions for three CCMs; the first is without an IrO_x layer (Figure 3.13a), the second and third are with an IrO_x layer with 35 and 55 wt.% ionomer loading (Figures 3.13b and 3.13c). The voltage drop showed good linearity with the current density. The overall resistance from H_2 pump test is obtained from the slope of the individual polarization curve, giving the cell resistance under different RH conditions.

3.2.4.2 Repeatability

Three cells with and without an IL were tested. Figure 3.14 shows the resistances obtained from the polarization curves. The measured resistance showed excellent reproducibility, with an average standard deviation of 12 and 20 $m\Omega \cdot cm^2$ for the cells without and with an IL, respectively. These standard deviations are less than 10% of the average measured resistance, thereby proving the repeatability of the method.

3.2.4.3 Validation

In order to validate the measured resistance, the experiment proposed by Iden et al. [169] was reproduced and our results were compared to the literature values. Figure 3.14a shows the resistance of the cell without an IL as a function of RH along with the same resistance data obtained by Iden et al. [169]. It can be observed that the obtained resistances in this study are in good agreement with the literature data.

3.2.4.3.1 Protonic conductivity of the carbon and ionomer IL To further validate the H_2 pump method, the effective protonic conductivities of two ILs with an I/C ratio of 0.9 made with either Vulcan XC-72 (Fuel Cell Store) or Ketjen black

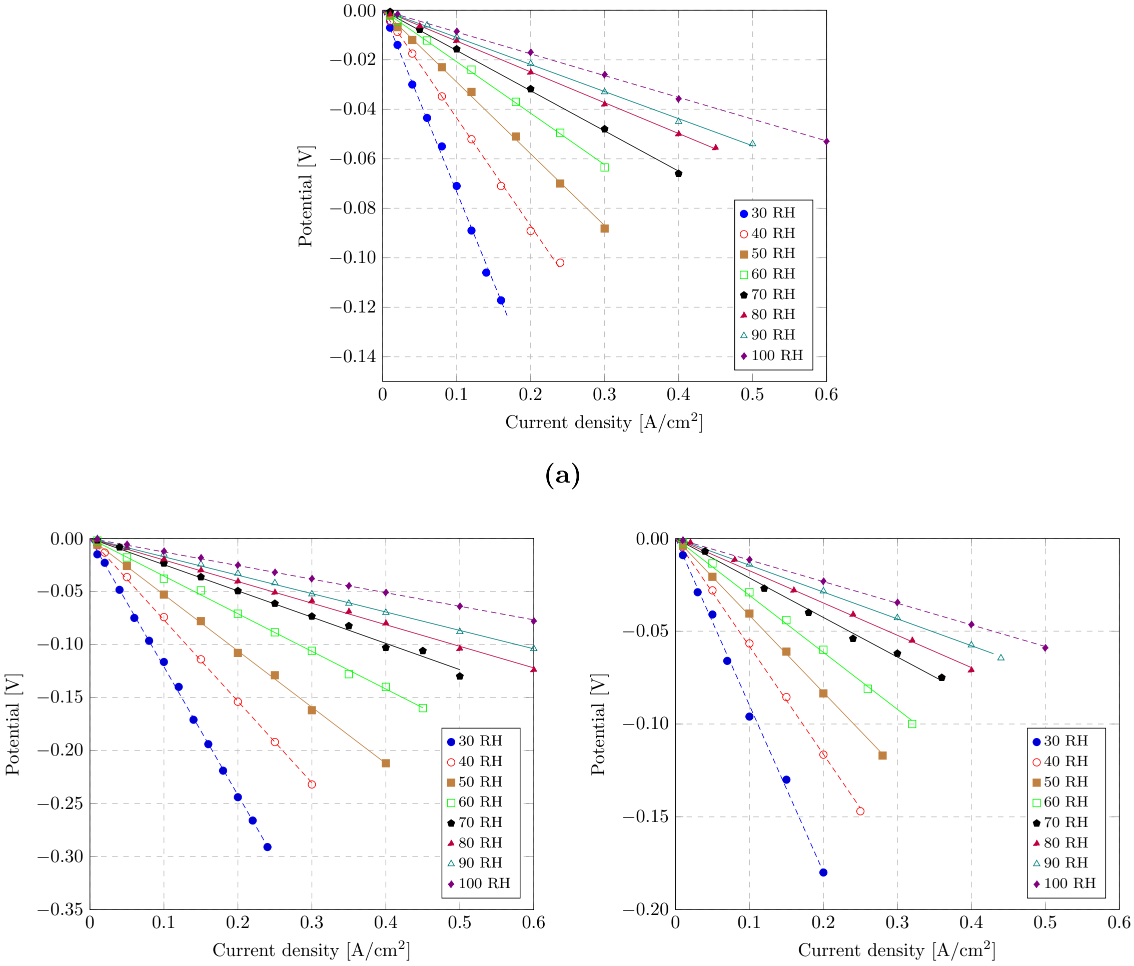

(a)

(b)

(c)

Figure 3.13 – Voltage drop as a function of current density at different RH conditions at 80 °C for a CCM without an IrO_x layer (a), with an IrO_x layer with 35 wt % (b), and 55 wt % (c) ionomer loading.

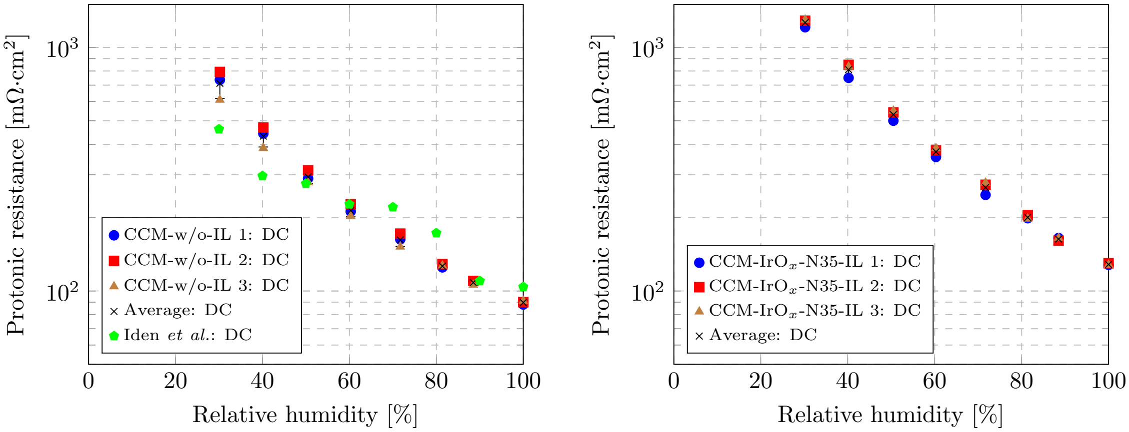

(a) **(b)**

Figure 3.14 – DC cell resistance of a CCM without intermediate layer, $R_{DC}^{w/oIL}$, (a), and with intermediate layer, $R_{DC}^{w/IL}$, (CCM-IrO$_x$-N35-IL) (b). (a) also compares results from this work to data from Iden et al. [169].

(HyPlat) were calculated using the two methods described by Iden et al. [169]. The first method involves subtracting the resistance of the cell without an IL from the resistance of a cell with an IL. The second method involves subtracting the high frequency resistance (HFR) of the cell with an IL from the overall cell resistance of the same cell obtained from the H_2 pump test. The obtained conductivities from this work and from several sources in the literature are shown in Figure 3.15. The two methods yield similar results in this study. Further, our results reproduce the trends observed in the literature, i.e., the conductivity increased with an increase in the RH. Even though a direct comparison of the conductivity is not possible due to differences in the carbon type, composition and fabrication method, the obtained results are in line with those reported in literature.

3.2.4.3.2 Protonic conductivity of the Nafion membrane A third validation of the H_2 pump method was done by calculating the protonic conductivity of the membrane and comparing to the literature. The conductivity was calculated from the HFR of the cell with a N212 membrane after accounting for the resistance of the cell hardware and assuming the electronic resistance of the anode/cathode CLs are

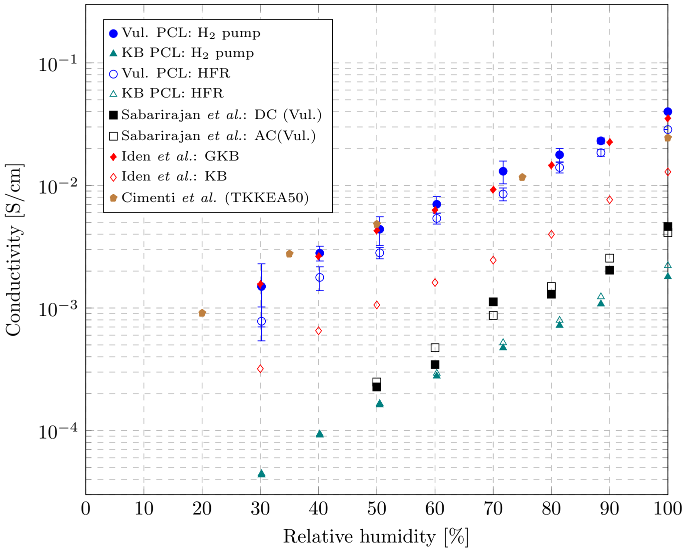

Figure 3.15 – Protonic conductivity of the Vulcan XC-72 and Ketjen black carbon and ionomer intermediate layer.

negligible (≈ 0.172 mΩ·cm^2, measured using the four-point collinear probe method). Figure 3.16 shows the dependence of the protonic conductivity of the Nafion 212 membrane on RH. The obtained protonic conductivity of the membrane is in excellent agreement with literature data [157, 169, 195, 222].

3.2.4.4 Ionomer loading study on intermediate layer protonic conductivity

The effective protonic conductivities of the ILs with varying ionomer loading were calculated using Equation (3.3) with the measured resistances and CL thicknesses. Figure 3.17 shows that, as expected, the conductivity increased with increasing RH and with increasing ionomer loading. Figure 3.17a that the protonic conductivity of the IrO$_x$ IL with 10 wt.% ionomer loading is one to two orders of magnitude lower than that of an IL with 15 wt.% ionomer loading. Similarly, the protonic conductivity of the IrO$_x$ IL with 15 wt.% ionomer loading is two to three orders of magnitude lower than the 25 wt.% ionomer loading IrO$_x$ ILs, indicating a strong dependance of the protonic conductivity on ionomer loading. ILs with Ir show a very different behaviour in Figure 3.17b. In this case, the protonic conductivities of the Ir ILs are nearly within the same magnitude and also similar to the IrO$_x$ IL with 25 wt.% ionomer loading

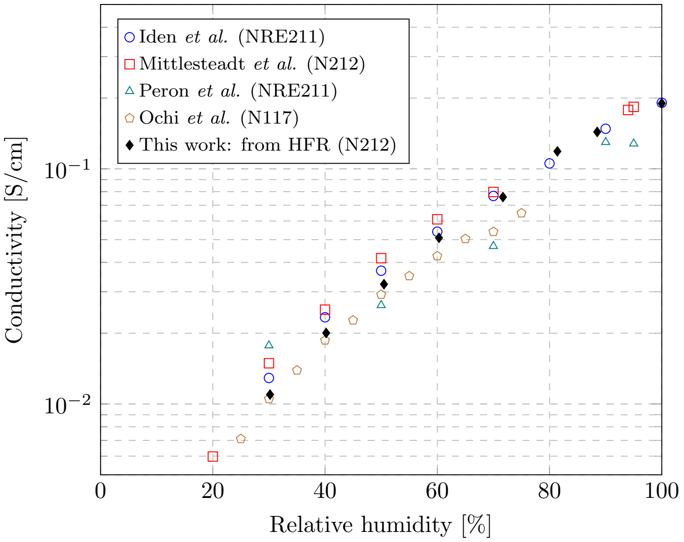

Figure 3.16 – Protonic conductivities of the Nafion membranes.

and above. This might be due to the different surface area of the catalyst. Due to a higher surface area of the IrO_x catalyst a higher amount of ionomer is required to obtain a ionomer connectivity. Further, the differences in the conductivities might be caused by the use of different catalysts, which would interact differently with the ionomer, leading to the different microstructural properties.

The protonic conductivity of the IrO_x with 25 wt.% ionomer loading is 6.07×10^{-3} S/cm at 100% RH, lower than previous values reported in the literature. Babic et al. [162] measured the protonic conductivity of a CL with 20 wt.% ionomer loading and 0.8 mg_{IrO_2}/cm^2 to be 8.3×10^{-3} S/cm. Bernt and Gasteiger [62] calculated the effective protonic conductivity of a CL with 28 wt.% ionomer content to be around 0.4–0.6 S/cm. This value however was obtained assuming the ionomer bulk conductivity in the CL to be the same as that of a PEM, which has been shown to not be the case [163].

A percolation model was used to estimate how the effective protonic conductivity of the IL changes with ionomer volume fraction. This is a semi-empirical model that is applied in order to relate CL conductivity to ionomer volume fraction for numerical simulations. It is very difficult to obtain a mechanistic understanding of

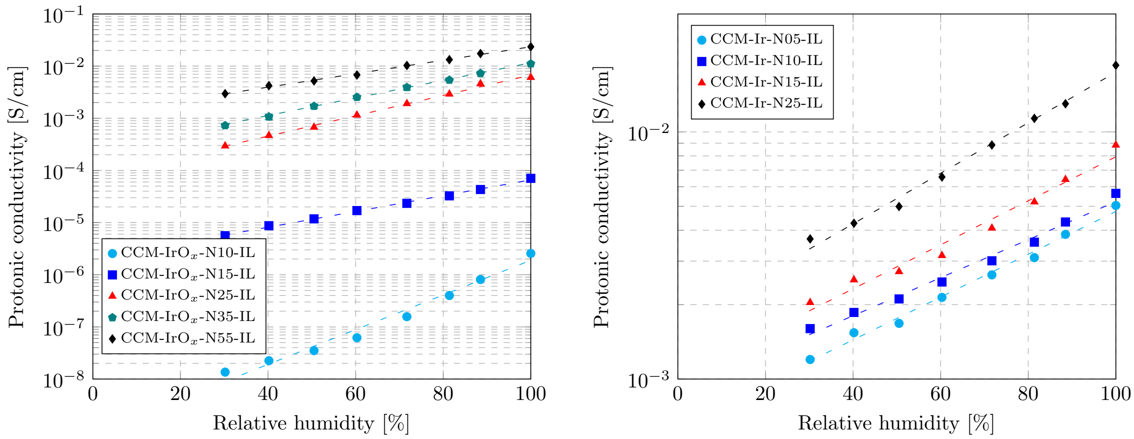

(a) **(b)**

Figure 3.17 – Protonic conductivity of the IrO$_x$ layer (a) and Ir layer (b).

proton transport in the CL using this model. According to this equation, the effective protonic conductivity, σ_{H+}^{eff}, can be expressed as [223]:

$$\sigma_{H^+}^{eff} = \sigma_{H^+}^{bulk} \left(\frac{\epsilon_N - \epsilon_{N_{th}}}{1 - \epsilon_{N_{th}}} \right)^{\gamma} \tag{3.7}$$

where $\sigma_{H^+}^{bulk}$ is the bulk protonic conductivity of the ionomer, ϵ_N is the volume fraction of the ionomer in the IL, $\epsilon_{N_{th}}$ is the threshold volume fraction of the ionomer in the IL, where ionomer volume fractions (ϵ_N) below this value will result in a conductivity of zero, and γ is the exponential factor, which is related to the tortuosity of the conducting media, and, for a three-dimensional lattice, is expected to be between 2 and 3 [224].

The percolation model was fitted to the protonic conductivities at 100% RH only, as it is most representative of the PEMWE operation in liquid water, by estimating three parameters, i.e., $\sigma_{H^+}^{bulk}$, $\epsilon_{N_{th}}$, and γ. The expansion percentage of ϵ_N at 100% RH is taken from Ref. 169. Further details on the fitting procedure is presented in Appendix A. Figure 3.18 shows the fitting of the conductivity data points to the percolation model. A good fit between the model and the experimental data was obtained. For this study, the best fit was obtained with $\epsilon_{N_{th}} = 0.077$, $\gamma = 3.18$, and the ionomer bulk conductivity in the CL of 0.0407 S/cm for the IrO$_x$ IL. The high

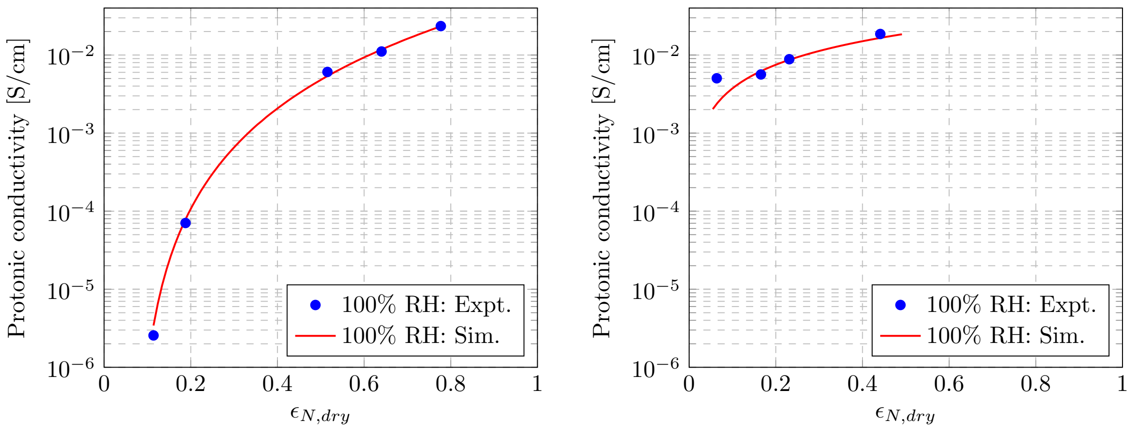

(a) IrO$_x$ **(b)** Ir

Figure 3.18 – Fitting of the protonic conductivity data at 100% RH to the percolation model.

value of γ implies a high tortuosity of the conducting media. For the Ir IL, the best fit was obtained with $\epsilon_{N_{th}} = 0.004$, $\gamma = 1.0$, and the ionomer bulk conductivity in the CL of 0.038 S/cm. A low value of γ implies a low tortuosity of the conducting media. The difference in the tortuosity of the CLs might be due to the difference in the catalyst surface area. However, the ionomer bulk conductivity in the CL in both cases is nearly the same, which validates the use of percolation model in this work and that the ionomer bulk conductivity in the CL is lower than the ionomer bulk conductivity of a membrane.

3.2.5 Electronic conductivity of the catalyst layer

The ionomer loading not only affects the protonic conductivity of the CL, but also the electronic conductivity of the CL. Table 3.5 shows the summary of the fabricated CLs printed on the gold plate for the through-plane electronic resistance measurement. Two CLs with different IrO$_x$ loadings and 35 wt.% ionomer loading and three CLs with different Ir loadings and 30 wt.% were printed on the gold plate to measure the TP electronic conductivity using the two-thickness method.

Table 3.5 – Summary of the fabricated CLs on the gold plate for the through-plane electrical resistance measurement.

	Cells tested	Cat. loading [mg/cm^2]	Naf. loading [%wt.]	Thickness [μm]	Nafion vol. frac.	Porosity	Cat. vol. frac.
Hardware	3	-	-	-	-	-	-
IrO$_x$-N05-IL	1	1	05	6.3	0.04	0.83	0.13
IrO$_x$-N10-IL	2	1	10	5.7	0.11	0.74	0.16
IrO$_x$-N15-IL	2	1	15	4.7	0.19	0.63	0.18
IrO$_x$-N25-IL	1	1	25	3.5	0.51	0.22	0.27
IrO$_x$-N35-IL	1	0.5	35	2.0	0.64	0.15	0.21
IrO$_x$-N35-IL	2	1	35	4.0	0.64	0.15	0.21
IrO$_x$-N60-IL	1	0.6	60	4.5	0.815	0.092	0.093
Ir-N05-IL	1	1.08	05	4.5	0.06	0.83	0.11
Ir-N30-IL	2	1.02	30	4.03	0.55	0.34	0.11
Ir-N30-IL	1	2.02	30	7.54	0.57	0.31	0.12
Ir-N30-IL	1	3.00	30	9.93	0.65	0.22	0.13

3.2.5.1 Through-plane electronic conductivity

3.2.5.1.1 Repeatability and validation: A modified two-probe method is used to measure the TP electronic resistance of the IL with varying RH in this study. In order to assess the reproducibility of the method, three IrO$_x$-N35-IL samples, two with different IrO$_x$ loadings, and three Ir-N30-IL were tested. Figure 3.19 shows the relationship between the voltage drop and the current density under various RH conditions for the IrO$_x$ layer printed on the gold plate with a 35 wt.% ionomer loading. The voltage drop showed good linearity with the current density. The overall resistance of the cell is obtained from the slope of the individual polarization curve.

Figure 3.20 shows the measured TP electronic resistance and the calculated TP electronic conductivity of the IrO$_x$-N35-IL and Ir-N30-IL using Equation (3.3). The TP electronic resistance of the two IrO$_x$-N35-IL with 1 mg/cm^2 IrO$_x$ loading show good repeatability (Figure 3.20a). The TP electronic resistance of the layer with half the loading (0.5 mg/cm^2) is almost half due to the linear increase of the IrO$_x$

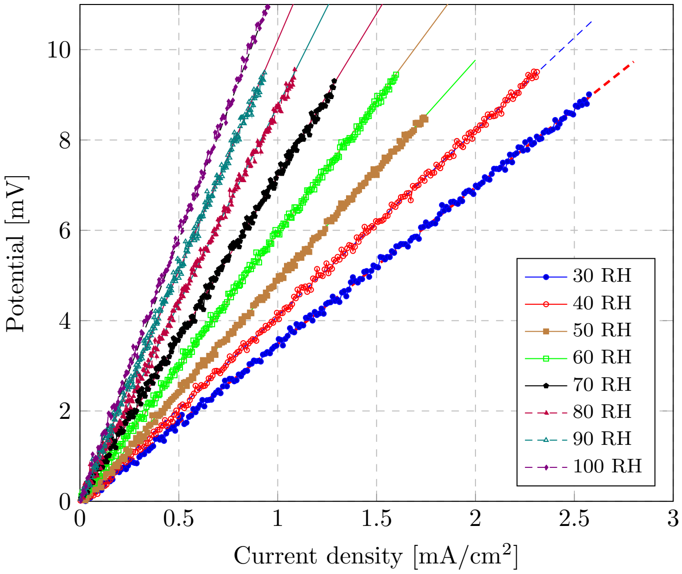

Figure 3.19 – Voltage drop as a function of current density at different RH conditions at 80 °C for IrO$_x$ layer printed on the gold plate with 35 wt % ionomer loading.

layer thickness with an increase in the IrO$_x$ loading in the range of 0–2.5 mg/cm^2 [40, 74]. Figure 3.20b shows the excellent agreement between the conductivities for each cell, as well as that computed using the two thickness method. The similarity of the results between the two methods, Equation (3.6) and Equation (3.3), validates the methodology used in this work. Figure 3.20b also shows excellent reproducibility between cells, with an average standard deviation of 1.65×10^{-6} S/cm, i.e., 3% of the measured average value. Additional repeatability tests were carried out for ionomer loadings of 10 and 15 wt.%. Two samples were prepared for each loading; variations of 3% and 40% were obtained for the TP electronic conductivity measurements at 100% RH. The measured conductivities from the repeated tests are shown in Figure 3.21a. The reason for the large variation for the 15 wt.% IL is unknown, however it might be due to a manufacturing defect as the two layers were fabricated several months apart. Figure 3.20c shows the electronic conductivity of Ir CL with 30 wt.% ionomer loading with excellent repeatability with an average standard deviation of 4.15×10^{-3} S/cm, i.e., 8% of the measured average value.

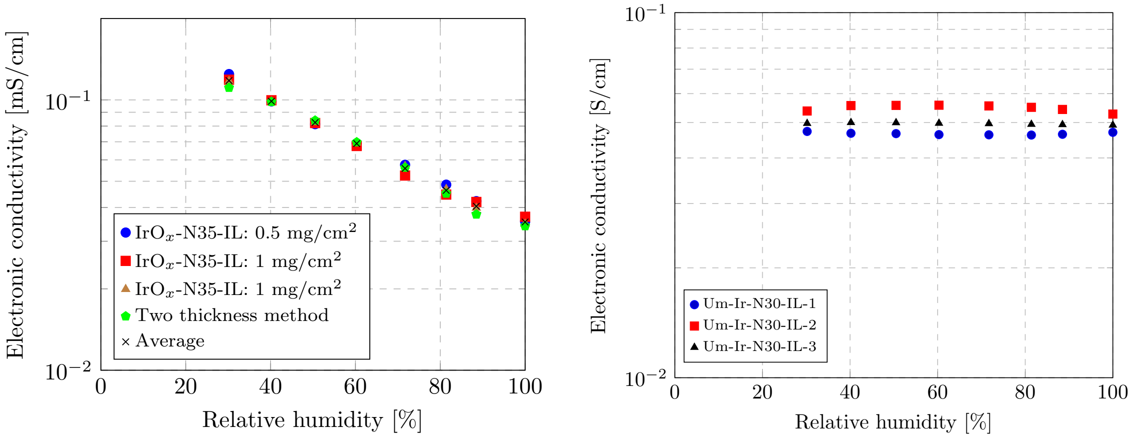

(a) **(b)**

Figure 3.20 – (a) Electronic conductivity of an IrO$_x$-N35-IL and (b) Ir layer with 30 wt.% ionomer loading.

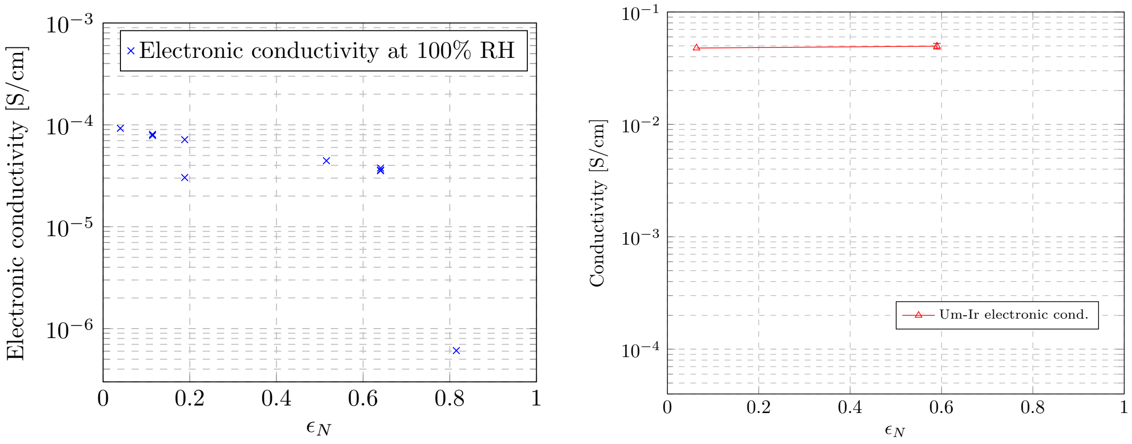

(a) **(b)**

Figure 3.21 – (a) Through-plane electronic conductivity of IrO$_x$ layer at 100% RH. Results from repeated tests are displayed at ionomer volume fractions of approximately 0.11, 0.19 and 0.64. (b) Through-plane electronic conductivity of Ir layer at 100% RH

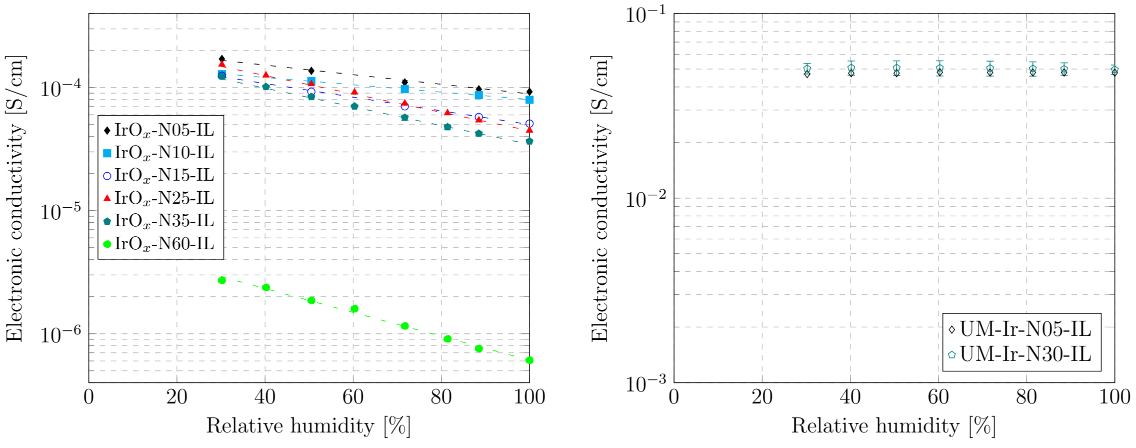

(a) **(b)**

Figure 3.22 – Through-plane electronic conductivity of the IrO_x (a) and Ir (b) layers.

3.2.5.1.2 Ionomer loading study on TP electronic conductivity: Figure 3.22 shows the calculated TP electronic conductivity of the CLs with varying ionomer loading. The TP electronic conductivity of the IrO_x CL decreased exponentially with an increase in the RH, indicating that the swelling of the ionomer is reducing the catalyst connectivity. The same trend was not observed in the Ir CL, where Figure 3.22b shows that the electronic conductivity did not change significantly with RH.

Regarding the effect of the ionomer loading, the TP electronic conductivity is similar for all IrO_x CLs except at very high ionomer loading. The electronic conductivity of the IrO_x CL with 60 wt.% ionomer loading (ϵ_N=0.81 in Figure 3.21a) is two orders of magnitude lower than the other lower ionomer loading CLs. This shows that the connectivity of the IrO_x particles in the CL is almost lost at higher ionomer loading.

The TP electronic conductivity of the IrO_x CL in this study, i.e., $\sim10^{-4}$ S/cm, is orders of magnitude lower than that observed for the Ir IL and the CL in previous studies. For example, Schuler et al. [160] measured electrical conductivities in the range of 3–7 S/cm for their IrO_2/TiO_2 catalyst layer.

Figure 3.21 shows the change in the electronic conductivity with changing ionomer volume fraction at 100% RH. The TP electronic conductivity of the IrO_x layer with 5 and 10 wt.% ionomer loading is higher than the other IrO_x layers despite the slightly lower IrO_x volume fraction. This might indicate that the electronic conductivity is sensitive to ionomer loading, as the ionomer might increase the contact resistance between particles. In addition, as was discussed in the SEM imaging section, lower ionomer loaded samples contain cracks which may have led to an overprediction of the low ionomer loading IrO_x layers porosities, and therefore an underprediction of the IrO_x volume fraction. As the IrO_x volume fraction is considered to be relatively constant as compared to the ionomer and void volume fractions, the TP electronic conductivity trends with respect to the IrO_x volume fraction are not discussed. Figure 3.21b hardly shows any change in the TP electronic conductivity for two Ir layers with different ionomer loading showing that ionomer loading might not have an effect on the TP electronic conductivity.

3.2.5.2 In-plane electronic conductivity

The measurement of in-plane electronic conductivity was attempted for each of the IrO_x layers. As stated previously, the pins of the four point probe punctured the catalyst layer as shown in Figure A.1 in Appendix A, which may have affected the measurement of in-plane electronic conductivity. While repeatable results were obtained for a single sample at various locations, large variations were observed between samples of the same composition. The conductivity ranged between 0.045 to 8.19×10^{-4} S/cm, which is at least an order of magnitude lower than that measured by Mo et al. [71]. This confirms that the conductivity of the CLs studied in this work are significantly lower than those reported in the literature. The obtained IP electronic conductivity range is higher than the obtained TP electronic conductivities. This was also observed by Ahadi et al. [181] in the case of Pt/C CLs. This indicates that the IrO_x ILs have some degree of structural anisotropy, likely due to the fabrication method.

3.2.6 Comparison of protonic and electronic conductivities

A comparison of the CL protonic and TP electronic conductivity at varying ionomer loadings at 100% RH is shown in Figure 3.23. At this RH, the TP electronic conductivities are lower than the protonic conductivity for ionomer loadings of 15 wt.% and above, whereas below 15 wt.%, the electronic conductivity is higher than the protonic conductivity for the IrO_x CL. On the other hand, the electronic conductivity of Ir CL is always higher than the protonic conductivity in the tested ionomer volume fraction range. The protonic conductivity might further increase and electronic conductivity might decrease in the presence of the liquid water, based on Schuler et al. [160] results which showed a severe drop in CL electronic conductivity when in contact with liquid water. It is possible, therefore, that the ionomer loading at which the two conductivities are equal will in practice be at a lower ionomer loading than that shown in Figure 3.23 for the IrO_x CL.

The obtained conductivities for the IrO_x CL are in contradiction with the data reported by Bernt and Gasteiger [62] and Schuler et al. [160], who reported electronic conductivities are orders of magnitude higher than those reported here. Bernt and Gasteiger [62] reported the HFR of the cell and did not report electronic resistance of the anode catalyst layer separately. The HFR will measure either the most conductive phase of the CL, or, in cases where both phases have similar conductivity, an intermediate value [225]; therefore, HFR cannot be used to decipher which phase is the least conductive. The measured HFR (50.362 $m\Omega \cdot cm^2$ for IrO_x CL with 35 wt.% ionomer loading) in this study is in agreement with the HFR obtained by Bernt and Gasteiger [62] (52.5–63 $m\Omega \cdot cm^2$ for CLs with 2.2-28 wt.% ionomer loading). Schuler et al. [160] reported a higher electronic conductivity for their CLs, however they used a different catalyst, and they observed a sharp decrease in electronic conductivity when exposed to liquid water.

As discussed above, only the more conducting phase in the CL contributes to the HFR, as was shown numerically for PEMFC [225]. To further demonstrate that the electronic resistance in electrolyzers can be larger than the protonic resistance in

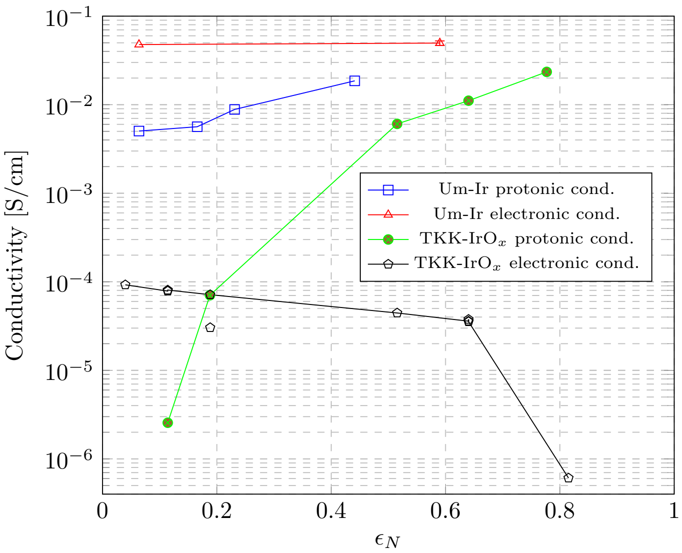

Figure 3.23 – Comparison of the protonic and through-plane electronic conductivity of the CLs with varying Nafion volume fraction at 100% RH.

the anode CL, the HFR of PEMWE cell with the anode CL with IrO$_x$ and 35 wt.% ionomer loading was measured. The HFR should measure the electronic resistance of the BPPs, CCs, PTL, GDL, cathode CL, and protonic resistance of the membrane and anode CL.

Galvanostatic EIS measurements were performed on an electrolyzer cell, with an IrO$_x$ based CL with 35 wt.% ionomer loading and PTL on the anode and Pt/C catalyst with a GDL (28BC, SGL) on the cathode of a NRE211 membrane. EIS was carried out at a constant current density of 0.02 A/cm^2 using a sinusoidal current with an amplitude of 30% of the total current and a frequency range between 10 kHz–1 Hz (50 points per decade). The cell was maintained at 80 °C and the water flowrate was set to 9.1 ml/min. The HFR was obtained at the point where impedance spectra intersected with the x-axis in the Nyquist plot as shown in Appendix A (Figure A.5).

The measured HFR is 50.362 m$\Omega\cdot$cm^2, which is in agreement with Bernt and Gasteiger [62]. If the electronic conductivity in the CL is limiting, then the HFR should be given by:

$$R_{HFR} = R_{H^+}^{IrO_x} + R_{N211} + R_{CHW} \tag{3.8}$$

where $R_{H^+}^{IrO_x}$ is the protonic resistance of the IrO_x CL, in this case 38.8 mΩ·cm^2 at 100% RH (Figure **??**), R_{N211} is the protonic resistance of the membrane in contact with the liquid water (= 12.23 mΩ·cm^2), and R_{CHW} is the electronic resistance of the cell hardware (= 19.7 mΩ·cm^2, which include two CCs, two BPPs, and one 28BC GDL). The electronic resistance of the Pt/C CL (= 0.174 mΩ·cm^2, measured using the 4PP method) and the Ti PTL (= 1.62×10^{-4} mΩ·cm^2, measured using the 4PP method) are not included as their resistance was negligible as compared to the HFR.

Using $R_{H^+}^{IrO_x}$ and $R_{e^-}^{IrO_x}$, the estimated HFR would be 70.76 mΩ·cm^2 and 11272 mΩ·cm^2, respectively. The measured value, 50.363 mΩ·cm^2, is very close to the estimated value using $R_{H^+}^{IrO_x}$, while the estimated HFR using $R_{e^-}^{IrO_x}$ is 223 times higher than the measured value. This analysis demonstrates that the HFR must include the protonic resistance rather than the electronic resistance, and that the electronic resistance must be significantly higher than the protonic resistance. The estimated HFR using $R_{H^+}^{IrO_x}$ is higher than the measured HFR as the protonic resistance of the CL at 100% RH was used rather than at liquid equilibrated.

The electronic conductivity is likely to dictate the reaction distribution in the IrO_x CL. This result aligns well with the experimental observations by Mo et al. [71] which showed that the reaction was concentrated at the PTL-CL contact points. The low electronic conductivity has major implications for the CL design and highlights the need for an electron conductive support in the CL [62, 89, 91]. For the Ir CL the reaction is likely to be more active at the CL-membrane interface as the electronic conductivity is higher than the protonic conductivity.

3.2.7 Modelling of the hydrogen pump

A numerical model of the hydrogen pump experimental set up with a 35 wt.% ionomer loading IL was developed by Michael Moore. Polarization curves were obtained with the IL being either active or inactive to the hydrogen oxidation and evolution reactions. The protonic and electronic conductivity values of the IrO_x IL from the previous section were used as input parameters. Figure 3.24 shows the experimental and numerically obtained polarization curves at 80% RH. The numerical data matches very well with the experiment, with the small discrepancy likely due to the contact resistances that are not included in the model. Of greater interest, however, is the difference between the model data with and without the hydrogen reactions in the IL. Identical results are obtained, indicating that the ohmic pathway is being utilized, and the reactive pathway is not active in the IL. This is expected as the IrO_x catalyst is known to be inactive to these reactions. However, even when the activity of the hydrogen reaction in the IL is increased (by increasing the exchange current density up to 8 orders of magnitude), no change in the numerically obtained polarization curve was seen. This is in contrast to the hydrogen pump experiment for PEMFC where an IL, without Pt, needed to be used [169]. As the electronic phase in the IrO_x IL is significantly less conductive than the protonic phase in this case, it is not favourable in terms of overpotential to by-pass the proton transport phase by converting the transport of protons across the IL to the transport of hydrogen and electrons via the reactive pathway. Therefore, the numerical model shows that the presence of the IrO_x in the IL does not impact the measurement of its protonic resistance. A carbon based IL that includes a platinum catalyst, or an IL made of unsupported iridium black, could catalyze the hydrogen reaction however, and impact the measurement of the protonic phase, as both these layers are likely to exhibit a higher electrical conductivity and higher activity towards the hydrogen reaction. A more detailed study on this possibility will be presented in a future work.

Figure 3.25 shows the reaction distribution for each CL at approximately 0.5 A/cm^2. The IL exhibits a much lower volumetric current density compared to the anode CL (ACL) and cathode CL (CCL), confirming the lack of reaction in the IL. The hypothesis that the IL could be bypassed by the reactive pathway is, however, demonstrated, as an minimal amount of charge is observed to flow through the electronic phase in the IL by first converting protons to hydrogen in the IL near the anode, and then oxidizing the hydrogen near the IL/cathode interface. This indicates that a minimal portion of the proton transport across the IL is in fact being bypassed via the hy-

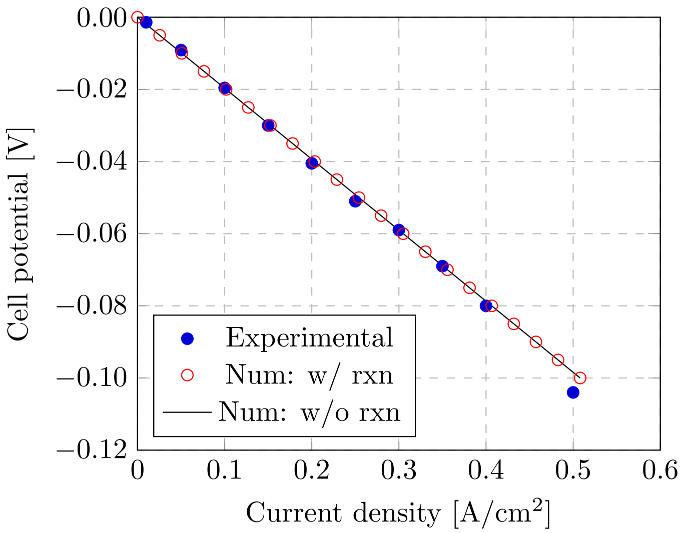

Figure 3.24 – Comparison of an experimentally obtained polarization curve with numerically obtained curves that are either with or without the reaction in the IrO$_x$ layer.

drogen reaction. Therefore, a layer that exhibits a higher activity to the hydrogen reaction and a higher electronic conductivity will have a higher portion of the proton transport being bypassed. Figure 3.26 shows the change in the protonic potential across the centre line of the cell. The protonic resistance of the IL incurs the largest drop in potential in the cell, which is significantly higher than that of the membrane despite being significantly thinner. This result allows us to conclude the proposed hydrogen pump technique is an accurate method to estimate the protonic conductivity of the IL, since all other resistances are significantly smaller.

Finally, the fact that the electronic conductivity of the IrO$_x$ CL is smaller than that of the protonic conductivity has significant implications for the ohmic losses in PEMWE cell. The ratio of the conductivities means that the reaction in the ACL of a PEMWE cell will occur at the PTL/ACL interface. The large drop in the protonic potential shown in Figure 3.26 will therefore also be incurred in the PEMWE cell ACL, and would likely be comparable to the membrane resistance and therefore a major contributor to the overall losses in the cell. Further study of the ohmic resistance in the ACL of PEMWE cells is required to verify this result, however it appears

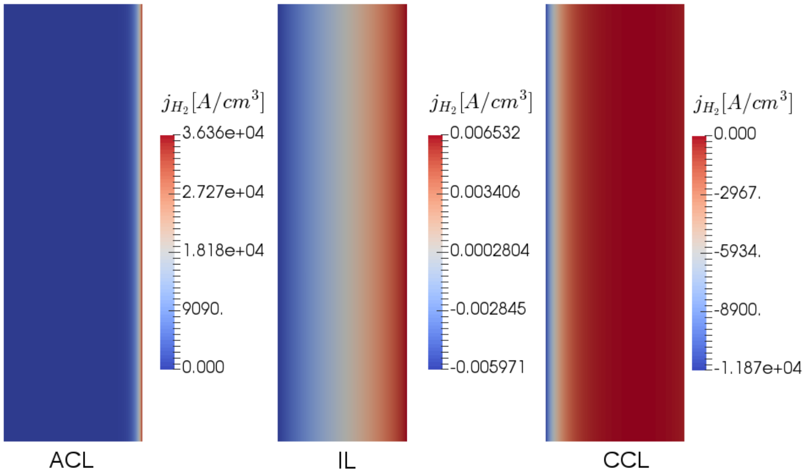

Figure 3.25 – Distribution of the hydrogen reaction in the three catalyst layers. There is a NRE211 membrane in between the IrO$_x$ layer and the other two CLs, while a GDL is to the left and right of the anode/cathode CL respectively.

that the ACL ohmic resistance is significant. The literature typically focuses on the PTL and membrane as the primary contributors to the ohmic resistance of the cell [32, 33, 66, 226]; this work highlights that the ohmic resistance of the ACL should also receive attention.

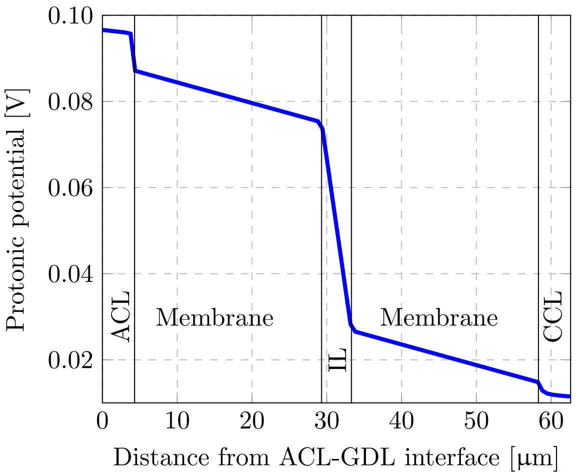

Figure 3.26 – Change in protonic potential across the centre of the cell, including each CL and the two membranes.

3.3 Summary and discussion

Reducing anode catalyst layer proton and electron transport resistances in PEMWE cell is critical to improving its performance and maximizing the catalyst utilization at high current density. A novel setup utilizing a hydrogen pump was developed to measure the protonic conductivity of anode catalyst layers. The protonic resistance of the CL was obtained by subtracting the protonic resistance of an assembly of two NRE211 membranes hot-pressed together from an assembly of two NRE211 membranes with an intermediate layer. The through-plane and in-plane electronic conductivities were also measured using a two- and four-probe method, respectively. Using these techniques, the protonic and electronic conductivities of CLs with varying ionomer loading were measured. Results show that the limiting charge transport phenomena in IrO_x CL can be either proton or electron transport depending on the ionomer loading in the CL and is protonic conductivity in Ir CLs. The results for IrO_x CLs are validated by numerical simulation, as well as by comparison to the HFR of an electrolyzer with the same layer. The main implication of the results obtained in this chapter is that the OER are likely to be more active at CL-membrane interface for the Ir CL and at CL-PTL interface for the IrO_x CL depending on the ionomer content.

Chapter 4

Improving PEMWE performance by using carbon as pore former[1]

The limiting PEMWE performance in the activation region of the polarization curve can be attributed to low ECSA. It might be due to the use of unsupported Ir/IrO_2 catalyst, which resulted in low CL porosity as shown in previous two chapters. By increasing the CL porosity, it is hypothesized that the ECSA would increase, as well as it might be possible to have better transportation of reactant and products, which will improve PEMWE performance in the ohmic/mass transport region. The CL porosity can be increased by incorporating pore former in the ink and removing it after the CL fabrication. In this chapter, carbon black is utilized in a novel way, i.e., as a pore former. In the previous chapter, it was observed that for the IrO_x CL the electronic conductivity is the limiting, whereas for the Ir CL the protonic conductivity is the limiting. The implication of this is that the OER would be more active near the CL-PTL interface for the IrO_x CL and near CL-membrane interface for the Ir CL. Due to this, it is hypothesized that the CL porosity would affect PEMWE performance differently. Hence, both catalysts were used in this chapter to understand the effect

---

[1] This chapter is partly based on M. Mandal, and Marc Secanell, "Improved PEM Electrolyzer Performance by Using carbon black as a Pore Former in the Anode Catalyst Layer", Submitted to *Journal of Power Sources*

of CL porosity on the PEMWE performance, however the results of IrO_x CLs are presented in Appendix B.

4.1 Fabrication and characterization

4.1.1 Ink fabrication

The anode catalyst inks were prepared by mixing 179 mg of Ir (3000020267, Umicore) and the carbon (Vulcan XC-72, 590106, Fuel Cell Store) with a mixture of isopropanol (IPA) (CAS: 67-63-0, Sigma-Aldrich), propylene glycol (PG) (CAS: 57-55-6, Sigma-Aldrich), and Nafion solution (Liquion solution LQ-1105 1100EW 5 wt.%, Ion Power) following the process discussed in Chapter 2. The carbon content in the anode catalyst ink was varied, such that the carbon to total solid volume fraction varied between 0 and 0.2. The ratio of IPA and PG in the ink was varied to maintain a constant solid volume fraction in the final ink. Ionomer was added to the inks to achieve a loading of 15 wt.%.

The cathode ink was fabricated by mixing 37.5 mg of Pt/C (46.7 wt.% Pt/C, TEC10EA50E, TKK) in a 48:52 wt.% ratio mixture of IPA and PG following the process discussed in Chapter 2. A 321 mg Nafion solution was added to achieve a 30 wt.% ionomer content in the cathode electrode.

4.1.2 CCM fabrication

The CLs were printed on N212 membrane following the procedure discussed in Chapter 2. For printing, a piezo-voltage of 32 V and a drop spacing of 20 μm was used. The electrodes were printed on an area of 5 cm^2 on the membrane. A catalyst loading of 1 mg/cm^2 was maintained in the anode CL. A Pt loading of 0.2 mg/cm^2 was maintained in the cathode CL.

4.1.3 Characterization of the CCM

4.1.3.1 Microscopic imaging

Scanning electron microscopy (SEM) was performed using Zeiss Sigma 300 VP-FESEM at an accelerating voltage of 5 kV to image CLs. Images were used to measure the CL thickness and to study the CL microstructure. The SEM samples were prepared by cryo-fracturing the CCMs using liquid nitrogen. Several images were taken at different locations of the CL to account for any inhomogeneities in the CL thickness. The CL thickness was measured using ImageJ software by measuring the thickness at ten locations of an image, and several images were considered. The thickness of the membrane was also measured and compared to the manufacturer's specification to verify that the measured CL thickness was not affected by image tilt. An error of less than 3% was observed.

The porosity of the CLs was calculated based on the CL thickness and ink composition, either including or neglecting the carbon content in the CL, as described in the Appendix B.

The SEM imaging of post-operation CLs were obtained after a short stability test. For this, the CCM was placed on a flat surface, and then the porous transport layer (PTL) on the anode side was lifted slowly from a corner. Similarly, the gas diffusion layer (GDL) on the cathode side was also removed before cryo-fracturing the used CCM.

4.1.3.2 Electrochemical characterization

4.1.3.2.1 Experimental setup A single cell with single serpentine bipolar plates, consisting of a custom-made titanium plate in the anode and a graphite plate in the cathode, was used for testing. A Pt coated Ti felt (2GDL10-0.25, Bekaert) of thickness 250 μm and a GDL without a microporous layer (SGL 28BA, Sigracet) were used in the anode and cathode, respectively. The cell and water temperatures were maintained at 80 °C by a thermal regulator/control (CN414-R1-R2, Omega). A variable power supply (1688B, BK Precision) was used to obtain the polarization curve range of current from 0.02 to 4 A/cm^2. The measurement of the cell voltage was performed using an Arduino card and custom-built software. A potentiostat (SP300, Bio-logic) was used for cyclic voltammetry (CV), linear scan voltammetry (LSV), and electrochemical impedance spectroscopy (EIS) tests. Water was supplied at a rate of 15 ml/min by a peristaltic pump (Minipulse 3, Gilson).

4.1.3.2.2 Conditioning of the cell To obtain a polarization curve, the cell was conditioned first by applying current densities of 0.02, 0.1, 0.2 and 1 A/cm^2 for 15 minutes each and then, 5 minutes at 2 A/cm^2. It is assumed that the carbon will corrode completely during the conditioning step, as it would take less than 15 minutes at 0.02 A/cm^2 to oxidize 0.42 mg of carbon present in the CL with carbon to total solid volume fraction of 0.2.

4.1.3.2.3 Measurement of electrochemical surface area (ECSA) Cyclic voltammograms were obtained after conditioning the cell, at 30 °C by flowing 0.2 slpm fully humidified H_2 in the Pt/C (reference) electrode and 0.05 slpm fully humidified N_2 in the working electrode. Potential scans were performed at 40 mV/s from 0.005 to 1.35 V.

The ECSA of the Ir CL after conditioning the cell ($ECSA^{\mathrm{Initial}}$) was estimated using the integral charges due to hydrogen underpotential deposition (HUPD) in the CV profiles (in the potential range of 0.03 to 0.35 V versus the reversible hydrogen electrode (RHE)) as shown by the green shaded region in Figure B.3, $Q^{\mathrm{Initial}}_{\mathrm{HUPD}}$, using

$$ECSA^{\mathrm{Initial}} = \frac{Q^{\mathrm{Initial}}_{\mathrm{HUPD}}}{q_{\mathrm{HUPD}}} \tag{4.1}$$

where q_{HUPD} is the charge constant associated with underpotentially deposited hydrogen on Ir, assumed to be 179 μC/cm^2 [96].

4.1.3.2.4 Polarization curve The galvanostatic polarization curves were obtained from a current density of 0.02 to 4 A/cm^2 by holding for 2 minutes at each current density to ensure stabilization and the data was averaged over the last 10 seconds. Two forward and backward current sweeps were performed to obtain two polarization curves, which were then averaged to obtain a single polarization curve.

4.1.3.2.5 Kinetic parameters Tafel curves were obtained from linear sweep voltammetry (LSV) data obtained with potentiostat (SP300, Biologic) in the current densities range of 2 to 2000 mA/cm^2. To obtain kinetic parameters, the linear region of the curves were fitted to a line using MATLAB. The overpotential is calculated as the difference between the cell potential and the theoretical potential (1.18 V) at the operating conditions.

4.1.3.2.6 Electrochemical impedance spectroscopy (EIS) Galvanostatic EIS measurements were performed at current densities of 0.02, 0.1, 0.2, 1, and 2 A/cm^2 using a sinusoidal current of amplitude 10% of the total current and a frequency range between 50 kHz–100 mHz (50 points per decade). The Pt/C electrode was used as the reference electrode and the Ir/IrO$_x$ electrode (anode) was used as the working electrode. The cells were maintained at 80 ^{o}C and the water flowrate was set to 15 ml/min. The impedance spectra were fitted to the equivalent circuit shown in Figure 4.11g using the "zfit" MATLAB code [196] in order to estimate the high frequency resistance (HFR), charge transfer resistance (R_{ct}) and exponent, n, and pre-exponential, Q_{dl}, factors of the constant phase element (CPE).

4.1.3.3 Stability test

Stability tests of Ir CLs were performed at 1 A/cm^2 for 24 hours at 80 °C with water flow rate of 15 mL/min. The cell was brought to room temperature and deionized water was refilled before starting the test. The data was measured every 10 seconds.

4.2 Results for Ir catalyst anode

In order to study the viability of carbon as a pore former, several cells comprised of anode CLs with varying carbon content were fabricated. A summary of all the fabricated and tested cells is shown in Table 4.1. The loading is calculated using a gravimetric method [200].

Table 4.1 – Composition of Ir CCMs under study and MEA configuration..

CCM	Cell tested	C to total solid vol. frac.	Cat. load. [mg/cm^2] Ir | Pt	Naf. load. [wt.%] An | Cath	MEA configuration PTL | ACL | PEM | CCL | GDL
CCM-C0-Um	3	0	0.99 | 0.19	15 | 30	Pt-Ti felt | Ir | N212 | Pt/C | 28BA
CCM-C0p1-Um	1	0.1	1.00 | 0.21	15 | 30	Pt-Ti felt | Ir | N212 | Pt/C | 28BA
CCM-C0p2-Um	3	0.2	1.04 | 0.2	15 | 30	Pt-Ti felt | Ir | N212 | Pt/C | 28BA

4.2.1 SEM characterization

Figure 4.1 shows the CL cross-sectional SEM images of new and post operation CLs. The measured thickness of the CLs is shown in Figure 4.2a. Since the catalyst loading was not identical in all cases, the CL thickness is divided by the loading to obtain a thickness per mg/cm^2 of catalyst. The normalized thickness of CLs increased with an increase in the carbon content.

The calculated porosity is shown in Figure 4.2b. The porosity of the CL is computed twice, once assuming the carbon is still present, and then assuming it is completely corroded, but the void space formed is maintained. The porosity of the CLs increased with an increase in the carbon content. It is interesting to note that most of the observed increase in the porosity occurred with the addition of carbon, and not after the carbon corrosion step. Therefore, the addition of carbon changes the ionomer-catalyst-solvent interaction such that additional pore volume is generated. The results from dynamic light scattering (DLS) of the ink showed little change in the particle size distribution (see Appendix B). This suggests that the main difference occurs during the drying process.

Post-operation, the thickness of the CL was again measured using SEM and the porosity was calculated. The CLs exhibited reduced porosity due to the compression of the CLs. The decrease in the porosity of the post operation CLs is higher with a higher carbon content, as these CLs have a higher porosity before assembly, making them more compressible. A side effect of this compressibility is that there may be a better contact between the CL and the PTL.

4.2.2 Catalyst layer surface imaging

In order to further characterize the CLs, the surface SEM images of the new Ir CLs were captured as shown in Figures 4.3.

Many cracks of size 1.74±0.33 μm were observed in the CL without carbon (Figures 4.3a and 4.3b) whereas no cracks were observed in CLs with carbon (Figures 4.3e and 4.3f). The porosity of the CL without carbon, once the volume of cracks is removed, might be even lower. Again, this might be due to the carbon and ionomer/-catalyst interactions; however, further research is needed to better understand the nature of these interactions.

After the performance and short-term durability were evaluated, the CLs were imaged again. Figure 4.4 shows the surface SEM images of post-operation CLs. A lot of indentations can be seen in all CLs from the Ti felt fibers. It was observed that the indentations are deeper for CLs with higher carbon loading due to the increased porosity. A deeper indentation could improve the contact with the PTL. This is a welcome impact due to the poor conductivity of the anode CL, causing a high interfacial resistance with the PTL [160, 227].

A lot of new small cracks have also appeared in the CL without carbon but not in CLs with carbon as shown in Figure 4.4b. The new cracks are in a star pattern and upon closer inspection, they appear to have a volcano-like shape with the CL lifting off the PEM as shown in Figure 4.5. This observation suggests that the new cracks may have been created by evolving oxygen gas bubbles within the CL as they forced their way out to the PTL. As the electronic conductivity is higher than the protonic conductivity, the OER would be more active at the anode CL–membrane interface and that the oxygen need to travel through the entire CL to reach the PTL. As the porosity of the CL without carbon is low, there may not have been sufficient pathways for the oxygen transport, hence new cracks were generated by the hypothesized build up of gas pressure within the layer. This phenomenon did not occur in CL with

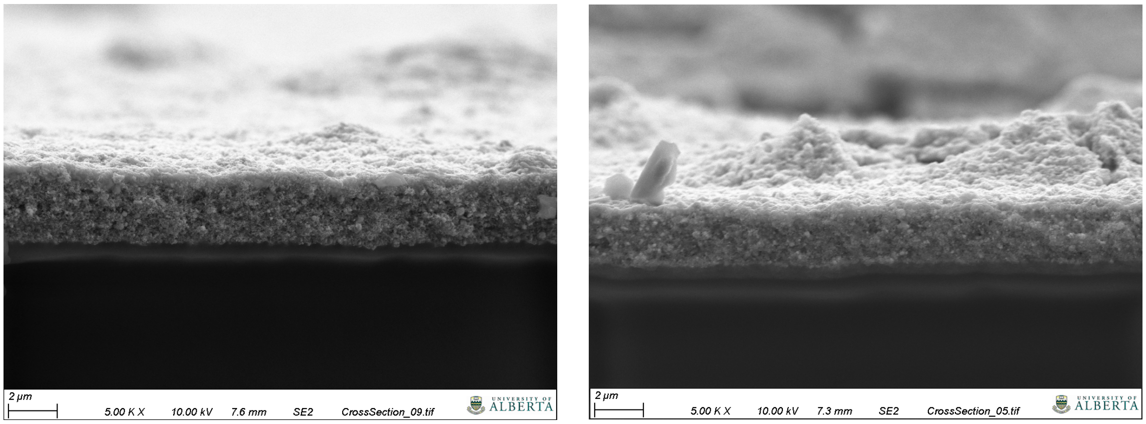

(a) New CCM-C0 **(b)** Used CCM-C0

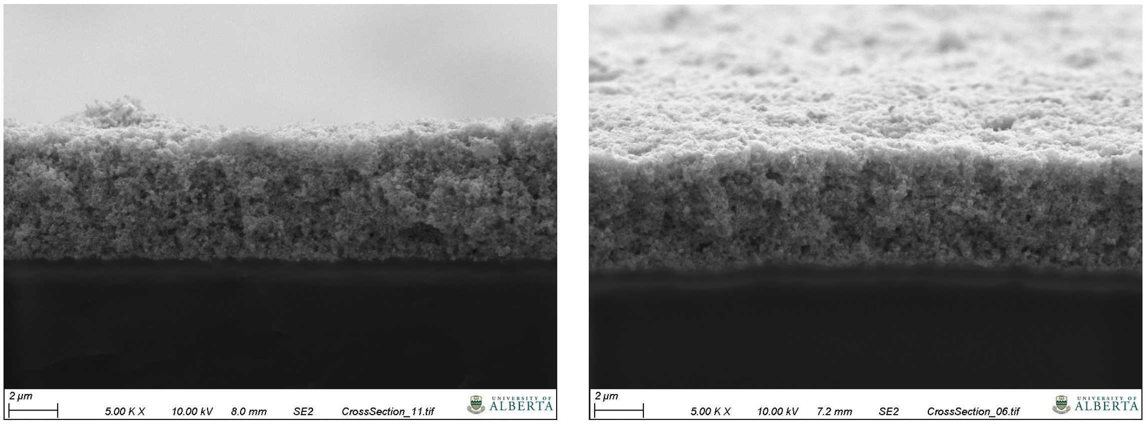

(c) New CCM-C0p1 **(d)** Used CCM-C0p1

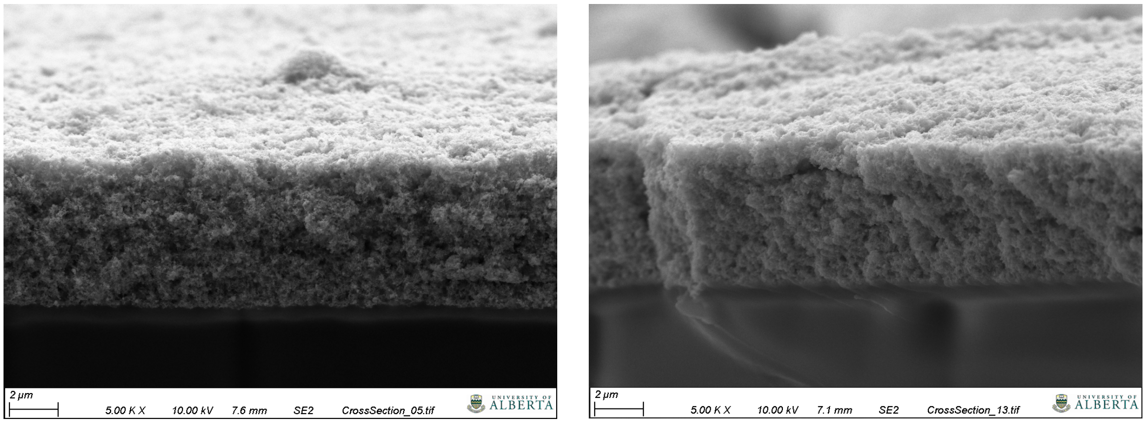

(e) New CCM-C0p2 **(f)** Used CCM-C0p2

Figure 4.1 – Cross-section SEM images of the new (left) and used (right) Ir catalyst layers with zero (top), 10% (middle) and 20% carbon volume fraction.

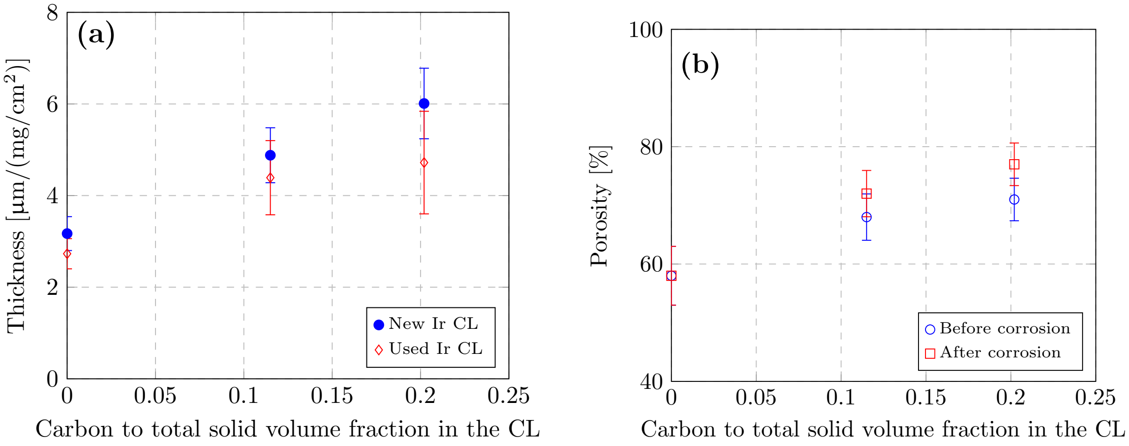

(a) **(b)**

Figure 4.2 – Catalyst layer thickness after normalizing with catalyst loading (a) and porosity (b).

carbon, as it is more porous and therefore likely has sufficient pathways for oxygen transport. The width of the cracks which were present in the new CL (seen as long cracks and not the star patterned) before assembly decreased from 1.74 ± 0.33 to 0.79 ± 0.22 μm. This might be due to in-plane swelling of CL once in contact with water.

4.2.3 Measurement of electrochemical surface area

Cyclic voltammetry tests were conducted to determine the ECSA. For repeatability, voltammograms were obtained for three CCMs without carbon (CCM-C0) and three CCMs with carbon to total solid volume fraction of 0.2 (CCM-C0.2). The obtained voltammograms are shown in Figure 4.6, which showed good repeatability.

The effect of the carbon content on initial voltammograms after conditioning the cell is shown in Figure 4.7. The estimated ECSA of the CCMs are shown in Table 4.2. The ECSA increased with an increase in the carbon content, which might be due to the increased CL porosity. The ECSA of CCM-C0.2 increased by 25% as compared to the CCM without carbon. The obtained ECSA is in agreement with literature data as shown in Table 4.2 for the Ir nanoparticle catalyst [96, 189]. The ECSA of all

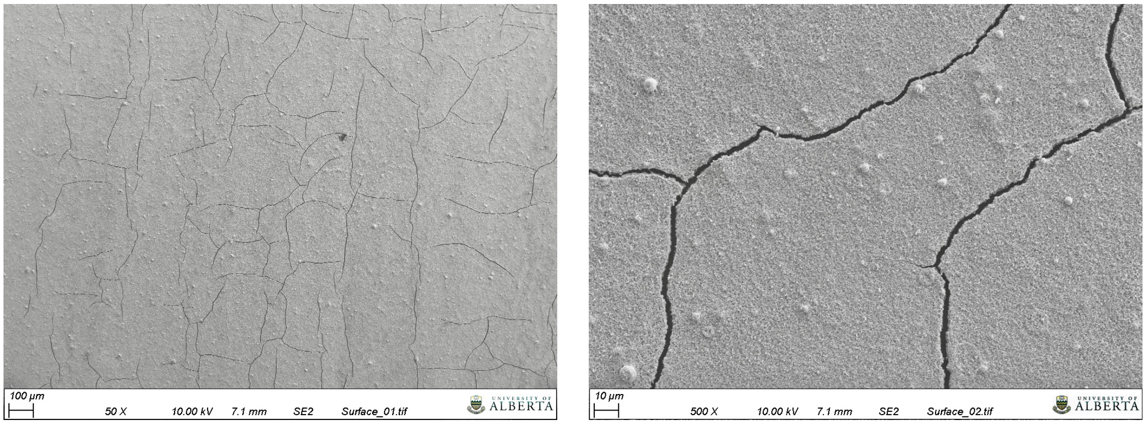

(a) CCM-C0 **(b)** CCM-C0

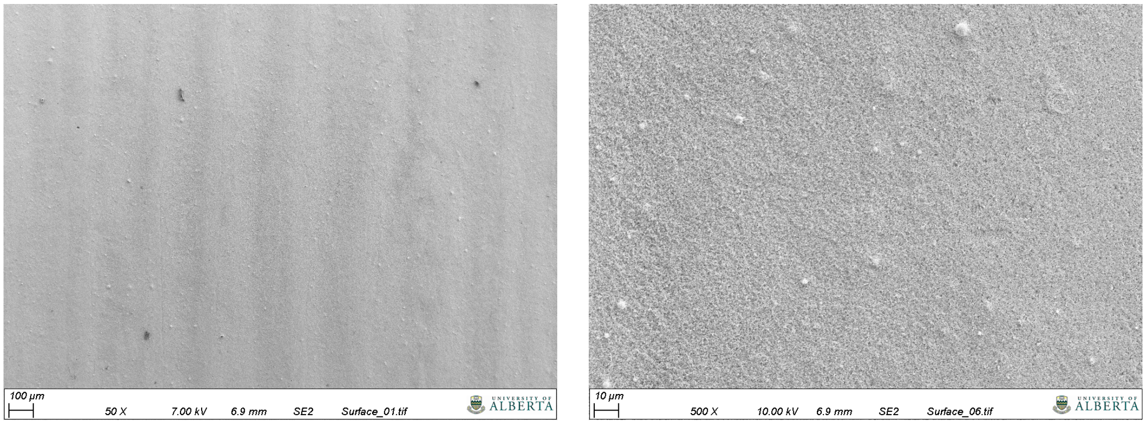

(c) CCM-C0.1 **(d)** CCM-C0.1

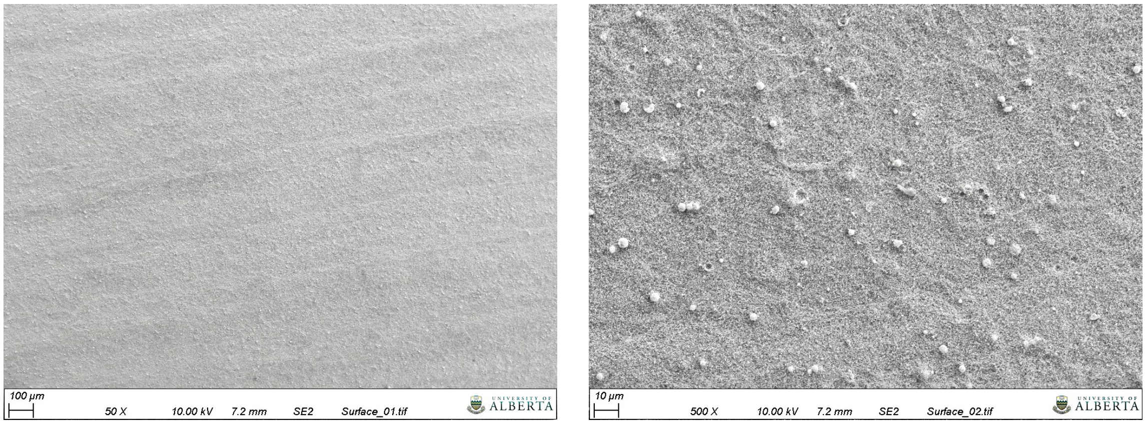

(e) CCM-C0.2 **(f)** CCM-C0.2

Figure 4.3 – SEM surface images of new CCM-C0 at low (50x) (a) and at high (500x) (b) magnification, CCM-C0.2 at low (50x) (c) and at high (500x) (b), and CCM-C0.2 at low (50x) (e) and at high (500x) (f).

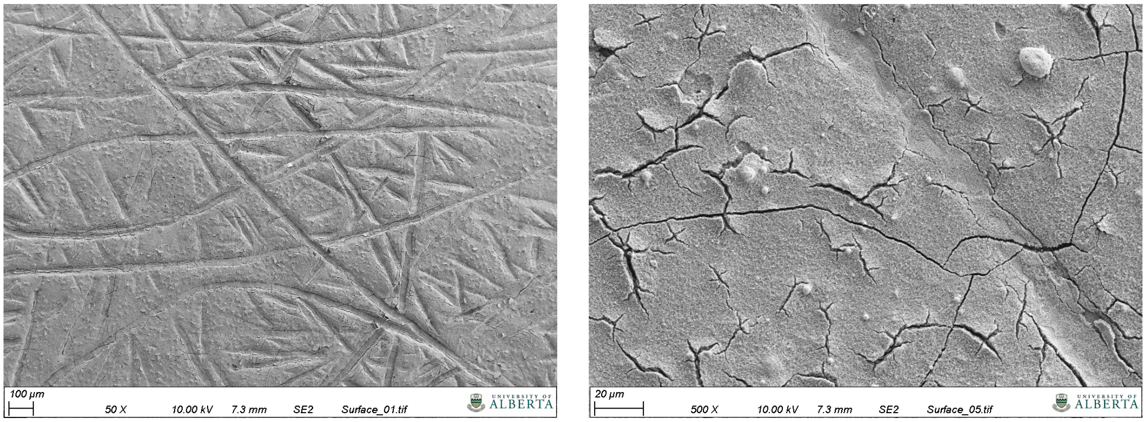

(a) CCM-C0 **(b)** CCM-C0

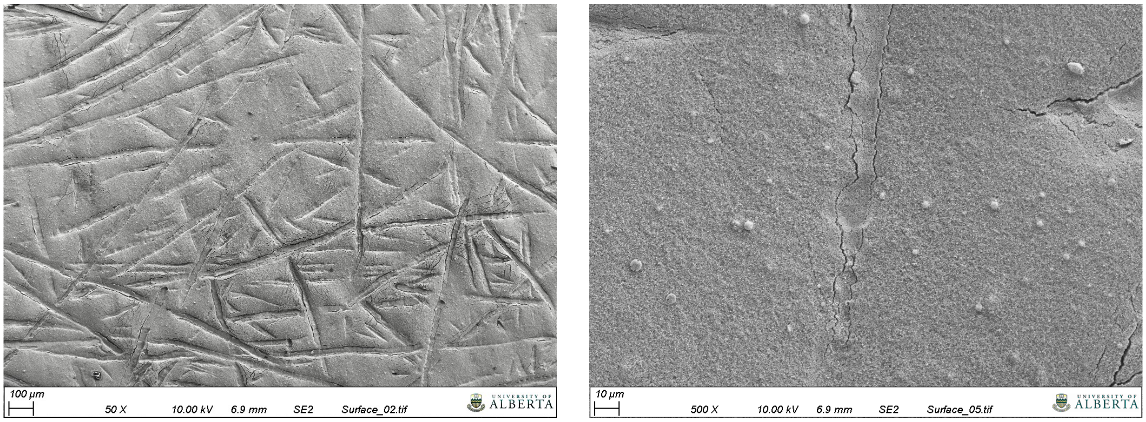

(c) CCM-C0.1 **(d)** CCM-C0.1

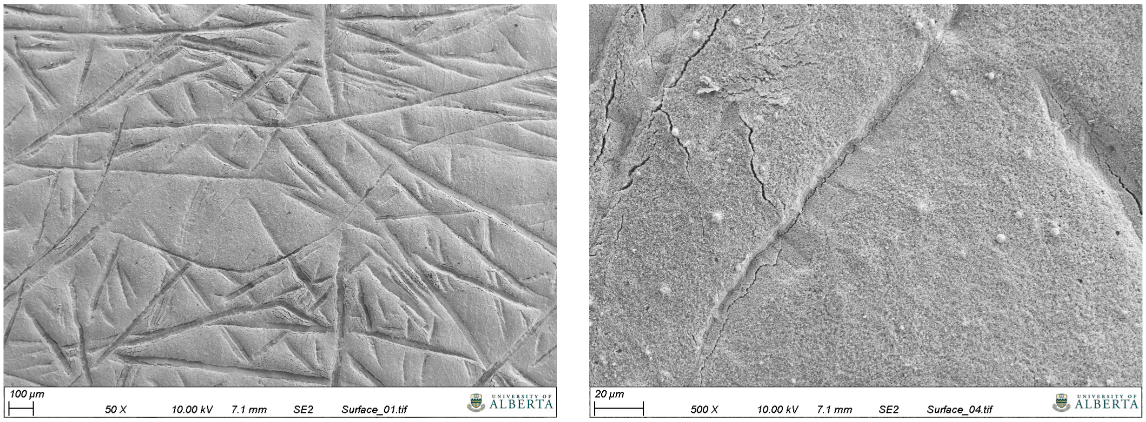

(e) CCM-C0.2 **(f)** CCM-C0.2

Figure 4.4 – Surface SEM images of the used CCM-C0-Um (a) and (b), CCM-C0.1-Um (c) and (d), and CCM-C0.2-Um (e) and (f).

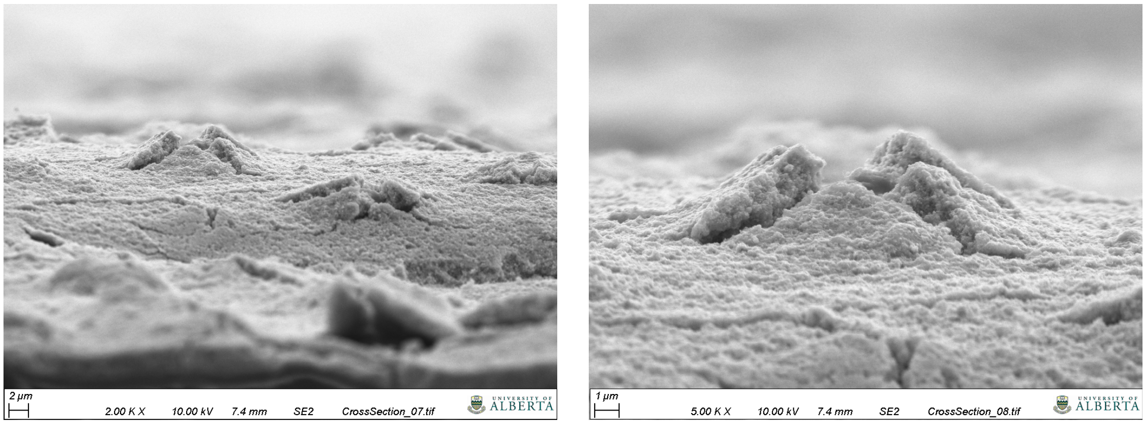

(a) **(b)**

Figure 4.5 – A closer look at the newly formed cracks in the Umicore CL without carbon. The surface image of the same CL is shown in Figure 4.4b.

CCMs after the polarization curve was also estimated and compared with the initial ECSA as presented in Appendix B. The ECSA before and after the polarization curve are similar and are in line with the BET surface area of 25 m^2/g of Ir catalyst, given by the supplier.

The shape of the initial voltammograms (Figure 4.7) is similar to those reported for Ir black electrodes, e.g., in ref. [96, 189]; however, the HUPD peak decreased slowly during the testing such that voltamograms obtained after testing showed a reduced HUPD and increased peak at 0.4 to 1.25 V. Tan et al. [96] showed that the HUPD peaks in the CV quickly diminished, as the metallic Ir surface quickly oxidizes to form an oxohydroxide layer, and a relationship existed between the decrease/increase of the two peaks, such that the latter peak could also be used to estimate ECSA. Therefore, when estimating the ECSA after testing, both peaks are taken into account as discussed in Appendix B. It should be noted that the reduction of the HUPD region in the CV after testing observed for the CCMs detailed in Table 4.1 was small compared to ref. [96] possibly due to the higher catalyst loading in CCMs. In this work, in order to observe a large reduction in the HUPD peak, and corresponding increase of the anodic charge in the potential range between 0.4 and 1.25 V, 240 cycles

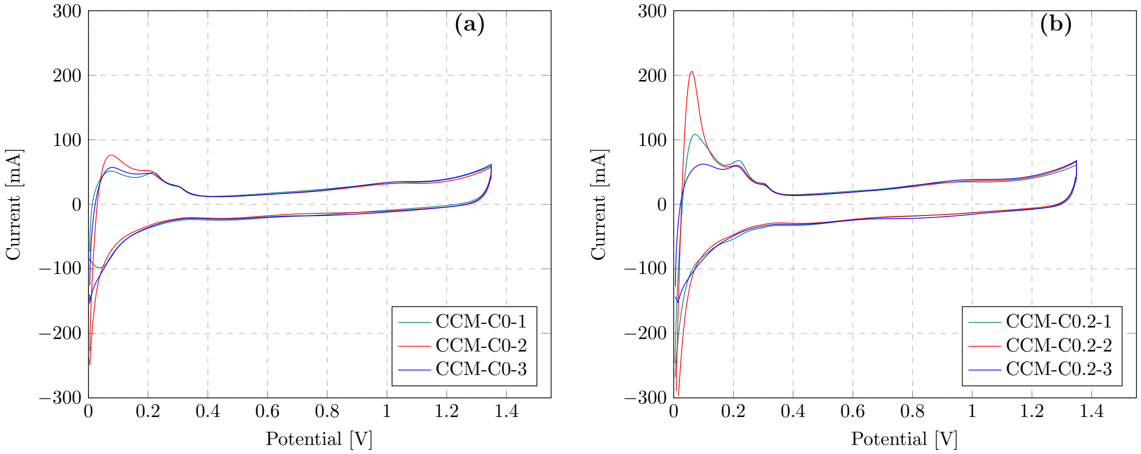

(a) **(b)**

Figure 4.6 – Repeatability of the voltammograms (a) CCM-C0, and (b) CCM-C0.2.

Table 4.2 – Electrochemical surface area (m^2/g) of the CCMs under study and literature.

CCM name	$ECSA^{\text{Initial}}$
CCM-C0-Um	21.5 ± 1.2
CCM-C0.1-Um	25.0
CCM-C0.2-Um	26.9 ± 0.2
Ref. [189]	28.7
Ref. [96]	21 ± 5

at 500 mV/s had to be performed for an Ir anode without carbon and with 5 wt.% ionomer loading, as presented in Appendix B.

4.2.4 Polarization curve

4.2.4.1 Repeatability

Three cells with and without carbon in the anode CL were tested for repeatability. The recorded polarization curves are shown in Figures 4.8a and 4.8b. The measured polarization curves showed excellent reproducibility, with an average standard deviation of 3 mV for both cells with and without the carbon.

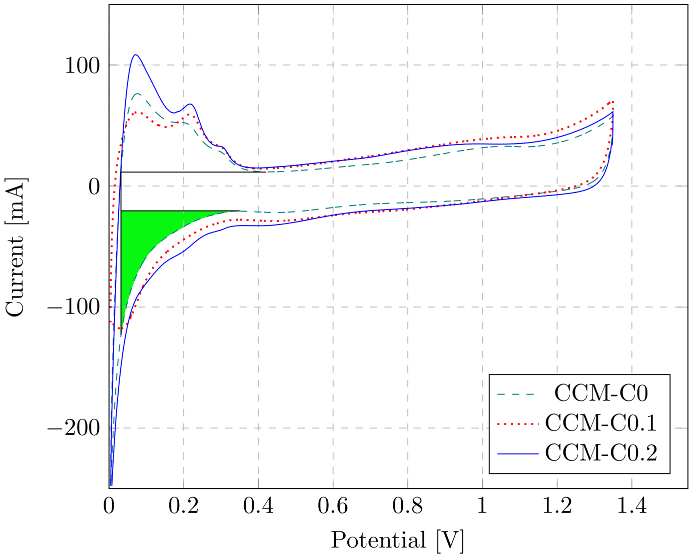

Figure 4.7 – Voltammograms of CCMs with varying carbon content after conditioning the cells (CCM-C0 and CCM-C0.2 are the average of three CVs with an average standard deviation of 2.4 mA)

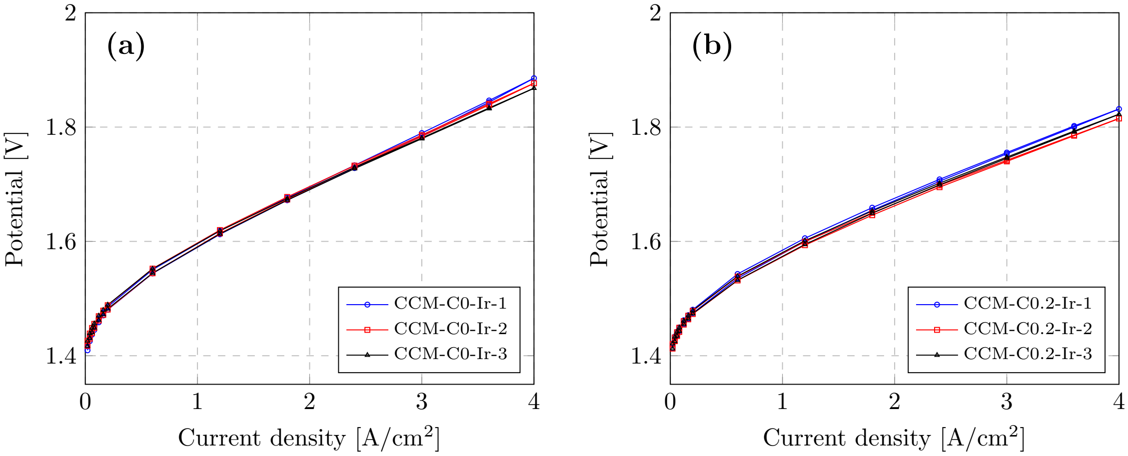

(a) CCM-C0-Um

(b) CCM-C0.2-Um

Figure 4.8 – Repeatability of the polarization curves of Ir catalyst layers (a) CCM-C0-Ir, (b) CCM-C0.2-Ir.

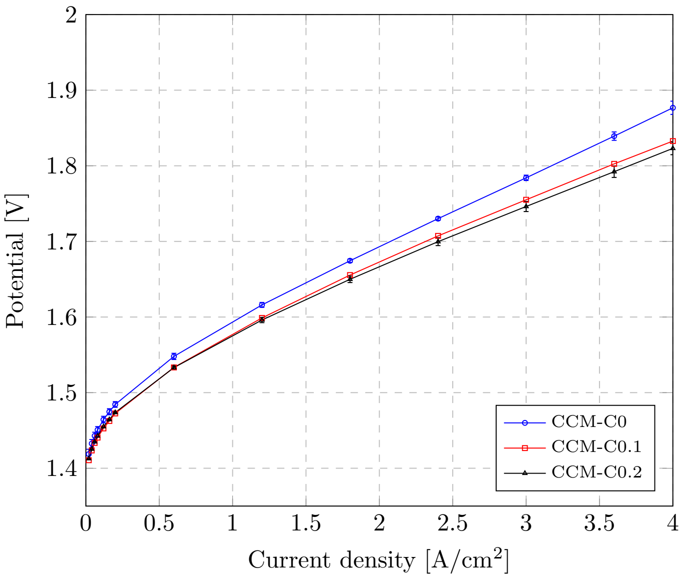

Figure 4.9 – Polarization curves of cells with varying carbon content (Error bar for CCM-C0 and CCM-C0.2 are based on standard deviation from three cells).

4.2.4.2 Effect of carbon loading

Figure 4.9 shows that the performance of cells improved with increasing carbon content. The potential improvement between the CCM without carbon and with carbon to total solid volume fraction of 0.2 was 25 and 54 mV at 2 and 4 A/cm^2, respectively. The improvement at low current density can be attributed to an increased ECSA, as shown in Section 4.2.3. At high current density, it can be attributed to decreased HFR, as will be shown in Section 4.2.6.

4.2.5 Kinetic parameters

To understand the effect of carbon on the activity of the CL, a Tafel plot analysis was performed. Figure 4.10 shows the Tafel plots where a linear region is only observed in a very narrow potential window, indicating either a change in Tafel slope at higher potential or mass/charge transport losses at less than 0.1 A/cm^2 even in the very porous electrodes. Kinetic parameters were calculated in the linear region between 1.36 and 1.41 V. Table 4.3 shows the parameters along with literature data. The Tafel slopes showed little variation with the carbon content, confirming the same reaction

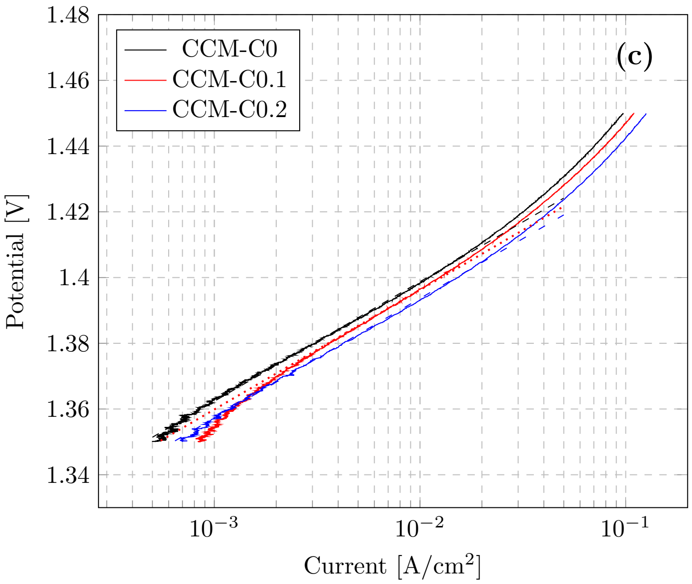

Figure 4.10 – Tafel curves of cells with varying carbon content (CCM-C0 and CCM-C0.2 are the average of three curves).

mechanism is taking place. The exchange current density increased by 38% with the addition of carbon, in line with the measured 25% increase in the ECSA. With respect to literature data, both Tafel slope and exchange current density show discrepancies; however, the differences are similar to those observed between the different references. The differences could be due to a number of factors, including different operating conditions such as temperature, different experimental set ups, e.g., RDE vs MEA, different metal and ionomer loadings, and the potential range used to fit the data.

4.2.6 Electrochemical impedance spectroscopy

Figure 4.11 shows the Nyquist and Bode plots obtained from EIS tests at different operating current densities. The Nyquist plot was fitted to the equivalent circuit shown in Figure 4.11g, and the fitting parameters are given in Table 4.4. The impedance spectra obtained using the EIS equivalent circuit are also shown in Figure 4.11 along with the experimental data. The fit is in excellent agreement with the experimental impedance data.

Table 4.3 – Kinetic parameters from Tafel analysis of the CCMs in Table 4.1 and literature reported values.

CCM name	Catalyst used	Tafel slope (mV/dec)	$i_0 \times 10^{-8}$ (A/cm$^2_{geo}$)	$i_0 \times 10^{-8}$ (A/mg$_{cat}$)
CCM-C0-Um	Ir	37.6 ± 1.5	1.54 ± 0.2	1.56 ± 0.2
CCM-C0.1-Um	Ir	38.2	2.10	2.10
CCM-C0.2-Um	Ir	37.9 ± 1.7	2.31 ± 0.6	2.22 ± 0.6
Ref. [228]	Ir	42.9	0.02	0.32
From data in ref. [96][a]	Ir	52.1	1.11	22.1
From data in ref. [229][b]	Ir	66.4	0.04	–
From data in ref. [230][c]	Ir	70.4	0.77	–

[a] [b] [c] Calculated by fitting a Tafel curve to the extracted data from the polarization curve between 1.45 and 1.50 V[a], between 1.54 and 1.6 V[b], and between 1.47 and 1.57 V[c] provided in the articles.

Table 4.4 – Parameters of the equivalent circuit fitted to impedance spectra of Ir catalyst layers

CCM name	J [A/cm^2]	HFR [m$\Omega\cdot$cm^2]	R$_{ct1}$ [m$\Omega\cdot$cm^2]	Q$_{dl1}$ [s^n/($\Omega\cdot$cm^2)]	n$_1$	R$_{ct2}$ [m$\Omega\cdot$cm^2]	Q$_{dl2}$ [s^n/($\Omega\cdot$cm^2)]	n$_2$
CCM-C0-Um	0.02	63.4	242.3	0.1477	0.79	651.3	0.2029	0.99
CCM-C0.1-Um	0.02	60.7	142.3	0.151	0.81	721.7	0.245	0.95
CCM-C0.2-Um	0.02	56.6	141.0	0.105	0.79	718.7	0.246	0.95
CCM-C0-Um	0.1	62.9	118.2	0.2045	0.77	147.6	0.1619	0.94
CCM-C0.1-Um	0.1	60.2	103.8	0.205	0.77	142.5	0.220	0.94
CCM-C0.2-Um	0.1	56.6	99.7	0.135	0.77	148.4	0.231	0.94
CCM-C0-Um	1	63.4	2.0	0.08	1.0	36.0	0.1886	0.82
CCM-C0.1-Um	1	60.1	4.2	0.063	1.00	33.1	0.161	0.87
CCM-C0.2-Um	1	56.8	5.5	0.497	1.00	30.9	0.189	0.84
CCM-C0-Um	2	64.3	2.2×10^{-5}	0.0717	0.98	20.2	0.3077	0.77
CCM-C0.1-Um	2	60.0	5.7×10^{-5}	0.082	0.98	20.8	0.301	0.77
CCM-C0.2-Um	2	57.0	1.1×10^{-4}	0.501	1.00	20.0	0.255	0.77

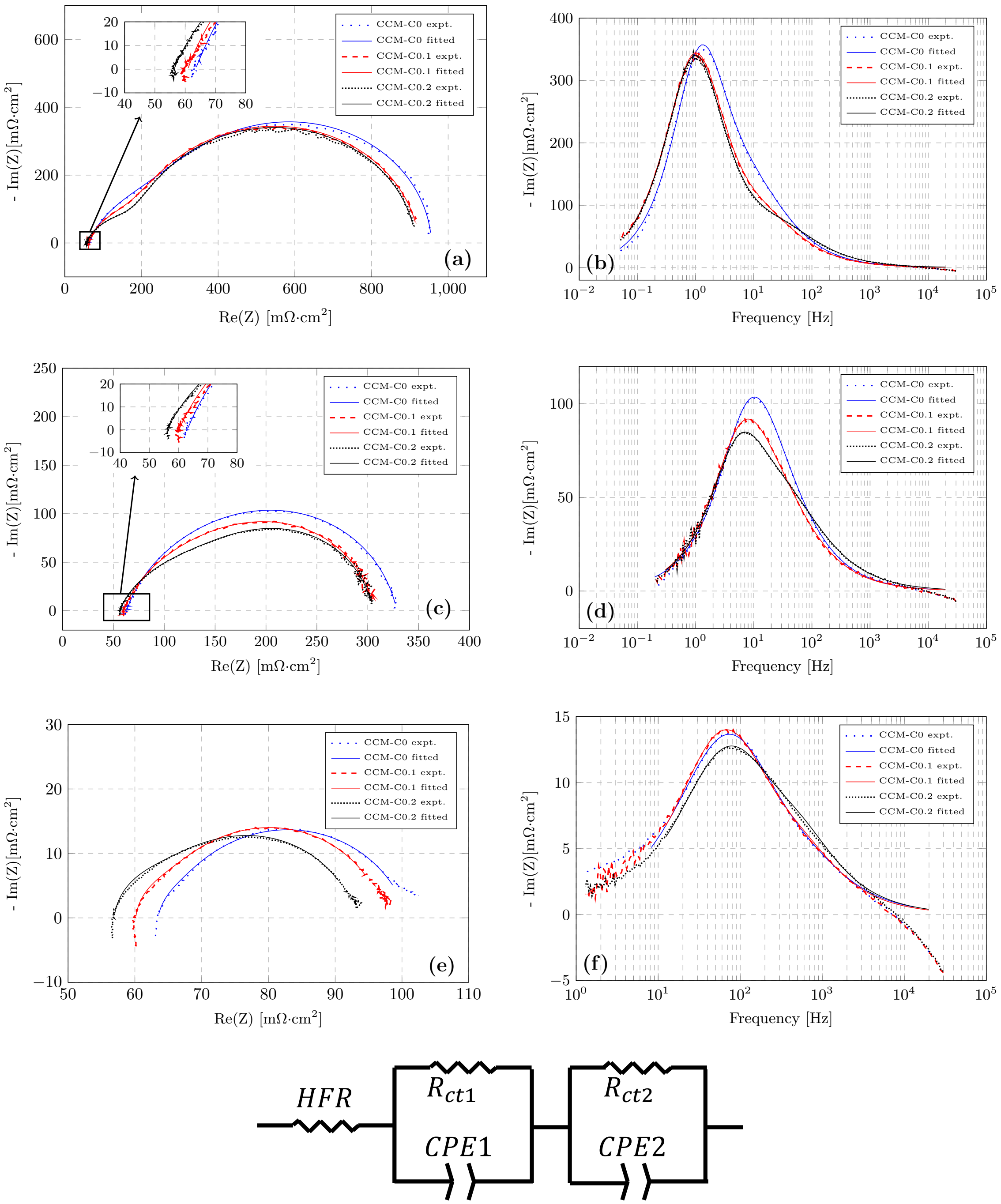

Figure 4.11 – Nyquist and Bode plots at a current density of 0.02 A/cm^2 (a) and (b), 0.1 A/cm^2 (c) and (d), 1 A/cm^2 (e) and (f) of Ir catalyst layer and equivalent circuit used for fitting of impedance spectra (g). HFR is the high frequency resistance, CPE is the constant phase element, and R$_{ct}$ is the charge transfer resistance.

The obtained HFR decreased with an increase in the carbon content, despite an increase in the CL thickness. The lower HFR is likely due to improved contact resistance between the anode CL and the PTL. The electronic conductivity of Ir CLs without carbon was measured to be an order of magnitude higher than the protonic conductivity, i.e., 4.8×10^{-2} S/cm vs 5.6×10^{-3} S/cm, using the procedure described in ref. [231]. The HFR only includes the most conductive phase in the CL [225], therefore the decreasing HFR must be due to increased electron conduction. This observation is in line with Figure 4.4 in Section 4.2.2, which showed that the surface of the high carbon loaded anode CL had deeper PTL fiber indentations in the CL than in the CL without carbon, indicating that there was an improved contact between the two layers.

Two charge transfer resistances (R_{ct1} and R_{ct2}) were obtained corresponding to the arcs in the high and low frequency range in Nyquist plot. It is usually assumed that the low frequency arc corresponds to the anodic (slow kinetics) charge transfer resistance and the high frequency arc corresponds to the cathodic (fast kinetics) charge transfer resistance [159]. In this case however, it is hypothesized that both arcs are due to the anode electrode for the following reasons: i) even though all cathode CLs are identical, the observed high frequency charge transfer resistance is different; ii) if the high frequency arc was due to the fast kinetics in the cathode, then R_{ct1} would have quickly reduced at higher overpotentials, i.e., at a current of 0.1 A/cm^2, as compared to R_{ct2}; iii) Kosakian and Secanell [232] showed by modelling the impedance data of a single electrode in PEMFC that high frequency arcs could also develop due to CL inhomogeneities. The EIS should be further investigated in order to assign a physical phenomenon to each arc. In this study, it is assumed that both resistances are caused by the anode kinetics, and so the combined charge transfer resistance ($R_{\text{ct1}}+R_{\text{ct2}}$) is used to study anode electrode kinetics. The combined charge transfer resistance decreased with an increase in the carbon content, in agreement with the measured higher ECSA and exchange current density.

In Section 4.2.4, a potential difference of 54 mV was observed at 4 A/cm^2 between the cell without carbon (CCM-C0) and with a carbon loading of 20 vol.% (CCM-

C0.2). Considering the HFR difference of 7.5 mΩ·cm^2 between the same cells, a cell potential improvement of 30 mV can be assigned to the lower HFR. The rest of the potential improvement, i.e., 24 mV, is due to improved kinetics and, possibly improvements in charge and mass transport.

4.2.7 Stability and post operation analysis

Figure 4.12 shows the results of a chronopotentiometry test at 1 A/cm^2 for 24 h. During first 6 h of operation, the cell voltage of CCM-C0, CCM-C0.1, and CCM-C0.2 increased quickly from 1.575, 1.566, and 1.565 V to 1.602, 1.593, and 1.589 V, respectively. The increase in voltage during this time was lowest for CCM-C0.2, which might be due to improved mass transport in the CL due to a higher CL porosity.

After 6 h, the cell voltage increased linearly. Degradation rates were calculated using a linear fit to experimental data after the first 6 hrs of operation. The linear fit is shown in Figure 4.12. The calculated degradation rate for CCM-C0, CCM-C0.1, and CCM-C0.2 are 626, 647, and 529 μV/h, respectively. In agreement with the initial increase in voltage, the lowest degradation rate was also obtained for the cell with a carbon to total solid volume fraction of 0.2.

As mentioned above, the electronic conductivity of the anode CL without carbon is an order of magnitude higher than the protonic conductivity, hence it is expected that the oxygen evolution reaction (OER) would be more active near the anode CL–membrane interface and that the oxygen would need to travel through the entire CL to reach the PTL. As the porosity of the CL without carbon is low, there may not have been sufficient pathways for oxygen transport. Hence, a build up of gas could be formed, leading to crack formation and degrading the CL. This agrees with the SEM images, where volcano-like shaped cracks were observed. These cracks were not observed in CL with carbon, as the CL is more porous and therefore likely to have sufficient pathways for oxygen transport. Hence, both the performance and stability were improved for the CL with carbon.

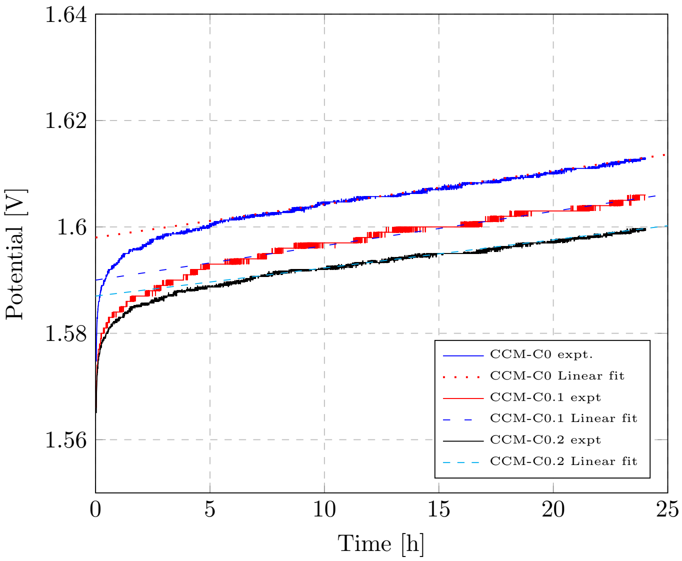

Figure 4.12 – Chronopotentiometry test results at 1 A/cm^2. The voltage is the average of three cells with an average standard deviation of 1.3 and 3 mV for CCM-C0 and CCM-C0.2, respectively.

4.3 Results for IrO$_x$ anode

In order to study the effect of pore former for CL with other catalyst, the addition of carbon in the ink was also studied for CLs with IrO$_x$ catalyst (ELC-0110, Tanaka Kikinzoku International (TKK)). The CL had a catalyst loading of 1 mg/cm^2 and a 35 wt.% ionomer loading. The results from SEM, cyclic voltammetry, polarization curve, and EIS tests for these cells are given in Appendix B. The three main differences between IrO$_x$ and Ir cells were: i) the IrO$_x$ CL has very poor electronic conductivity (the electronic conductivity is three orders of magnitude lower than the protonic conductivity, see Chapter 3), ii) a Ti sintered PTL was used in the anode instead of a felt, and iii) an NRE211 membrane was used instead of NRE212. The latter two changes were not intentional, but due to material availability. As in the case for Ir catalyst, the IrO$_x$ CL porosity increased and cracks were reduced with increasing carbon content. The SEM images of post operation CLs surface however did not show the volcano-like shaped cracks observed in the Ir CL without carbon, indicating that, unless the change was due to the different PTL, the IrO$_x$ CL does not suffer from the hypothesized high gas pressure build up in Ir CL. This is despite having a lower CL porosity, which would be expected to reduce the permeability of the layer. In addition, a significant loss of catalyst for CL with carbon in areas under the land was observed when the carbon to IrO_x volume ratio was 0.25. This might be due to: i) the higher content of carbon in the CL which, when corroded, led to dislodgement of catalyst particles, ii) the removal of the PTL from the CCM for imaging purposes which resulted in the section of the CL being peeled off. Since the CL with a low carbon content did not show the same loss of catalyst, there might be an upper carbon content above which the structural integrity of the IrO_x CL is reduced. The porosity of the IrO_x CLs were much lower than the Ir CLs. This might be due to a higher ionomer loading and due to different particle shape and size.

The calculated ECSA increased and then decreased with an increase in the carbon content. The initial increase is expected due to the increase in the CL porosity, leading to an increased exposure of catalyst to the electrolyte. However, the subsequent decrease in the ECSA was not expected and may have been caused by detachment of the catalyst particles from the CL during the corrosion of the carbon. The actual ECSA might not have decreased. As the loss of catalyst is not known, the initial IrO_x loading was used to calculate the ECSA and hence, a decrease in the ECSA was obtained. This is reflected in the surface SEM images of post-operation IrO_x CL with carbon to IrO_x volume ratio of 0.25, which showed significant loss of the catalyst.

The variation in the cell performance of IrO_x CLs with carbon is shown in Figure 14 in Appendix B. Unlike the previous case, the cell performance only increased at low current density. As discussed earlier, a significant difference between Ir and IrO_x is the low electrical conductivity of the latter. While the proton conductivity is limiting for the Ir CL, in the IrO_x CL the electronic conductivity is limiting. In this case, the OER would be more active near the CL-PTL interface and the increased CL thickness with increased porosity would induce higher proton transport losses, due to the longer path the protons must travel. As a result, despite an increase in ECSA, an improvement at high current density was not observed due to an increase in the HFR, as shown in Figure 15 of Appendix B. Another possible reason for the lack of improved performance might be the type of PTL used.

These results show that the use of a pore former to increase the cell performance is highly dependent on the type of catalyst and PTL used in the cell. The difference between the two catalysts in terms of the impact of the pore former is stark, and should be studied further so that pore formers can be correctly utilized in the future.

4.4 Summary

The addition of carbon nanoparticles was studied as a method to increase the porosity of PEMWE anode CLs. CCMs with varying carbon content were fabricated. Cross-section SEM imaging revealed an increase in the CL porosity due to the addition of carbon, even without removing it. Carbon corrosion resulted in an even higher porosity. Surface SEM imaging of CLs without carbon also showed that the addition of carbon helped eliminate cracks during manufacturing, as well as volcano-shaped cracks during operation. It is hypothesized that the volcano-shaped cracks are indicative of gas being trapped within the CL, as the OER is likely to occur near the membrane. The increased porosity is hypothesized to allow the CL to remove the gas more effectively. CV showed that the ECSA increased with an increase in the carbon content, from 21.5 to 26.9 m^2/g, in agreement with the observed increase in exchange current density from the Tafel analysis. The electrochemical performance showed an improvement of 25 and 54 mV at 2 and 4 A/cm^2 for the CCM with carbon to total volume fraction of 0.2. At low current density, the improvement was due to increased ECSA. Using EIS, it was shown that the improvement at high current density was mainly due to a decrease in the HFR. The decreased HFR is due to better contact between the CL and the PTL. Short-term degradation result showed a lower degradation rate of 529 $\mu V/h$ for the CCM with carbon to total volume fraction of 0.2. The addition of carbon to an electrode made with IrO_x catalyst instead of Ir also achieved an increase in porosity and ECSA. Unfortunately, the performance did not increase at high current density. It is hypothesized the lack of improvement is due to the reaction distribution for this catalyst being close to the CL-PTL interface, thereby leading to increased proton transport overpotential due to the increased CL thickness. The other hypothesis, which cannot be rejected, is that the change was due to the use of a different PTL.

Chapter 5

Conclusions and future work

Hydrogen production from renewable sources of energy, such as solar and wind, using water electrolysis is necessary to limit the GHG emissions from fossil fuel. While PEM electrolysis have been studied since 1960s, the capital and operating costs still need to be decreased and durability still needs to be increased for the widespread utilization of this technology. In order to increase PEMWE cell performance and decrease cost, it is necessary to understand which MEA properties must severely affect these parameters. Identifying these parameters will facilitate the design of optimum CLs. For example, by identifying the parameters that limit activation losses, such as catalyst activity and ECSA, activation losses can be minimized. Similarly, by measuring the proton and electron transport resistances, the ionomer loading can be optimized to achieve a trade off between proton and electron transport and, as a result, ohmic losses can be minimized.

5.1 Conclusions

PEMWE CCMs were fabricated using inkjet printing by developing a unique ink formulation for anode PEMWE cell CLs. The anode CL morphology was analyzed using optical and electron microscopy for surface and thickness characterization. The CL was found to be uniform and well adhered to the membrane. EDX imaging showed even distribution of ionomer and catalyst in the CL. Hydrogen crossover, CV, and electrochemical performance tests were also performed. The hydrogen crossover, in line with Nafion membrane permeability measurements, showed that the PEM was not damaged during the CCM fabrication. The double layer capacitance obtained from CV and EIS tests were similar at low current densities, but the double layer capacitance measured by EIS appeared to decrease with increasing current density. The Tafel slope was similar to literature data while the exchange current density appeared to be lower, most likely due to the use of the commercial IrO_2 catalyst from Alfa Aesar. The electrolyzer CCMs fabricated by inkjet printing could generate 1 and 2 A/cm^2 at potentials of 1609 mV and 1696 mV, respectively, using an NRE211 membrane. Using Nafion 117 membrane, the same current densities were obtained at 1743 mV and 1977 mV. These results outperformed most of the previously reported results in the literature using similar loading and more active catalysts. The CCMs also showed stable performance when tested for 24 hours. These results suggest that inkjet printing can be used to fabricate electrolyzer electrodes with good performance. In this study, only 44 mg IrO_2 were used to produce three 5 cm^2 CCMs, thereby showing that the inkjet printing can be used to produce CCMs with very small amount of catalyst and with minimal wastage, making the method ideal for screening new catalysts under MEA conditions.

In order to decrease ohmic losses, understanding the trade-off between protonic and electronic conductivity of the CL with ionomer loading is necessary. For the second part of this thesis, the effective protonic and electronic conductivities of anode CLs made of TKK IrO_x and Umicore Ir with varying ionomer loading were measured. To measure the protonic conductivity of the anode CLs, a novel setup utilizing the H_2 pump technique was developed. The through-plane and in-plane electronic conductivity were also measured using a modified two-probe and a four-probe method, respectively. For IrO_x CLs, at 100% RH, the electronic conductivity was measured to be much lower than the protonic conductivity at above 15 wt.% ionomer loading and higher than protonic conductivity below 15 wt.%. Increasing the ionomer loading from 5 to 25 wt.% resulted in an increased protonic conductivity and the cell performance. The through-plane electronic conductivity of IrO_x CLs decreased with increasing ionomer loading. The in-plane electronic conductivity is higher than the TP electronic conductivity for IrO_x CLs, indicating some anisotropy in the layer.

Numerical modelling of the hydrogen pump cell showed that the presence of the IrO_x catalyst in the intermediate layer did not impact the measurement of the protonic resistance of the IrO_x layer as the hydrogen reactions will not take place in the intermediate layer. Further, most of the drop in cell voltage in the hydrogen pump experiment occurred in the intermediate layer, thereby proving the accuracy of the setup. For Ir CLs, at 100% RH, the electronic conductivity is always higher than the protonic conductivity. The trade-off between protonic and electronic conductivity is likely to influence the OER distribution. If the proton conductive electrolyte is the least conductive phase, the OER would be more active at the CL–membrane interface. This is the case for the Ir CL. For the IrO_x CL, however, electron conduction is limiting and, as a result the OER will be more active at the at the CL–PTL interface. This result suggests different optimal ionomer distributions for different cases and highlights the importance of the electronic and protonic conductivities of the anode CL, properties that are seldom reported in PEMWE literature.

In the third part of the thesis, the addition of carbon nanoparticles to the ink formulation was studied for the first time in the literature as a method to increase the porosity of PEMWE cell anode CLs. CCMs with catalysts of varying electrical conductivity and different carbon volume fractions were fabricated. SEM imaging revealed an increase in the CL porosity due to the addition of carbon, even without carbon removal. Carbon corrosion resulted in an even higher porosity. The addition of carbon also helped eliminate cracks during manufacturing. The SEM imaging of the surface of Ir CLs without the carbon showed numerous cracks and, after testing, volcano shaped figures, possibly due to oxygen bubbles. These disappeared with the addition of carbon. It is hypothesized the cracks are indicative of gas being trapped within the Ir CL, as the OER is likely to be more active near the membrane. The increased porosity allowed the CL to transport the gas more effectively. The SEM imaging of the surface of IrO_x CLs showed significant damage at high carbon content, indicating that there is a maximum carbon content above which the mechanical integrity of the IrO_x CL is compromised. Cyclic voltammetry showed that the ECSA of Ir and IrO_x CLs increased with an increase in the carbon content. For IrO_x CLs the ECSA, however, decreased at carbon to IrO_x volume fraction higher than 0.1, possibly due to the loss of catalyst particles during carbon corrosion. The electrochemical performance showed an improvement of 25 and 54 mV at 2 and 4 A/cm^2 for the Ir CL with carbon. Using EIS, it is noted that the improvement is due to an increase in the HFR and charge transfer resistance. The improved HFR is hypothesized to be due to a better contact between the Ir CL and the PTL, whereas the decreased charge transfer resistance is due to the higher ECSA. A similar performance improvement was not observed in the case with IrO$_x$ CL. The polarization curve of IrO$_x$ CCMs with carbon showed improved performance at lower current densities, but did not at higher current density. The performance improvement was due to an increase in the ECSA, however due to a higher HFR when carbon was added, the performance decreased at higher current densities. While CCM with carbon to IrO$_x$ volume fraction of 0.1 showed the highest ECSA, a similar improvement was not seen for higher carbon loading, indicating that the removal of carbon was having an impact beyond increasing the ECSA. A short-term degradation result of Ir CLs showed a lower degradation rate of 529 μV/h for the CCM with carbon to total volume fraction of 0.2. These results indicated that, for some catalysts, the PEMWE cell performance can be improved by using carbon as a pore former, and that there might be an optimal pore former content.

5.2 Future work

The ionomer loading plays a critical role in determining the ECSA and ohmic losses. The optimized ionomer content varies greatly in literature, from 5–25 wt.% [52, 62, 69, 72, 233]. It is hypothesized that the reason for the widespread optimum ionomer loading is because its value may depend on the catalyst electronic conductivity and its specific surface areas [106]. A catalyst with low electronic conductivity will require more ionomer as the OER will be more active at the PTL-CL interface, and therefore the electrolyte network will have to transport more charge. Similarly, a higher surface area catalyst would require a higher ionomer loading to coat all the particles in the electrode, whereas a lower surface area catalyst would require a lower ionomer loading. The latter is illustrated in Figure 5.1, where Figure 5.1b shows the optimum ionomer loading for higher surface area catalyst and Figure 5.1e shows for

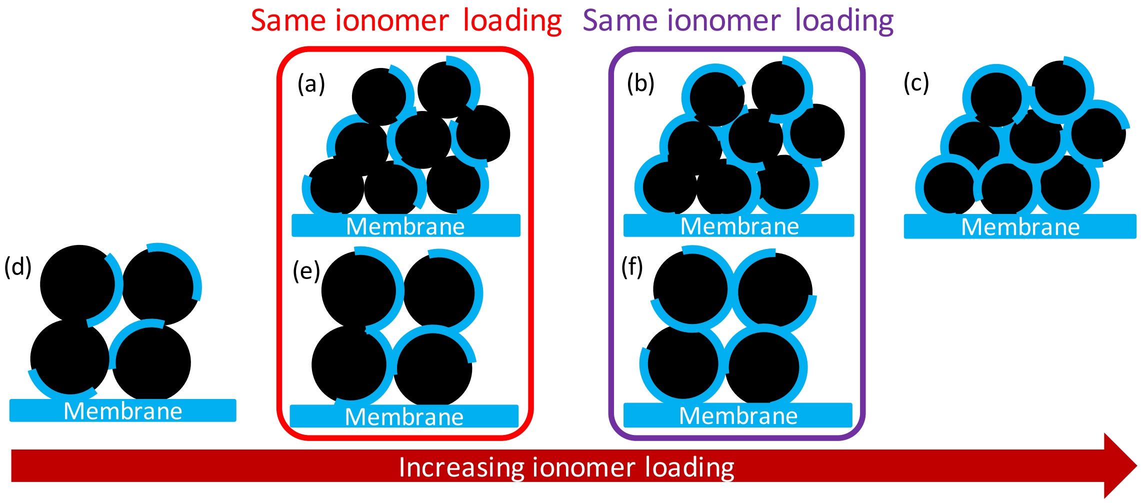

Figure 5.1 – Schematic of the illustration to show the effect of ionomer loading with varying catalyst surface area. High surface area catalyst (a), (b), and (c). Low surface area catalyst (d), (e), and (f).

Table 5.1 – Optimum ionomer loading in literature.

Name	Catalyst	BET Surface area [m^2/g]	Optimum Nafion content [wt%]
Ref. [72]	IrO_2 (JM)	3.1	5
Ref. [62]	IrO_2/TiO_2 (Umicore)	31	11.6

lower surface area catalyst. Table 5.1 shows the optimum ionomer loading in the literature for different catalysts as well as the catalyst BET surface area. The table seems to support both hypotheses. Understanding the relationship between the catalyst conductivity and surface area, and the optimum ionomer loading could be a future work. The hypothesis could be validated by obtaining the ionomer loading for IrO_x and Ir catalysts with different surface area.

In the third chapter, the protonic conductivity was measured to be higher than the electronic conductivity of the IrO_x CL. The implication of this is that the OER would be more active near the CL-PTL interface, therefore, allowing for a reduction of the catalyst loading. This was demonstrated by Taie et al. [99], where a loading of 0.01 mg/cm^2 was used to achieve a 250x mass activity over commercial PEMWE cell. Similarly, the electronic conductivity of the Ir CL is measured to be higher than the protonic conductivity and its implication is that the OER will be more active near the CL-membrane interface as shown in the fourth chapter, where evolution of oxygen bubble created volcano shaped figures. Two commonly used catalysts, Ir and IrO_x, in the PEMWE cell are likely to show OER activity at different sides of the CL, rendering part of the CL inactive. It is hypothesized that by mixing these two catalysts, a better balance between the protonic and electronic conductivity can be achieved, and the OER can be made more uniform within the CL, thereby maximizing the catalyst utilization. Hence, controlling the CL conductivity by changing the mixing ratio could be a second future objective.

As hypothesized above, a part of the Ir or IrO_x CL would be inactive, allowing for a reduction of the catalyst loading [99]. However, activation losses would be higher. Grigoriev and Kalinnikov [85] numerically predicted the dependency of activation and ohmic losses with anode and cathode catalyst loading. They showed that increasing the catalyst loading decreases activation losses. However, the ohmic losses increase and starts to dominate over the activation losses as catalyst loading is further increased. Therefore, numerical results suggest that an optimum catalyst loading exists such that the combined activation and ohmic losses is minimized. This prediction, however, has not been verified experimentally. Most of the catalyst loading studies did not study how activation and ohmic losses varied with catalyst loading except for the numerically predicted results by Grigoriev and Kalinnikov [85]. The optimized catalyst loading is either lower than 0.5 mg/cm^2 or higher than 2 mg/cm^2 [69, 72, 74, 84, 125]. A different CCM fabrication technique used in these studies resulted in a different optimized catalyst loadings. It might be possible that the optimum catalyst loading for inkjet printed CCM is different from the other conventional CCM fabrication methods. Hence, third future objective could be to understand the relationship between activation and ohmic losses with catalyst loading and to find the optimum catalyst loading for inkjet printed CCMs.

References

[1] IEA (2020), Global Energy Review 2020, IEA, Paris. `https://www.iea.org/reports/global-energy-review-2020`, 2020; [Online; accessed 25-January-2021].

[2] G., V. D.; Zhou, D.; Ahmed, E. H. M.; Dadhich, P. K.; Olivier, J.; Rogner, H.-H.; Sheikho, K.; Yamaguchi, M. In *Climate Change 2014: Mitigation of Climate Change. Contribution of Working Group III to the Fifth Assessment Report of the Intergovernmental Panel on Climate Change*; O., E. et al. , Eds.; Cambridge University Press, Cambridge, United Kingdom and New York, NY, USA, 2014.

[3] Harris, D. C. Charles david keeling and the story of atmospheric CO_2 measurements. *Analytical Chemistry* **2010**, *82*, 7865–7870.

[4] Mann, M. E.; Bradley, R. S.; Hughes, M. K. Northern hemisphere temperature during the past millennium: Inferences, Uncertainties, and Limitations. *Geophysical Research Letters* **1999**, *26*, 759–762.

[5] Schwanen, T.; Banister, D.; Anable, J. Scientific research about climate change mitigation in transport: A critical review. *Transportation Research Part A* **2011**, *45*, 993–1006.

[6] Cao, L.; Bala, G.; Caldeira, K.; Nemani, R.; Ban-Weiss, G. Importance of carbon dioxide physiological forcing to future climate change. *Proceedings of the National Academy of Sciences of the United States of America* **2010**, *107*, 9513–9518.

[7] Global direct primary energy consumption. `https://ourworldindata.org/energy`, 2019; [Online; accessed 18-December-2020].

[8] Primary energy consumption by energy source. `https://www.eia.gov/energyexplained/renewable-sources/`, 2019; [Online; accessed 21-Dec-2020].

[9] U.S. Energy Information Administration / Monthly Energy Review June 2017. `https://www.eia.gov/totalenergy/data/monthly/pdf/sec2.pdf`, 2017; [Online; accessed 09-July-2017].

[10] resources Canada, N. Energy Markets Fact Book 2014-2015. 2014.

[11] Primary energy production by energy source. `https://energy-information.canada.ca/en/subjects/overview-energy-sector`, 2019; [Online; accessed 10-Jan-2022].

[12] `https://climateactiontracker.org/countries/canada/`.

[13] Renewable energy will power up to 30 percent of Alberta's electricity grid by 2030. `https://www.alberta.ca/release.cfm?xID=389297B6E1245-F2DD-D96D-329E36A4573C598B`.

[14] Moseley, P. T., Garche, J., Eds. *Electrochemical Energy Storage for Renewable Sources and Grid Balancing*; Elsevier: Amsterdam, 2015; pp 465–473.

[15] Abdin, Z.; Zafaranloo, A.; Rafiee, A.; Mérida, W.; Lipiński, W.; Khalilpour, K. R. Hydrogen as an energy vector. *Renewable and Sustainable Energy Reviews* **2020**, *120*, 109620.

[16] Godula-Jopek, A. In *Hydrogen production by electrolysis*; Godula-Jopek, A., Ed.; Wiley-VCH Verlag GmbH & Co. KGaA, 2015; Chapter Ch. 1.

[17] Mooney, D. Large-Scale Energy Storage. `https://gcep.stanford.edu/pdfs/symposium2015/Presentations/Mooney_GCEPSymposium2015_EnergyStorage101.pdf`, 2015; [Online; accessed 09-July-2017].

[18] Hauer, A.; Quinnell, J.; Lavemann, E. *Transition to Renewable Energy Systems*; Wiley-VCH Verlag GmbH & Co., 2013; Chapter 27.

[19] Kumar, S. S.; Himabindu, V. Hydrogen production by PEM water electrolysis – A review. *Materials Science for Energy Technologies* **2019**, *2*, 442–454.

[20] Jensen, J. O.; Bandur, V.; Bjerrum, N. J.; Jensen, S. H.; Ebbesen, S.; Mogensen, M.; Tophøj, N.; Yde, L.; Technical Univ. of Denmark, K. L. D.; Technical Univ. of Denmark, R. N. L. f. S. E., et al. *Pre-investigation of Water Electrolysis*; Contract FORSKEL-6287; 2008.

[21] Millet, P.; Andolfatto, F.; Durand, R. Design and performance of a solid polymer electrolyte water electrolyzer. *International Journal of Hydrogen Energy* **1996**, *21*, 87–93.

[22] Grigoriev, S. A.; Millet, P.; Volobuev, S. A.; Fateev, V. N. Optimization of porous current collectors for PEM water electrolysers. *International Journal of Hydrogen Energy* **2009**, *34*, 4968–4973.

[23] Rasten, E.; Hagen, G.; Tunold, R. Electrocatalysis in water electrolysis with solid polymer electrolyte. *Electrochimica Acta* **2003**, *48*, 3945–3952.

[24] Grigoriev, S. A.; Millet, P.; Korobtsev, S. V.; Porembskiy, V. I.; Pepic, M.; Etiévant, C.; Puyenchet, C.; Fateev, V. N. Hydrogen safety aspects related to high-pressure polymer electrolyte membrane water electrolysis. *International Journal of Hydrogen Energy* **2009**, *34*, 5986–5991.

[25] Grigoriev, S. A.; Porembskiy, V. I.; Korobtsev, S. V.; Fateev, V. N.; Auprêtre, F.; Millet, P. High-pressure PEM water electrolysis and corresponding safety issues. *International Journal of Hydrogen Energy* **2011**, *36*, 2721–2728.

[26] Narayanan, S. R.; Kindler, A.; Kisor, A.; Valdez, T.; Roy, R. J.; Eldridge, C.; Murach, B.; Hoberecht, M.; Graf, J. Dual-Feed Balanced High-Pressure Electrolysis of Water in a Lightweight Polymer Electrolyte Membrane Stack. *Journal of The Electrochemical Society* **2011**, *158*, B1348–B1357.

[27] Russell, J. H.; Nuttall, L. J.; Fickett, A. P. Hydrogen generation by solid polymer electrolyte water electrolysis. *American Chemical Society Division of Fuel Chemistry Preprints* **1973**, *18*, 24–40.

[28] LaConti, A. B.; Balko, E. N.; Coker, T. G.; Fragala, A. G. Development of the SPE electrolyzer to achieve energy efficient improvements for some important electrochemical processes. 1981.

[29] Hamdan, M.; Norman, T. *PEM electrolyzer incorporating and advanced low-cost membrane*; 2010.

[30] Ayers, K. E.; Anderson, E. B.; Capuano, C. B.; Carter, B. D.; Dalton, L. T.; Hanlon, G.; Manco, J.; Niedzwiecki, M. Research Advances Towards Low Cost, High Efficiency PEM Electrolysis. *ECS Transactions* **2010**, *33*, 3–15.

[31] Marangjo, F.; Pagani, M.; Santarelli, M.; Calí, M. Concept of a high pressure PEM electrolyser prototype. *International Journal of Hydrogen Energy* **2011**, *36*, 7807–7815.

[32] Babic, U.; Suermann, M.; Büchi, F. N.; Gubler, L.; Schmidt, T. J. Review-Identifying Critical Gaps for Polymer Electrolyte Water Electrolysis Development. *Journal of the Electrochemical Society* **2017**, *164*, F387–F399.

[33] Carmo, M.; Fritz, D. L.; Mergel, J.; Stolten, D. A comprehensive review on PEM water electrolysis. *International Journal of Hydrogen Energy* **2013**, *38*, 4901–4934.

[34] Feng, Q.; Yuan, X.-Z.; Liu, G.; Wei, B.; Zhang, Z.; Li, H.; Wang, H. A review of proton exchange membrane water electrolysis on degradation mechanisms and mitigation strategies. *Journal of Power Sources* **2017**, *366*, 33–55.

[35] Kokoh, K. B.; E.Mayousse,; Napporn, T. W.; Servat, K.; Guillet, N.; Soyez, E.; Grosjean, A.; Rakotondrainibé, A.; Paul-Joseph, J. Efficient multi-metallic anode catalysts in a PEM water electrolyzer. *International Journal of Hydrogen Energy* **2014**, *39*, 1924–1931.

[36] Corona-Guinto, J. L.; no García, L. C.; Martínez-Casillas, D. C.; Sandoval-Pineda, J. M.; Tamayo-Meza, P.; Silva-Casarin, R.; González-Huerta, R. G. Performance of a PEM electrolyzer using RuIrCoO$_x$ electrocatalysts for the

oxygen evolution electrode. *International Journal of Hydrogen Energy* **2013**, *38*, 12667–12673.

[37] Grigoriev, S. A.; Mamat, M. S.; Dzhus, K. A.; Walker, G. S.; Millet, P. Platinum and palladium nano-particles supported by graphitic nano-fibers as catalysts for PEM water electrolysis. *International Journal of Hydrogen Energy* **2011**, *36*, 4143–4147.

[38] Cheng, J.; Zhang, H.; Chen, G.; Zhang, Y. Study of $Ir_xRu_xO_2$ oxides as anodic electrocatalysts for solid polymer electrolyte water electrolysis. *Electrochimica Acta* **2009**, *54*, 6250–6256.

[39] Ravichandran, S.; Venkatkarthick, R.; Sankari, A.; Vasudevan, S.; Davidson, D. J.; Sozhan, G. Platinum deposition on the nafion membrane by impregnation reduction using nonionic surfactant for water electrolysis - An alternate approach. *Energy* **2014**, *68*, 148–151.

[40] Slavcheva, E.; Radev, I.; Bliznakov, S.; Topalov, G.; Andreev, P.; Budevski, E. Sputtered iridium oxide films as electrocatalysts for water splitting via PEM electrolysis. *Electrochimica Acta* **2007**, *52*, 3889–3894.

[41] Grigoriev, S. A.; Millet, P.; Fateev, V. N. Evaluation of carbon-supported Pt and Pd nanoparticles for the hydrogen evolution reaction in PEM water electrolysers. *Journal of Power Sources* **2008**, *177*, 281–285.

[42] Siracusano, S.; Baglio, V.; Blasi, A. D.; Briguglio, N.; Stassi, A.; Ornelas, R.; Trifoni, E.; Antonucci, V.; Aricò, A. Electrochemical characterization of single cell and short stack PEM electrolyzers based on a nanosized IrO_2 anode electrocatalyst. *International Journal of Hydrogen Energy* **2010**, *35*, 5558–5568.

[43] Siracusano, S.; Baglio, V.; Stassi, A.; Ornelas, R.; Antonucci, V.; Aricò, A. S. Investigation of IrO_2 electrocatalysts prepared by a sulfite-couplex route for the O_2 evolution reaction in solid polymer electrolyte water electrolyzers. *International Journal of Hydrogen Energy* **2011**, *36*, 7822–7831.

[44] Millet, P.; Ngameni, R.; Grigoriev, S. A.; Mbemba, N.; Brisset, F.; Ranjbari, A.; Etiévant, C. PEM water electrolyzers: From electrocatalysis to stack development. *International Journal of Hydrogen Energy* **2010**, *35*, 5043–5052.

[45] Siracusano, S.; Baglio, V.; Lufrano, F.; Staiti, P.; Aricò, A. S. Electrochemical characterization of a PEM water electrolyzer based on a sulfonated polysulfone membrane. *Journal of Membrane Science* **2013**, *448*, 209–214.

[46] Mittelsteadt, C. K.; Staser, J. A. In *Polymer Science: A Comprehensive Reference*; Matyjaszewski, K., Möller, M., Eds.; Elsevier, Amsterdam, 2012; Chapter 10.42-electrolyzer membranes, pp 849–871.

[47] Wei, G.; Xu, L.; Huang, C.; Wang, Y. SPE water electrolysis with SPEEK/PES blend membrane. *International Journal of Hydrogen Energy* **2010**, *35*, 7778–7783.

[48] Grigoriev, S. A.; Dzhus, K. A.; Bessarabov, D. G.; Millet, P. Failure of PEM water electrolysis cells- Case study involving anode dissolution and membrane thinning. *International Journal of Hydrogen Energy* **2014**, *39*, 20440–20446.

[49] Sawada, S.; Yamaki, T.; Maeno, T.; Asano, M.; Suzuki, A.; Terai, T.; Maekawa, Y. Solid polymer electrolyte water electrolysis systems for hydrogen production based on our newly developed membranes, Part I: Analysis of voltage-current characteristics. *Progress in Nuclear Energy* **2008**, *50*, 443–448.

[50] Jang, I.-Y.; Kweon, O.-H.; Kim, K.-E.; Hwang, G.-J.; Moon, S.-B.; Kang, A.-S. Application of polysulfone (PSf)– and polyether ether ketone (PEEK)–tungstophosphoric acid (TPA) composite membranes for water electrolysis. *Journal of Membrane Science* **2008**, *322*, 154–161.

[51] Ivanchev, S. S. Fluorinated proton-conduction nafion-type membranes, the past and the future. *Russian Journal of Applied Chemistry* **2008**, *81*, 569–584.

[52] Xu, W.; Scott, K. The effects of ionomer content on PEM water electrolyser membrane electrode assembly performance. *International Journal of Hydrogen Energy* **2010**, *35*, 12029–12037.

[53] Ito, H.; Maeda, T.; Nakano, A.; Kato, A.; Yoshida, T. Influence of pore structural properties of current collectors on the performance of proton exchange membrane electrolyzer. *Electrochimica Acta* **2013**, *100*, 242–248.

[54] Ito, H.; Maeda, T.; Nakano, A.; Hwang, C. M.; Ishida, M.; Kato, A.; Yoshida, T. Experimental study on porous current collectors of PEM electrolyzers. *International Journal of Hydrogen Energy* **2012**, *37*, 7418–7428.

[55] Langemann, M.; Fritz, D. L.; Müller, M.; Stolten, D. Validation and characterization of suitable materials for bipolar plates in PEM water electrolysis. *International Journal of Hydrogen Energy* **2015**, *40*, 11385–11391.

[56] Ni, J.; Chen, Y.; Cohen, S.; Carter, B. D.; Boehm, R. F. Numerical and experimental study of three-dimensional fluid flow in the bipolar plate of a PEM electrolysis cell. *International Journal of Thermal Sciences* **2009**, *48*, 1914–1922.

[57] Wang, J.-T.; Wang, W.-W.; Wang, C.; Mao, Z.-Q. Corrosion behavior of three bipolar plate materials in simulated SPE water electrolysis environment. *International Journal of Hydrogen Energy* **2012**, *37*, 12069–12073.

[58] Nie, J.; Chen, Y. Numerical modeling of three-dimensional two-phase gas–liquid flow in the flow field plate of a PEM electrolysis cell. *International Journal of Hydrogen Energy* **2010**, *35*, 3183–3197.

[59] Doucet, G.; Etiévant, C.; Puyenchet, C.; Grigoriev, S.; Millet, P. Hydrogen-based PEM auxiliary power unit. *International Journal of Hydrogen Energy* **2009**, *34*, 4983–4989.

[60] Suermann, M.; Schmidt, T. J.; Büchi, F. N. Investigation of Mass Transport Losses in Polymer Electrolyte Electrolysis Cells. *ECS Transactions* **2015**, *69*, 1141.

[61] Lewinski, K. A.; van der Vliet, D.; Luopa, S. M. NSTF Advances for PEM Electrolysis - the Effect of Alloying on Activity of NSTF Electrolyzer Catalysts and Performance of NSTF Based PEM Electrolyzers. *ECS Transactions* **2015**, *69*, 893.

[62] Bernt, M.; Gasteiger, H. A. Influence of Ionomer Content in IrO_2/TiO_2 Electrodes on PEM Water Electrolyzer Performance. *Journal of the Electrochemical Society* **2016**, *163*, F3179–F3189.

[63] Smolinka, T.; Ojong, E. T.; Lickert, T. In *PEM Electrolysis for Hydrogen Production: Principles and Applications*; Bessarabov, D., Wang, H., Li, H., Zhao, N., Eds.; CRC Press, Taylor & Francis Group, 6000 Broken Sound Parkway NW, Suit 300, 2016; Chapter Fundamentals of water electrolysis, p 29.

[64] Nouri-Khorasani, A.; Ojong, E. T.; Smolinka, T.; Wilkinson, D. P. Model of oxygen bubbles and performance impact in the porous transport layer of PEM water electrolysis cells. *International Journal of Hydrogen Energy* **2017**, *42*, 28665–28680.

[65] Miles, M. H.; Thomason, M. A. Periodic variations of overvoltages for water electrolysis in acid solutions from cyclic voltammetric studies. *Journal of the Electrochemical Society* **1976**, *123*, 1459–1461.

[66] Ayers, K. The potential of proton exchange membrane–based electrolysis technology. *Current Opinion in Electrochemistry* **2019**, *18*, 9–15.

[67] Cherevko, S.; Geiger, S.; Kasian, O.; Mingers, A.; Mayrhofer, K. J. J. Oxygen evolution activity and stability of iridium in acidic media. Part 2. – Electrochemically grown hydrous iridium oxide. *Journal of Electroanalytical Chemistry* **2016**, *774*, 102–110.

[68] Ömer F. Selamet,; Acar, M. C.; Mat, M. D.; Kaplan, Y. Effects of operating parameters on the performance of a high-pressure proton exchange membrane electrolyzer. *International Journal of Energy Reserarch* **2013**, *37*, 457–467.

[69] Ma, L.; Sui, S.; Zhai, Y. Investigations on high performance proton exchange membrane water electrolyzer. *International Journal of Hydrogen Energy* **2009**, *34*, 678–684.

[70] Siracusano, S.; Blasi, A. D.; Baglio, V.; Brunaccini, G.; Briguglio, N.; Stassi, A.; Ornelas, R.; Trifoni, E.; Antonucci, V.; Aricò, A. Optimization of components and assembling in a PEM electrolyzer stack. *International Journal of Hydrogen Energy* **2011**, *36*, 3333–3339.

[71] Mo, J.; Kang, Z.; Yang, G.; Retterer, S. T.; Cullen, D. A.; Toops, T. J.; Jr., J. B. G.; Zhang, F.-Y. Thin liquid/gas diffusion layers for high-efficiency hydrogen production from water splitting. *Applied Energy* **2016**, *117*, 817–822.

[72] Su, H.; Linkov, V.; Bladergroen, B. J. Membrane electrode assemblies with low noble metal loadings for hydrogen production from solid polymer electrolyte water electrolysis. *International Journal of Hydrogen Energy* **2013**, *38*, 9601–9608.

[73] Fabbri, E.; Habereder, A.; Waltar, K.; Kötz, R.; Schmidt, T. J. Developments and perspectives of oxide-based catalysts for the oxygen evolution reaction. *Catalysis Science and Technology* **2014**, *4*, 3800–3821.

[74] Rozain, C.; Mayoussea, E.; Guilleta, N.; Millet, P. Influence of iridium oxide loadings on the performance of PEM water electrolysis cells: Part I-Pure IrO_2-based anodes. *Applied Catalysis B: Environmental* **2016**, *182*, 153–160.

[75] Knöppel, J.; Möckl, M.; Escalera-López, D.; Stojanovski, K.; Bierling, M.; Böhm, T.; Thiele, S.; Rzepka, M.; Cherevko, S. On the limitations in assessing stability of oxygen evolution catalysts using aqueous model electrochemical cells. *Nature communications* **2021**, *12*, 2231.

[76] Bladergroen, B.; Su, H.; Pasupathi, S.; Linkov, V. In *Electrolysis*; Linkov, V., Kleperis, J., Eds.; IntechOpen, 2012; Chapter 3, pp 45–60.

[77] Millet, P. In *Hydrogen production by electrolysis*; Godula-Jopek, A., Ed.; Wiley-VCH Verlag GmbH & Co. KGaA, 2015; Chapter Ch. 2.

[78] Garcìa-Valverde, R.; Espinosa, N.; Urbina, A. Simple PEM water electrolyser model and experimental validation. *International Journal of Hydrogen Energy* **2012**, *37*, 1927–1938.

[79] Mo, J.; Kang, Z.; Retterer, S. T.; Cullen, D. A.; Toops, T. J.; Jr., J. B. G.; Mench, M. M.; Zhang, F.-Y. Discovery of true electrochemical reactions for ultrahigh catalyst mass activity in water splitting. *Science Advances* **2016**, *2*, e1600690.

[80] Geiger, S.; Kasian, O.; Mingers, A. M.; Nicley, S. S.; Haenen, K.; Mayrhofer, K. J. J.; Cherevko, S. Catalyst Stability Benchmarking for the Oxygen Evolution Reaction: The Importance of Backing Electrode Material and Dissolution in Accelerated Aging Studies. *ChemSusChem* **2017**, *10*, 4140–4143.

[81] Bard, A. J.; Faulkner, L. R. *Electrochemical methods : Fundamentals and Applications*, 2nd ed.; John Wiley and Sons, Inc: 605 Third Avenue, New York, NY 10158-0012, 2001.

[82] de Oliveira-Sousa, A.; da Silva, M. A. S.; Machado, S. A. S.; Avaca, L. A.; de Lima-Neto, P. Influence of the preparation method on the morphological and electrochemical properties of Ti/IrO_2-coated electrodes. *Electrochimica Acta* **2000**, *45*, 4467–4473.

[83] Kadakia, K.; Datta, M. K.; Velikokhatnyi, O. I.; Jampani, P.; Park, S. K.; Chung, S. J.; Kumta, P. N. High performance fluorine doped $(Sn,Ru)O_2$ oxgen evolution reaction electro-catalysts for proton exchange membrane based water electrolysis. *Journal of Power Sources* **2014**, *245*, 362–370.

[84] Su, H.; Bladergroen, B. J.; Linkov, V.; Pasupathi, S.; Ji, S. Study of catalyst sprayed membrane under irradiation method to prepare high performance membrane electrode assemblies for solid polymer electrolyte water electrolysis. *International Journal of Hydrogen Energy* **2011**, *36*, 15081–15088.

[85] Grigoriev, S. A.; Kalinnikov, A. A. Mathematical modeling and experimental study of the performance of PEM water electrolysis cell with different loadings of platinum metals in electrocatalytic layers. *International Journal of Hydrogen Energy* **2017**, *42*, 1590–1597.

[86] Xu, J.; Liu, G.; Li, J.; Wang, X. The electrochemical properties of an IrO_2/SnO_2 catalyst using SnO_2 as a support and an assisting reagent for the oxygen evolution reaction. *Electrochimica Acta* **2012**, *59*, 105–112.

[87] Xu, J.; Miao, R.; Zhao, T.; Wu, J.; Wang, X. A novel catalyst layer with hydrophilic-hydropholbic meshwork and pore structure for solid polymer electrolyte water electrolysis. *Electrochemistry Communications* **2011**, *13*, 437–439.

[88] Marshall, A.; Borresen, B.; Hagen, G.; Tsypkin, M.; Tunold, R. Electrochemical characterisation of $Ir_xSn_{1-x}O_2$ powders as oxygen evolution electrocatalysts. *Electrochimica Acta* **2006**, *51*, 3161–3167.

[89] Karimi, F.; Peppley, B. A. Metal Carbide and Oxide Supports for Iridium-Based Oxygen Evolution Reaction Electrocatalysts for Polymer-Electrolyte-Membrane Water Electrolysis. *Electrochimica Acta* **2017**, *246*, 654–670.

[90] Nikiforov, A. V.; García, A. L. T.; Petrushina, I. M.; Christensen, E.; Bjerrum, N. J. Preparation and study of IrO_2/SiC-Si supported anode catalyst for high temperature PEM steam electrolysers. *International Journal of Hydrogen Energy* **2011**, *36*, 5797–5808.

[91] Puthiyapura, V. K.; Mamlouk, M.; Pasupathi, S.; Pollet, B. G.; Scott, K. Physical and electrochemical evaluation of ATO supported IrO_2 catalyst for proton exchange membrane water electrolyser. *Journal of Power Sources* **2014**, *269*, 451–460.

[92] Rozain, C.; Mayousse, E.; Guilleta, N.; Millet, P. Influence of iridium oxide loadings on the performance of PEM water electrolysis cells: Part II - Advanced oxygen electrodes. *Applied Catalysis B: Environmental* **2016**, *182*, 123–131.

[93] Puthiyapura, V. K.; Pasupathi, S.; Su, H.; Liu, X.; Pollet, B.; Scott, K. Investigation of supported IrO_2 as electrocatalyst for the oxygen evolution reaction in proton exchange membrane water electrolyser. *International Journal of Hydrogen Energy* **2014**, *39*, 1905–1913.

[94] Mazúr, P.; Paidar, J. P. M.; Bouzek, K. Non-conductive TiO_2 as the anode catalyst support for PEM water electrolysis. *International Journal of Hydrogen Energy* **2012**, *37*, 12081–12088.

[95] Böhm, D.; Beetz, M.; Gebauer, C.; Bernt, M.; Schröter, J.; Kornherr, M.; Zoller, F.; Bein, T.; Fattakhova-Rohlfing, D. Highly conductive titania supported iridium oxide nanoparticles with low overall iridium density as OER catalyst for large-scale PEM electrolysis. *Applied Materials Today* **2021**, *24*, 101134.

[96] Tan, X.; Shen, J.; Semagina, N.; Secanell, M. Decoupling structure-sensitive deactivation mechanisms of Ir/IrO_x electrocatalysts toward oxygen evolution reaction. *Journal of Catalysis* **2019**, *371*, 57–70.

[97] Ardizzone, S.; Bianchi, C. L.; Cappelletti, G.; Oinita, M.; Minguzzi, A.; Rondinini, S.; Vertova, A. Composite ternary SnO_2-IrO_2-Ta_2O_5 oxide electrocatalysts. *Journal of Electroanalytical Chemistry* **2006**, *589*, 160–166.

[98] Zlotorowicz, A.; Jayasayee, K.; Dahl, P. I.; Thomassen, M. S.; Kjelstrup, S. Tailored porosities of the cathode layer for improved polymer electrolyte fuel cell performance. *Journal of Power Sources* **2015**, *287*, 472–477.

[99] Taie, Z.; Peng, X.; Kulkarni, D.; Zenyuk, I. V.; Weber, A. Z.; Hagen, C.; Danilovic, N. Pathway to complete energy sector decarbonization with available iridium resources using ultralow loaded water electrolyzers. *ACS Applied Materials and Interfaces* **2020**, *12*, 52701–52712.

[100] Rahim, A. H. A.; Tijani, A. S.; Kamarudin, S. K.; Hanapi, S. An overview of polymer electrolyte membrane electrolyzer for hydrogen production: Modeling and mass transport. *Journal of Power Sources* **2016**, *309*, 56–65.

[101] Yigit, T.; Selamet, O. F. Mathematical modeling and dynamic simulink simulation of high-pressure PEM electrolyzer system. *International Journal of Hydrogen Energy* **2016**, *41*, 13901–13914.

[102] Kim, Y.; Ketpang, K.; Jaritphun, S.; Park, J. S.; Shanmugam, S. A polyoxometalate coupled graphene oxide– Nafion composite membrane for fuel cells operating at low relative humidity. *Journal of Materials Chemistry A* **2015**, *3*, 8148.

[103] Siracusano, S.; Baglio, V.; Dijk, N. V.; Merlo, L.; Aricò, A. S. Enhanced performance and durability of low catalyst loading PEM water electrolyser based on a short-side chain perfluorosulfonic ionomer. *Applied Energy* **2017**, *192*, 477–489.

[104] Trinke, P.; Haug, P.; Brauns, J.; Bensmann, B.; Hanke-Rauschenbach, R.; Turek, T. Hydrogen Crossover in PEM and Alkaline Water Electrolysis: Mechanisms, Direct Comparison and Mitigation Strategies. *Journal of The Electrochemical Society* **2018**, *165*, F502–F513.

[105] Sasikumar, G.; Ihm, J. W.; Ryu, H. Optimum Nafion content in PEM fuel cell electrodes. *Electrochimica Acta* **2004**, *50*, 601–605.

[106] Shukla, S.; Bhattacharjee, S.; Weber, A. Z.; Secanell, M. Experimental and theoretical analysis of ink dispersion stability for polyer electrolyte fuel cell applications. *Journal of The Electrochemical Society* **2017**, *164*, F600–F609.

[107] Rakousky, C.; Reimer, U.; Wippermann, K.; Carmo, M.; Lueke, W.; Stolten, D. An analysis of degradation phenomena in polymer electrolyte membrane water electrolysis. *Journal of Power Sources* **2016**, *326*, 120–128.

[108] Gago, A. S.; Ansar, S. A.; Saruhan, B.; Schulz, U.; Lettenmeier, P.; Cañas, N. A.; Gazdzicki, P.; Morawietz, T.; Hiesgen, R.; Arnold, J.; Friedrich, K. A. Protective coatings on stainless steel bipolar plates for proton exchange membrane (PEM) electrolysers. *Journal of Power Sources* **2016**, *307*, 815–825.

[109] Görgünn, H. Dynamic modelling of a proton exchange membrane (PEM) electrolyzer. *International Journal of Hydrogen Energy* **2006**, *31*, 29–38.

[110] Ni, M.; Leung, M. K.; Leung, D. Y. Electrochemistry modeling of proton exchange membrane (PEM) water electrolysis for hydrogen production. 2006.

[111] Lee, B.; Park, K.; Kim, H.-M. Dynamic simulation of PEM water electrolysis and comparison with experiments. *Journal of Electrochemical Science* **2013**, *8*, 235–248.

[112] Spöri, C.; Kwan, J. T. H.; Bonakdarpour, A.; Wilkinson, D. P.; Strasser, P. The Stability Challenges of Oxygen Evolving Catalysts: Towards a Common Fundamental Understanding and Mitigation of Catalyst Degradation. *Angewandte Chemie International Edition* **2017**, *56*, 5994–6021.

[113] Kim, K.-H.; Lee, K.-Y.; Kim, H.-J.; Cho, E.; Lee, S.-Y.; Lim, T.-H.; Yoon, S. P.; Hwang, I. C.; Jang, J. H. The effects of ionomer content in PEMFC MEAs prepared by a catalyst-coated membrane (CCM) spraying method. *International Journal of Hydrogen Energy* **2010**, *35*, 2119–2126.

[114] Shin, S.-J.; Lee, J.-K.; Ha, H.-Y.; Hong, S.-A.; Chun, H.-S.; Oh, I.-H. 2002 Effect of the catalytic ink preparation method on the performance of polymer

electrolyte membrane fuel cells.pdf. *Journal of Power Sources* **2002**, *106*, 146–152.

[115] Tang, H.; Wang, S.; Pan, M.; Jiang, S. P.; Ruan, Y. Performance of direct methanol fuel cells prepared by hot-pressed MEA and catalyst-coated membrane (CCM). *Electrochimica Acta* **2007**, *52*, 3714–3718.

[116] Park, I.-S.; Li, W.; Manthiram, A. Fabrication of catalyst-coated membrane-electrode assemblies by doctor blade method and their performance in fuel cells. *Journal of Power Sources* **2010**, *195*, 7078–7082.

[117] Litster, S.; McLean, G. PEM fuel cell electrodes. *Journal of Power Sources* **2004**, *130*, 61–76.

[118] Chun, Y.-G.; Kim, C.-S.; Peck, D.-H.; Shin, D.-R. Performance of a polymer electrolyte membrane fuel cell with thin film catalyst electrodes. *Journal of Power Sources* **1998**, *71*, 174–178.

[119] Bhosale, A. C.; Ghosh, P. C.; Assaud, L. Preparation methods of membrane electrode assemblies for proton exchange membrane fuel cells and unitized regenerative fuel cells: A review. *Renewable and Sustainable Energy Reviews* **2020**, *133*, 110286.

[120] Talukdar, K.; Helmly, S.; Schulze, M.; Sanchez, D. G.; Handl, M.; Hiesgen, R.; Kraut, J.; Friedrich, K. A. Enveloping of catalyst powder by ionomer for dry spray coating in polymer electrolyte membrane fuel cells. *Journal of Power Sources* **2019**, *424*, 82–90.

[121] Bender, G.; Zawodzinski, T. A.; Saab, A. P. Fabrication of high precision PEFC membrane electrode assemblies. *Journal of Power Sources* **2003**, *124*, 114–117.

[122] Kim, C.; Chun, Y.; Peck, D.; Shin, D. A novel process to fabricate membrane electrode assemblies for proton exchange membrane fuel cells. *International Journal of Hydrogen Energy* **1998**, *23*, 1045–1048.

[123] Søndergaard, R. R.; Hösel, M.; Krebs, F. C. Roll-to-Roll Fabrication of Large Area Functional Organic Materials. *Journal of Polymer Science Part B: Polymer Physics* **2013**, *51*, 16–34.

[124] Cho, Y. H.; Park, H. S.; Cho, Y. H.; Park, I. S.; Sung, Y. E. The improved methanol tolerance using Pt/C in cathode of direct methanol fuel cell. *Electrochimica Acta* **2008**, *53*, 5909–5912.

[125] Lee, B.-S.; Ahn, S. H.; Park, H.-Y.; Choi, I.; Yoo, S. J.; Kim, H.-J.; Henkensmeier, D.; Kim, J. Y.; Park, S.; Nam, S. W.; Lee, K.-Y.; Jang, J. H. Development of electrodeposited IrO2 electrodes as anodes in polymer electrolyte membrane water electrolysis. *Applied Catalysis B: Environmental* **2015**, *179*, 285–291.

[126] Martin, S.; Garcia-Ybarra, P.; Castillo, J. High platinum utilization in ultra-low Pt loaded PEM fuel cell cathodes prepared by electrospraying. *International Journal of Hydrogen Energy* **2010**, *35*, 10446–10451.

[127] Taylor, A.; Kim, E.; Humes, V.; Kizuka, J.; Thompson, L. Inkjet printing of carbon supported platinum 3-D catalyst layers for use in fuel cells. *Journal of Power Sources* **2007**, *171*, 101–106.

[128] Towne, S.; Viswanathan, V.; Holbery, J.; Rieke, P. Fabrication of polymer electrolyte membrane fuel cell MEAs utilizing inkjet print technology. *Journal of Power Sources* **2007**, *171*, 575–584.

[129] Shukla, S.; Domican, K.; Karan, K.; Bhattacharjee, S.; Secanell, M. Analysis of Low Platinum Loading Thin Polymer Electrolyte Fuel Cell Electrodes Prepared by Inkjet Printing. *Electrochimica Acta* **2015**, *156*, 289–300.

[130] Shukla, S.; Stanier, D.; Saha, M.; Stumper, J.; Secanell, M. Analysis of Inkjet Printed PEFC Electrodes with Varying Platinum Loading. *Journal of the Electrochemical Society* **2016**, *163*, F677–F687.

[131] Saha, M. S.; Tam, M.; Berejnov, V.; Susac, D.; McDermid, S.; Hitchcock, A.; Stumper, J. Characterization and performance of catalyst layers prepared by inkjet printing technology. *ECS Transactions* **2013**, *58*, 797–806.

[132] Owejan, J. P.; Owejan, J. E.; Gu, W. Impact of platinum loading and catalyst layer structure on PEMFC performance. *Journal of The Electrochemical Society* **2013**, *160*, F824–F833.

[133] Yamaguchi, M.; Yagiuchi, K.; Okisawa, K. R&D of high performance solid polymer electrolyte water electrolyzer in WE-NET. *Hydrogen Energy Progress XI* **1996**, *1-3*, 781–786.

[134] Yamaguchi, M.; Okisawa, K.; Nakanori, T. Development of high performance solid polymer electrolyte water electrolyzer in WE-NET. *IECEC-97-Proceedings of the thirty-second intersociety energy conversion engineering conference* **1997**, *1-4*, 1958–1965.

[135] Yamaguchi, M.; Shinohara, T.; Taniguchi, H.; Nakanori, H.; Okisawa, K. Development of 2500 cm^2 five cell stack water electrolyzer in WE-NET. Environmental aspects of electrochemical technology. 2000.

[136] Shao, Z. G.; Yi, B. L.; Han, M. The membrane electrodes assembly for SPE water electrolysis. 2000.

[137] Rasten, E.; Hagen, G.; Tunold, R. Effect of thermal treatment of IrO_2 anode catalysts for PEM water electrolysis. 2001.

[138] Zhang, Y.; Wang, C.; Wan, N.; Liu, Z.; Mao, Z. Study on a novel manufacturing process of membrane electrode assemblies for solid polymer electrolyte water electrolysis. *Electrochemistry Communications* **2007**, *9*, 667–670.

[139] Song, S.; Zhang, H.; Ma, X.; Shao, Z.; Baker, R. T.; Yi, B. Electrochemical investigation of electrocatalysts for the oxygen evolution reaction in PEM water electrolyzers. *International Journal of Hydrogen Energy* **2008**, *33*, 4955–4961.

[140] Siracusano, S.; Baglio, V.; Briguglio, N.; Brunaccini, G.; Blasi, A. D.; Stassi, A.; Ornelas, R.; Trifoni, E.; Antonucci, V.; Aricò, A. An electrochemical study of a PEM stack for water electrolysis. *International Journal of Hydrogen Energy* **2012**, *37*, 1939–1946.

[141] Baglio, V.; Ornelas, R.; Matteucci, F.; Martina, F.; Ciccarella, G.; Zama, I.; Arriaga, L. G.; Antonucci, V.; Aricò, A. S. Solid Polymer Electrolyte Water Electrolyser Based on Nafion-TiO_2 Composite Membrane for High Temperature Operation. *Fuel Cells* **2009**, *9*, 247–253.

[142] Shukla, S.; Domican, K.; Secanell, M. Effect of electrode patterning on PEM fuel cell performance using inkjet printing method. *ECS Transactions* **2014**, *64*, 341–352.

[143] Saha, M. S.; Paul, D. K.; Malevich, D.; Peppley, B. A.; Karan, K. Preparation of ultra-thin catalyst layers by piezo-electric printer for PEMFCs applications. *ECS Transactions* **2009**, *25*, 2049–2059.

[144] Malevich, D.; Saha, M. S.; Halliop, E.; Peppley, B. A.; Pharoah, J. G.; Karan, K. Performance characteristics of PEFCs with patterned electrodes prepared by piezo-electric printing. *ECS Transactions* **2012**, *50*, 423–427.

[145] Yazdanpour, M.; Esmaeilifar, A.; Rowshanzamir, S. Effects of hot pressing conditions on the performance of Nafion membranes coated by Ink-Jet printing of Pt/MWCNTs electrochatalyst for PEMFCs. *International Journal of Hydrogen Energy* **2012**, *37*, 11290–11298.

[146] Mandal, M.; Valls, A.; Gangnus, N.; Secanell, M. Analysis of Inkjet Printed Catalyst Coated Membranes for Polymer Electrolyte Electrolyzers. *Journal of the Electrochemical Society* **2018**, *165*, F543–F552.

[147] Huang, Q.; Jiang, J.; Chai, J.; Yuan, T.; Zhang, H.; Zou, Z.; Zhang, X.; Yang, H. Construction of porous anode by sacrificial template for a passive direct methanol fuel cell. *Journal of Power Sources* **2014**, *262*, 213–218.

[148] Song, Y.; Wei, Y.; Xu, H.; Williams, M.; Liu, Y.; Bonville, L. J.; Kunz, H. R.; Fenton, J. M. Improvement in high temperature proton exchange membrane fuel cells cathode performance with ammonium carbonate. *Journal of Power Sources* **2005**, *141*, 250–257.

[149] Reshetenko, T. V.; Kim, H.-T.; Kweon, H.-J. Cathode structure optimization for air-breathing DMFC by application of pore-forming agents. *Journal of Power Sources* **2007**, *171*, 433–440.

[150] Fischer, A.; Jindra, J.; Wendt, H. Porosity and catalyst utilization of thin layer cathodes in air operated PEM-fuel cells. *Journal of Applied Electrochemistry* **1998**, *28*, 277–282.

[151] Hartmut, W.; Andreas, F.; Ralf, Z. European patent EP 0797265B1. 1997.

[152] Cho, Y.-H.; Jung, N.; Kang, Y. S.; Chung, D. Y.; Lim, J. W.; Choe, H.; Cho, Y.-H.; Sung, Y.-E. Improved mass transfer using a pore former in cathode catalyst layer in the direct methanol fuel cell. *International Journal of Hydrogen Energy* **2012**, *37*, 11969–11974.

[153] Gamburzev, S.; Appleby, A. J. Recent progress in performance improvement of the proton exchange membrane fuel cell (PEMFC). *Journal of Power Sources* **2002**, *107*, 5–12.

[154] Uribe, F. A.; Gottesfeld, S.; Jr., T. A. Z. Effect of ammonia as potential fuel impurity on proton exchange membrane fuel cell performance. *Journal of The Electrochemical Society* **2002**, *149*, A293–A296.

[155] Bard, A. J.; Parsons, R.; Jordan, J. *Standard Potentials in Aqueous Solution, Monographs in Electroanalytical Chemistry and Electrochemist*; Taylor & Francis Inc., New York United States, 1985.

[156] Ross, P. N.; Sokol, H. The Corrosion of carbon black anodes in alkaline electrolyte. *Journal of the Electrochemical Society* **1984**, *131*, 1742–1750.

[157] Mittelsteadt, C.; Staser, J. Electrolyzer Membranes. *Polymer Science: A Comprehensive Reference* **2012**, *10*, 849–871.

[158] Ito, H.; Maeda, T.; Nakano, A.; Takenaka, H. Properties of Nafion membranes under PEM water electrolysis conditions. *International Journal of Hydrogen Energy* **2011**, *36*, 10527–10540.

[159] Lettenmeier, P.; Kolb, S.; Sata, N.; Fallisch, A.; Zielke, L.; Thiele, S.; Gago, A. S.; Friedrich, K. A. Comprehensive investigation of novel pore-graded gas diffusion layers for high-performance and cost-effective proton exchange membrane electrolyzers. *Energy and Environmental Science* **2017**, *10*, 2521–2533.

[160] Schuler, T.; Ciccone, J. M.; Krentscher, B.; Marone, F.; Peter, C.; Schmidt, T. J.; Büchi, F. N. Hierarchically Structured Porous Transport Layers for Polymer Electrolyte Water Electrolysis. *Advanced Energy Materials* **2020**, *10*, 1903216.

[161] Babic, U.; Schmidt, T. J.; Gubler, L. Communication-Contribution of Catalyst Layer Proton Transport Resistance to Voltage Loss in Polymer Electrolyte Water Electrolyzers. *Journal of The Electrochemical Society* **2018**, *165*, J3016–J3018.

[162] Babic, U.; Nilsson, E.; Pătru, A.; Schmidt, T. J.; Gubler, L. Proton Transport in Catalyst Layers of a Polymer Electrolyte Water Electrolyzer: Effect of the Anode Catalyst Loading. *Journal of The Electrochemical Society* **2019**, *166*, F214–F220.

[163] Karan, K. Interesting Facets of Surface, Interfacial, and Bulk Characteristics of Perfluorinated Ionomer Films. *Langmuir* **2019**, *35*, 13489–13520.

[164] Papaderakis, A.; Tsiplakides, D.; Balomenou, S.; Sotiropoulos, S. Electrochemical impedance studies of IrO_2 catalysts for oxygen evolution. *Journal of Electroanalytical Chemistry* **2015**, *757*, 216–224.

[165] Malevich, D.; Jayasankar, B. R.; Halliop, E.; Pharoah, J. G.; Peppley, B. A.; Karan, K. On the Determination of PEM Fuel Cell Catalyst Layer Resistance from Impedance Measurement in H_2/N_2 Cells. *Journal of the Electrochemical Society* **2012**, *159*, F888–F895.

[166] Cimenti, M.; Bessarabov, D.; Tam, M.; Stumper, J. Investigation of Proton Transport in the Catalyst Layer of PEM Fuel Cells by Electrochemical Impedance Spectroscopy. *ECS Transactions* **2010**, *28*, 147–157.

[167] Makharia, R.; Mathias, M. F.; Baker, D. R. Measurement of Catalyst Layer Electrolyte Resistance in PEFCs Using Electrochemical Impedance Spectroscopy. *Journal of the Electrochemical Society* **2005**, *152*, A970–A977.

[168] Boyer, C.; Gamburzev, S.; Velev, O.; Srinivasan, S.; Appleby, A. J. Measurements of proton conductivity in the active layer of PEM fuel cell gas diffusion electrodes. *Electrochimica Acta* **1998**, *43*, 3703–3709.

[169] Iden, H.; Ohma, A.; Shinohara, K. Analysis of Proton Transport in Pseudo Catalyst Layers. *Journal of the Electrochemical Society* **2009**, *156*, B1078–B1084.

[170] Iden, H.; Sato, K.; Ohma, A.; Shinohara, K. Relationship among Microstructure, Ionomer Property and Proton Transport in Pseudo Catalyst Layers. *Journal of the Electrochemical Society* **2011**, *158*, B987–B994.

[171] Marshall, A.; Børresen, B.; Hagen, G.; Tsypkin, M.; Tunold, R. Preparation and characterisation of nanocrystalline $Ir_xSn_{1-x}O_2$ electrocatalytic powders. *Materials Chemistry and Physics* **2005**, *94*, 226–232.

[172] Oakton, E.; Lebedev, D.; Fedorov, A.; Krumeich, F.; Tillier, J.; Sereda, O.; Schmidt, T. J.; Copéret, C. A simple one-pot Adams method route to conductive high surface area IrO_2–TiO_2 materials. *New Journal of Chemistry* **2016**, *40*, 1834–1838.

[173] Patil, P.; Chigare, P.; Sadale, S.; Seth, T.; Amalnerkar, D.; Kawar, R. Thickness-dependent properties of sprayed iridium oxide thin films. *Materials Chemistry and Physics* **2003**, *80*, 667–675.

[174] Liao, P. C.; Ho, W. S.; Huang, Y. S.; Tiong, K. K. Characterization of sputtered iridium dioxide thin films. *Journal of Journal of Materials Reseach* **1998**, *13*, 1318–1326.

[175] Yang, G.; Yu, S.; Kang, Z.; Li, Y.; Bender, G.; Pivovar, B. S.; Jr., J. B. G.; Cullen, D. A.; Zhang, F.-Y. Building Electron/Proton Nanohighways for Full Utilization of Water Splitting Catalysts. *Advanced Energy Materials* **2020**, *10*, 1903871.

[176] Mo, J.; Yang, G.; Li, Y.; Kang, Z.; Bender, G.; Pivovar, B. S.; Jr., J. B. G.; Zhang, F.-Y. Experimental studies on the effects of sheet resistance and wettability of catalyst layer on electro-catalytic activities for oxygen evolution reaction in proton exchange membrane electrolysis cells. *International Journal of Hydrogen Energy* **2020**, *45*, 26595–26603.

[177] Gode, P.; Jaouen, F.; Lindbergh, G.; Lundblad, A.; Sundholm, G. Influence of the composition on the structure and electrochemical characteristics of the PEFC cathode. *Electrochimica Acta* **2003**, *48*, 4175–4187.

[178] Suzuki, T.; Murata, H.; Hatanaka, T.; Morimoto, Y. Analysis of the Catalyst Layer of Polymer Electrolyte Fuel Cells. *R&D Rev. Toyota CRDL* **2003**, *39*, 33–38.

[179] Morris, D. R. P.; Liu, S. P.; Gonzalez, D. V.; Gostick, J. T. Effect of Water Sorption on the Electronic Conductivity of Porous Polymer Electrolyte Membrane Fuel Cell Catalyst Layers. *ACS Applied Materials and Interfaces* **2014**, *6*, 18609–18618.

[180] Du, C. Y.; Shi, P. F.; Cheng, X. Q.; Yin, G. P. Effective protonic and electronic conductivity of the catalyst layers in proton exchange membrane fuel cells. *Electrochemistry Communications* **2004**, *6*, 435–440.

[181] Ahadi, M.; Tam, M.; Stumper, J.; Bahrami, M. Electronic conductivity of catalyst layers of polymer electrolyte membrane fuel cells: Through-plane vs. in-plane. *International Journal of Hydrogen Energy* **2019**, *44*, 3603–3614.

[182] Derby, B. Inkjet Printing of Functional and Structural Materials: Fluid Property Requirements, Feature Stability, and Resolution. *Annual Review of Materials Research* **2010**, *40*, 395–414.

[183] Jettable Fluid Formulation Guidelines. 2019; `https://www.fujifilm.ca/shared/bin/Dimatix_Materials_Printer_Jettable_Fluid_Formulation_Guidelines_05-13.pdf`.

[184] Uchida, M.; Fukuoka, Y.; Sugawara, Y.; Ohara, H.; Ohta, A. Improved preparation process of very-low-platinum-loading electrodes for polymer electrolyte fuel cells. *Journal of The Electrochemical Society* **1998**, *145*, 3708–3713.

[185] Kundu, S.; Fowler, M. W.; Simon, L. C.; Grot, S. Morphological features (defects) in fuel cell membrane electrode assemblies. *Journal of Power Sources* **2006**, *157*, 650–656.

[186] Woods, R. Hydrogen adsorption on platinum, iridium and rhodium electrodes at reduced temperatures and the determination of real surface area. *Journal of Electroanalytical Chemistry* **1974**, *49*, 217–226.

[187] Carter, R. N.; Kocha, S. S.; Wagner, F. T.; Fay, M.; Gasteiger, H. A. Artifacts in measuring electrodes catalyst area of fuel cells through cyclic voltammetry. *ECS Transactions* **2007**, *11*, 403–410.

[188] Zhao, S.; Yu, H.; Maric, R.; Danilovic, N.; Capuano, C. B.; Ayers, K. E.; Mustain, W. E. Calculating the electochemically active surface area of irodium oxide in operating proton exchange membrane electrolyzers. *Journal of the Electrochemical Society* **2015**, *162*, F1292–F1298.

[189] Alia, S. M.; Hurst, K. E.; Kocha, S. S.; Pivovar, B. S. Mercury Underpotential Deposition to Determine Iridium and Iridium Oxide Electrochemical Surface Areas. *Journal of the Electrochemical Society* **2016**, *163*, F3051–F3056.

[190] da Silva, L. A.; Alves, V. A.; da Silva, M. A. P.; trasatti, S.; Boodts, J. F. C. Oxygen evolution in acid solution on IrO_2 + TiO_2 ceramic films. A study by impedance, voltammetry and SEM. *Electrochimica Acta* **1997**, *42*, 271–281.

[191] Bensmann, B.; Hanke-Rauschenbach, R.; Sundmacher, K. In-situ measurement of hydrogen crossover in polymer electrolyte membrane water electrolysis. *International journal of Hydrogen Energy* **2014**, *39*, 49–53.

[192] Cooper, K. R. *Experimental methods and data analyses for polymer electrolyte fuel cells*; Electrochemical Innovation; Scribner Associates, 2005.

[193] Wu, J.; Yuan, X.; Wang, H.; Blanco, M.; Martin, J.; Zhang, J. Diagnostic tools in PEM fuel cell research: Part I-Electrochemical techniques. *International Journal of Hydrogen Energy* **2008**, *36*, 1735–1746.

[194] Kreuer, K. D. On the development of proton conducting polymer membranes for hydrogen and methanol fuel cells. *Journal of Memb. Science* **2001**, *185*, 29–39.

[195] Peron, J.; Mani, A.; Zhao, X.; Edwards, D.; Adachi, M.; Soboleva, T.; Shi, Z.; Xie, Z.; Navessin, T.; Holdcroft, S. Properties of Nafion NR-211 membrane for PEMFCs. *Journal of Memb. Science* **2010**, *356*, 44–51.

[196] Dellis, J.-L. Impedance data fit. `https://in.mathworks.com/matlabcentral/fileexchange/19460-zfit`.

[197] Millet, P. In *Hydrogen production by electrolysis*; Godula-Jopek, A., Ed.; Wiley-VCH Verlag GmbH & Co. KGaA, 2015; Chapter Ch. 3.

[198] Lettenmeier, P.; Wang, R.; Abouatallah, R.; Helmly, S.; Morawietz, T.; Hiesgen, R.; Kolb, S.; Burggraf, F.; Kallo, J.; Gago, A. S.; Friedrich, K. A. Durable Membrane Electrode Assemblies for Proton Exchange Membrane Electrolyzer Systems Operating at High Current Densities. *Electrochimica Acta* **2016**, *210*, 502–511.

[199] Suzuki, T.; Murata, H.; Hatanaka, T.; Morimoto, Y. Analysis of the Catalyst Layer of Polymer Electrolyte Fuel Cells. *R&D Rev. Toyota CRDL* **2004**, *39*, 33–38.

[200] Skoog, D.; West, D.; Holler, F. *Fundamentals of Analytical Chemistry*, 7th ed.; Fort Worth: Saunders College Publishing Harcourt Brace, 1996; pp 71–96.

[201] Graton, L.; Fraser, H. Systematic packing of spheres: with particular relation to porosity and permeability. *The Journal of Geology* **1935**, *43*, 785–909.

[202] Lee, B.-S.; Park, H.-Y.; Choi, I.; Cho, M. K.; Kim, H.-J.; Yoo, S. J.; Henkensmeier, D.; Kim, J. Y.; Nam, S. W.; Park, S.; Lee, K.-Y.; Jang, J. H. Polarization characteristics of a low catalyst loading PEM water electrolyzer operating at elevated temperature. *Journal of Power Sources* **2016**, *309*, 127–134.

[203] Trasatti, S. Physical electrochemistry of ceramic oxides. *Electrochimica Acta* **1991**, *36*, 225–241.

[204] Labou, D.; Slavcheva, E.; Schnakenberg, U.; Neophytides, S. Performance of laboratory polymer electrolyte membrane hydrogen generator with sputtered iridium oxide anode. *Journal of Power Sources* **2008**, *185*, 1073–1078.

[205] Pathiraja, G. C.; Nanayakkara, N.; Wijayasinghe, A. Oxygen evolution reaction of Ti/IrO_2–SnO_2 electrode: a study by cyclic voltammetry, Tafel lines, EIS and SEM. *Bulletin of Materials Science* **2016**, *39*, 803–809.

[206] Alvesa, V. A.; da Silva, L. A.; Boodts, J. F. C. Surface characterisation of $IrO_2/TiO_2/CeO_2$ oxide electrodes and Faradaic impedance investigation of the oxygen evolution reaction from alkaline solution. *Electrochimica Acta* **1998**, *44*, 1525–1534.

[207] Broka, K.; Ekdunge, P. Oxygen and hydrogen permeation properties and water uptake of Nafion 117 membrane and recast film for PEM fuel cell. *Journal of Applied Electrochemistry* **1997**, *27*, 117–123.

[208] Kocha, S.; Yang, J.; Yi, J. Characterization of gas crossover and its implications in PEM fuel cells. *AIChE Journal* **2006**, *52*, 1916–1925.

[209] Yeo, R.; McBreen, J. Transport properties of Nafion membranes in electrochemically regenerative hydrogen/ halogen cells. *Journal of the Electrochemical Society* **1979**, *126*, 1682–1687.

[210] Gasteiger, H.; Gu, W.; Makharia, R.; Mathias, M.; Sompalli, B. *Handbook of Fuel Cells*; John Wiley & Sons Ltd, 2010.

[211] Schalenbach, M.; Hoefner, T.; Paciok, P.; Carmo, M.; Lueke, W.; Stolten, D. Gas Permeation through Nafion. Part 1: Measurements. *The Journal of Physical Chemistry C* **2015**, *119*, 25145–25155.

[212] Sakai, T.; Takenaka, H.; Wakabayashi, N.; kawami, Y.; Torikai, E. Gas permeation properties of solid polymer electrolyte (SPE) membranes. *Journal of the Electrochemical Society* **1985**, *132*, 1328–1332.

[213] Sakai, T.; Takenaka, H.; Torikai, E. Gas diffusion in the dried and hydrated Nafions. *Journal of the Electrochemical Society* **1986**, *133*, 88–92.

[214] Kreuer, K. D. The role of internal pressure for the hydration and transport properties of ionomers and polyelectrolytes. *Solid State Ionics* **2013**, *252*, 93–101.

[215] Dedigama, I.; Angeli, P.; Ayers, K.; Robinson, J.; Shearing, P.; Tsaoulidis, D.; Brett, D. In situ diagnostic techniques for characterisation of polymer electrolyte membrane water electrolysers - Flow visualisation and electrochemical impedance spectroscopy. *International Journal of Hydrogen Energy* **2014**, *39*, 4468–4482.

[216] Millet, P.; Mbemba, N.; Grigoriev, S. A.; Fateev, V. N.; Aukauloo, A.; Etiévant, C. Electrochemical performances of PEM water electrolysis cells and perspectives. *International Journal of Hydrogen Energy* **2011**, *36*, 4134–4142.

[217] Sadeghifar, H. In-plane and through-plane electrical conductivities and contact resistances of a Mercedes-Benz catalyst-coated membrane, gas diffusion and micro-porous layers and a Ballard graphite bipolar plate: Impact of humidity, compressive load and polytetrafluoroethylene. *Energy Conversion and Management* **2017**, *154*, 191–202.

[218] Secanell, M.; Putz, A.; Wardlaw, P.; Zingan, V.; Bhaiya, M.; Moore, M.; Zhou, J.; Balen, C.; Domican, K. Openfcst: An open-source mathematical modelling software for polymer electrolyte fuel cells. *ECS Transactions* **2014**, *64*, 655–680.

[219] Secanell, M.; Songprakorp, R.; Suleman, A.; Djilali, N. Multi-objective optimization of a polymer electrolyte fuel cell membrane electrode assembly. *Energy and Environmental Science* **2008**, *1*, 378–388.

[220] Elbert, K.; Hu, J.; Ma, Z.; Zhang, Y.; Chen, G.; An, W.; Liu, P.; Isaacs, H. S.; Adzic, R. R.; Wang, J. X. Elucidating hydrogen oxidation/evolution kinetics in base and acid by enhanced activities at the optimized Pt shell thickness on the Ru core. *ACS Catalysis* **2015**, *5*, 6764–6772.

[221] Soboleva, T.; Malek, K.; Xie, Z.; Navessin, T.; Holdcroft, S. PEMFC Catalyst Layers: The Role of Micropores and Mesopores on Water Sorption and Fuel Cell Activity. *ACS Applied Materials and Interfaces* **2011**, *3*, 1827–1837.

[222] Ochi, S.; Kamishima, O.; Mizusaki, J.; Kawamura, J. Investigation of proton diffusion in Nafion®117 membrane by electrical conductivity and NMR. *Solid State Ionics* **2009**, *180*, 580–584.

[223] Secanell, M. Computational Modeling and Optimization of Proton Exchange Membrane Fuel Cells. Ph.D. thesis, University of Victoria, 2007.

[224] Stauffer, D.; Aharony, A. *Introduction to Percolation Theory*; Taylor & Francis, London, 2nd edition, 1992.

[225] Kosakian, A.; Urbina, L. P.; Heaman, A.; Secanell, M. Understanding single-phase water-management signatures in fuel-cell impedance spectra: A numerical study. *Electrochimica Acta* **2020**, *350*, 136204.

[226] Bensmann, B.; Hanke-Rauschenbach, R. (Invited) Engineering Modeling of PEM Water Electrolysis: A Survey. *ECS Transactions* **2016**, *75*, 1065–1072.

[227] Mo, J.; Kang, Z.; Yang, G.; Li, Y.; Retterer, S. T.; Cullen, D. A.; Toops, T. J.; Bender, G.; Pivovar, B. S.; Jr, J. B. G.; Zhang, F.-Y. In situ investigation on ultrafast oxygen evolution reactions of water splitting in proton exchange membrane electrolyzer cells. *Journal of Materials Chemistry A* **2017**, *5*, 18469–18475.

[228] Lettenmeier, P.; Majchel, J.; Wang, L.; Saveleva, V. A.; Zafeiratos, S.; Savinova, E. R.; Gallet, J.-J.; Bournel, F.; Gago, A. S.; Friedrich, K. A. Highly active nano-sized iridium catalysts: synthesis and operando spectroscopy in a proton exchange membrane electrolyzer. *Chemical Science* **2018**, *9*, 3570–3579.

[229] Cherevko, S.; Geiger, S.; Kasian, O.; Mingers, A.; Mayrhofer, K. J. Oxygen evolution activity and stability of iridium in acidic media. Part 1. – Metallic iridium. *Journal of Electroanalytical Chemistry* **2016**, *773*, 69–78.

[230] Cherevko, S.; Geiger, S.; Kasian, O.; Kulyk, N.; Grote, J.-P.; Savan, A.; Shrestha, B. R.; Merzlikin, S.; Breitbach, B.; Ludwig, A.; Mayrhofer, K. J. Oxygen and hydrogen evolution reactions on Ru, RuO_2, Ir, and IrO_2 thin film electrodes in acidic and alkaline electrolytes: A comparative study on activity and stability. *Catalysis Today* **2016**, *262*, 170–180.

[231] Mandal, M.; Moore, M.; Secanell, M. Measurement of the Protonic and Electronic Conductivities of PEM Water Electrolyzer Electrodes. *ACS Applied Materials and Interfaces* **2020**, *12*, 49549–49562.

[232] Kosakian, A.; Secanell, M. Estimating charge-transport properties of fuel-cell and electrolyzer catalyst layers via electrochemical impedance spectroscopy. *Electrochimica Acta* **2020**, *367*, 137521.

[233] Ma, H.; Yue, L.; Dong, X.; Fu, Y.; Liao, J.; Liu, C.; Xing, W. Effect of nafion loading in the oxygen electrode on performance of the PEM-type water electrolyzer. *Journal of New Materials for Electrochemical Systems* **2013**, *16*, 013–017.

[234] Morris, D. R. P.; Gostick, J. T. Determination of the in-plane components of the electrical conductivity tensor in PEM fuel cell gas diffusion layers. *Electrochimica Acta* **2012**, *85*, 665–673.

[235] Ismail, M.; Damjanovic, T.; Ingham, D.; Pourkashanian, M.; Westwood, A. Effect of polytetrafluoroethylene-treatment and microporous layer-coating on the electrical conductivity of gas diffusion layers used in proton exchange membrane fuel cells. *Journal of Power Sources* **2010**, *195*, 2700–2708.

[236] Nitta, I.; Hottinen, T.; Himanen, O.; Mikkola, M. Inhomogeneous compression of PEMFC gas diffusion layer Part I. Experimental. *Journal of Power Sources* **2007**, *171*, 26–36.

[237] Saab, A. P.; Garzon, F. H.; Zawodzinski, T. A. Determination of Ionic and Electronic Resistivities in Carbon/Polyelectrolyte Fuel-Cell Composite Electrodes. *Journal of The Electrochemical Society* **2002**, *149*, A1541–A1546.

[238] Siroma, Z.; Hagiwara, J.; Yasuda, K.; Inaba, M.; Tasaka, A. Simultaneous measurement of the effective ionic conductivity and effective electronic conductivity in a porous electrode film impregnated with electrolyte. *Journal of Electroanalytical Chemistry* **2010**, *648*, 92–97.

Appendices

Appendix A

Electrode characterization

A.1 Porosity and volume fractions of IrO$_x$ layer

The porosity was calculated based on the IrO$_x$ layer thickness (t$_{CL}$) and composition using

$$porosity = \frac{V_{tot} - V_s}{V_{tot}} \tag{A.1}$$

where V_{tot} is the total IrO$_x$ layer volume (= 5 cm^2× t$_{CL}$) and V_s is the solid (IrO$_x$+ionomer) volume of the IrO$_x$ layer, which is obtained from

$$V_s = \frac{m_s\,(1 - W_N)}{\rho_{IrO_x}} + \frac{m_s\,W_N}{\rho_N} \tag{A.2}$$

where m_s is the mass of the electrode, i.e., iridium oxide and Nafion, W_N is the ionomer loading, and the densities used for IrO$_x$ (ρ_{IrO_x}) and Nafion (ρ_N) are 11.66 and 2 g/cm^3, respectively.

The volume fraction of each component of the IrO$_x$ layer was calculated using

$$Volume fraction = \frac{V_i}{V_{tot}} \tag{A.3}$$

where V_i is the volume of the each component in the IrO$_x$ layer where i stands for IrO$_x$, and ionomer.

Table A.1 – Fitted parameters of the percolation model to the protonic conductivity.

	$\sigma_{bulk}^{H^+}$ [S/cm]	$\epsilon_{N_{th}}$	γ
Estimated value	0.0407	0.077	3.18
Lower bound	1×10^{-6}	0	0
Upper bound	5	0.1	10

A.2 Fitting of the conductivity data

To fit the protonic conductivity data to the percolation model, the ionomer bulk conductivity in the CL, $\sigma_{H^+}^{bulk}$, the threshold ionomer volume fraction, $\epsilon_{N_{th}}$, and the exponential factor, γ, were estimated using the $lsqcurvefit$ function in MATLAB. The ionomer volume fraction was taken as a function of the RH and the expansion of the ionomer is assumed to be the same as a Nafion membrane and was taken from Ref. 169. The Nafion volume fraction, ϵ_N, is given by (Eq. A.4).

$$\epsilon_N(\mathrm{RH}) = \epsilon_{N,dry}\left(1 + 2.536\times10^{-3}\times e^{(3.44\times10^{-2}\times\mathrm{RH})}\right) \tag{A.4}$$

where $\epsilon_{N,dry}$ is the dry ionomer volume fraction and RH is the relative humidity in %.

The estimated $\sigma_{H^+}^{bulk}$, $\epsilon_{N_{th}}$, and γ are presented in Table A.1 along with the bounds used for the fitting. The wide range of bounds were chosen to allow as much variability as possible, except for the upper ionomer volume fraction threshold which was chosen to be slightly lower than the lowest ionomer volume fraction of the IrO_x layer used for fitting in this study as loss of a percolating network was observed.

A.3 Validation of four-point collinear probe method

The in-plane (IP) electronic conductivity of IrO_x layers was measured using four-point collinear probe (4PP) method. The probe did puncture the CL as shown in Figure A.1 which is not ideal when measuring the in-plane electronic conductivity. Therefore, to validate the 4PP method, the IP electronic conductivity of different types of GDLs were determined using the 4PP method. The obtained conductivities

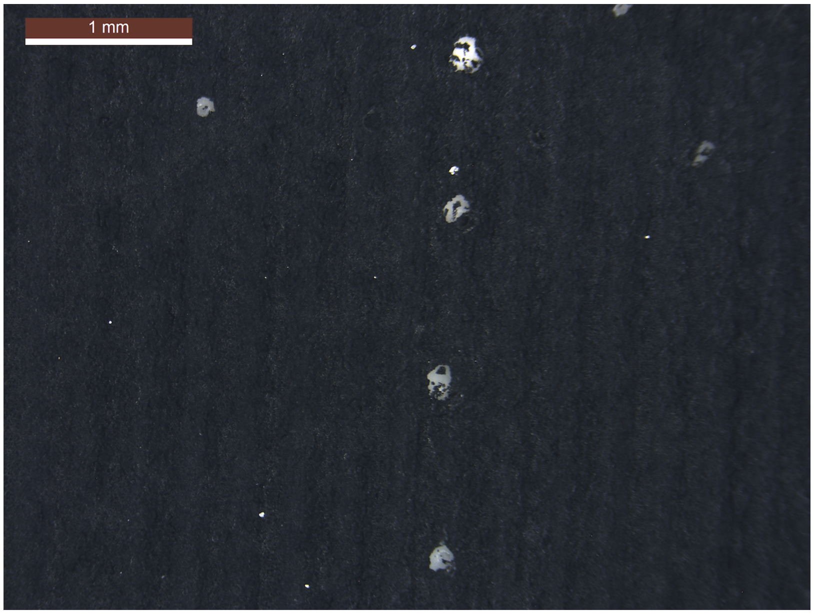

Figure A.1 – Puncture of the CL with 15 wt % ionomer loading by four-point probes.

Table A.2 – The electronic conductivity of various GDL samples using four-point collinear probe method.

GDL	Average in-plane conductivity [S/m]		
	Morris and Gostick [234]	Reported [234]	This work (average of 5 points)
Toray inc. TGP-H-090	14376 ± 156	17860	17119 ± 1839 (11%)
Freudenberg H2315-T30A	6322 ± 32	6360	5718 ± 629 (11%)
SGL-10AA	3789 ± 80	4000 [235]	3476 ± 354 (10%)

are presented in Table A.2 along with literature data. The average IP electronic conductivity results are in excellent agreement with literature data.

Next, the electronic conductivity of the carbon and ionomer layers were measured using the 4PP method. The averaged obtained IP electronic conductivity are shown in Table A.3 along with the electronic conductivities of various CLs from literature. The IP electronic conductivity in literature spreads over wide range between 0.07 to 3.9 S/cm and the measured conductivity in this work lies within this range.

Table A.3 – The electronic conductivity of the carbon and ionomer layer and Pt/C catalyst layer.

CL	Average in-plane conductivity [S/cm]	
	This work	Literature
Vulcan XC-72 IL	1.864 ± 0.359	0.07-3 [179]
Ketjen black IL	2.326 ± 0.292	
CCM from Mecedes-Bennz Fuel Cell div.		2.1 [217]
MEA from PRIMEA series 58 by W.L. Gore & Associates, Inc.		3.2 ± 0.2 [236]
CCM (20 %wt. Pt/C$_{E-tek}$)		0.25-2.25 [180]
CCM (20 %wt. Pt/C$_{Vul.XC-72}$)		0.9-3.9 [177], 1.3 [237]
Pt/C CL		0.1-1.1 [178]
Denkablack (Denki Kagaku Kogyo) IL		0.28 [238]

A.4 Reactive pathway through IL

Figure A.2 shows the two potential pathways for protons to transverse the IL. In the ohmic pathway, protons generated in the anode catalyst layer (ACL) simply cross the IL in accordance with Ohm's Law. A corresponding Ohmic resistance across the IL can be obtained, and used to find the conductivity of the layer. In the reactive pathway, protons reaching the IL near the ACL side undergo the hydrogen evolution reaction. The evolved hydrogen then crosses the IL, and is oxidised at other side of the IL near the CCL. The produced protons continue across the membrane to the CCL, while the electrons travel back to the ACL side of the IL to take part in the evolution reaction. For a highly conductive support and highly active catalyst, such as the Pt—C catalyst layers used in PEMFCs, the reactive pathway could dominate the Ohmic pathway during the hydrogen pump experiment and in effect disguise the protonic resistance of the IL. While Iden et al. [169, 170] could remove the catalyst from their IL and still obtain conductivities that would be representative of a PEMFC CL, this is not possible for the unsupported catalysts that are used in PEMWE. Therefore, numerical modelling is used to investigate whether the reactive pathway is active in this work.

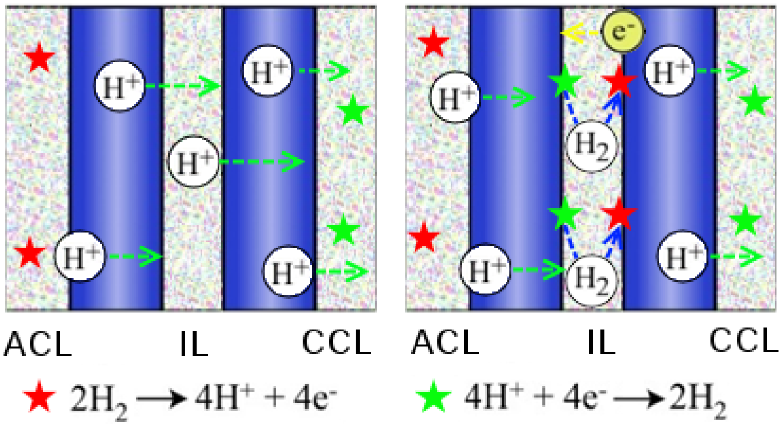

Figure A.2 – Left: Ohmic pathway for protons through the IL. Right: reactive pathway via the hydrogen reactions.

A.5 Model description

The hydrogen pump model developed was based on the PEMFC model published by Secanell et al. [219], however as the current densities simulated are small and the diffusion coefficient of hydrogen is large, mass transport effects are not considered and the transport of the gaseous species was not solved for. Further, since the model is used for a hydrogen pump instead of a fuel cell, both cathode and anode are fed with humidified hydrogen, and the hydrogen reduction and oxidation reactions are considered using a Butler-Volmer model with the kinetic parameters as shown in Table A.4. The governing equation used are:

$$\begin{aligned} \nabla \cdot (\sigma_m^{eff} \nabla \phi_m) &= S_m && \text{(A.5)} \\ \nabla \cdot (\sigma_s^{eff} \nabla \phi_s) &= S_s && \text{(A.6)} \\ \nabla \left(n_d \frac{\sigma_m^{eff}}{F} \nabla \phi_m + \frac{\rho_{dry}}{EW} D_\lambda^{eff} \nabla \lambda \right) &= -S_\lambda && \text{(A.7)} \end{aligned}$$

where the source terms, S_i, are the same as those used in Ref. 219. The solution variables are the potentials of the solid and ionomer phase, ϕ_m and ϕ_s, and the ionomer water content, λ. The computational domain simulated is shown in Figure A.3.

The model parameters used in this work are given in Table A.4. The parameters shown are limited to those that have the biggest impact on the performance, namely

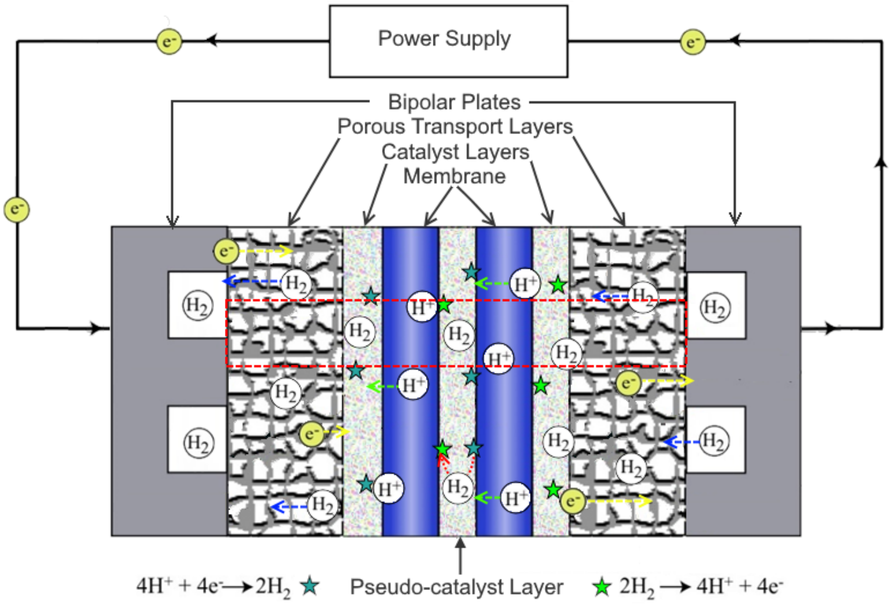

Figure A.3 – Cell configuration showing the pseudo-catalyst layer. The simulation domain is shown in the dashed red box.

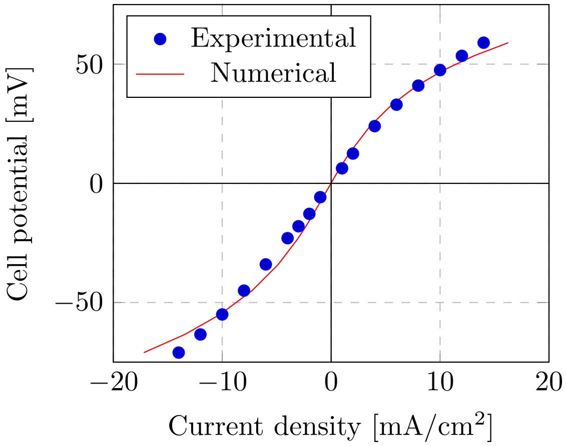

Figure A.4 – Polarization curve for the hydrogen pump test on the electrolyzer cell.

those related to the electron and proton transport in the intermediate layer, membranes, and the anode and cathode CL, and those related to kinetics. The kinetic parameters for the intermediate layer were determined by performing a hydrogen pump test using chronopotentiometry on an electrolyzer cell in order to obtain a polarization curve. One electrode was comprised of a Pt/C and the other was IrO_x. The operating conditions were 100% RH, 1 atm and 80 ℃. The performance, shown in Figure A.4, was significantly worse than that shown in Figure **??**b, despite the absence of the second membrane and the intermediate layer, indicating that hydrogen reaction is severely limited on the IrO_x catalyst. The Butler-Volmer equation was fit to the entire data range, as the overpotential from the cell resistance was negligible under these current densities. The anodic and cathodic transfer coefficients and the exchange current density were from fitting using *LibreOffices DEPS* fitting software. The electrochemical surface area was obtained from a voltammogram using the methodology from Tan et al. [96], while the hydrogen concentration is determined based on the partial pressure of 80% RH hydrogen gas dissolving into a infinitely thin ionomer film, according to Henry's Law.

Table A.4 – Model parameters used in the simulations. All parameters were measured in this work, unless otherwise stated.

Parameter	Value
Membrane thickness	25 μm
Membrane conductivity	0.106 S/cm
IL thickness	4 μm
IL electronic conductivity	$4.5\text{x}10^{-5}$ S/cm
IL protonic conductivity	$4.2\text{x}10^{-3}$ S/cm
IL exchange current density	$2.51\text{x}10^{-6}$ A/cm^2_{Pt}
IL active area	$1.8\text{x}10^{6}$ cm^2/cm^3
IL cathodic transfer coefficient	0.965
IL anodic transfer coefficient	1.15
IL Equilibrium potential	0.00025 V
IL Reference hydrogen concentration	$8.06\text{x}10^{-7}$ mol/cm^3
ACL/CCL thickness	4.3 μm
ACL/CCL kinetic parameters	Elbert et al. [220]
ACL/CCL active area	$1.26\text{x}10^{5}$ cm^2/cm^3
ACL/CCL protonic conductivity	$8.04\text{x}10^{-3}$ S/cm
Temperature	80 ℃
Anode/Cathode pressure	1 atm
Relative humidity	80 %

A.6 Electrochemical impedance spectroscopy (EIS)

Galvanostatic EIS measurements were performed on an electrolyzer cell, with an IrO_x catalyst with 35 wt % ionomer content. Figure A.5 shows the obtained impedance spectra of the electrolyzer cell. The measured HFR is 50.362 m$\Omega\cdot$cm^2.

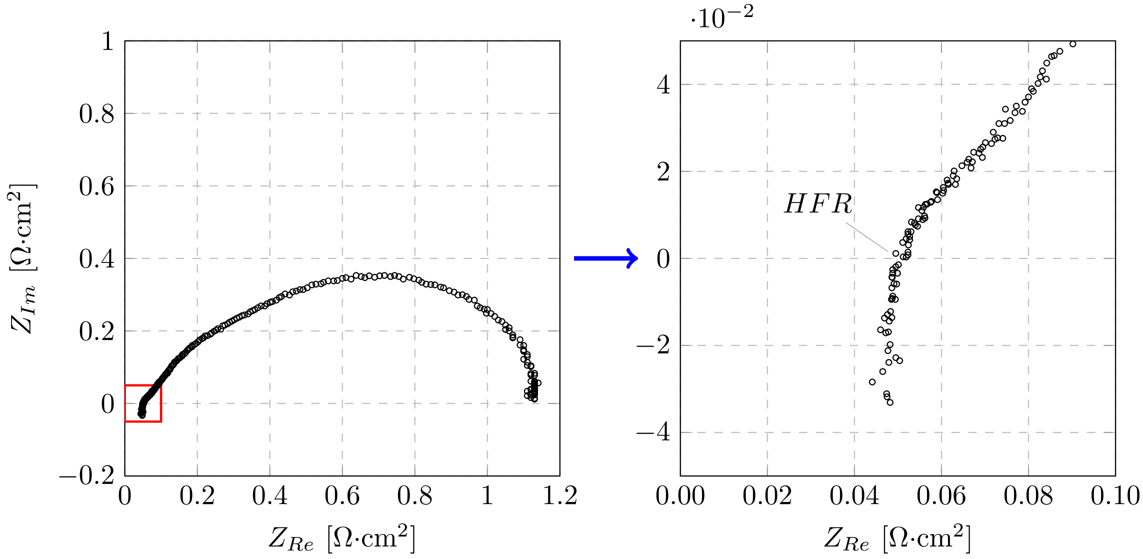

Figure A.5 – Impedance spectra at 0.02 A/cm^2 of an electrolyzer cell.

Appendix B

Improving PEMWE performance by using carbon as pore former

B.1 Ir CL

B.1.1 Catalyst layer porosity

The porosity of the catalyst layer (CL), ϵ, was calculated based on the CL thickness (t_{CL}) and the catalyst ink composition using

$$\epsilon = \frac{V_{\mathrm{tot}} - V_{\mathrm{s}}}{V_{\mathrm{tot}}} \tag{B.1}$$

where V_{tot} is the total CL volume (i.e., 5 $\mathrm{cm}^2 \times$ t_{CL}) and V_{s} is the total solid volume of the CL, which is computed using,

$$V_{\mathrm{s}} = \frac{m_{\mathrm{s}}\,(1 - w_{\mathrm{N}} - w_{\mathrm{C}})}{\rho_{\mathrm{cat}}} + \frac{m_{\mathrm{s}}\,w_{\mathrm{N}}}{\rho_{\mathrm{N}}} + \frac{m_{\mathrm{s}}\,w_{\mathrm{C}}}{\rho_{\mathrm{C}}} \tag{B.2}$$

where m_{s} is the mass of the electrode, w_{N} is the ionomer loading, w_{C} is the carbon loading, and the densities used for catalyst (ρ_{cat}) are 22.65 g/cm^3 for Ir, 11.66 g/cm^3 for IrO$_x$, and for carbon (ρ_C) and Nafion (ρ_{N}) are 2.2 and 2 g/cm^3, respectively.

It is expected that carbon will quickly corrode at high potentials, therefore, the porosity is also estimated without carbon by computing the solid volume without carbon as,

$$V_{\mathrm{s}} = \frac{m_{\mathrm{s}}\,(1 - w_{\mathrm{N}})}{\rho_{\mathrm{cat}}} + \frac{m_{\mathrm{s}}\,w_{\mathrm{N}}}{\rho_{\mathrm{N}}} \tag{B.3}$$

Table B.1 – Iridium catalyst layer thickness before and after normalizing with catalyst loading and porosity.

	CL thickness		Porosity [%]	
	[μm]	[μm/(mg/cm^2)]	w/ carbon	w/o carbon
	New | Used	New | Used	New | Used	New | Used
CCM-C0-Ir	3.13±0.37 | 2.69±0.33	3.17±0.37 | 2.73±0.33	58±4.7 | 51±5.4	58±4.7 | 51±5.4
CCM-C0.1-Ir	4.86±0.60 | 4.37±0.81	4.88±0.60 | 4.39±0.81	68±4.4 | 65±6.8	71±4.4 | 68±6.8
CCM-C0.2-Ir	6.26±0.77 | 4.91±1.12	6.01±0.77 | 4.72±1.12	72±4.3 | 63±8.9	77±4.3 | 70±8.9

Table B.1 shows the measured normalized CL thickness of new and post operation CLs.

B.1.2 Dynamic light scattering (DLS)

To understand the interaction between the Ir catalyst particle/carbon with ionomer, DLS tests were conducted on the prepared inks to find a correlation between particle size and the CL thickness. A Litesizer 500 by Anton Paar was used for conducting the DLS experiments. The inbuilt Kalliope software was used to input parameters, such as viscosity and refractive index of solvents, and to record the data. Approximately 1 mL of catalyst ink was placed within a quartz cuvette and inserted in the Litesizer, and a temperature of 32 °C was maintained. The particle size was analyzed at an angle of 175°. Five consecutive tests were conducted on successive days.

Figure B.1a shows the variation of particle hydrodynamic diameter with successive tests. The variation in diameter between dais is within the standard deviation of the samples. Figure B.1b shows the variation of particle diameter with carbon content. DLS results to not show a strong correlation between particle diameter and carbon content.

B.1.3 Cyclic voltammetry

Figure B.2 shows the voltammograms obtained for three CCMs each with Ir catalyst and without carbon, and with carbon to total volume fraction of 0.2 before and after the polarization curve. The voltammograms showed a good repeatability.

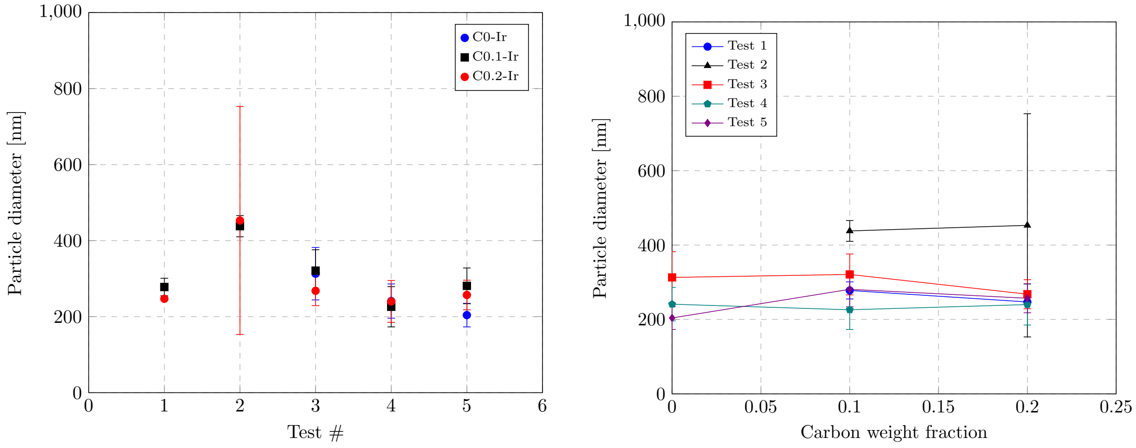

(a) **(b)**

Figure B.1 – Particle diameter of the fresh inks with successive tests (a). Variation of particle diameter of the fresh with carbon content (b).

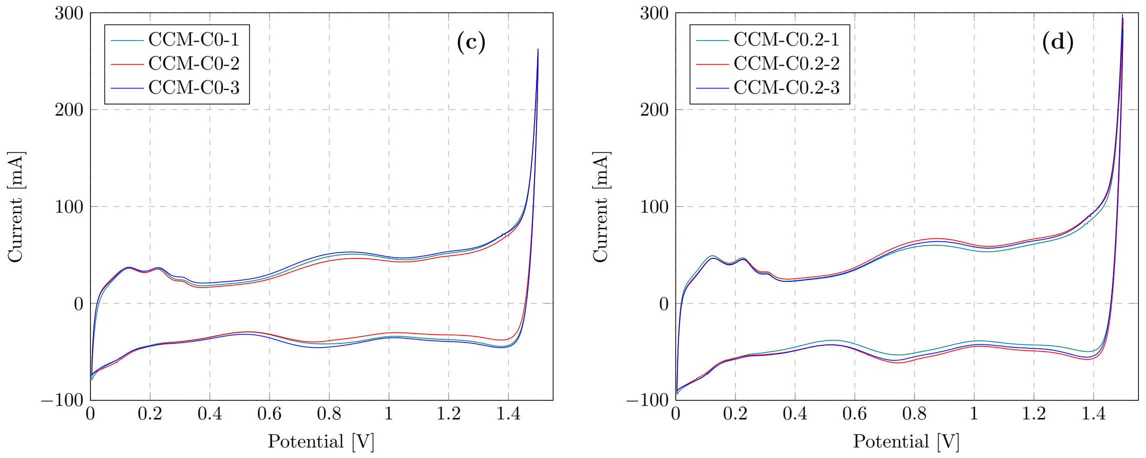

Figure B.2 – Repeatability of the voltammograms after the polarization curve (a) CCM-C0, (b) CCM-C0.2.

B.1.3.1 Measurement of electrochemical surface area

In order to calculate the ECSA after the polarization curve, an alternative method was used. Tan et al. [96] showed that for Ir catalyst, during cycling there was a decrease in the hydrogen underpotentially deposited (HUPD) charge in the CV profiles that coincides with a corresponding increase in anodic charge between 0.4 and 1.25 V, which is also shown later in this section. Therefore, to obtain an accurate ECSA both integral charges needed to be analyzed to obtain the total ECSA. The ECSA after the polarization curve, $ECSA^{\text{After iV}}$, accounted for the HUPD change and the difference in the anodic charge between 0.4 and 1.25 V before and after the polarization curve. Equation (B.4) was used to calculate the ECSA after the polarization curve.

$$ECSA^{\text{After iV}} = ECSA^{\text{After iV}}_{\text{HUPD}} + \frac{\left(Q^{\text{After iV}}_{\text{deprotonation}} - Q^{\text{Initial}}_{\text{deprotonation}}\right)}{q_{\text{deprotonation}}} \tag{B.4}$$

where $Q^{\text{Initial}}_{\text{deprotonation}}$ is the anodic charge of the CV profiles in the potential range of 0.4 to 1.25 V after conditioning as shown by the orange shaded region in Figure B.3a, $Q^{\text{After iV}}_{\text{deprotonation}}$ is the anodic charge of the CV profiles in the potential range of 0.4 to 1.25 V after the polarization curve as shown by the orange shaded region in Figure B.3b, and $q_{\text{deprotonation}}$ is the charge constant associated with the anodic processes between 0.4 and 1.25 V, estimated to be 440 ± 14 $\mu\text{C/cm}^2_{\text{ECSA}}$ [96].

The calculated ECSA after conditioning the cell and after the polarization curve are shown in Table B.2, where it can be observed that the initial ECSA ($ECSA^{\text{Initial}}$) and the ECSA after the polarization curve ($ECSA^{\text{After iV}}$) are similar in value, verifying the methodology developed by Tan et al. [96] can also be utilized for an MEA. The ECSA after the polarization was similar to the initial, indicating that all the carbon was likely oxidized during conditioning.

To test the impact of increased potential cycling and the applicability of using Equation (B.4) to find the ECSA, a CCM with Ir in the anode and a 5 wt.% ionomer loading and without carbon was cycled between 0.005-1.53 V 240 times at a scanrate of 500 mV/s. Figure B.4a shows the evolution of the voltammograms. Under these conditions, the H_{upd} peak was completely removed, with a corresponding increase in the anodic charge in the potential range of 0.4 to 1.25 V, as observed in ref. [96], indicating the metallic Ir is oxidizing slowly. The ECSA of the cycled CCM was

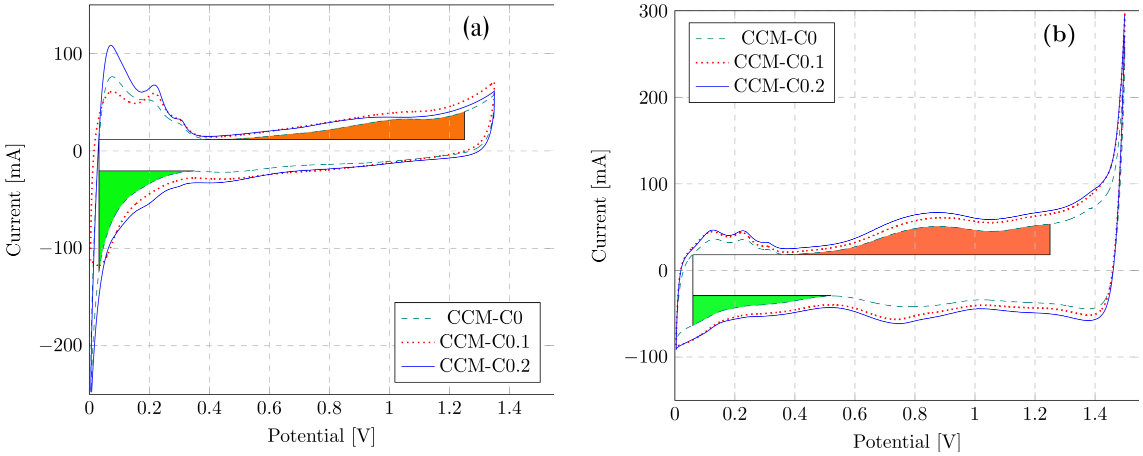

Figure B.3 – Voltammograms of CCMs with varying carbon content. Voltammograms after conditioning of the cells (a), and after the polarization curve (b) (The voltammograms of CCM-C0 and CCM-C0.2 are the average of three voltammograms with an average standard deviation of 2.4 mA).

Table B.2 – Electrochemical surface area (m^2/g) before and after the polarization curve.

CCM name	$ECSA^{\text{Initial}}$	$ECSA^{\text{After iV}}_{\text{Hupd}}$	$\Delta ECSA^{\text{After iV}}_{\text{Deprotonation}}$	$ECSA^{\text{After iV}}$
CCM-C0-Um	21.5 ± 1.2	14.2 ± 1.1	8.1 ± 0.2	22.4 ± 1.3
CCM-C0.1-Um	25.0	14.4	10.0	24.4
CCM-C0.2-Um	26.9 ± 0.2	16.5 ± 0.4	11.1 ± 0.8	27.5 ± 0.8

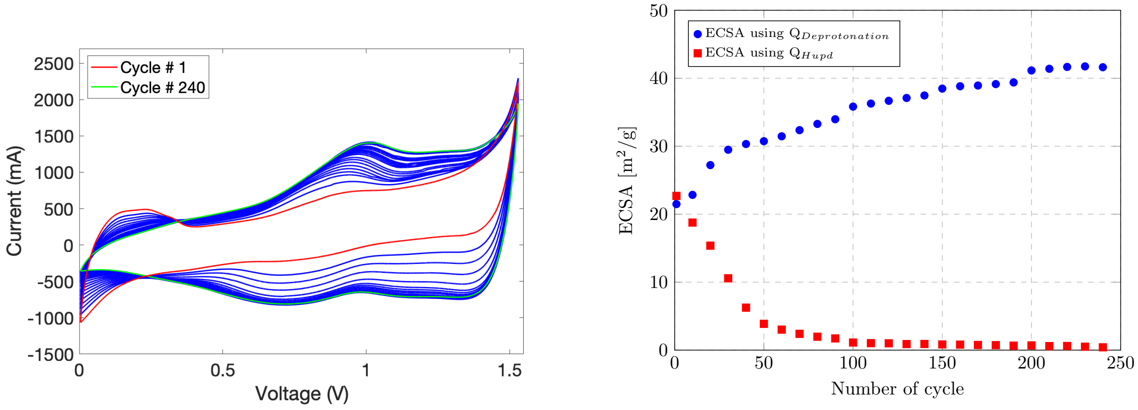

(a) **(b)**

Figure B.4 – Evolution of voltammograms (a), and the electrochemical surface area with cycle (b).

calculated using the integral charges of underpotentially deposited hydrogen of the CV profiles in the potential range of 0 to 0.5 V ($ECSA_{\text{HUPD}}$) and total anodic charges of the CV profiles in the potential range of 0.4 to 1.25 V ($ECSA_{\text{Deprotonation}}$) over the 240 potential cycles, as shown in Figure B.4b. The $ECSA_{\text{HUPD}}$ diminished from 21 to ∼0 m^2/g, while the $ECSA_{\text{Deprotonation}}$ increased from 21 to 42 m^2/g. This result is in agreement with that observed by Tan et al. [96], whereby the ECSA 'lost' in the HUPD region is replaced by that in the anodic charge in the potential range of 0.4 to 1.25 V and confirms the applicability of using Equation (B.4) to calculate the ECSA of a partially oxidized CL.

B.2 IrO_x CL

The anode catalyst inks were prepared by mixing 179 mg of IrO_x (ELC-0110, Tanaka Kikinzoku International (TKK)) and the carbon (Vulcan XC-72, 590106, Fuel Cell Store) with a mixture of isopropanol (IPA) (CAS: 67-63-0), propylene glycol (PG) (CAS: 57-55-6, Sigma-Aldrich), and Nafion solution (Liquion solution LQ-1105 1100EW 5 wt.%, Ion Power) following the process discussed in Chapter 2. The carbon content in the anode catalyst ink was varied, such that the carbon to IrO_x volume

Table B.3 – Composition of IrO_x catalyst layers and MEA configuration.

CCM	Cells tested	C to IrO_x vol. frac.	Cat. load. [mg/cm^2] IrO_x | Pt	Naf. load. [wt.%] An | Cath	MEA configuration PTL | ACL | PEM | CCL | GDL
CCM-C0-IrOx	2	0	0.99 | 0.12	35 | 30	Sin. Ti | IrO_x | N211 | Pt/C | 28BC
CCM-C0p1-IrOx-1	1	0.1	0.81 | 0.11	35 | 30	Sin. Ti | IrO_x | N211 | Pt/C | 28BC
CCM-C0p1-IrOx-2	1	0.1	0.99 | 0.1	35 | 30	Sin. Ti | IrO_x | N211 | Pt/C | 28BC
CCM-C0p25-IrOx	1	0.25	0.80 | 0.1	35 | 30	Sin. Ti | IrO_x | N211 | Pt/C | 28BC
CCM-C0p53-IrOx	0	0.53	0.69 | 0.1	35 | 30	–

fraction varied between 0 and 0.53. The ratio of IPA and PG in the ink was varied to maintain a constant solid volume fraction in the final ink. Ionomer was added to the inks to achieve a loading of 35 wt.%. The carbon content was varied due to the different densities of the catalyst and the different ionomer loading in the anode CL.

The ink was deposited in an NRE211 membrane with the same cathode as the Ir cells and sandwiched between a Ti sinter and a SGL 28BC GDL. Details of the cell configuration are provided in Table B.3.

B.2.1 SEM characterization

Figures B.5 and B.6 show SEM images of the new and post operation IrO_x CL cross-section. The measured CL thicknesses are presented in Table **??**. The normalized thickness of IrO_x CLs increased with an increase in the carbon content. The porosity of the CLs increased with an increase in the carbon content. The porosity of the new IrO_x CLs is lower than the Ir CLs despite having a higher CL thickness due to a higher ionomer content of IrO_x CLs than Ir CLs. The higher ionomer content occupied the pore volumes of the CL, making it less porous.

Figure B.7 shows a comparison of the cross-sectional SEM images of Ir and IrO_x CLs after operation. It can be observed that the IrO_x CL was deformed from the compression due to the use of sintered Ti PTL. But, hardly any deformation can be

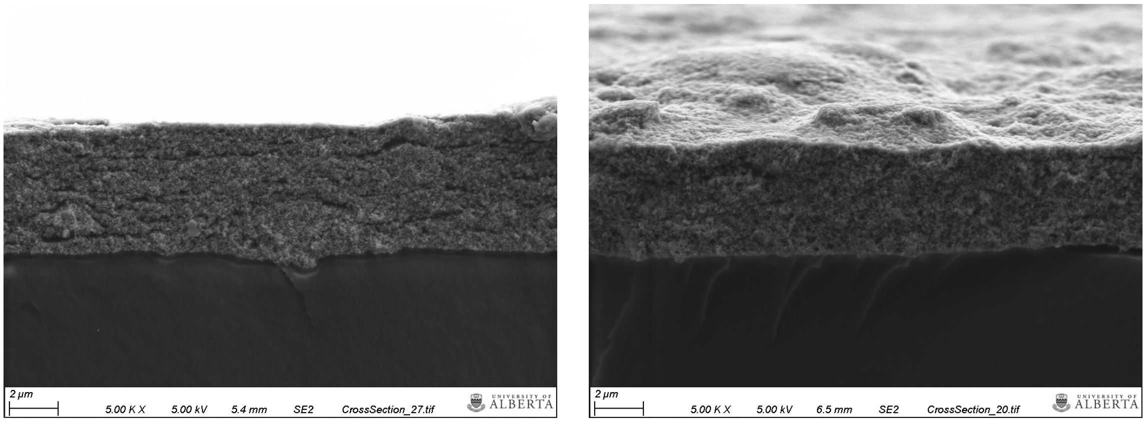

(a) New CCM-C0-IrOx **(b)** New CCM-C0.1-IrOx

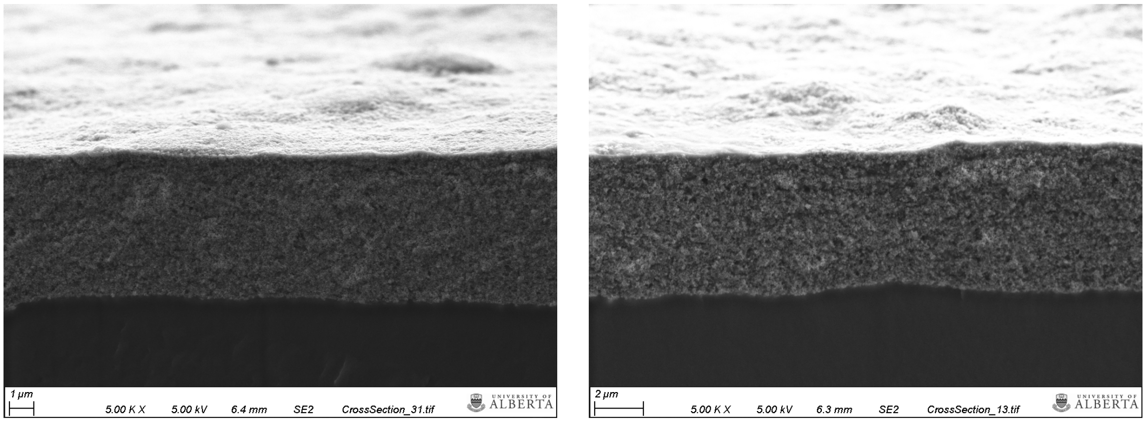

(c) New CCM-C0.25-IrOx **(d)** New CCM-C0.53-IrOx

Figure B.5 – Cross-section SEM images of new catalyst layers with IrO_x catalyst.

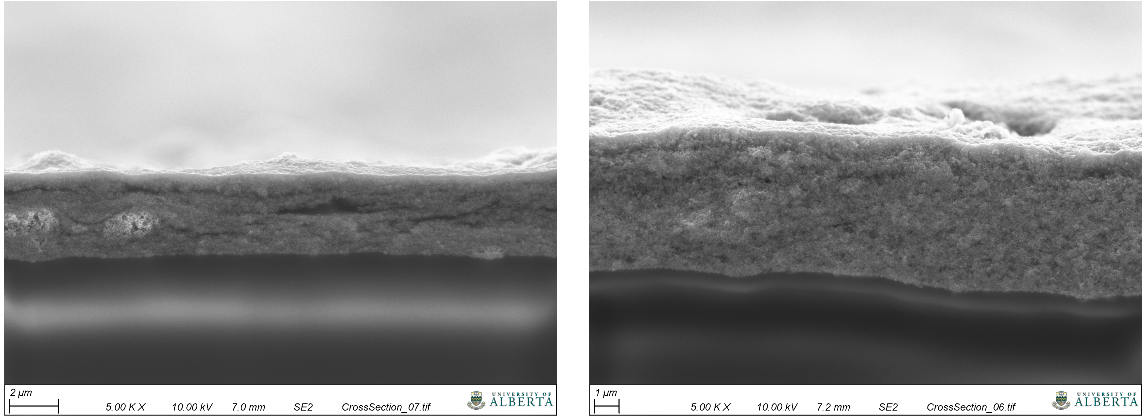

(a) **(b)**

Figure B.6 – Cross-section SEM images of used CCM-C0-IrOx (a), and CCM-C0.25-IrOx (b).

observed in the Ir CL where Pt coated Ti felt was used. The different membrane thickness might have contributed to the differences.

The measured thickness of the IrO_x CLs is shown in Table B.4. The normalized thickness of CLs increased with an increase in the carbon content. The normalized thickness of IrO_x CL is higher than the Ir CLs for a given carbon content. This might be due to either the higher ionomer loading in the IrO_x CL or the Ir particle morphology, which is not particulate like IrO_x, but a flake-like [96]. The porosity of the IrO_x CLs increased with an increase in the carbon content. For the post-operation cells (used), the SEM images of the CL under the channel, rather than the land, were used to measure the thickness of the used TKK CLs.

Figure B.8 shows the SEM images of new IrO_x CL surface. Many cracks were seen in the new IrO_x CLs without carbon (Figure B.8b). The number of cracks decreased with increasing carbon content (Figure B.8f). Due to the cracks, the porosity of the CL without the carbon might be even lower.

Figure B.9 shows the surface SEM images of the post operation IrO_x CLs. Two significant regions can be observed; i) a relatively smooth surface area under the channel, and ii) a relatively uneven surface area under the land. A lot of catalysts is lost in areas under the land of the CL with carbon to IrO_x volume ratio of 0.25. This might be due to: i) a higher content of carbon in the CL which, when corroded, led

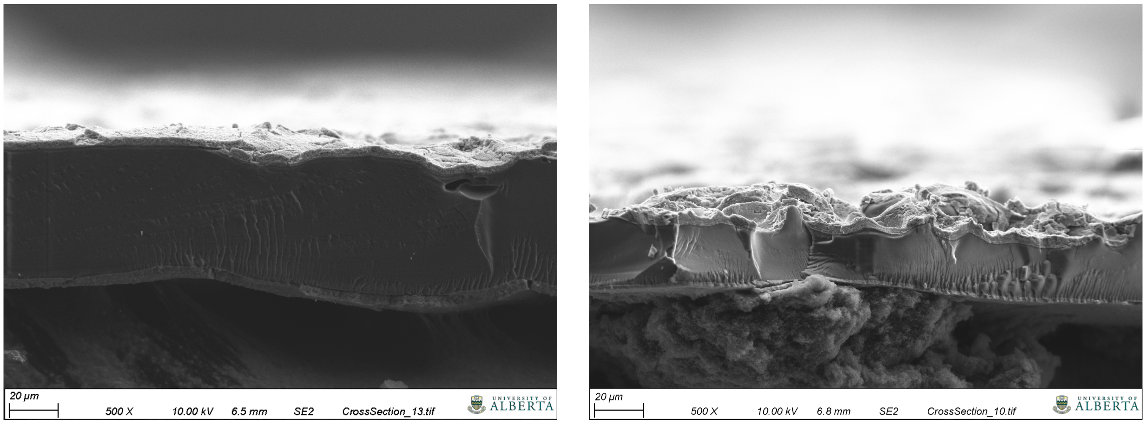

(a) Used CCM-C0-Um **(b)** Used CCM-C0-TKK

Figure B.7 – Comparison of the cross-sectional SEM image of used Umicore CL vs used TKK Cl.

Table B.4 – IrO_x catalyst layer thickness before and after normalizing with catalyst loading and porosity..

	CL thickness		Porosity [%]	
	[µm]	[µm/(mg/cm^2)]	w/ carbon	w/o carbon
	New | Used	New | Used	New | Used	New | Used
CCM-C0-IrOx	4.58±0.59 | 4.38±0.65	4.64±0.59 | 4.44±0.65	23±11 | 20±15	23±11 | 20±15
CCM-C0.1-IrOx-1	4.06±0.50 | 3.7±0.34	5.06±0.50 | 4.62±0.34	27±9.5 | 20±9.3	29±9.5 | 20±9.3
CCM-C0.25-IrOx	5.23±1.01 | 4.61±0.45	6.58±1.01 | 5.78±0.45	41±10 | 33±6.3	44±10 | 37±6.3
CCM-C0.53-IrOx	6.43±0.87 | –	9.46±0.87 | –	46±7.5 | –	52±7.5 | –

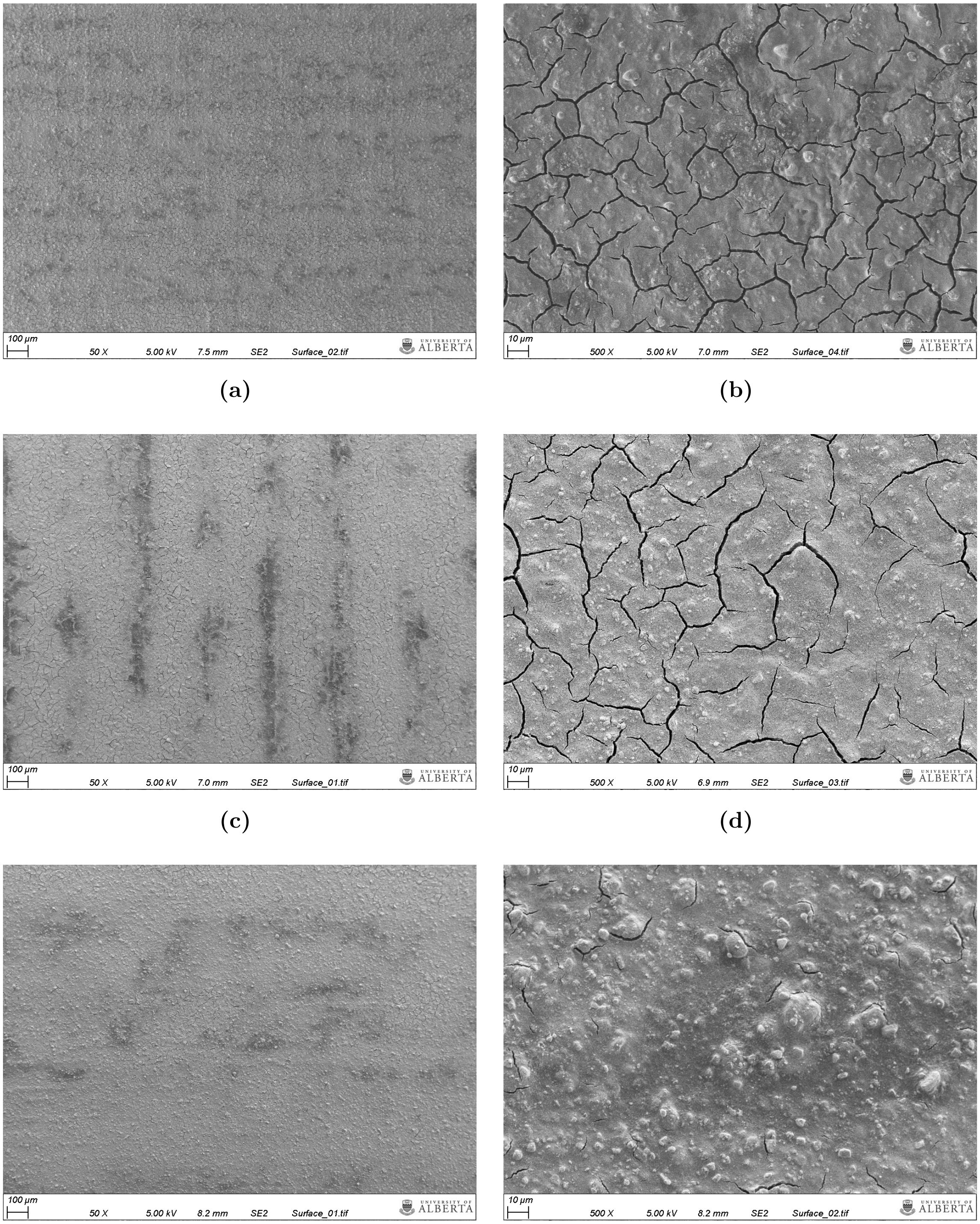

(a) **(b)**

(c) **(d)**

(e) **(f)**

Figure B.8 – SEM surface images of CCM-C0-TKK (a) and (b), CCM-C0.1-TKK (c) and (d), and CCM-C0.25-TKK (e) and (f).

to dislodgement of catalyst particles, ii) the removal of the PTL from the CCM for imaging purpose which peeled some portion of the CL. Since the CL was not peeled off the PEM for low carbon content, the latter shows that there might be an upper carbon content above which the structural integrity of the CL is reduced. The star patterned cracks observed in the Ir CL without carbon were not formed in the IrO_x CL, despite having a lower CL porosity than the Ir CL. This might be due to the protonic conductivity of the IrO_x CL being higher than the electronic (see Chapter 3), resulting in the OER being more active at the CL–PTL interface and hence there is no need for the oxygen gas bubble to travel through the CL. Therefore, star patterned cracks were not formed in the IrO_x CL even with the lower porosity than the Ir CL without carbon.

B.2.2 Measurement of electrochemical surface area

Figure B.10 shows the voltammograms obtained for two cells with the IrO_x catalyst and without carbon for repeatability, and a comparison of voltammograms with varying carbon. The voltammograms of cells with the IrO_x catalyst and without carbon showed a good repeatability.

The ECSA of IrO_x CLs were calculated using Equation B.4, where the HUPD area was considered negligible. The ECSA increased and then decreased with an increase in the carbon content. This indicates that there is an optimum carbon to catalyst volume ratio for which the ECSA is maximized. The initial increase is expected due to the increase in the CL porosity, leading to an exposure of a higher surface area. However, the subsequent decrease in the ECSA is not expected and may have been caused by detachment of the catalyst particles from the CL during the corrosion of the carbon. This is reflected in the surface SEM images of the post operation IrO_x CL with carbon to IrO_x volume ratio of 0.25.

B.2.3 Polarization curve

Two cells with IrO_x without and with 10%vol. carbon were tested to assess repeatability. Figures B.11a and B.11b show the cells had good reproducibility, with an average standard deviation of 10 mV. The difference in the cell repeatable perfor-

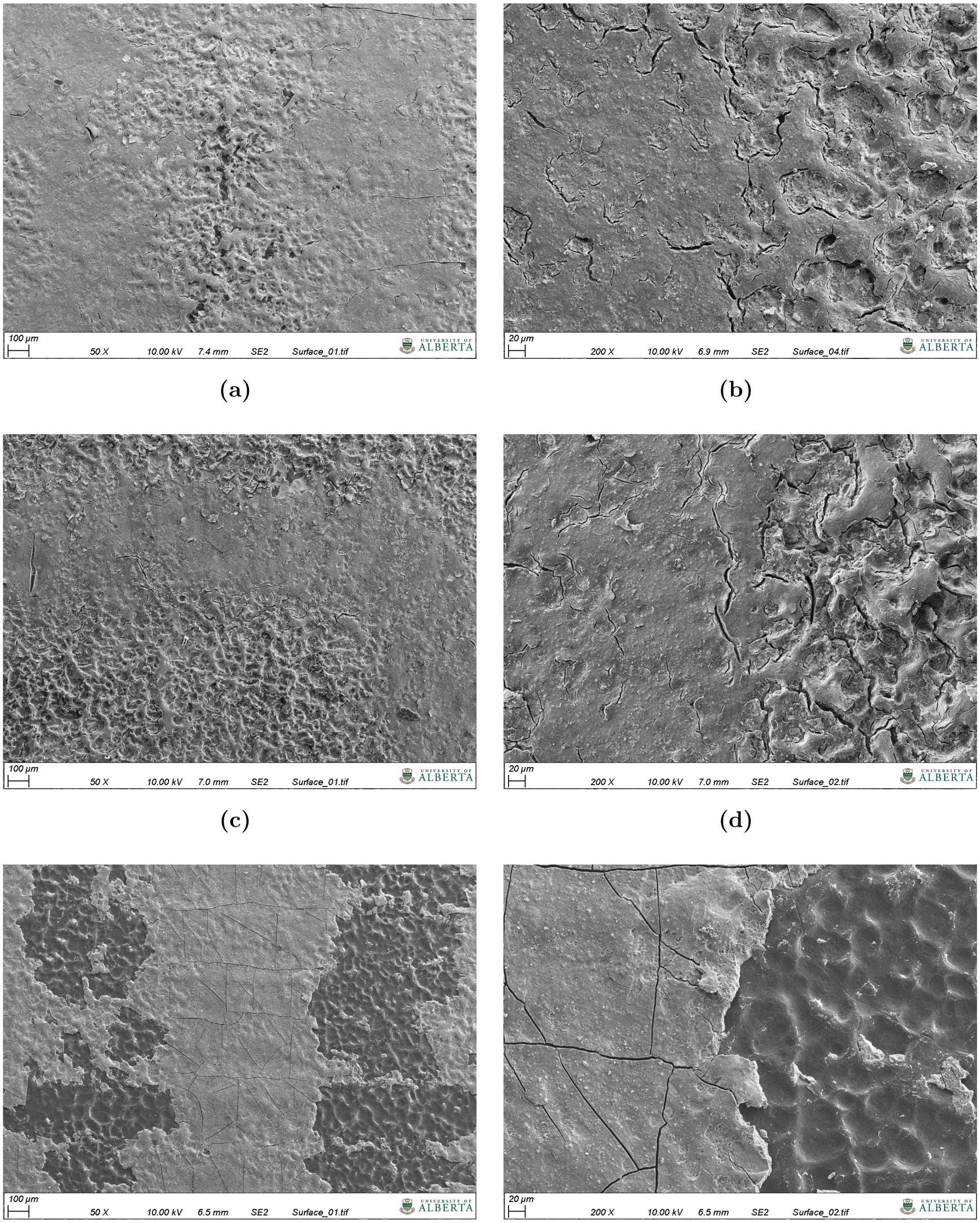

(a) **(b)**

(c) **(d)**

(e) **(f)**

Figure B.9 – Comparison of the surface SEM images of the used CCM-C0-TKK (a) and (b), CCM-C0.1-TKK (c) and (d), and CCM-C0.25-TKK (e) and (f).

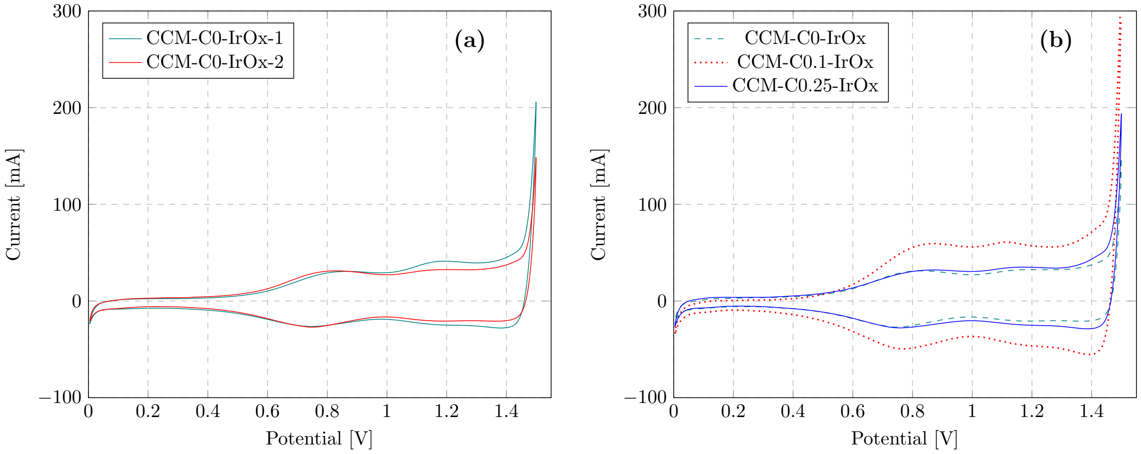

Figure B.10 – Repeatability of the voltammograms of CCM-C0-IrOx (a), Voltammograms of CCMs with varying carbon content (b) (The voltammogram of CCM-C0-IrOx in (b) is the average of two voltammograms).

Table B.5 – Electrochemical surface area of IrO_x catalyst layers.

CCM name	ECSA (m^2/g)
CCM-C0-IrOx	28 ± 2
CCM-C0.1-IrOx-1	50
CCM-C0.25-IrOx	30

mance is due to differences in the activation region of the polarization curve. This might be due to the use of used sintered Ti PTL after sonicating it in IPA.

Figure B.11c shows the comparison of polarization curves with varying carbon content. In the activation region, the performance of the cell with carbon to IrO_x volume fraction of 0.1 (CCM-C0.1) is better than the cell without the carbon (CCM-C0) and cell with carbon to IrO_x volume fraction of 0.25 (CCM-C0.25), which follows the trend of the ECSA. In the Ohmic region, the slopes of the polarization curve increased with an increase in the carbon content. This trend follows that of the CL thickness with increasing carbon content, and is likely caused by the resistance of the anode CL, as is discussed in Section B.2.4. As the electronic conductivity is two orders of magnitude lower than the protonic conductivity of the IrO_x CL with 35 wt.% ionomer loading, the OER is more active near the anode CL–PTL interface, resulting in protons having to travel across the entire CL thickness. Hence, the thicker the CL, the higher the resistance, therefore the performance of the cell without the carbon (CCM-C0) is better than the other two cells at higher current densities. As such, the use of a pore former with a CL that is electron transport limited might not be suitable when the cell is operated at a higher current density, as the increased thickness will induce additional Ohmic losses, negating any improvement from the improved ECSA and mass transport. This can be avoided if a thinner CL with high CL porosity is used. Hence, care should be taken when using the pore former with IrO_x catalyst, as there will be a trade-off between the Ohmic and kinetic losses.

B.2.4 Electrochemical impedance spectroscopy (EIS)

Figures B.12 shows the Nyquist plots obtained from EIS tests. The fitted parameters are given in Table B.6. The HFR increased with an increase in the carbon content, which might be due to a higher CL thickness with increasing carbon content. The HFR includes the CL resistance of the more conductive phase [225]. In the case of CL with 35 wt.% ionomer loading, protonic and electronic conductivities are low, thereby being a significant contributor to HFR. Furthermore, based on our previous results, protonic conductivity is higher, therefore proton transport resistance of the CL is included in the HFR. The thicker the CL, the higher the CL resistance and, as

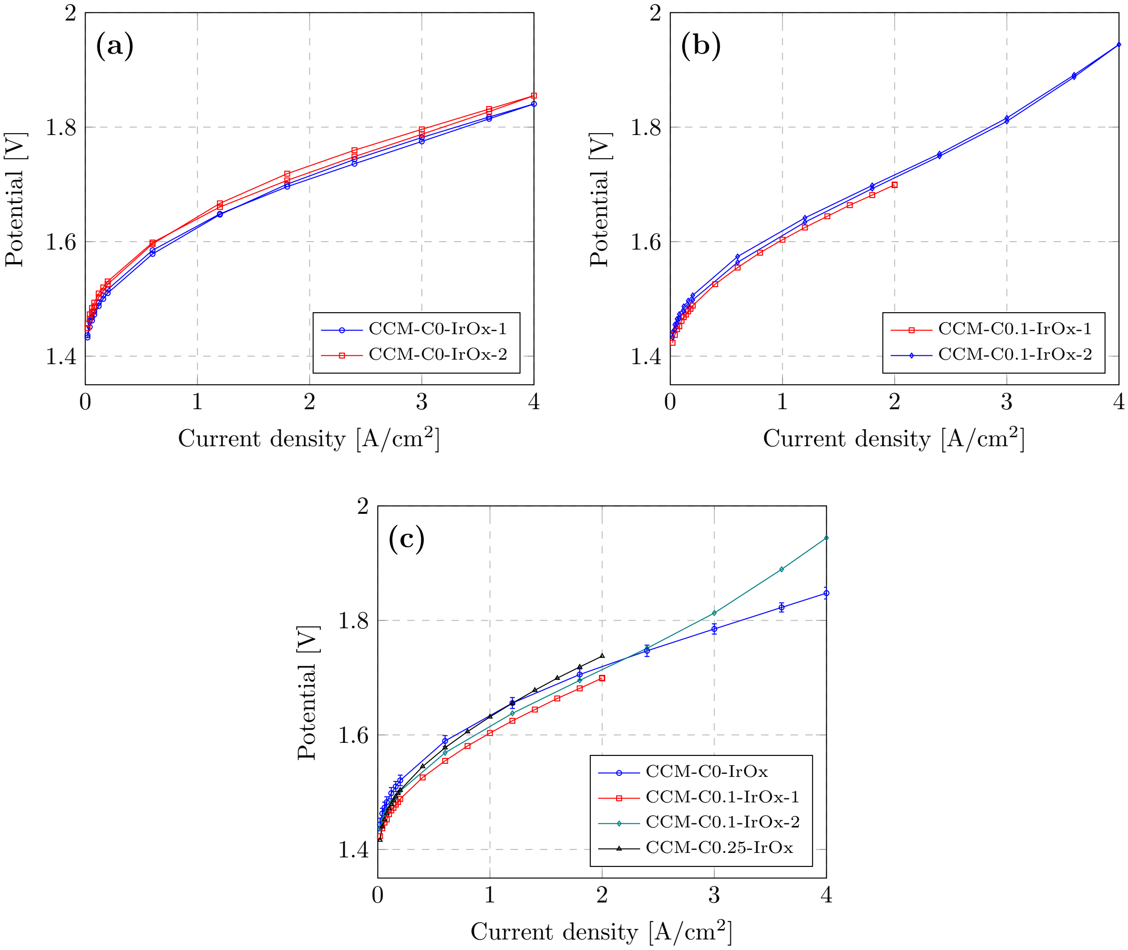

Figure B.11 – Repeatability of the polarization curves CCM-C0-IrO$_x$ (a), and CCM-C0.1-IrO$_x$ (b). Comparison of polarization curves of cells with varying carbon content (c).

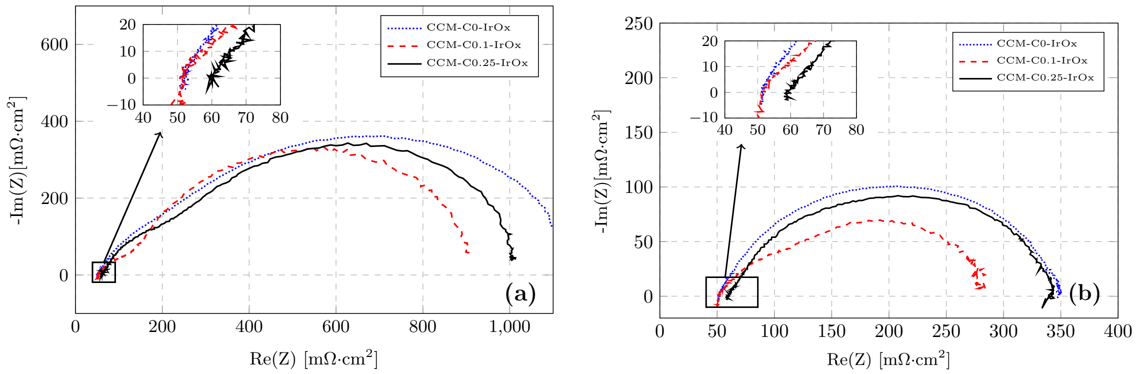

(a) @ 0.02 A/cm^2 **(b)** @ 0.1 A/cm^2

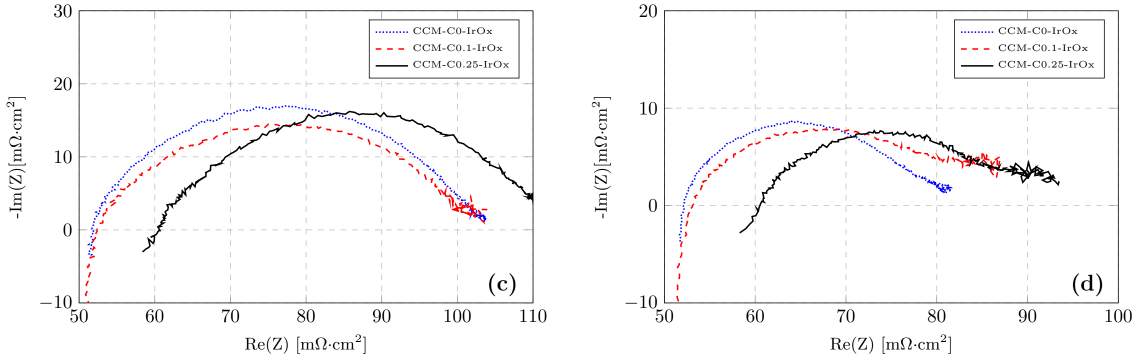

(c) @ 1 A/cm^2 **(d)** @ 2 A/cm^2

Figure B.12 – Nyquist plot of cells with TKK IrO$_x$ catalyst.

a result, the HFR, despite contact resistance improvements.

The obtained total charge transfer resistance decreased initially and then increased with an increase in the carbon content, in line with the obtained ECSA.

Table B.6 – Parameters of the equivalent circuit fitted to the impedance spectra of CCMs with IrO_x catalyst.

CCM name	J [A/cm^2]	HFR [mΩ·cm^2]	R_{ct1} [mΩ·cm^2]	Q_{dl1} [s^n/(Ω·cm^2)]	n_1	R_{ct2} [mΩ·cm^2]	Q_{dl2} [s^n/(Ω·cm^2)]	n_2
CCM-C0-IrOx	0.02	50.6	379.6	0.075	0.69	708.5	0.087	0.91
CCM-C0.1-IrOx	0.02	50.2	114.4	0.12	0.64	760.5	0.162	0.90
CCM-C0.25-IrOx	0.02	60.6	277.3	0.065	0.72	680.3	0.098	0.95
CCM-C0-IrOx	0.1	51.4	76.2	0.082	0.76	223.4	0.052	0.80
CCM-C0.1-IrOx	0.1	50.8	98.6	0.122	0.67	135.8	0.202	0.88
CCM-C0.25-IrOx	0.1	60.2	112.4	0.087	0.73	174.1	0.092	0.81
CCM-C0-IrOx	1	52.0	9.8	0.127	0.99	40.7	0.073	0.75
CCM-C0.1-IrOx	1	52.6	19	0.043	0.83	29.5	0.234	0.74
CCM-C0.25-IrOx	1	60.4	1.7	0.020	1.00	49.8	0.091	0.71
CCM-C0-IrOx	2	51.9	5.9×10^{-4}	0.109	1.00	25.4	0.048	0.77
CCM-C0.1-IrOx	2	52.2	6.1×10^{-5}	0.019	0.99	30.4	0.242	0.62
CCM-C0.25-IrOx	2	59.9	1.5×10^{-4}	0.014	1.00	28.1	0.192	0.64